D1.7 -- Intermediate Report on the WHERE2 Channel Model

Steinböck, Gerhard; Pedersen, Troels; Fleury, Bernard Henri; Corre, Yoann; Laaraiedh, Mohamed; Pedersen, Troels; Raspopoulos, Marios; Raulefs, Ronald; Stéphan, Julien; Steinböck, Gerhard; Uguen, Bernhard; Wang, Wei

Publication date:
2012

Document Version
Early version, also known as pre-print

ICT–248894 WHERE2
D1.7
Intermediate Report on the WHERE2 Channel Model

Contractual Date of Delivery to the CEC: M24
Actual Date of Delivery to the CEC: 03.07.2012
Editor: Gerhard Steinboeck, Troels Pedersen, Bernard H. Fleury
Authors: Yoann Corre, Mohamed Laaraiedh, Troels Pedersen, Marios Raspopoulos, Ronald Raulefs, Julien Stéphan, Gerhard Steinboeck, Bernard Uguen, Wei Wang
Participants: AAU, DLR, SIG, SIR, UR1
Work package: WP1 – Scenarios, Relevant Models and Market Feedback
Est. person months:
Security: PU
Nature: R
Version: 1.0
Total number of pages: 132

Abstract:

This deliverable is an intermediate report on the activities towards a collection of common WHERE2 channel models. The report introduces the heterogenous simulation scenario and summarizes the activities and achievements in WP1 to simulate such a scenario. In WHERE2 two aspects of heterogeneity are considered: the radio access technologies and the environments. As such, investigations with respect to narrowband, wideband and ultra wideband channel characterization in multi-link scenarios are reported. Furthermore, indoor and indoor-to-outdoor environments are considered. The channel variability due to human crowd activity and the variations of the antenna response are investigated as well.

Keyword list: Multi-link channels, delay-power spectrum, ray tracing, heterogenous communication system, indoor-to-outdoor, indoor, reverberation, non-line of sight bias, sparse parameter estimation, antenna response, measurement insertion refined ray tracing.

EXECUTIVE SUMMARY

This deliverable presents the intermediate research results, achieved in WHERE2 WP1 for the purpose of channel modeling for localization with heterogenous communication systems. The deliverable contains two parts: A body part (Section 2 to 5) which summarizes the reported activities and outcomes organized topic-wise and an appendix containing the related publications and reports which provide further details.

Section 2 summarizes the envisioned common channel simulation scenario. This scenario is heterogenous with respect to the used radio access technologies and the considered environments.

Section 3 presents results on channel modeling for cooperative communication and localization systems. It is the continuation of the work previously reported in deliverable D1.3. We present in Subsection 3.1 additional results on the model for the distance dependent delay power spectrum introduced in D1.3, i.e. higher moment generating function, kurtosis and Rice factor versus transmitter-receiver distance and the characterization of the so called reverberation region. We report in Subsection 3.2 results on the delay dispersion modeling using spatial point processes and provide a mathematical framework to study the impact of the delay dispersion on time of arrival-based ranging. Additionally, we report results on the behavior of the received power in a multi-link scenario. Combining the results of Subsection 3.3 “In-room Reverberant Multi-link Channels: Preliminary Investigations” and Subsection 3.4 “Multi-link Channel: Statistical Description of Received Power and Ongoing Work”, we obtain a multi-link model for the received power.

Section 4 reports ray tracing technologies for the use in the envisioned heterogenous channel simulation scenario. This is a continuation of the work presented in deliverables D1.5 and D1.6. This section covers the conversion of a narrowband ray tracing tool to operate in the ultra wideband regime in Subsection 4.1. We consider heterogenous environment aspects in Subsection 4.2. Furthermore, we contrast indoor-to-outdoor measurements from a specific site with ray tracing simulations of the said site. This lead to several extensions in the ray tracing tool. Subsection 4.3 discusses the refinement of ray tracing results by insertion of measurements. The use of a graph based ray tracing simulator for multi-link scenarios is detailed in Subsection 4.4.

Section 5 is concerned with estimation and modeling of channel variability. A proposal to estimate common multipath components (common scattering objects) in a multi-link indoor scenario is introduced in Subsection 5.1. The proposal is based on the estimator already described in D1.4 to investigate e.g. the multipath life time (distance) in outdoor-to-indoor scenarios. Subsection 5.2 presents simulation and measurement results on the variation of received power due to human crowd activity. The human crowd activity is part of the envisioned common channel simulation scenario. Subsection 5.3 introduces a measurement campaign of frequency dependent antenna responses for ultra wideband antennas. We use these measurements to study and model the influence of the antenna response and its variability on fingerprint databases. Sparse channel estimation in the context of communications is presented in Subsection 5.4. This estimator may be used to extract channel features for fingerprint databases or to extract the “essential” radio channel parameters for localization and communication purposes from measurements.

The results and the ongoing activities presented in this deliverable extend the achievements reported previously in deliverable D1.3 to D1.6 to characterize the multi-link radio propagation channel for heterogenous communication systems. The work is continuously extended and parts are already used in other work packages, i.e. WP2 T2.2 and T2.3, within WHERE2.

TABLE OF CONTENTS

Authors

Partner	Name	Phone/e-mail
AAU	Bernard H. Fleury	Phone: +45 9940 8629
		e-mail: bfl@es.aau.dk
	Troels Pedersen	Phone: +45 9940 8672
		e-mail: troels@es.aau.dk
	Gerhard Steinboeck	Phone: +45 9940 8615
		e-mail: gs@es.aau.dk
DLR	Ronald Raulefs	Phone: +49 8153 28 2803
		e-mail: Ronald.Raulefs@dlr.de
	Wei Wang	Phone: +49 8153 28 2801
		e-mail: Wei.Wang@dlr.de
SIR	Julien Stéphan	Phone: +33 223 480 500
		e-mail: jstephan@siradel.com
	Yves Lostanlen	Phone: N/A
		e-mail: ylostanlen@siradel.com
	Yoann Corre	Phone: +33 223 480 500
		e-mail: ycorre@siradel.com
SIG	Marios Raspopoulos	Phone: N/A
		e-mail: m.raspopoulos@sigintsolutions.com
UR1	Bernard Uguen	Phone: N/A
		e-mail: bernard.uguen@univ-rennes1.fr
	Mohamed Laaraiedh	Phone: +33 223 235 075
		e-mail: mohamed.laaraiedh@univ-rennes1.fr

List of Acronyms and Abbreviations

3GPP	3rd Generation Partnership Project
AP	Access Point
CIR	Channel Impulse Response
CW	Continuous Wave
FDP	First Detectable Path
GLoS	Geometrical Line-of-Sight
GSCM	Geometric Stochastic Channel Model
GSM	Global System for Mobile Communications
GNSS	Global Navigation Satellite Systems
GPS	Global Positioning System
IR	Impulse Response
IR-UWB	Impulse Response - Ultra Wideband
LDR-WSN	Low Data Rate Wireless Sensor Network
LoS	Line-of-Sight
LTE	Long Term Evolution
NLoS	None Line-of-Sight
OFDM	Orthogonal Frequency-division Multiplexing
PDP	Power Delay Profile
RAT	Radio Access Technology
RMS	Root Mean Square
RSS	Received Signal Strength
RSSI	Received Signal Strength Indicator
TB	Time Based
UMTS	Universal Mobile Telecommunications System
UWB	Ultra Wideband
WHERE2	Wireless Hybrid Enhanced Mobile Radio Estimators - Phase 2
WiFi	Wireless Fidelity (IEEE 802.11)
WiMAX	Worldwide Interoperability for Microwave Access
WP	Work Package
WSN	Wireless Sensor Network

1 INTRODUCTION

This deliverable is entitled "Intermediate Report on the WHERE2 Channel Model". During the progress of the project we realized that a single channel model will not suffice to fulfill the needs in radio localization; rather a collection of models with different specific purposes will be necessary. Based on the WHERE2 deliverable D1.1 [1] we define in this deliverable a synthetic heterogenous scenario. We consider heterogeneity of the radio channel in two respects: i) heterogeneity of the radio access technology (RAT) and ii) heterogeneity of the propagation environment. The WHERE2 Workpackage 1 (WP1) deliverables D1.3 to D1.6 [2, 3, 4, 5] focused on different aspects of modeling such heterogenous environments for localization. In the present deliverable we combine and extend this work. Thus, we describe the progress of the research focussing on obtaining a collection of models that cover the different aspects in heterogenous channels.

This report is structured in two parts: a body part that provides a summary of the activities and results towards the common channel simulation scenario; and an appendix containing related publications and reports produced within WP1 after the submission of previous deliverables. The latter part is meant to provide the readers with more detailed information on the activities if needed or wanted. The structure of the deliverable is as follows:

Section 2: *The envisioned channel simulation scenario.* The challenges of heterogenous radio channel modeling are also emphasized.

Section 3: *Results on channel modeling for cooperative communication and localization systems.* The section includes for instance extensions of the distance dependent delay power spectrum model and the use of this model in multi-link scenarios. For the multi-link scenario the experimentally obtained received power values have been analyzed and a preliminary model is presented. Furthermore the mathematical framework of spatial point process is studied. This framework is important for the stochastic description of the delay dispersion of impulse responses as these random characteristics impact the accuracy of time of arrival-based range estimators.

Section 4: *Improvements of ray tracing techniques for heterogenous channel simulations.* Those improvements include the extension towards ultra wideband (UWB) ray tracing, indoor to outdoor simulation scenarios, the refinement of ray tracing simulations with measurement data for RSS fingerprinting databases and as well the graph based ray tracing to improve the simulation of multi-link (multi-user) scenarios.

Section 5: *Results and ongoing investigations of the channel variability due to movement and human interaction.* This is part in the considered channel simulation scenario. Experimental investigations and simulations have been conducted to study the received signal strength (RSS) variability due to human crowd activity. A measurement campaign of different UWB-antenna responses and the influence of human interaction on the antenna responses is presented. These measurements aim at aiding the statistical description of antenna responses and the influence of these responses on e.g. RSS fingerprinting databases. Furthermore, we discuss a proposal for the estimation of path life time and common paths in an indoor multi-link scenario. We include results of a novel sparse channel estimator. This estimator may provide reliable estimation of channel parameters to be used for localization.

Section 6: Conclusions.

Appendix A: The appendix contains a collection of already published or soon to be published articles and reports produced within WP1 of WHERE2. These documents provide with additional detail information on Sections 3 to 5.

2 COMMON CHANNEL SIMULATION SCENARIO

WP1 partners have decided to simulate channel realizations from a common realistic scenario that combines new channel prediction techniques developed in WHERE2. This scenario, derived from the D1.1 scenarios [1], includes multiple Access Points (APs), multiple Radio Access Technologies (RATs), fixed and mobile terminals as well as human crowd activity. The selected environment is an indoor office (based on the SIRADEL realistic layout [6]) including mobile pedestrians equipped or not with multi-standard terminals. Two kinds of radio links are addressed: Indoor-to-indoor short range links (between fixed APs and terminals as well as between terminals) and outdoor-to-indoor long-range links. Proposed radio network includes 3 LTE macrocell Base Stations (BS), 2 LTE and 2 Wi-Fi APs, and 2 short-range Low Data Rate Wireless Sensor Networks (LDR-WSN) based on Impulse Radio – Ultra Wideband (IR-UWB). Figure 1 illustrates the scenario.

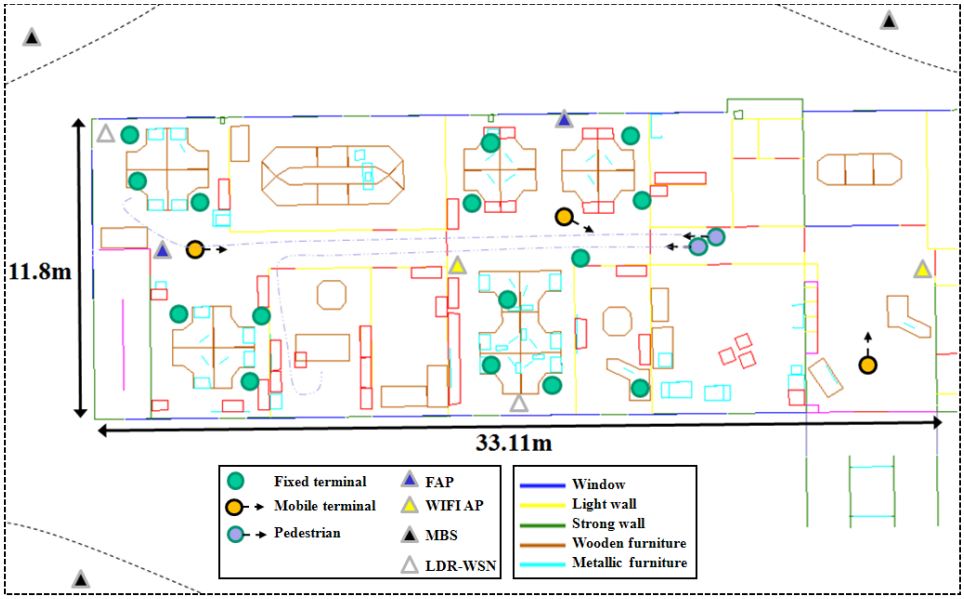

Figure 1: Target scenario.

Locations of APs and terminals are selected to correspond to a realistic scenario occurring during working hours. Fixed multi-standard terminals (green circles) are supposed to be located either on desk, in a pants pocket or in a jacket set on coat rack whereas the mobile multi-standard terminals are supposed to be held either in hand or in a pocket by 3 pedestrians (orange circles). Furthermore, 2 other pedestrians not equipped with terminals (blue circles) are supposedly moving inside the office.

Scenario duration is expected to be 30 s with a time resolution of 10 ms (i.e. a spatial resolution of 1 cm if pedestrians are moving at 1 m/s). Obviously, this target scenario is quite complex and involves many links and many time-variant situations to simulate. Its realization will be progressive: the definition and realization of simpler basic scenarios dedicated to the investigation of a particular technology (only Wi-Fi, LTE, LDR-WSN) or modeling method (pedestrian mobility model, impact of human crowd activity) is imagined. Each of them may be thus considered as a brick of the target scenario and supports a part of its realization. Results generated with this scenario will be available for any WHERE2 simulation test. Channel realizations will be provided as Matlab® files: one data structure for each time-variant radio link.

3 CHANNEL MODELING FOR COOPERATIVE COMMUNICATION AND LOCALIZATION SYSTEMS

In Section 3.1 AAU and DLR present further developments of the distance dependent delay power spectrum model introduced in deliverable D1.3 considering single-link scenarios. AAU investigates the delay dispersion of impulse responses obtained from radio channel models exhibiting similar delay power spectra. This is essential for the ranging accuracy of time of arrival (ToA) based range estimators. Subsection 3.2 presents a mathematical framework relying on spatial point processes to analyze and contrast different delay dispersive channel models. This mathematical framework can provide further insight for localization purposes. As appears from the scenario in Section 2, multiple links are an important part of the heterogenous simulation scenario. In Subsection 3.3 AAU and DLR investigate the use of the delay power spectrum model of Subsection 3.1 in multi-link situations. AAU and DLR devise a model for the correlation of the received power in multi-link situations in Subsection 3.4. We propose to use this correlation model together with the path loss model from Subsection 3.1.

3.1 Modeling the Delay Power Spectrum of Reverberant In-Room Channels

Experimental observations [7, 8] of the behavior of the delay-power spectrum for reverberant in-room channels show that the tail of the delay-power spectrum exhibits the same constant exponential decay regardless of the transmitter and receiver positions. Furthermore, a peak at the early part of the delay-power spectrum is strong at short transmitter-receiver distances and gradually vanishes as the distance increases. A similar behavior is observed in room acoustics [9] and electromagnetic fields in cavities [10].

Based on the observations from [7, 8], we propose in [11] a model for the distance dependent delay-power spectrum with a "primary" and a "reverberant" component. As already presented in deliverable D1.3 this model allows to predict the path loss, the mean delay and the rms delay spread as a function of transmitter-receiver distance via closed form expressions. This work is continued and elaborated in the paper included in Appendix A.2 where additionally the distance dependent higher order moments of the delay power spectrum, the kurtosis and the Rice factor from the proposed delay-power spectrum model are investigated.

The Appendix also includes a detailed investigation of the distance dependence of the primary and the reverberant components, leading to the definition of the reverberation region, i.e. the range of distances where the reverberant component has equal or larger power than the primary component. The implications of the reverberation region on path gain, main delay, rms delay spread and kurtosis are also discussed. The predictions of the model agree well with experimental observations.

An open issue is the coupling between neighboring rooms, which would allow for the extension of the proposed model to neighboring rooms. Ray tracing simulations may be used to predict the reverberation time for specific environments if measurements of the reverberation time are lacking. Or if reverberation time measurements are available, ray tracing tools may be "calibrated" when a detailed environment description is lacking.

3.2 Statistical Characterization of Delay Dispersion for Time of Arrival Based Range Estimators

The delay dispersion of radio signals is an important effect, which impacts e.g. the accuracy of time of arrival (TOA)-based range estimators. For TOA-based estimation, the early part of the channel impulse response is particularly important, as this part governs the estimation errors. Stochastic radio channel models relying on a random spikes representation of the

channel impulse response are commonplace for wideband and ultra-wideband communications. In this context, location-dependent parameters of the channel response can be seen as random variables with statistical properties depending on the random mechanism underlying the generation of this response. Interestingly, the random mechanism for generating the channel response is traditionally well-known, but the resulting statistical properties of features in the response that are potentially critical for localization purpose, such as the rate (intensity) of occurrence of the delays of multipath components and the delay power profile are not familiar within the localization community, and actually the communications community as well. An emblematic example is the model by Saleh & Valenzuela that we discuss below.

Two classic and seminal stochastic radio channel models are those by Turin et al. [13] and Saleh & Valenzuela [14]. To some extent the model by Saleh & Valenzuela (the S-V model) can be seen as a generalization of the model by Turin. Specifically, this generalization aims at mimicking cluster alike behavior. Subsequently, several variants of the S-V model have appeared since it was originally proposed in 1987. Unfortunately, these channel models have not been developed within any unifying mathematical framework. Instead their individual treatment is of rather ad-hoc nature and for this reason any two different models are not easily contrasted.

In Appendix A.1 we showcase how the general theory for spatial point processes provides an insightful view upon the inherent structure of the classical S-V model. Specifically, we revisit the model and reformulate it as a particular point process. Contrary to Saleh & Valenzuela's original double-layer construct we show that the component delays can be identified as the union of a Poisson point process and a Cox point process. We derive the associated intensity function as an immediate consequence of *Campbell's Theorem*. This intensity function increases linearly with propagation delay. Furthermore, we obtain the delay-power intensity in a simple and direct way by invoking once more Campbell's Theorem. In fact, this function does not decay exponentially. Our approach and results demonstrate the wide potential of Campbell's well-known theorem from the theory of spatial point processes in the context of stochastic radio channel modeling. In view of this, our conclusion is that the theory of spatial point processes and its powerful tools have not been fully exploited yet to analyze the properties of most proposed stochastic radio channel models. This theory appears to provide the necessary unifying framework for these models to be contrasted within.

3.3 In-room Reverberant Multi-link Channels: Preliminary Investigations

The distance dependent delay power spectrum model introduced in Section 3.1 and detailed in [12] characterizes the behavior for an entire room. As such, the model parameters are valid for the entire room regardless of the transmitter receiver locations within the room. Thus a single set of model parameters allows for the prediction of path gain (inverse of path loss), mean delay and rms delay spread versus transmitter receiver distance.

Appendix A.3 describes preliminary results on the delay power spectrum model used in a multi-link scenario. We validate the model by comparing the predicted received power, mean delay and rms delay spread with estimates obtained from multi-link measurements. We observe a good agreement of the model prediction trends with the estimates from the multi-link measurements. We observe a random fluctuation of the estimates around the model predictions. Those fluctuations may be generated as a combination of small and large scale fading. To obtain a full multi-link model we need to statistically characterize these fluctuations. Such a model may be used to obtain more robust distance estimators. Thus it is important to investigate the statistical dependencies of received power, mean delay and rms delay spread between different links and the inter parameter dependencies on each link. In

Section 3.4 is the statistical behavior of the power fluctuations investigated for the multi-link case. Investigation of the statistical characterization of the mean delay and rms delay spread and the inter parameter dependencies are ongoing work.

3.4 Multi-link Channel: Statistical Description of Received Power and Ongoing Work

We characterize the received power for cooperative positioning. The characterization is based on the indoor channel measurement campaign conducted at the German Aerospace Center (DLR) facilities as presented in WP1 D1.3 [2]. The measurements were performed with a measurement platform allowing for accurate transceiver position information during the quasi-static measurement. In Appendix A.4 we evaluate the multi-link cross covariance characteristics of the received power in a cooperative scenario. The correlation between the log power values of different links is insignificant. This is in accordance with the observations in [15]. We observe the log power values to be Gaussian distributed with a range dependent mean. The behavior of the mean versus range can be described according to a path loss model as for instance described in Appendix A.2. In the presented results the variance of the log power values appears to be constant with range. As a result, the received power can be modeled as a summation of two terms, the distance dependent mean value plus an additional random term which is generated by a zero mean Gaussian process independently for individual links.

Apart from the power, preliminary observations in ongoing work indicate a similar behavior for the root mean square (RMS) delay spread and mean delay. The varying terms of these delay dispersion parameters are found to be uncorrelated between links. Further evaluations similar to the one conducted for the received power in Appendix A.4 are currently performed for the time dispersive parameters. A joint model describing the received power, mean delay and rms delay spread in multi-link scenarios is envisioned.

Another open topic is a similar description of the joint multi-link model for received power and delay dispersion parameters in the NLoS scenario, where transceiver antennas are located in different rooms.

4 EVOLVED RAY TRACING FOR LOCALIZATION

The heterogenous channel simulation scenario in Section 2 uses various radio access technologies and considers the combination of different environments. The radio access technologies vary for instance in the used bandwidth. Material properties depend on the considered frequency range and this needs to be considered in ray tracing simulations. Sigint presents in Subsection 4.1 a method to extend ray tracing tools from narrowband (or wideband) to ultra wideband. Subsection 4.2 considers indoor to outdoor measurements which Siradel uses to improve a ray tracing tool. In indoor environments Siradel uses measurements to refine ray tracing simulations in Subsection 4.3. Such refinement improves predictions of radio maps used in RSS fingerprinting-based localization techniques. Finally, UR1 presents in Subsection 4.4 improvements for ray tracing in multi-link scenarios. UR1 uses graphs to structure and reuse communalities for multi-link scenarios which reduces complexity in the simulation.

4.1 Conversion of a Ray Tracing Tool from Narrowband into Ultra Wideband

This section presents the implementation and results of the band-divided method for converting a narrowband (NB) ray tracing (RT) simulator into ultra-wideband (UWB). As presented in Deliverable D1.6 [5] the band-divided method proposed by [16] is implemented to convert Sigint Solutions RT simulator (*3DTruEM*) into UWB. The algorithm is detailed in Appendix A.10.

The method, implemented in *MATLAB*, reads the impulse responses (IR) of each narrowband simulation, obtained using *3DTruEM*, combines them and generates an UWB impulse response. Depending on the required bandwidth of the UWB simulation the UWB band is split into a number of sub-bands of narrower bandwidth in each of which the characteristics of the antennas and electrical parameters are constant.

In order to verify the developed technique we carried out UWB measurements in an indoor environment using a vector network analyzer (VNA). The considered bandwidth is 1.5 GHz (3.1-4.6 GHz). This band is split into 15 subbands each with 100 MHz bandwidth. The indoor environment was recreated in the ray tracing tool. The subbands were simulated in the ray tracing tool *3DTruEM* and combined to obtain the full measured bandwidth for validation purposes. First results and a more detailed information regarding the simulations and the measurements can be found in Appendix A.10.

For the purpose of the simulations presented in the Appendix A.10 were constant values assumed for all the electrical parameters of the walls in the modeled environment throughout the whole UWB frequency band. Practically this is not the case, therefore we plan to carry out measurements in order to characterize the frequency dependence of the materials in the environment in the bandwidth of the simulation (3.1-4.6 GHz). This work will be done in the frame work of task T2.2.2.3 (See deliverable D2.2 [17]). Also we plan to investigate the accuracy of the UWB simulation against the number and bandwidth of the individual narrowband simulations which are needed to generate the UWB IR.

4.2 Design of a Novel Indoor-to-outdoor Site Specific Model

We propose an advanced ray-tracing model to predict the indoor-to-outdoor radio wave propagation. This model is an enriched version of a ray-tracing tool already developed for urban environments that is able to predict the path-loss for indoor-to-outdoor radio links [18]. Several successive enhancements have been first designed and introduced in the model in order to improve the path-loss prediction. These enhancements are based on a fine characterization of the initial model performance from a large CW measurement campaign. Enhancements

notably include the integration of building windows and internal partitions in the environment representation in order to make distinction between different indoor-to-outdoor interface losses (>=2dB for the window, >=10dB for the exterior building wall) and generate diffractions at the window vertical frames. Besides, the path from the indoor terminal to the first outdoor interaction is no more necessarily a straight line; the model searches for a dominant path with lowest possible loss (short indoor paths and propagation through window are then favored). These first enhancements sensibly improve the matching between measured and predicted path loss (see D1.6 [5] for more details).

Though the model calculates 3D ray paths from interaction with the building facades (or with any other outdoor clutter like vegetation or ground), it does not yet allow getting a fully realistic multipath channel prediction for indoor-to-outdoor links. Current investigations are focused on the enhancement of the prediction of multipath characteristics (power delay profile and angle power profiles in particular). To that end, new dominant multi-paths are computed, which are resulting from in-building interactions on the partitions as well as diffraction at window frames. This computation is based on the Uniform Theory of Diffraction (UTD). An evaluation of these enhancements is on-going based on wideband MIMO channel measurements collected in another environment. These measurements were collected (in frame of a previous project) for several indoor/outdoor radio links from a channel sounder operating at the frequency of 3.5 GHz. Measured multi-paths have been extracted from application of a high resolution algorithm (i.e. SAGE algorithm [19]). The measurement environment is a typical 6-floor building located in a university campus, composed of offices, classrooms and long corridors. The analysis is currently based on six radio links for which the direct-path is only obstructed by a window. These radio links have been selected in order to be the most confident as possible on the multipath parameters extracted from the measurements. The receiver locations are distributed on the first and second floor.

This model is expected to be used in task T2.3 to investigate extraction of context-aware features from indoor-to-outdoor data (see D2.3 [20] for details).

4.3 Refined Ray Tracing Simulations by Measurement Insertion

The initial approach for this task was introduced in deliverable D1.5 [4] and was to locally correct the ray-tracing coverage maps with the insertion of measurement data. This technique should ease the construction of the RSS fingerprint database (which requires significant time and effort if only based on measurements) as well as its accuracy (compared to common techniques using only propagation models). Nevertheless, as detailed in the previous deliverable D1.6 [5], we recently refined the scope of our work to investigate another promising solution: manifold alignment. This solution is based on a semi-supervised transfer learning algorithm that exploits manifold properties between the radio model and calibration fingerprints for direct localization. It has the advantage to combine both objectives of radio map and localization refinements into a joint formulation. Indeed, once alignment between the three input data sets (ray-tracing coverage maps, measured calibration data (limited number of data) and observations collected without any supervision) is achieved, this solution provides an enriched and refined RSS fingerprint database as well as an estimated localization for the observations. We currently evaluate its performance from the WHERE1 indoor measurements [21] [22], for which 4 access points are disseminated in a typical recent office building (350 m^2) and a receiver is moved over a grid of 302 points (resolution of the grid is lower than 1 m). A small part of measured points have been arbitrarily extracted from the database to emulate the calibration measurements whereas another part is used to emulate the observations collected by a walking person. First outcomes show that this solution provides accurate location performances for a limited number of calibration measurements. A complete description of this evaluation will be detailed in the next

WP2 T2.2 deliverable.

4.4 Ray Tracing Propagation Modeling for Indoor Localization Purposes Using Graphs

Ray-tracing tools have been used for many years to deterministically model radio propagation channels in order to design communications systems [23, 24, 25]. Recently, these tools are also being used for the design of localization systems [26, 27, 28, 29]. Within *WHERE2* project, *UR1* is continuing developing the ray-tracing tool *PyRay* and adapting it to heterogeneous radio channels.

PyRay is reinforced by a graph-based description of indoor channels based on four types of graphs: the structure graph, the visibility graph, the topological graph and the graph of rooms [30]. Based on this graph representation and using Dijkstra's algorithm, the signature of a ray is determined as the sequence of interactions of the ray from the transmitter to the receiver. In addition, a two-step process is developed in order to determine rays from their signatures. This ray determining process is used together with the graph-based representation of the radio channel to make its simulation faster [30]. This graph-based ray tracing technique is presented in Appendix A.6.

PyRay is used to carry out UWB simulations of the synthetic environment defined within Task T2.3 [20]. The obtained realistic simulations are used within localization algorithms. The applications of those simulations are the extraction of location dependent parameters and the establishment of fingerprinting databases. These two applications would allow to substitute and/or complement measurement campaigns which are usually very laborious to carry out. The results obtained using simulations are compared to those obtained using measurements in the same environment in order to show the reliability of ray tracing tools in localization algorithms. The comparison shows a good agreement between measurements and simulations provided that environment and antennas are fairly described in the ray-tracing tool. All these results are shown and developed in Appendix A.7

5 ESTIMATION AND MODELING OF CHANNEL VARIABILITY

In this Section DLR considers variability due to path lifetime (Subsection 5.1). Siradel investigates channel variability due to human crowds in Subsection 5.2. Together, AAU and UR1 conducted a antenna response measurement campaign to study the channel variation due to antenna responses (Subsection 5.3). AAU presents in Subsection 5.4 a novel sparse channel estimator which is able to estimate parameters of an unknown number of multipath components.

5.1 Estimation of In-room Time Variant Channel Parameters

In realistic scenarios for location-tracking/navigation applications, the multipaths are time-variant in delays, amplitudes, phases and incoming angles due to movements of transmitters, receivers, and/or reflectors. This results into the requirement of knowledge of spatial characteristics of the channel. We have evaluated the measurement data of outdoor-to-indoor scenarios as described in [3, 31]. The paths are tracked in terms of delay in sub-sample domain and furthermore the smooth time evolution of the CIR based on the estimated parameters using the SAGE based Kalman filter.

In the future contribution we are going to perform the same evaluations based on the measurement data in the in-room cooperative scenarios. One open topic in this contribution is to investigate the spatial features, like life-time or life-distance like in [31, 32]. Furthermore, we will evaluate the correlation of path lives from different links together with corresponding AoAs.

5.2 Time-variant Channel Modeling Related to Indoor Human Crowd Activity

We extended a geometric stochastic channel model (GSCM) and a deterministic ray-tracing model to simulate indoor time-variant channel properties related to human crowd activity. The deterministic method, detailed in the previous deliverables D1.5 [4] and D1.6 [5], has been recently evaluated and refined based on a CW measurement campaign conducted in January and March 2012 at the Siradel premises. The main specifications of the measurements are provided in the Appendix A.5. Two different scenarios are addressed for the same static LoS radio link:

- Scenario M1: Measurements collected during long periods at different times without Human Crowd Activity (HCA) or with a monitored (but uncontrolled) HCA.
- Scenario M2: Characterization of time variations from the controlled movement of one single person.

Scenario M1 aims at collecting some reference statistics (quantitative data) for characterization of the radio channel dynamic in the measurement area, whereas scenario M2 is used to validate and refine the simulation methods as well as to provide a precise characterization of the fading (on large and small scale components).

Analysis of scenario M1 allows to demonstrate that the received power is very stable (standard deviation is 0.013dB) when there is no human crowd activity. It globally increases and is more dispersive when there are several moving or static standing persons in the open space: the mean standard deviation is 5.5dB when 5 persons are standing in the room. The analysis has also put forward that the Ricean K-factor sensibly decreases as soon as a person moves near the radio link. Scenario M2 has been divided in 6 different sub-scenarios. Each one has been measured several times with same HCA, or changing the direction of the person movement to the opposite, in order to confirm the reproducibility of the observations. The sub-scenarios are detailed in Appendix A.5.

A shadowing pattern has been extracted from each scenario, obtained from a 70ms-long (i.e. half-wavelength for a walking speed of 1 m/s) sliding window filtering of received power plus an averaging of all reproductions of the same measurement. These measured patterns are compared to the ones simulated by the deterministic simulation method. We get two important conclusions:

- The phase associated to the simulated ray paths (before adding impact of the human body) strongly impacts the simulated pattern; the importance of these initial phases is confirmed by analysis of one measured sub-scenario (i.e. M2.6 in Appendix A.5).
- The measured patterns may be reproduced by the deterministic approach once the initial phases are tuned. The tuning process is detailed in Appendix A.5 and results are shown.

Several enhancements have been derived from this analysis, including a new technique for simulation of the time-variant phase spectrum and calculation of the Doppler shift.

A detailed description of this work can be found in Appendix A.5. Next step are first to derive new enhancements for the GSCM simulation method, and second to integrate the human crowd activity impact in the simulation of the common WHERE2 channel scenario (see Section 2).

5.3 UWB Antenna Measurement Campaign

In fingerprinting, the position is found by comparing an observed measurement with fingerprints in a pre-recorded database. One cannot assume, that the database is recorded with exactly the same equipment as the equipment used for the positioning and in particular the antennas used to record the database and at the terminal to be localized. The observed signal, and thus the matching of fingerprints, are affected by the antenna systems used to record the database and to record new fingerprints at the terminal to be localized. As a result, the observed signal may differ from the fingerprints in the database, even when the terminal is located at exactly the same position as used in the database. Moreover, this difference is affected by an unknown antenna response due to user operation, along with an unknown antenna orientation due to user movement. To study the variability of fingerprints induced by the unknown and varying antenna response, along with the unknown, and possibly time-varying antenna orientation, it is necessary to propose stochastic models including these effects.

As a first stage in this effort we have planned and conducted a two-day antenna measurement campaign performed in cooperation between AAU and UR1 using the nearfield measurement chamber at INSA, Rennes, April 2012. The objective of the campaign is to collect data for characterizing the variability of the radiation pattern of ultra wideband (UWB) antennas due to antenna structure and the human body in the vicinity of the antenna. In the measurements the human body was represented by a phantom of an arm. The complete measurement campaign consists of a series of four measurements: S1: Responses were measured of 17 UWB antennas for the purpose of characterizing the variability due to change of antennas. S2: Antenna responses were measured in the presence of the phantom at various antenna-phantom distances. S3: The antenna responses were measured for different phantom-antenna angles and distances. S4: The measurement series S4 is an auxiliary measurement series. The measurement report in Appendix A.9 gives a full description of the equipment and measurement series.

The next steps are to finalize the necessary postprocessing software, to run it on the data, and to propose a stochastic model for the antenna responses which can be used in the evaluation of fingerprinting techniques.

5.4 Bayesian Hierarchical Prior Modeling for Sparse Channel Estimation

In today's broad spectrum systems, the need to estimate frequency responses over a wide range of frequencies is not uncommon; in modern multicarrier communication systems, for instance, the wireless receiver needs to estimate a channel frequency response coefficient for each data subcarrier in the system, which could amount to hundreds of coefficients to estimate. Improved estimation accuracy can be obtained by, instead, estimating the parameters of the channel response in the delay domain, in which the response is expected to be sparse.

In Appendix A.8, we present an application of a sparse estimation technique to the problem of channel estimation for orthogonal frequency-division multiplexing (OFDM) for communication purposes. A sparse channel representation, however, may as well be used in localization for instance using those sparse channel representations as finger prints. Additionally estimating sparse channel representations from radio channel measurements may indicate the most important channel features to be included in simulation models, not only for communication but as well for localization purposes.

The proposed approach relies on the Bayesian formalism presented in [33] for the design of hierarchical prior models capturing the sparsity properties of the signal to be estimated. Based on the proposed models, realized with complex Gaussian scale mixtures, iterative inference schemes yielding sparse estimates of the signal of interest can be applied. The hierarchical models proposed in [33] are used in Appendix A.8 to model the prior distributions of the complex weights of the channel multipath components. By doing so and using a Fourier matrix as a basis, channel estimation for OFDM can be re-cast into the canonical form of sparse Bayesian learning [34]. Inference in the proposed model is solved by means of a variational message-passing algorithm.

From the analysis in Appendix A.8, the virtues of using sparse estimation techniques compared to linear filtering techniques become apparent. In addition, the numerical results illustrate how the models proposed in [33] lead to an improved accuracy of the estimates compared to other sparse estimation methods, thus resulting in an improved BER performance of the overall receiver. In the future, the robustness of the proposed technique against different types of channels (e.g. including a diffuse component) shall be tested. Another result of the estimation technique is the "optimum" number of estimated multipath components for the sparse channel representation. This for instance is of particular interest for tracking of multipath components in Section 5.1 where new components may be added and others fade out over time.

6 CONCLUSIONS

This intermediate deliverable summarizes the works conducted within the ongoing activities of task T1.2 in WP1. The envisioned common channel simulation scenario encompasses heterogenous radio access technologies and heterogenous environments. The scenario clearly shows the challenge for radio channel modeling and indicates that not all aspects for localization purposes can be modeled with a single channel model. Instead this challenge calls for a selection of different models with different specific purposes. We observe, however, that some of these models share commonalities and complement each other.

Consequently the ongoing and future work for the characterization of the radio channel still focuses for instance on multi-link channel characterization, channel variability caused by transmitter receiver movement, human crowd activity, antenna response variability and characterization of the delay power spectra versus distance. Additionally, the heterogeneous channel aspects related to the different radio access technologies are studied, i.e. the extension from narrowband to ultra wideband ray tracing tools or how to efficiently model the multi-user case in ray tracing with the use of graphs. The heterogenous channel related to different environments is covered by investigations of ray tracing in indoor and indoor to outdoor environments. Refinement of ray tracing results by measurement insertion is considered too.

The combination of all these channel modeling technologies leads to a common heterogeneous channel modeling "environment" covering the different purposes in localization which is envisioned for the final deliverable. The results obtained so far are already used in other work packages, for instance WP2 T2.2 and T2.3. The continuous work towards the common channel simulation scenario is shared with the other work packages of WHERE2 to support their contributions.

A APPENDIX

The appendix contains the collection of articles and reports which have been produced so far within the activities in WP1 of WHERE2. These documents provide the reader with more detailed and specific information on the outcome of these activities.The appendix contains the contributions:

A.1 Analysis of the Stochastic Channel Model by Saleh & Valenzuela via the Theory of Point Processes

M. L. Jakobsen, T. Pedersen, and B.H. Fleury Analysis of the Stochastic Channel Model by Saleh & Valenzuela via the Theory of Point Processes. *International Zurich Seminar on Communications proceedings Eidgenössische Technische Hochschule Zürich (2012).*, February 29-March 2, 2012, Sorell Hotel Zürichberg, Zurich, Switzerland.
http://dx.doi.org/10.3929/ethz-a-007023900

Analysis of the Stochastic Channel Model by Saleh & Valenzuela via the Theory of Point Processes

Morten Lomholt Jakobsen, Troels Pedersen and Bernard Henri Fleury {mlj,troels,bfl}@es.aau.dk
Section Navigation and Communications, Dept. of Electronic Systems, Aalborg University
Fredrik Bajers Vej 7B, DK-9220 Aalborg East, Denmark

***Abstract*—In this paper we revisit the classical channel model by Saleh & Valenzuela via the theory of spatial point processes. By reformulating this model as a particular point process and by repeated application of Campbell's Theorem we provide concise and elegant access to its overall structure and underlying features, like the intensity function of the component delays and the delay-power intensity. The flexibility and clarity of the mathematical instruments utilized to obtain these results lead us to conjecture that the theory of spatial point processes provides a unifying mathematical framework to define, analyze, and compare most channel models already suggested in literature and that the powerful tools of this framework have not been fully exploited in this context yet.**

I. Introduction

Literature regarding channel models for (indoor) radio propagation dates back earlier than 1960, and most commonly the wireless multipath channel is characterized via its (time and space varying) impulse response [1]. Two classic and seminal contributions within channel modeling are those by Turin et al. [2] and Saleh & Valenzuela [3]. To some extent the (indoor) model by Saleh & Valenzuela can be seen as a generalization of the (urban) model by Turin. Specifically, the generalization aimed at mimicking cluster alike behavior since this effect was reported to have been observed experimentally.

Ever since the model by Saleh & Valenzuela (for short the S-V model) was proposed in 1987, many refined or marginally extended variants have appeared, see e.g. [4] and [5]. Unfortunately, these channel models have not been developed within any unifying mathematical framework. Instead their treatment is of rather ad-hoc nature and, as a result, their inherent features remain essentially veiled and any two different models are not easily comparable.

Recently the authors of [6] and [7] reformulated and outlined the S-V model in terms of marked point processes. The S-V model has also been revisited in [8] by use of shot-noise tools and point process theory. Among other things the analysis in [7] and [8] show that the overall intensity of the relative delays of multipath components grows linearly with the propagation delay. Unfortunately, the mathematical tools used in [7] to extract the features of the model are not directly associated with the general theory of point processes. On the other hand, the tools used in [8] are rather advanced and the derivations less transparent. Accordingly, the potential theoretical benefits arising through these point process reformulations are not immediately evident.

In this paper we showcase how the general theory of spatial point processes provides an insightful view upon the inherent structure and features of the classical S-V model. Like [7] and [8] we revisit the model and reformulate it as a particular point process. Aligned with [7] we show that the component delays consist of the union of a Poisson point process and a Cox point process and we derive the associated intensity function as an immediate consequence of Campbell's Theorem. The derivation in [7] is similar but with no reference to Campbell's Theorem. Furthermore, and in contrast to the involved proofs relying on shot-noise tools in [8], we obtain the delay-power intensity in a simple and direct way by invoking once more Campbell's Theorem. These results demonstrate the potential of this well-known theorem from the theory of spatial point processes in the context of stochastic channel modeling. In view of this, our conclusion is that the theory of spatial point processes and its powerful tools have not been fully exploited yet to analyze the properties of most proposed stochastic channel models. This theory appears to provide the necessary unifying framework for which these models can be contrasted within.

II. Point Process Framework

We assume familiarity with the basics of the theory of spatial point processes (see [9, Sec. 1.3, Chap. 2] and [10, Sec. 1.5, 6.2] for highly recommendable introductions). Concepts from abstract measure theory will be kept at a minimum.

A. Locally finiteness and simplicity

Denote by Y a *locally finite* and *simple* point process defined on a d-dimensional space $S \subseteq \mathbb{R}^d$. For intuitive, practical and mathematical reasons, these two properties are convenient to impose since several technical aspects can then be disregarded. A point process is locally finite if the number of points falling in every *bounded Borel set* $B \subseteq S$ is *almost surely* finite. A point process is simple if, almost surely, no two points of the process coincide. Accordingly, any realization of the point process Y can be identified as a countable set of points $\{\boldsymbol{y}_1, \boldsymbol{y}_2, \boldsymbol{y}_3, \dots\}$, $\boldsymbol{y}_i \in S$, where the index i of $\boldsymbol{y}_i$ serves solely as a dummy label. Thus, the index is used only to distinguish points and to indicate countability. It does not indicate any ordering of the points.

B. The intensity function and Campbell's Theorem

Consider the *counting function* defined, using a generic indicator function $\mathbb{1}[\cdot] \in \{0, 1\}$, as

$$N_{Y}(B) := \sum_{\boldsymbol{y} \in Y} \mathbb{1}[\boldsymbol{y} \in B],$$

which equals the random number of points from Y falling in the set B. For any fixed and *bounded* B, the count $N_{Y}(B)$ is

a non-negative integer-valued random variable. The expected value of the counting function $\mu_{_Y}(B) := \mathbb{E}\big[N_{_Y}(B)\big]$ defines a *measure* on S, the so-called *intensity measure* of Y. If the intensity measure can be expressed as

$$\mu_{_Y}(B) = \int_B \varrho_{_Y}(\boldsymbol{y})\mathrm{d}\boldsymbol{y}, \quad B \subseteq S,$$

for a *locally integrable* function $\varrho_{_Y} : S \to [0, \infty)$, then $\varrho_{_Y}$ is called the *intensity function* of Y. The case when the intensity function exists is by far the most important for applications [11]. The importance of the intensity function is evident from the following result, often referred to as *Campbell's Theorem*.

Campbell's Theorem. *Let Y be a point process on $S \subseteq \mathbb{R}^d$ with intensity function $\varrho_{_Y}$. Then for a real or complex-valued measurable function $h : S \to \mathbb{R}$ (or $\mathbb{C}$), the random variable $\sum_{\boldsymbol{y}\in Y} h(\boldsymbol{y})$ has expected valued*

$$\mathbb{E}\Big[\sum_{\boldsymbol{y}\in Y} h(\boldsymbol{y})\Big] = \int_S h(\boldsymbol{y})\varrho_{_Y}(\boldsymbol{y})\mathrm{d}\boldsymbol{y}, \tag{1}$$

provided that the integral on the right exists.

Proofs with varying degrees of detail can be found in [9, Sec. 3.2], [11, Prop. 4.1] and [12, Thm. 2.2]. Often, the theorem is stated only for non-negative functions h, since the equality in (1) is then unconditionally true, i.e. the integral is always well-defined but possibly divergent. When h is real-valued some care must be taken since the integral at the right hand side of (1) has no meaning if the positive and the negative part of h are not integrable. Similar care must be taken for complex h.

C. Poisson and Cox point processes

We now define two classes of point processes which are particularly important for our treatment in the forthcoming section, namely Poisson point processes and Cox point processes. These definitions can be found in many text books covering the theory of spatial point processes. Our treatment is directly inspired by [11] and the interested reader may consult [10]–[12] for further details.

Definition. *A point process Y on $S \subseteq \mathbb{R}^d$ is called a Poisson point process with intensity function $\varrho_{_Y}$ if:*

- (i) *For any $B \subseteq S$ with $\mu_{_Y}(B) = \int_B \varrho_{_Y}(\boldsymbol{s})d\boldsymbol{s} < \infty$ the count $N_{_Y}(B)$ is Poisson distributed with mean $\mu_{_Y}(B)$.*
- (ii) *Given that $N_{_Y}(B) = n \in \mathbb{N}$ where $0 < \mu_{_Y}(B) < \infty$, the distribution of $Y \cap B$ is the same as that of n points drawn i.i.d. according to $f_{_B}$, where*

$$f_{_B}(\boldsymbol{s}) := \frac{\varrho_{_Y}(\boldsymbol{s})\mathbb{1}[\boldsymbol{s} \in B]}{\mu_{_Y}(B)}.$$

We write $Y \sim \texttt{PoissonPP}\big(S,\ \varrho_{_Y}\big)$.

Definition. *Let $Z(\boldsymbol{s}),\ \boldsymbol{s} \in S$, be a non-negative random field such that, almost surely, every realization of Z is a locally integrable function on S. If a point process Y, conditioned on Z, is a Poisson point process with intensity function Z, then Y is called a Cox point process driven by Z.*

Cox point processes (also often referred to as *doubly stochastic Poisson point processes* [10]) are flexible models for clustered point patterns. Specifically, the two-level construction most commonly entails the Cox class to exhibit so-called *over-dispersion* compared to the Poisson class [11, Sec. 5.2].

III. The Model by Saleh & Valenzuela

In this section we analyze the impulse response of the classical S-V model within the framework of spatial point processes. The main purpose of this effort is to straightforwardly derive the features of this model through a flexible and powerful theory. Several relevant aspects of the model are revealed through this reformulation, e.g. its overall delay intensity, a concise and clear derivation of the average power gain and, a simple derivation of the delay-power intensity as well.

A. Classical formulation

Saleh & Valenzuela define the channel impulse response with *cluster* and *within-cluster* delays as [3, Eq. (25)]

$$h(t) = \sum_{\ell=0}^{\infty}\sum_{k=0}^{\infty} \beta_{k,\ell}\exp(j\theta_{k,\ell})\delta\big(t - (T_\ell + \tau_{k,\ell})\big), \tag{2}$$

where δ is the Dirac delta and j is the imaginary unit. The index ℓ indicates a certain cluster and k is the within-cluster index. By definition in [3], $T_0 = 0$ and $\tau_{0,\ell} = 0$ for each $\ell \in \mathbb{N}_0 := \{0\} \cup \mathbb{N}$. Beside these fixed delay components, a sequence of Poisson point processes are suggested such that

- $\big\{T_\ell\big\}_{\ell\in\mathbb{N}} \sim \texttt{PoissonPP}\big(\mathbb{R}_+,\ \Lambda\big)$
- $\big\{\tau_{k,\ell}\big\}_{k\in\mathbb{N}} \sim \texttt{PoissonPP}\big(\mathbb{R}_+,\ \lambda\big)$ for each $\ell \in \mathbb{N}_0$,

with $\Lambda, \lambda > 0$ being two parameters. Moreover, conditional second-order moments are modeled such that [3, Eq. (26)]

$$\mathbb{E}\big[\beta_{k,\ell}^2\big|T_\ell, \tau_{k,\ell}\big] = Q\exp\big(-T_\ell/\Gamma\big)\exp\big(-\tau_{k,\ell}/\gamma\big), \tag{3}$$

with $\Gamma, \gamma > 0$ and Q being the average power gain of the first component within the first cluster (i.e. corresponding to the fixed delay T_0). Conditioned on all T_ℓ's and all $\tau_{k,\ell}$'s, the $\beta_{k,\ell}$'s are assumed to be mutually independent random variables. Specifically, each power gain $\beta_{k,\ell}^2$, conditioned on T_ℓ and $\tau_{k,\ell}$, should follow an exponential distribution with mean parameter decaying as described by (3). Fig. 1 illustrates the Poisson point processes involved in the S-V model.

Finally, it was mentioned in [3] that practically the doubly-infinite sum in (2) should "stop" whenever each of the exponentially decaying terms in (3) had become small enough. Through the insight gained via the forthcoming reformulation of this classical channel model we are able to motivate a less heuristic "stopping criterion".

B. Point process formulation

Naturally, we select the space $S = \mathbb{R}_+$ and let $T_0 = 0$ as above. In addition, we introduce the point processes:

$$\begin{aligned}
C &:= \big\{T_\ell\big\}_{\ell\in\mathbb{N}} && \big(\text{all } \textit{cluster} \text{ delays except } T_0\big)\\
W_\ell &:= \big\{T_\ell + \tau_{k,\ell}\big\}_{k\in\mathbb{N}} && \big(\text{delays } \textit{within} \text{ the } \ell\text{'th cluster}\big)\\
W &:= \bigcup_{\ell=0}^{\infty} W_\ell && \big(\text{all } \textit{within-cluster} \text{ delays}\big)\\
Y &:= C \cup W && \big(\text{all propagation delays except } T_0\big).
\end{aligned}$$

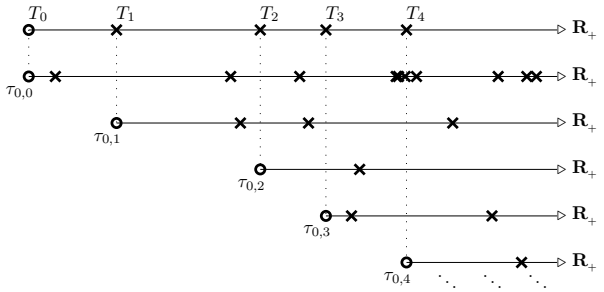

Figure 1. Realization of Poisson point processes corresponding to the S-V model. Circle points indicate fixed delay components. The top process occurs with rate Λ while each of the lower processes occurs with rate λ. A new point process is initialized whenever a new point emerges from the top process.

Notice that C is the Poisson point process specified at first in the previous paragraph. Its intensity function has a simple form, namely $\varrho_{C}(t) = \Lambda$ for all $t \in S$. By conditioning, we immediately identify a sequence of Poisson point processes

$$W_\ell \big| T_\ell \sim \texttt{PoissonPP}\Big(\mathbb{R}_+,\ \lambda \mathbb{1}\big[t > T_\ell\big]\Big), \quad \ell \in \mathbb{N}_0,$$

and since the Poisson class is stable with respect to countable superpositions [11, Prop. 3.6], we see that

$$W \big| C \sim \texttt{PoissonPP}\Big(\mathbb{R}_+,\ \widetilde{\varrho}_{W}\Big),$$

with the staircase-alike intensity function

$$\widetilde{\varrho}_{W}(t) = \lambda + \lambda \sum_{c \in C} \mathbb{1}\big[t > c\big], \quad t \in S. \tag{4}$$

Accordingly, we identify that the point process W, without conditioning on C, is a Cox point process driven by a stochastic process Z having the same functional form as $\widetilde{\varrho}_{W}$ in (4) but with C being random. The intensity function of the Cox point process W is $\varrho_{W}(t) = \mathbb{E}\big[Z(t)\big]$ [11, Sec. 5.2], and by direct application of Campbell's Theorem we get

$$\varrho_{W}(t) = \lambda + \lambda \mathbb{E}\left[\sum_{c \in C} \mathbb{1}\big[t > c\big]\right] = \lambda + \lambda \Lambda t, \quad t \in S.$$

Since $Y = C \cup W$ is a union of almost surely disjoint point processes, its associated intensity function reads [10, Sec. 6.2.3]

$$\varrho_{Y}(t) = \varrho_{C}(t) + \varrho_{W}(t) = \Lambda + \lambda + \lambda \Lambda t, \quad t \in S.$$

It is interesting to notice that the entire set of propagation delays (excluding the first component T_0) is the *union of a Poisson point process and a Cox point process*. Of course, the realization of W depends upon the realization of C, i.e. these two point processes are not independent. In [7] this interpretation was inherently adopted, without being explicitly mentioned. Another interesting yet expected observation is that the intensity function ϱ_{Y} rises linearly with propagation delay, see Fig. 2. The jump of height $\Lambda + \lambda$ at $T_0 = 0$ in the graph of ϱ_{Y} appears due to the cluster delays and the delays within the very first cluster. The term $\lambda \Lambda t$ result from the fact that, on average, a total of Λt additional clusters emerge during the interval $[0, t]$, with each and every one of them spawning further delay components at rate λ.

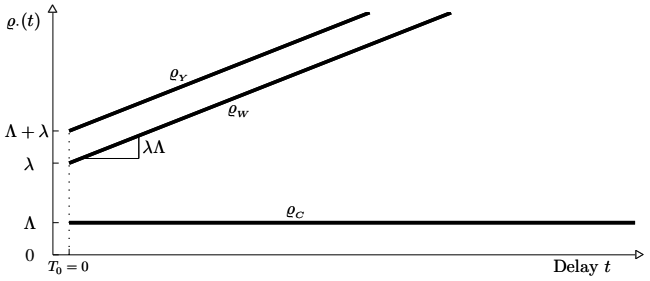

Figure 2. Intensity functions associated with the S-V model.

C. Multipath power gain

Analogous to the approach in [3], we consider the following non-negative random variable

$$G := \sum_{\ell=0}^{\infty} \sum_{k=0}^{\infty} \beta_{k,\ell}^2, \tag{5}$$

referred to as the total *multipath power gain* [3]. By splitting G into three terms corresponding to T_0 and arrivals in C and W, its expectation can be calculated as

$$\mathbb{E}\big[G\big] = \mathbb{E}\big[\beta_{0,0}^2\big] + \mathbb{E}\Bigg[\underbrace{\sum_{\ell=1}^{\infty} \beta_{0,\ell}^2}_{(\star)}\Bigg] + \mathbb{E}\Bigg[\underbrace{\sum_{\ell=0}^{\infty} \sum_{k=1}^{\infty} \beta_{k,\ell}^2}_{(\diamond)}\Bigg].$$

As in [3] we write $\beta\big(T_\ell, \tau_{k,\ell}\big)$ in substitute for $\beta_{k,\ell}$ to facilitate a comprehensible notation in the following. For additional clarity we introduce the function

$$f\big(t, \tilde{t}\big) := Q \exp\big(-t/\Gamma - \tilde{t}/\gamma\big), \quad t, \tilde{t} \in S.$$

Notice that $f\big(T_\ell, \tau_{k,\ell}\big) = f\big(T_\ell, (T_\ell + \tau_{k,\ell}) - T_\ell\big)$ coincides with the expression in (3). Then, by intermediate conditioning on C, we calculate the expectation of the term $(\star)$ as

$$\mathbb{E}\big[(\star)\big] = \mathbb{E}\left[\sum_{c \in C} \beta^2(c, 0)\right] = \mathbb{E}\left[\sum_{c \in C} \underbrace{\mathbb{E}\Big[\beta^2(c, 0)\,\Big|\, C\Big]}_{f(c,0)}\right] = Q\Lambda\Gamma,$$

where the final step follows by application of Campbell's Theorem. Next, by defining $C_0 := \{T_0\} \cup C$ and with a similar sequence of manipulations involving intermediate conditioning and Campbell's Theorem, we find the expected value of $(\diamond)$ to be[1]

$$\begin{aligned} \mathbb{E}\big[(\diamond)\big] &= \mathbb{E}\left[\sum_{c \in C_0} \sum_{w \in W_c} \beta^2(c, w - c)\right] \\ &= \mathbb{E}\left[\sum_{c \in C_0} \mathbb{E}\left[\sum_{w \in W_c} \underbrace{\mathbb{E}\Big[\beta^2(c, w - c)\Big| c, w\Big]}_{f(c, w-c)}\right]\right] = Q\big(1 + \Lambda\Gamma\big)\lambda\gamma. \end{aligned} \tag{6}$$

Accordingly, the average total power gain is given by

$$\begin{aligned} \mathbb{E}\big[G\big] &= \mathbb{E}\big[\beta_{0,0}^2\big] + \mathbb{E}\big[(\star)\big] + \mathbb{E}\big[(\diamond)\big] \\ &= \quad Q \quad + Q\Lambda\Gamma \ + \ Q\big(1 + \Lambda\Gamma\big)\lambda\gamma \\ &= Q\big(1 + \lambda\gamma\big)\big(1 + \Lambda\Gamma\big), \end{aligned} \tag{7}$$

[1]Note that in (6) we abuse notation since the collections W_c are not explicitly defined. We only defined these as W_ℓ via the counting index ℓ.

as was also reported in a footnote in [3]. Yet, the original sequence of arguments used to obtain this result may appear less instructive, see [3, Eq. (27), (31)] for comparison. Notice that, depending on how we choose to write out the product in (7), we end up with different interpretations of individual average power contributions.

D. Delay-power intensity

Motivated by the definition of G in (5) together with the relationship in (7), we consider

$$p(t) := \sum_{\ell=0}^{\infty}\sum_{k=0}^{\infty} \beta_{k,\ell}^2 \delta\big(t - (T_\ell + \tau_{k,\ell})\big).$$

We wish to calculate how the average power gains are distributed across delay. From (7) we already know the mean total power gain, yet we seek to obtain further insight. The above definition of $p(t)$ is motivated by the fact that $\int_0^\infty p(t)\mathrm{d}t = G$, and since $\mathbb{E}[G]$ is finite, the non-negative random variable G is itself finite almost surely. Accordingly, we define

$$P(t) := \mathbb{E}\big[p(t)\big], \quad t \in S,$$

and we refer to this function as the *delay-power intensity*. By similar manipulations as in the previous paragraph (conditioning, Campbell's Theorem, etc.) we find

$$\frac{P(t)}{Q} = \delta(t) + \begin{cases} k_1 \exp\big(-\frac{1}{\Gamma}t\big) + k_2 \exp\big(-\frac{1}{\gamma}t\big), & \Gamma \neq \gamma \\ \varrho_{_Y}(t)\exp\big(-\frac{1}{\gamma}t\big), & \Gamma = \gamma \end{cases}$$

where we have conveniently introduced the two constants

$$k_1 := \Lambda\Big(1 + \lambda\tfrac{\Gamma\gamma}{\Gamma-\gamma}\Big) \quad \text{and} \quad k_2 := \lambda\Big(1 - \Lambda\tfrac{\Gamma\gamma}{\Gamma-\gamma}\Big).$$

The same expression for $P(t)$ is obtained in [8, Chap. 2,3] using rather involved shot-noise tools with weighty notational overhead. Notice the particular relationship

$$\mathbb{E}[G] = \mathbb{E}\bigg[\int_0^\infty p(t)\mathrm{d}t\bigg] = \int_0^\infty \mathbb{E}\big[p(t)\big]\mathrm{d}t = \int_0^\infty P(t)\mathrm{d}t.$$

The delay-power intensity of the S-V model is depicted in Fig. 3. Notice that $P(t)$ is *not exponentially decaying*, not even when $\Gamma = \gamma$ since $\varrho_{_Y}$ rises linearly (compare with the dotted line in Fig. 3).

Finally, as mentioned in the beginning of this section, we are now able to motivate a simple "stopping criterion" suitable, e.g. for simulation purposes. Specifically, select a delay threshold $t_{\max}(\alpha)$ such that

$$\int_0^{t_{\max}(\alpha)} P(t)\mathrm{d}t = \alpha\mathbb{E}[G],$$

for a relevant choice of $\alpha \in (0,1)$, e.g. $\alpha = 0.99$.

IV. Conclusion

In this contribution we have revisited the radio channel model by Saleh & Valenzuela (the S-V model) within the framework of spatial point processes. We have shown that the component delays in the S-V model emerge from the union of a Poisson point process and a Cox point process. Furthermore, we have demonstrated that the intensity function of the component delays and the delay-power intensity can be derived in a straightforward and rigorous manner as an immediate consequence of Campbell's Theorem.

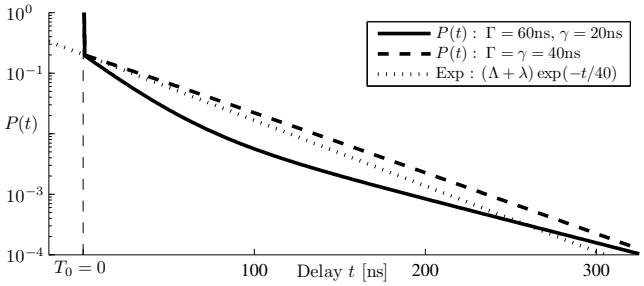

Figure 3. Delay-power intensity of the S-V model (solid line). The parameter values of $\Lambda, \lambda, \Gamma, \gamma$ correspond to the estimates reported in [3]. The dashed curve correspond to the selection $\Gamma = \gamma = 40$ns. For comparison, the dotted curve provides a purely exponential decay.

The above results indicate that the theory of spatial point processes yields a natural, unifying theoretical framework for dealing with stochastic channel models. This applies in particular to most channel models already suggested in literature, including the models by Turin et al. [2], Spencer et al. [4], and Chong et al. [5]. Our results also reveal that the powerful tools available in this framework, like Campbell's Theorem, have not been exploited to their full extent in this context yet. Overall the considered application to the S-V model and to some extent the work in [6]–[8] show that the resulting mathematical treatments inherit clarity and conciseness, in addition to rigorousness, in contrast to the traditionally used ad-hoc and heuristic arguments.

Acknowledgment

This work has been funded by the project ICT-248894 Wireless Hybrid Enhanced Mobile Radio Estimators 2 (WHERE2), the 4GMCT cooperative research project co-financed by Intel Mobile Communications, Agilent Technologies, AAU and the Danish National Advanced Technology Foundation, and by the Danish Agency for Science, Technology and Innovation.

References

[1] H. Hashemi, "The Indoor Radio Propagation Channel", *Proc. IEEE*, '93.
[2] G. L. Turin et al, "A statistical model of urban multipath propagation", *IEEE Trans. Vehic. Techn.*, 1972.
[3] A. A. M. Saleh and R. A. Valenzuela, "A statistical model for indoor multipath propagation", *IEEE J. Selected Areas in Commun.*, 1987.
[4] Q. H. Spencer et al, "Modeling the statistical time and angle of arrival characteristics of an indoor multipath channel", *IEEE JSAC*, 2000.
[5] C.-C. Chong et al, "A modified S-V clustering channel model for the UWB indoor residential environment", *IEEE VTC*, 2005.
[6] A. Ridolfi, "Power Spectra of Random Spikes and Related Complex Signals", PhD thesis, EPFL, Lausanne, Switzerland, 2004.
[7] R. F. Brøndum and E. Rubak, "Stochastic Channel Modelling - A Bayesian approach using reversible jump Markov chain Monte Carlo methods", Master's thesis, Aalborg University, Denmark, 2006.
[8] K. Hao, "Modeling and Statistical Analysis of Ultra-Wideband (UWB) Channels and Systems: A Point-Process Approach", PhD thesis, University of Wisconsin-Madison, Wisconsin, USA, 2006.
[9] J. F. C. Kingman, "Poisson Processes", Oxford University Press, 1993.
[10] J. Illian et al, "Statistical Analysis and Modelling of Spatial Point Patterns", John Wiley & Sons, 2008.
[11] J. Møller and R. P. Waagepetersen, "Statistical Inference and Simulation for Spatial Point Processes", Chapman & Hall/CRC, 2004.
[12] A. J. Baddeley, "Spatial Point Processes and their Applications" (in "Stochastic Geometry - Lecture Notes in Mathematics"), Springer, 2007.

A.2 Distance Dependent Model for the Delay Power Spectrum of In-room Reverberant Channels

G. Steinböck, T. Pedersen, B.H. Fleury, W. Wang, and R. Raulefs Distance Dependent Model for the Delay Power Spectrum of In-room Reverberant Channels. *IEEE Trans. Antennas Propagat.*, submitted.

Distance Dependent Model for the Delay Power Spectrum of In-room Reverberant Channels

Gerhard Steinböck, Troels Pedersen, Bernard Henri Fleury, Wei Wang and Ronald Raulefs

***Abstract*—A model based on experimental observations of the delay power spectrum in closed rooms is proposed. The model includes the distance between the transmitter and the receiver as a parameter which makes it suitable for range based radio localization. The experimental observations motivate the proposed model of the delay power spectrum with a primary (early) component and a reverberant component (tail). The primary component is modeled as a Dirac delta function weighted according to an inverse distance power law (d^{-n}). The reverberant component is an exponentially decaying function with onset equal to the propagation time between transmitter and receiver. Its power decays exponentially with distance. The proposed model allows for the prediction of e.g. the path loss, mean delay, rms delay spread, and kurtosis versus the distance. The model predictions are validated by measurements.**

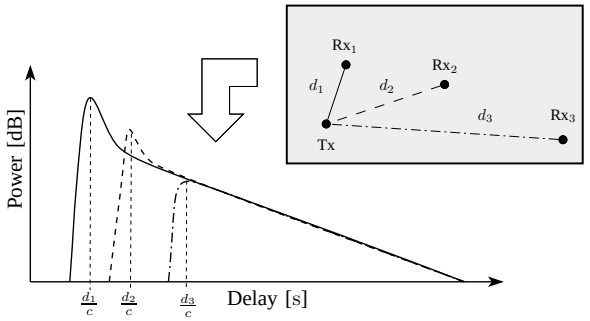

Fig. 1. Typical behavior of the bandlimited delay power spectrum experimentally observed at three different transmitter-receiver distances in an in-room environment (schematically presented by the grey box).

I. Introduction

Range based radio localization relies on models of the radio channel that incorporate distance as a parameter [1]. Such models allow for inferring on the transmitter-receiver distance from observations of range dependent channel features. For example currently deployed communication systems estimate the distance from the received signal strength based on a validated path loss model [1]. Wideband communication systems potentially allow for exploiting additional distance dependent information inherent in the temporal dispersive behavior of the radio channel. Delay dispersion is characterized by means of the delay power spectrum, which is defined as the averaged squared impulse response. Thus, models describing the behavior of the delay power spectrum versus distance are in demand.

In wireless communications the delay power spectrum is a key component of most stochastic models of the channel impulse response. It is typically modeled as a one-sided exponentially decaying function of the delay [2]. Moreover, it is normalized to some peak power and it is shifted in the delay domain in such a way that its onset is at zero delay. These transformations do not affect the bit error rate evaluation but remove distance information potentially exploitable for localization. Coverage analysis relies on separate path loss models for an entire building [2]–[5] or for a single room [6]–[8].

Manuscript submitted January 23rd, 2012. This work was supported by the EU project ICT-248894 Wireless Hybrid Enhanced Mobile Radio Estimators 2 (WHERE2).

Gerhard Steinböck, Troels Pedersen and Bernard Henri Fleury are with the Dept. of Electronic Systems, Section Navigation and Communications at Aalborg University, Denmark. Wei Wang and Ronald Raulefs are with the Institute of Communications and Navigation, German Aerospace Center (DLR), Germany.

Models of the delay power spectrum of in-room channels relying on reverberation theory, or room electromagnetics, have been recently proposed [9]–[13]. These room electromagnetic models characterize the tail of the delay power spectrum, which is caused by reverberation, an effect similar to that occurring in room acoustics [14]. However, these models ignore the early part of the delay power spectrum, which is typically exploited for localization.

As a starting point we consider models for the in-room scenario, which may be the basic elements of models covering entire buildings. The model's structure is motivated by experimental observations [9], [11], [15]. These results indicate that the delay power spectrum has an early, or primary, spike-like component followed by an exponential decaying tail. A non-distance dependent model with a similar shape ("spike"+ exponential tail) for outdoor scenarios was considered in [16]. The model proposed here is a refinement of the model presented in [17]. It consists of a primary component which is a Dirac delta function weighted according to an inverse distance power law (d^{-n}) and an exponentially decaying reverberant component with distance-dependent onset.

The proposed model yields prediction of path loss, mean delay, rms delay spread and kurtosis. It is validated with experimental data. The path loss prediction shows good agreement with the two distinct behaviors observed at both short and long transmitter-receiver distances. So far this different behavior was not considered in path loss models, see e.g. [7] and references therein. We observe a good agreement between predicted values and estimates of the mean delay together with a predictable distance dependency, which is critical for localization purposes. The predicted and estimated values of the rms delay spread are close with a distance behavior similar to that reported in [18] for small to intermediate ranges.

TABLE I
PARAMETERS OF THE PROPOSED MODEL.

Parameter	Meaning
G_0	Path gain at reference distance d_0.
d_0	Reference distance, typically 1 m.
n	Path gain exponent.
R_0	Ratio $G_{\mathrm{rev}}(d_0)/(G_{\mathrm{pri}}(d_0)+G_{\mathrm{rev}}(d_0))$.
T	Reverberation time.

II. MODEL OF THE DELAY POWER SPECTRUM

We consider an in-room environment as illustrated in Fig. 1 and define the delay power spectrum as the expectation of the squared magnitude of the impulse response $h(\tau, d)$:

$$G(\tau, d) = \mathrm{E}[|h(\tau, d)|^2], \tag{1}$$

where τ is the delay and d is the transmitter-receiver distance.

The delay power spectrum is sampled at different transmitter and receiver locations. The wavelength λ is assumed small compared to the smallest dimension of the room. The bandwidth of the considered system is assumed high enough to observe frequency fading (delay dispersion), but too low to separate single propagation paths in the environment.

In [9]–[11], [15] it is observed that the delay power spectra measured in such an in-room scenario exhibit the typical behavior depicted in Fig. 1. The tail of the delay power spectrum exhibits the same constant exponential decay regardless of the transmitter-receiver distance. The early part is strong at short distance and gradually vanishes as the distance increases.

We propose to model the delay power spectrum as a superposition of a primary and a reverberant component similarly to the spike plus exponential tail model in [16] with the difference that each component is distance dependent:

$$G(\tau, d) = G_{\mathrm{pri}}(\tau, d) + G_{\mathrm{rev}}(\tau, d). \tag{2}$$

Subscript pri indicates the primary component and subscript rev the reverberant component. The primary component represents the early part of the delay power spectrum. It consists of the component resulting from direct propagation and possibly a superposition of components that may originate from first-order reflections on the floor, ceiling, and walls. We model the primary component as

$$G_{\mathrm{pri}}(\tau, d) = G_0 \left(\tfrac{d_0}{d}\right)^n \delta\left(\tau - \tfrac{d}{c}\right), \tag{3}$$

where n is the path gain exponent, $\delta(\,\cdot\,)$ is the Dirac delta function, c the speed of light, and $G_0 > 0$ is the gain at an arbitrary reference distance d_0. We chose the Dirac delta function as an approximation of the superimposed multipath components resulting from direct propagation and first order reflections as they cannot be resolved due to the bandwidth limitation.

The reverberant component is contributed by the multitude of higher order reflections in the room, which yield the diffuse tail in the measured delay power spectra. We model the reverberant component as an exponentially decaying function with onset equal to the propagation time between the transmitter and receiver:

$$G_{\mathrm{rev}}(\tau, d) = \begin{cases} G_{0,\mathrm{rev}}\, e^{-\tau/T}, & \tau > \frac{d}{c} \\ 0, & \text{otherwise,} \end{cases} \tag{4}$$

where $G_{0,\mathrm{rev}}$ is the reference gain of the reverberant component. In analogy to room acoustics [11], [14] we term T the reverberation time.

We now contrast our model to the two models derived based on the room acoustic theory in [9] and [11]. Both models neglect the transmitter-receiver distance. In [9] the delay power spectrum of the reverberant component, i.e. corresponding to (4), is non-exponential. It has maximum power one and constant onset at delay zero. In [11] the model only accounts for the exponentially decaying component due to reverberation in (2).

A. Path Gain and Path Loss

The path gain at distance d is obtained by integration of the delay power spectrum (2) with respect to delay:

$$G(d) = \int G(\tau, d)\mathrm{d}\tau, \tag{5}$$

$$= \underbrace{G_0 \left(\tfrac{d_0}{d}\right)^n}_{G_{\mathrm{pri}}(d)} + \underbrace{G_{0,\mathrm{rev}}\, T\, e^{\frac{-d}{c\,T}}}_{G_{\mathrm{rev}}(d)}. \tag{6}$$

The component $G_{\mathrm{pri}}(d)$ decays as d^{-n}, while $G_{\mathrm{rev}}(d)$ decays exponentially. We remark that the path loss is defined as the inverse of the path gain: $L(d) = G(d)^{-1}$. For mathematical convenience we consider the path gain in the sequel.

It is convenient to define a reverberation ratio $R(d)$ as the fraction of the total power contained in the reverberant component:

$$R(d) = \frac{G_{\mathrm{rev}}(d)}{G(d)}. \tag{7}$$

By definition $R(d)$ ranges from zero to unity. The introduction of the reverberation ratio simplifies the equations in the sequel. Furthermore, we chose to parameterize the model in terms of the reverberation ratio at the reference distance d_0, i.e. we recast (6) and (7) with $R_0 = R(d_0)$ as a parameter:

$$G(d) = G_0 \left(\tfrac{d_0}{d}\right)^n + G_0\, \tfrac{R_0}{1-R_0}\, e^{\frac{d_0-d}{c\,T}}, \tag{8}$$

$$R(d) = \frac{1}{1 + \frac{1-R_0}{R_0}\left(\frac{d_0}{d}\right)^n e^{\frac{d-d_0}{c\,T}}}. \tag{9}$$

The parameter $R_0 \in [0, 1]$ indicates the balance between the primary and reverberant components at the reference distance. The ratio $\frac{1-R_0}{R_0}$ corresponds to the ratio of primary versus reverberant component ($G_{\mathrm{pri}}(d_0)/G_{\mathrm{rev}}(d_0)$) at the reference distance. The special case with $R_0 = 0$ (or equivalently $G_{0,\mathrm{rev}} = 0$) leads to the standard path gain model

$$G_{\mathrm{std}}(d) = G_{\mathrm{pri}}(d) = G_0 \left(\tfrac{d_0}{d}\right)^n. \tag{10}$$

In the other extreme, where the primary component vanishes, i.e. $R(d) = R_0 = 1$,

$$G(d) = G_{\mathrm{rev}}(d) = G_{0,\mathrm{rev}}\, T\, e^{-\frac{d}{c\,T}}. \tag{11}$$

Fig. 2a depicts example graphs of $G(d)$ versus d with R_0 as parameter. For small distances d, the primary component dominates and the path gain decays as d^{-n}. For intermediate distances we observe a deviation from d^{-n} due to the reverberant component. For very large distances the influence of the reverberant component vanishes again.

To our best knowledge, this different behavior of the path loss at short and intermediate distances was not considered in the literature. The used simple models, such as (10), neglect this effect. That the total power decays versus distance differently than the power of the early component is investigated in [19], [20]. However, both the early component and the total power are modeled using (10) with different path gain exponents. The proposed model inherently includes such a distinction.

B. Properties of the Reverberation Ratio

The reverberation ratio ranges by definition between zero and one. We observe from (9), which is graphed in Fig. 3, that $R(d)$ vanishes for very small and very large distances, where the primary component dominates the reverberant component. More specifically,

$$\lim_{d\to 0} R(d) = 0 \qquad \text{and} \qquad \lim_{d\to\infty} R(d) = 0. \tag{12}$$

For intermediate distances $R(d)$ approaches its maximum when the reverberant component dominates over the primary component. The distance $d_{\max}$ where $R(d)$ is maximum is obtained by differentiation of (9) and equating the result to zero:

$$d_{\max} = c\,T\,n. \tag{13}$$

At this distance the value of the reverberation ratio is

$$R(d_{\max}) = \frac{1}{1 + \frac{1-R_0}{R_0} e^{-\frac{d_0}{c\,T}} \left(\frac{d_0\, e}{c\,T\,n}\right)^n}. \tag{14}$$

Notice that $d_{\max}$ only depends on n, T and c, the speed of light. The value $R(d_{\max})$ depends in addition on R_0 and d_0. $R(d_{\max})$ is less than unity except for the case $R_0 = 1$, i.e. when only the reverberant component is present. For the examples shown in Fig. 3, $d_{\max} = 12\,\mathrm{m}$.

C. Mean Delay and Root Mean Squared Delay Spread

The mean delay is defined as the first moment of the delay power spectrum (2), i.e.

$$\mu_\tau(d) = \frac{1}{G(d)} \int \tau\, G(\tau, d)\mathrm{d}\tau \tag{15}$$

$$= \tfrac{d}{c} + T\, R(d). \tag{16}$$

The first term in (16) is the delay of a directly propagating component and the second term results from the reverberant component. The mean delay is a function of the distance between transmitter and receiver and its value increases with distance. Fig. 2b depicts examples of the mean delay versus distance for different values of R_0. Using $R(d_{\max})$ and the upper bound of $R(d)$, which is unity, in (16), we can establish for $\mu_\tau(d)$ the following bounds:

$$0 \le \mu_\tau(d) \le \tfrac{d}{c} + T\, R(d_{\max}) \le \tfrac{d}{c} + T. \tag{17}$$

From the behavior of $R(d)$ for small and large distances (12) and from (16) we conclude that

$$\lim_{d\to 0} \mu_\tau(d) = 0 \qquad \text{and} \qquad \lim_{d\to\infty} \mu_\tau(d) - \tfrac{d}{c} = 0. \tag{18}$$

Note that the distance range considered in the plot of Fig. 2b is too small to observe the convergence of $\mu_\tau(d)$ towards its asymptote $\frac{d}{c}$ for $d \to \infty$. The mean delay approaches $\frac{d}{c} + T$ for intermediate distances where $R(d)$ is close to unity.

An important parameter characterizing temporal dispersion in the radio channel is the rms delay spread $\sigma_\tau(d)$:

$$\sigma_\tau^2(d) = \frac{1}{G(d)} \int \tau^2\, G(\tau, d)\mathrm{d}\tau - (\mu_\tau(d))^2\,, \tag{19}$$

$$= T^2 R(d)\,(2 - R(d))\,. \tag{20}$$

The rms delay spread is depicted as a function of distance in Fig. 2c. From (20) we see that the behavior of $R(d)$ determines that of $\sigma_\tau^2(d)$. Using (14) and the fact that $R(d)$ is unity in the case where there is only a reverberant component we obtain the following upper bounds:

$$\sigma_\tau^2(d) \le T^2 R(d_{\max})\ (2 - R(d_{\max})) \le T^2. \tag{21}$$

Furthermore, as an immediate consequence of (12), $\sigma_\tau^2(d)$ is determined in these ranges:

$$\lim_{d\to 0} \sigma_\tau^2(d) = 0 \qquad \text{and} \qquad \lim_{d\to\infty} \sigma_\tau^2(d) = 0. \tag{22}$$

As for Fig. 2b the distance range considered in Fig. 2c is too small to observe the convergence of $\sigma_\tau(d)$ towards 0 as $d \to \infty$. The distance dependent trends of the rms delay spread model show good agreement with the measurements reported in [18] and the therein proposed delay spread model.

D. Centered Moment of Order k and Kurtosis

The proposed model allows for the derivation of the normalized centered moment generating function of the delay power spectrum (see Appendix A). The distance dependent trend of the third and fourth moments, obtained from (42), is similar to that of the rms delay spread and therefore we omit presenting curves. We have observed that the third and fourth moments rise steeper than the rms delay spread for short distances. In localization the kurtosis of $|h(\tau, d)|$ is used to identify line of sight or non-line of sight situations [21]–[25]. The kurtosis of the delay power spectrum is

$$\kappa(d) = \frac{\mu_4(d)}{\mu_2^2(d)}, \tag{23}$$

where $\mu_k(d)$ is the normalized kth centered moment of the delay power spectrum (42). From (43) we see that for small and large distances $\kappa(d)$ approaches infinity. For intermediate distances $\kappa(d)$ approaches its minimum value of nine, which coincides with the kurtosis of the exponential distribution [26].

For moments of order $k \ge 2$, we find the maximum by equating the derivative of $\mu_k(d)$ to zero. It can be seen ((42) in Appendix A) that the kth moment is a function of $R(d)$. Thus,

$$\frac{\mathrm{d}\mu_k(d)}{\mathrm{d}d} = \frac{\mathrm{d}\mu_k(d)}{\mathrm{d}R(d)} \frac{\mathrm{d}R(d)}{\mathrm{d}d}. \tag{24}$$

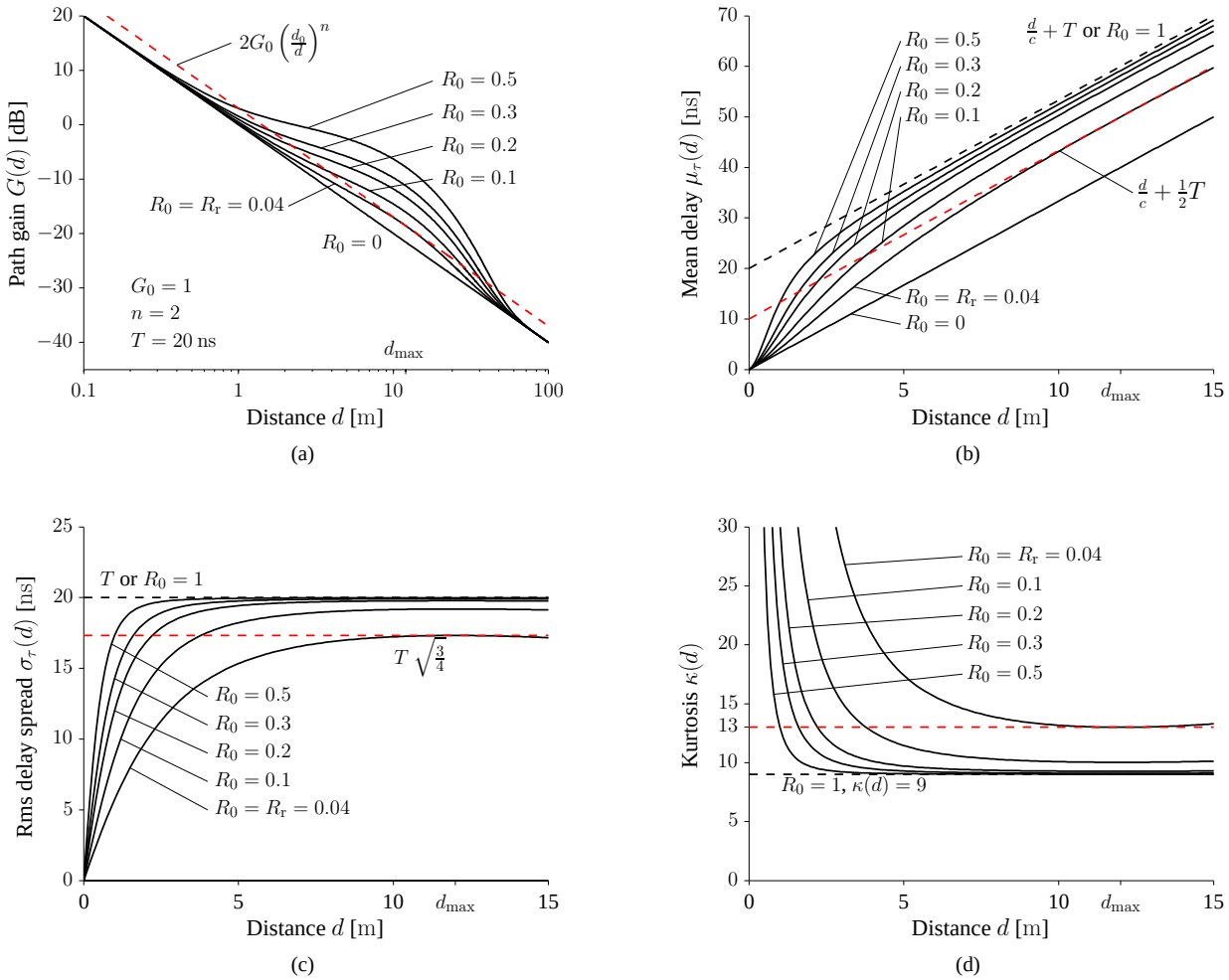

Fig. 2. Path gain (a), mean delay (b), rms delay spread (c) and kurtosis (d) versus distance predicted by the proposed model for $d_0 = 1\,\mathrm{m}$. The intersections of the various functions with the red dashed line mark the beginning and end of the reverberation region. The intersection at the end or the reverberation is not visible in (b), (c) and (d) due to chosen axis limitation. The reverberation region is observed if, and only if, $R_0 \geq R_\mathrm{r} = 0.04$.

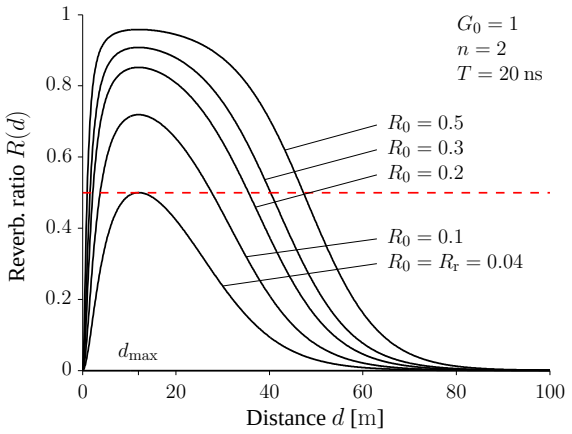

Fig. 3. Reverberation ratio versus the distance in linear scale. The intersections of $R(d)$ with the red dashed line mark the beginning and end of the reverberation region for the various parameter settings.

Since the first factor in the right-hand product is positive, the root of (24) coincides with the root of the second factor, which is d_max. Thus, all moments of order $k \geq 2$ attain their maximum value at distance d_max. This value can be obtained by inserting (14) into (42) in Appendix A. Furthermore, by using the upper bound of $R(d)$, which is unity, the upper bound of μ_k for $k \geq 2$ is given as

$$\mu_k(d) \leq T^k \sum_{\ell=0}^{k} \frac{k!}{\ell!} (-1)^\ell . \tag{25}$$

For $k = 2$, (25) combined with the identity $\sigma_\tau = \sqrt{\mu_2}$ yields the upper bound of the rms delay spread in (21).

E. Reverberation Region

For particular parameter values, it may occur that the power of the reverberant component exceeds the power of the primary component at some distances, i.e. $G_\mathrm{rev}(d) \geq G_\mathrm{pri}(d)$ or equivalently $R(d) \geq \frac{1}{2}$. The reverberation region is the closed interval of distances for which $G_\mathrm{rev}(d) \geq G_\mathrm{pri}(d)$:

$$D_\mathrm{rev} = \{d \geq 0; R(d) \geq \tfrac{1}{2}\}. \tag{26}$$

The reverberation region is non empty if, and only if,

$$R_0 \geq \frac{1}{1 + e^{\frac{d_0}{c\,T}} \left(\frac{d_0\, e}{c\,T\,n}\right)^{-n}} = R_\mathrm{r}. \tag{27}$$

For the examples shown in Fig. 2 and Fig. 3 $R_\mathrm{r} = 0.04$. We consider the following three cases:

Case $R_0 < R_\mathrm{r}$*:* In this case the primary component is dominating over the reverberant component over all distances and D_rev is the empty set.

Case $R_0 = R_\mathrm{r}$*:* The reverberation region is a singleton: $D_\mathrm{rev} = \{d_\mathrm{rl}\} = \{d_\mathrm{max}\}$. In the graph of the path gain versus distance we observe a maximum of 3 dB deviation from $G_\mathrm{pri}(d_\mathrm{rl})$. We denote this maximum possible reverberation distance $d_\mathrm{r,max} = d_\mathrm{max}$. The parameter $d_\mathrm{r,max}$ is of importance since it can be used for interpreting measurements: If the measured power does not exceed $G_\mathrm{pri}(d)$ by 3 dB at distances smaller than $d_\mathrm{r,max}$, it will never occur. This result may be useful e.g. for the planning of in-room channel measurements.

Case $R_0 > R_\mathrm{r}$*:* In this case $D_\mathrm{rev} = [d_\mathrm{rl}, d_\mathrm{ru}]$, with $0 < d_\mathrm{rl} < d_\mathrm{ru}$. We refer to the smallest endpoint d_rl as reverberation distance. The endpoints of the reverberation region are the two solutions of the identity $G_\mathrm{pri}(d) = G_\mathrm{rev}(d)$. The identity can be written after some algebraic manipulations as

$$-\frac{d_0}{c\,T\,n}\left(\frac{R_0}{1-R_0}\, e^{\frac{d_\mathrm{rl}-d_0}{c\,T}}\right)^{-\frac{1}{n}} = -\frac{1}{c\,T\,n}\, d_\mathrm{rl}\, e^{-\frac{1}{c\,T\,n} d_\mathrm{rl}}. \tag{28}$$

This expression can be solved in terms of the Lambert W function $W(\,\cdot\,)$. This function is defined as the solution of $z = W(z)\, e^{W(z)}$ and has two real $(W_0(z), W_{-1}(z))$ and infinitely many complex solutions [27]. The smaller solution of (28) reads

$$d_\mathrm{rl} = -c\,T\,n\,W_0\left(-\frac{d_0}{c\,T\,n}\left(\frac{R_0}{1-R_0}\, e^{\frac{d_0}{c\,T}}\right)^{-\frac{1}{n}}\right). \tag{29}$$

The larger real solution corresponds to the larger endpoint of D_rev. It is obtained by replacing $W_0(\,\cdot\,)$ with $W_{-1}(\,\cdot\,)$ in (29).

In acoustics [14] and room electro magnetics [11], d_rl is derived assuming a fixed exponent $n = 2$ and a constant reverberant component. In our context, we derive d_rl for arbitrary n and include a distance dependent onset in the reverberant component. This onset yields that the power of the reverberant component decays exponentially with distance.

We obtain the following special values at distances d_rl and d_ru:

$$\mu_\tau(d_\mathrm{rl}) = \tfrac{d_\mathrm{rl}}{c} + \tfrac{T}{2}, \tag{30}$$

$$\mu_\tau(d_\mathrm{ru}) = \tfrac{d_\mathrm{ru}}{c} + \tfrac{T}{2}, \tag{31}$$

$$\sigma_\tau(d_\mathrm{rl}) = \sigma_\tau(d_\mathrm{ru}) = T\sqrt{\tfrac{3}{4}}, \tag{32}$$

$$\kappa(d_\mathrm{rl}) = \kappa(d_\mathrm{ru}) = 13. \tag{33}$$

We see from (32) that $\sigma_\tau(d_\mathrm{rl})$ depends only on the reverberation time. We can use this result, together with an estimate of T, to estimate d_rl for a given room. To obtain an estimate of T from the rms delay spread one might simply average the rms delay spread estimates obtained for distances where these estimates do no longer change with distance. For the case that $R_0 \leq R_\mathrm{r}$ the maximum of the rms delay spread is $\max\{\sigma_\tau(d)\} \leq T\sqrt{\frac{3}{4}}$ and, similarly, for the mean delay $\max\{\mu_\tau(d)\} \leq \frac{d}{c} + \frac{T}{2}$.

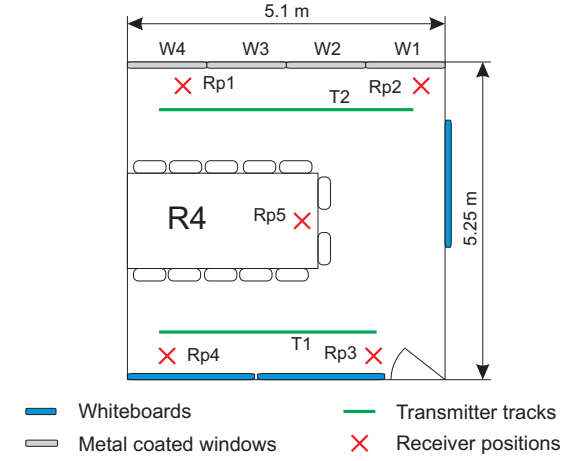

(a)

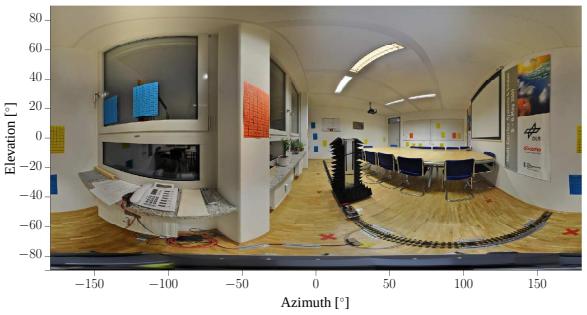

(b)

Fig. 4. Schematic of the room where the measurements were performed (a) and panograph (spherical panoramic photo) of the investigated room seen from Rp1 using an equi-rectangular projection (b).

III. Measurement Data

We validate the proposed model by means of measurement data from a campaign [28] conducted at the DLR premises in Oberpfaffenhofen, Germany. In the following we describe in detail the measurement campaign and the post-processing of the measurement data.

A. Measurement Campaign

Measurements were taken in a meeting room depicted in Fig. 4. The dimensions of the room are $5.1 \times 5.25 \times 2.78\,\mathrm{m}^3$. The three inner walls are made of plaster boards. As visible in the panograph, the outer "wall" consists mainly of four windows (W1–W4) and two concrete pillars. The frames of the windows are metallic and the glass is metal coated. The height of the transmit and receive antenna was 1.26 m and 1.1 m, respectively. The environment was static and no one was in the room while the measurements were taken.

The measurement data were collected using the Rusk-DLR channel sounder [29] operating at 5.2 GHz. The transmitter and receiver were synchronized to a common Rubidium clock via cables throughout the measurements. The settings of the sounder are summarized in Table II. The used transmit antenna

TABLE II
SETTINGS OF THE CHANNEL SOUNDER AND PARAMETERS FOR DATA POST-PROCESSING.

Sounder Settings	Value
Carrier frequency f_c	5.2 GHz
Bandwidth B	120 MHz
Number of sub-carriers N_c	1537
Carrier separation Δf	78.125 kHz
Signal duration T_{S}	12.8 µs
Cycle duration T_{C}	204.8 µs
Cycles per burst C	20
Burst duration T_{B}	4096 µs
Burst repetition time T_{BR}	131.072 ms
Transmit power	0 dBm
Delay MUX and cable τ_{mux}	3.86 ns
Post-processing Settings	
Threshold θ	-61 dB
Start delay range T estimator τ_{s}	25 ns
End delay range T estimator τ_{max}	150 ns

[30] is omni-directional with 3 dBi gain. The receiver was equipped with a uniform circular array of eight monopoles with diameter 75.18 mm. These monopoles were connected to the receiver via a multiplexer. The multiplexer and the cables connecting the receive antennas to it introduce an additional known delay τ_{mux} which could not be removed in the calibration process but can be accounted for during the post-processing. In a measurement cycle T_{C} all eight channel frequency responses are sequentially measured. The sounder was operating in "burst" mode. In each burst C consecutive measurement cycles are performed. The duration of one burst is $T_{\mathrm{B}} = C \cdot T_{\mathrm{C}}$. In between bursts, the sounder pauses for data storage, resulting in the burst repetition time T_{BR}.

Channel measurements were obtained for five fixed receive antenna array locations (Rp1 to Rp5), shown in Fig. 4a. The transmit antenna was mounted on a model train which moved on two tracks (T1 and T2). The positions Rp1 to Rp5 and the trajectories along the tracks were measured with a tachymeter. The odometer of the model train was connected to the channel sounder to record the traveled distance during the movement. For each receiver position the frequency response was measured while the transmitter was moving along each track with a constant speed of approximately 0.05 m/s corresponding to a movement of 0.0035λ within a burst. Over this distance the channel response can be considered quasi-static. Between two consecutive bursts, the transmitter moved $\lambda/8.8$.

B. Post-processing of the Measurement Data

The measured frequency responses are averaged over all cycles in a burst to reduce noise. The obtained averaged frequency response is denoted by $\widehat{H}_{m,r,p,q,f}$ where m is the index of the receive array element at receiver position index r and at transmitter positions p along track q for frequency sample f. We estimate the path gain as

$$\widehat{G}_{r,p,q} = \frac{1}{M}\sum_{m=1}^{M}\frac{1}{F}\sum_{f=1}^{F}|\widehat{H}_{m,r,p,q,f}|^2. \tag{34}$$

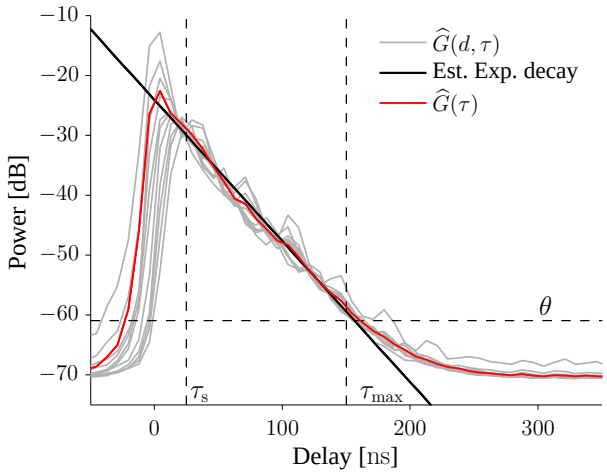

Fig. 5. Spatially averaged delay power spectra obtained from averaging the experimentally obtained power delay profiles collected in distance sections of size 4λ. For displaying convenience the obtained spectrum for every second distance section is shown. The straight line depicts an exponentially decaying function with decay constant $\widehat{T} = 18.4$ ns corresponding to -0.24 dB/ns.

The delay power spectrum is estimated by averaging over the receive antennas as

$$\widehat{G}'_{r,p,q}[\tau] = \frac{1}{M}\sum_{m=1}^{M}\left|\mathrm{IDFT}\left\{\widehat{H}_{m,r,p,q,f}\, W_f\right\}[\tau]\right|^2, \tag{35}$$

where $\mathrm{IDFT}\{\cdot\}[\cdot]$ is the inverse discrete Fourier transform and W_f denotes a Hann window applied to suppress sidelobes. The brackets around τ indicate that the delay variable has been discretized, due to the measurement process. We remove the additional delay due to the cable and multiplexer by translating the estimated delay power spectrum by τ_{mux}:

$$\widehat{G}_{r,p,q}[\tau] = \widehat{G}'_{r,p,q}[\tau + \tau_{\mathrm{mux}}]. \tag{36}$$

The mean delay estimate is obtained by numerical integration of (15) with $G(\tau, d)$ replaced by the estimated delay power spectrum $\widehat{G}_{r,p,q}[\tau]$. The rms delay spread and higher order moments are estimated similarly, e.g. using (19). The limited bandwidth of the measurement system affects the estimation of the rms delay spread of the channel. We compensate for this by subtracting the second central moment of the bandlimited pulse obtained from W_f from the estimates of the second central moment of the delay power spectrum. To reduce the effect of noise we use only the parts of the delay power spectra exceeding a threshold θ; see Fig. 5.

The complete post processed data set $\mathcal{M}$ used for the validation of the model consists of the estimates of delay power spectra, path gains, mean delays, rms delay spreads, higher moments, the kurtosis and the transmitter-receiver distances for all transmitter-receiver positions.

IV. VALIDATION OF THE PROPOSED MODEL

The estimated delay power spectra in Fig. 5 confirm the observations from [9]–[11], [15]: i) that the reverberant tails coincide and ii) that the primary component vanishes for large

TABLE III
PARAMETER ESTIMATES AND ROOT MEAN SQUARED ERRORS (RMSE) OF PATH GAINS.

Model	Parameter estimates				RMSE† [dB]	
	$\widehat{G}_0$	$\widehat{n}$	$\widehat{R}_0$	$\widehat{T}$ [ns]	Fit to $\mathcal{M}_F$	Pred. of $\mathcal{M}_V$
Standard	$1.14 \cdot 10^{-5}$	1.13	—	—	1.27	1.33
Proposed	$6.85 \cdot 10^{-6}$	2.2	0.35	18.4	1.17	1

Reverberation region: $\widehat{d}_{rl} = 1.39$ m, $\widehat{d}_{ru} = 42$ m, $\widehat{d}_{\max} = 12$ m.
† The path gain values in dB are used to obtain the RMSE.

distances. Thus, the modeling assumptions of the delay power spectrum are fulfilled.

We now validate the proposed model by checking its predictions of path gain, mean delay, rms delay spread and kurtosis. To this end, we split the data set $\mathcal{M}$ into a fitting (or training) set $\mathcal{M}_F$ and a validation set $\mathcal{M}_V$. We let $\mathcal{M}_F$ be the data set for receiver positions Rp1 to Rp4 and $\mathcal{M}_V$ be the data for receiver position Rp5. Notice that $\mathcal{M} = \mathcal{M}_F \bigcup \mathcal{M}_V$, but $\mathcal{M}_F \bigcap \mathcal{M}_V = \emptyset$.

We fit the model by first estimating T from the estimated delay power spectra and afterwards estimating the remaining model parameters by non-linear least squares fitting of the scatter plot of estimated path gains versus distance. The reverberation time is the least square estimate of the slope of the estimated log delay power spectra within the delay range $\tau_{\rm s} \leq \tau \leq \tau_{\max}$ as indicated in Fig. 5. The value of $\tau_{\rm s}$ is chosen to reduce the influence of the primary component on the slope estimate. We chose $\tau_{\rm s}$ to be the propagation time between transmitter and receiver at the maximum transmitter-receiver distance occurring in the measurement campaign plus one pulse duration. The value of $\tau_{\max}$ is the largest delay sample such that $\widehat{G}_{r,p,q}[\tau]$ exceeds the threshold θ. For $\mathcal{M}_F$ we obtain $\widehat{T} = 18.4$ns. We obtain the same value for $\mathcal{M}_V$. The parameters G_0, n and R_0 are estimated by fitting the path gain model (8) to the scatter plot of the estimated path gain values of $\mathcal{M}_F$ versus distance. We use a non-linear least squares estimator [31] with $\widehat{T}$ as input. The estimates are listed in Table III. For comparison we also report parameter estimates for the standard model obtained via linear least squares fitting.

The ability of the two models to fit and predict the experimental log-power values is evaluated by comparing their respective root mean squared errors (RMSEs) which are reported in Table III. The proposed model yields a lower fitting RMSE than the standard model. This is expected since the former model contains more parameters than the latter and includes it as a special case. Furthermore, it appears that the prediction RMSE achieved with the standard model increases, while it is reduced with the proposed model. Compared to the standard model, the proposed model not only fits the data better, but also yields a better prediction, thus justifying its added complexity. The reason for the proposed model's superior prediction ability appears from Fig. 6a: it provides a close fit at all distances whereas the standard model shows its best fit for the range of distances corresponding to the bulk of observations. Fitting the standard model to the $\mathcal{M}_F$ data, where the bulk of observations is at distances above 4 m leads to larger deviations at short distances. This is apparent by swapping the roles of the data sets $\mathcal{M}_V$ and $\mathcal{M}_F$: In this case, the standard model shows poor predictions for $d > 3$ m.

The proposed model allows for the prediction of wideband parameters such as mean delay, rms delay spread and kurtosis. The prediction values are compared to estimates obtained from the experimental data in Fig. 6. We observe a good agreement in trend between the predicted wideband parameters for both $\mathcal{M}_F$ and $\mathcal{M}_V$. This agreement is remarkable considering that the model parameters are obtained by fitting the path gain model, but not the wideband parameters. This agreement can be further quantified by comparison of the spatial averages of the experimental results and the wideband parameters predicted by the proposed model. We compute the average of mean excess delay $\mu_\tau(d) - \frac{d}{c}$, rms delay spread and kurtosis evaluated at the same set of distances exceeding 2 m as used during obtaining the experimental data. The difference between the average values of estimates obtained from the experimental data and model prediction are 2.4 ns for mean excess delay, 1.9 ns for rms delay spread, and 3.4 for the kurtosis. The relative errors amount to 16%, 11% and 35%, respectively. The estimated values of the experimental data are observed to be close to the model predictions, especially when considering that $\widehat{T}$ varies by ± 1 ns for different settings of $\tau_{\rm s}$ and/or $\tau_{\max}$.

The truncation of the delay power spectrum in the post-processing may distort the estimated parameters. To evaluate the relevance of this effect, we modified the proposed model to include the truncation in the delay power spectrum. For the investigated environment and chosen θ this led to no significant changes of the predicted path gain and mean delay. However, in the considered scenario the truncation reduced the predicted rms delay spread by at most 0.5 ns. We also noticed a reduction of the predicted $d_{\rm ru}$. This effect is, however, of no practical relevance, since the value is still much larger than the length of the diagonal of the room.

A. Model Parameter Estimates

Estimates of model parameters are listed in Table III. The path loss exponent of $\widehat{n} = 1.13$ reported for the standard model is slightly below published values obtained from in-room measurement data; see [7] and references therein. The path gain exponent estimate computed from $\mathcal{M}_V$ is $\widehat{n} = 1.41$ which is in the range of values reported in [7]. Path loss exponents below two are traditionally attributed to wave guiding effects. However, considering the room dimensions, a reverberation phenomenon seems to provide a more plausible explanation of the low values.

The estimated path gain exponent $\widehat{n} = 2.2$ of the proposed model's primary component is close to the exponent of free-space propagation. The value $\widehat{R}_0 = 0.35$ indicates that at 1 m distance 35% of the total power is contained in the reverberant component and with increasing distance the reverberant component will gain importance. Thus, the reverberant component is in this case significant to the total path gain.

The estimate of the reverberation time is within the range of values reported in [11], [12], [15], [32], [33]. The estimated reverberance distance $\widehat{d}_{rl}$ is about one fifth of the maximum

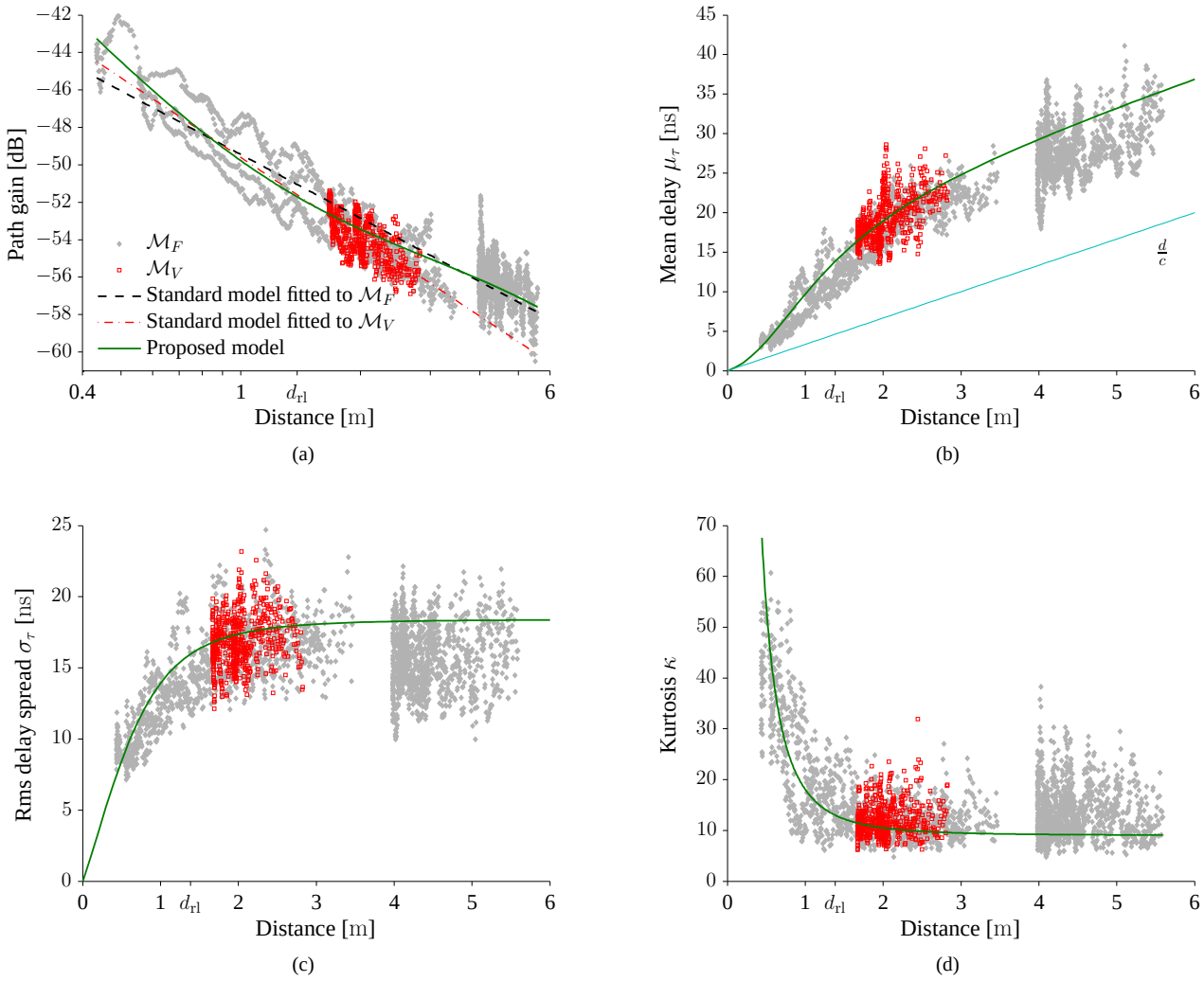

Fig. 6. Experimental results for $\mathcal{M}_F$ and $\mathcal{M}_V$ together with the model predictions (solid lines) using the reported parameters in Table III. The dashed and dashed dotted lines in (a) correspond to the standard path gain model. For reference we also plot the line corresponding to $\frac{d}{c}$ in (b).

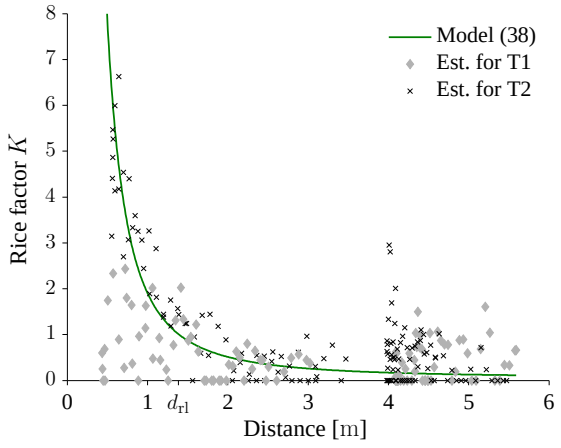

Fig. 7. Estimated Rice factors for measurement set $\mathcal{M}_F$ separated for track T1 and T2 and predicted by the model.

possible distance in the room. This indicates that the reverberant component dominates over the primary component for a large portion of the room. This would in turn lead to the low path loss exponents we also observe. In addition, $\widehat{d}_{\max}$ is larger than the length of the room diagonal.

B. Rice Factor as a Function of Distance

In the literature the statistical function of the amplitude of the radio channel response is often modeled using a Rice distribution, characterized by the Rice factor. The proposed model describes only the delay power spectrum, i.e. average values for the power. We have not introduced any statistical model for the amplitude of the channel response which is needed to consider a Rice model for the amplitude of the narrowband response. Thus to consider the Rice factor, it is necessary to impose additional statistical assumptions.

It seems compelling to make two hypothesis: i) that the primary component contains a strong line-of-sight component and thus (locally) exhibits a constant amplitude; and ii) that the complex amplitude of the reverberant component is a

zero mean Gaussian. Under these assumptions the receive amplitude is Rice distributed with a Rice factor

$$K(d) = \frac{G_{\mathrm{pri}}(d)}{G_{\mathrm{rev}}(d)} \tag{37}$$

$$= \frac{1 - R(d)}{R(d)}, \tag{38}$$

varying with distance. For short and very large distances where $R(d)$ vanishes, the Rice factor is large. At the reverberance distance $K(d)$ is unity and for distances within the reverberation region, where $R(d)$ approaches unity, $K(d)$ approaches zero.

Fig. 7 shows the predicted Rice factor along with the experimental values obtained as described in Appendix B. We observe for track T2 a good agreement of the experimentally obtained Rice factors and the model prediction except for a few outliers at approximately $4\,\mathrm{m}$. For track T1 the Rice factor estimates do not agree with the model prediction for distances shorter than d_{rl}. We tested hypothesis ii) via the empirical cumulative probability density function of the sum of complex amplitudes of the reverberant component within the delay range of $\tau_s < \tau < \tau_{\max}$. For both tracks we observe that the magnitudes of these sums are close to Rayleigh which corroborates the validity of hypothesis ii). Thus the difference of Rice factor estimates for the two tracks ought to occur because hypothesis i), the description of the primary component, does not hold. The near surroundings of the two tracks differ. Track T1 runs closely along a metallic white board leading to a strong first order reflection resulting in fading of the primary component and thus in small Rice factors. Track T2 runs along windows with metallic frames and metal coated glass. We expect this to yield lower reflection coefficients compared to the whiteboard, and thus results in higher Rice factors at short distances. In conclusion, it seems that hypothesis i) is valid for Rice factor estimates of track T2 but not for T1. To improve the model of the Rice factor for T1 a more detailed description of the primary component is necessary. This could be obtained e.g. by means of a two ray model.

V. Conclusions

The proposed model of the delay power spectrum of an in-room reverberant channel includes a primary component which follows an inverse distance power law (d^{-n}) and a reverberant component which decays exponentially versus delay and exhibits a distance dependent onset. The proposed model allows for the prediction of path gain, mean delay and rms delay spread, higher order centered moments and the kurtosis value versus distance. We obtained the moment generating function from the analytic expression of the delay power spectrum. The model was validated using measurement data. The prediction of mean delay, rms delay spread and kurtosis agrees with the respective estimates obtained from the measurement data. In the investigated environment the ratio of the reverberant component path gain to the total path gain at the reference distance of $1\,\mathrm{m}$ is 0.35. Hence, the reverberant component is prominent in this environment.

The estimated path gain exponent of the primary component in the proposed model is close to the free-space path gain exponent. Due to its inability to separate the primary component from the reverberant component the standard path gain model yields path gain exponents close to 1.1 for our data set. The standard path gain model merely provides a fit of the path gain that blends the contributions from the primary and reverberant component and gives different results for the same environment but different measurement locations. The proposed model of the delay power spectrum resembles the second moment of the amplitude fading statistics. To predict the Rice factor further assumptions on the fading statistics of the primary and the reverberant component are necessary. The introduced assumptions on the fading statistics resulted in a distance dependent Rice factor model. For a subset of the experimental data, the trend of estimated Rice factor and predicted values showed good agreement. However, a prediction with the made assumptions is not valid for all cases. A more detailed description of the fading statistics of the primary component is necessary.

Appendix A
Derivation of Normalized Centered Moment Generating Function and Kurtosis

The centered moment generating function for the proposed model reads

$$M(x,d) = \frac{1}{G(d)} \int e^{x(\tau - \mu_\tau(d))} G(\tau, d) \mathrm{d}\tau. \tag{39}$$

The kth order centered moment is obtained by taking the kth derivative of $M(x,d)$ and evaluating at $x = 0$. By Leibnitz's rule and evaluating the k^{th} derivative at $x = 0$ we have

$$\begin{aligned}\tfrac{\mathrm{d}^k}{\mathrm{d}^k x} M(0,d) = \tfrac{G_0}{G(d)} \Big(\big(\tfrac{d}{c} - \mu_\tau(d)\big)^k \ \big(\tfrac{d_0}{d}\big)^n \\ + \tfrac{R_0}{1-R_0} e^{\frac{d_0 - 2d + \mu_\tau(d)}{c\,T}} T^k \Gamma\Big(k+1, \tfrac{d - c\mu_\tau(d)}{c\,T}\Big)\Big),\end{aligned} \tag{40}$$

where $\Gamma(s,x)$ is the upper incomplete gamma function for positive integers s [26]:

$$\Gamma(s,x) = (s-1)! e^{-x} \sum_{k=0}^{s-1} \frac{x^k}{k!}. \tag{41}$$

Inserting for μ_τ the normalized k^{th} centered moment generating function reads

$$\begin{aligned}\mu_k(d) &= \tfrac{\mathrm{d}^k}{\mathrm{d}^k x} M(0,d) \\ &= R(d)\, T^k \Big[(-1)^k \left(R^{k-1}(d) - R^k(d) \right) \\ &\quad + e^{-R(d)} \Gamma(k+1, -R(d)) \Big].\end{aligned} \tag{42}$$

The kurtosis in (23) thus reads

$$\kappa(d) = R^{-1}(d) \frac{R^3(d) - R^4(d) + e^{-R(d)}\Gamma(5, -R(d))}{\left[R(d) - R^2(d) + e^{-R(d)}\Gamma(3, -R(d))\right]^2}. \tag{43}$$

APPENDIX B
ESTIMATION OF RICE FACTORS

We use the averaged measured frequency response of each receive antenna at a specific receiver position and ten consecutive bursts collected while the transmitter moves along the tracks. We apply the method of moments [34] on the magnitude of the frequency responses of the ten bursts to estimate the Rice factor. As in [34] we set $\widehat{K} = 0$ for the cases where the ratio of the first and second moment of the experimental data is below the theoretical value obtained for $K = 0$. During the ten bursts the transmitter moves approximately one wavelength and we obtain a transmitter-receiver distance for a specific receiver position and a transmitter position corresponding to the center of the ten bursts.

REFERENCES

[1] H. Liu, H. Darabi, P. Banerjee, and J. Liu, "Survey of Wireless Indoor Positioning Techniques and Systems," *Systems, Man, and Cybernetics, Part C: Applications and Reviews, IEEE Transactions on*, vol. 37, no. 6, pp. 1067–1080, Nov. 2007.

[2] H. Hashemi, "The Indoor Radio Propagation Channel," *Proc. IEEE*, vol. 81, no. 7, pp. 943–968, Jul. 1993.

[3] J. Keenan and A. Motley, "Radio coverage in buildings," in *Br. Telecom Technol. J.*, vol. 8, no. 1, Jan. 1990, pp. 19–24.

[4] E. Damosso, Ed., *Digital mobile radio towards future generation systems: Cost 231 Final Report*. Bruxelles, Belgium: European Commission, 1999.

[5] R. Vaughan and J. B. Andersen, *Channels, Propagation and Antennas for Mobile Communications*. Institution of Engineering and Technology, Feb. 2003.

[6] P. Nobles and F. Halsall, "Indoor Propagation at 17 GHz and 60 GHz – Measurements and Modelling," in *Antennas and Propagation, 1999. IEE National Conference on.*, Mar. 1999, pp. 93–96.

[7] D. Xu, J. Zhang, X. Gao, P. Zhang, and Y. Wu, "Indoor Office Propagation Measurements and Path Loss Models at 5.25 GHz," *Vehicular Technology Conference, 2007. VTC-2007 Fall. 2007 IEEE 66th*, pp. 844–848, 30 Sep. - 3 Oct. 2007.

[8] J. Kunthong and C. Bunting, "A Novel Hybrid Propagation Model," in *Antennas and Propagation Society International Symposium, 2008. AP-S 2008. IEEE*, Jul. 2008, pp. 1–4.

[9] C. Holloway, M. Cotton, and P. McKenna, "A model for predicting the power delay profile characteristics inside a room," *IEEE Trans. Veh. Technol.*, vol. 48, no. 4, pp. 1110–1120, 1999.

[10] R. Rudd, "Statistical prediciton of indoor radio channel impulse response," Ph.D. dissertation, University of Surrey, Sep. 2007.

[11] J. Andersen, J. Nielsen, G. Pedersen, G. Bauch, and J. Herdin, "Room electromagnetics," *IEEE Antennas Propag. Mag.*, vol. 49, no. 2, pp. 27–33, 2007.

[12] J. Nielsen, J. Andersen, G. Pedersen, and M. Pelosi, "On Polarization and Frequency Dependence of Diffuse Indoor Propagation," in *Vehicular Technology Conference, 2011 IEEE 74th*, Sep. 2011.

[13] D. A. Hill, *Electromagnetic Fields in Cavities: Deterministic and Statistical Theories*, ser. IEEE Press Series on Electromagnetic Wave Theory. Piscataway, NJ: Wiley/IEEE Press, 2009.

[14] H. Kuttruff, *Room Acoustics*, 4th ed. London: Taylor & Francis, 2000.

[15] J. Kunisch and J. Pamp, "Measurement results and modeling aspects for the uwb radio channel," *Ultra Wideband Systems and Technologies, 2002. Digest of Papers. 2002 IEEE Conf. on*, pp. 19–23, 2002.

[16] V. Erceg, D. Michelson, S. Ghassemzadeh, L. Greenstein, J. Rustako, A.J., P. Guerlain, M. Dennison, R. Roman, D. Barnickel, S. Wang, and R. Miller, "A Model for the Multipath Delay Profile of Fixed Wireless Channels," *IEEE J. Sel. Areas Commun.*, vol. 17, no. 3, pp. 399–410, Mar. 1999.

[17] G. Steinböck, T. Pedersen, B. Fleury, W. Wang, T. Jost, and R. Raulefs, "Model for the Path Loss of In-room Reverberant Channels," in *Vehicular Technology Conference, 2011 IEEE 73rd*, May 2011, pp. 1–5.

[18] R. Bultitude, P. Melancon, H. Zaghloul, G. Morrison, and M. Prokki, "The Dependence of Indoor Radio Channel Multipath Characteristics on Transmit/Receiver Ranges," *IEEE J. Sel. Areas Commun.*, vol. 11, no. 7, pp. 979–990, Sep. 1993.

[19] K. Siwiak, H. Bertoni, and S. Yano, "Relation between multipath and wave propagation attenuation," *IET Electron. Lett.*, vol. 39, no. 1, pp. 142–143, Jan. 2003.

[20] N. Alsindi, B. Alavi, and K. Pahlavan, "Measurement and Modeling of Ultrawideband TOA-Based Ranging in Indoor Multipath Environments," *IEEE Trans. Veh. Commun.*, vol. 58, no. 3, pp. 1046–1058, Mar. 2009.

[21] J. Khodjaev, Y. Park, and A. Saeed Malik, "Survey of NLOS identification and error mitigation problems in UWB-based positioning algorithms for dense environments," *Annals of Telecommunications*, vol. 65, pp. 301–311, 2010.

[22] L. Mucchi and P. Marcocci, "A new UWB indoor channel identification method," in *Cognitive Radio Oriented Wireless Networks and Communications, 2007. CrownCom 2007. 2nd International Conference on*, Aug. 2007, pp. 58–62.

[23] F. Montorsi, F. Pancaldi, and G. M. Vitetta, "Statistical Characterization and Mitigation of NLOS Bias in UWB Localization Systems," in *NEWCOM++ / COST 2100 Joint Workshop on Wireless Communications*, Paris, France, 1-2 Mar. 2011.

[24] S. Maranò and, W. Gifford, H. Wymeersch, and M. Win, "NLOS Identification and Mitigation for Localization Based on UWB Experimental Data," *IEEE J. Sel. Areas Commun.*, vol. 28, no. 7, pp. 1026–1035, Sep. 2010.

[25] Z. Xiao, Y. Hei, Q. Yu, and K. Yi, "A survey on impulse-radio uwb localization," *SCIENCE CHINA Information Sciences*, vol. 53, pp. 1322–1335, 2010.

[26] M. Abramowitz and I. Stegun, *Handbook of mathematical functions: with formulas, graphs, and mathematical tables*. Dover Publications, 1965.

[27] R. M. Corless, G. H. Gonnet, D. E. G. Hare, D. J. Jeffrey, and D. Knuth, "On the Lambert W function," *Advances in Computational Mathematics*, vol. 5, no. Apr., pp. 329–359, 1996.

[28] G. Steinböck, T. Pedersen, and W. Wang, "AAU-DLR 2010 Indoor Measurement Campaign – Measurements for Validation of Models for Reverberant and Cooperative Channels," AAU and DLR, Report, 2011.

[29] J. Stephan, Y. Lostanlen, J. Keignart, W. Wang, D. Slock, and F. Kaltenberger, "Measurements of location-dependent channel features," ICT- 217033 WHERE, Deliverable 4.1, Oct. 2008, http://www.ict-where.eu/.

[30] Huber+Suhner, "Datasheet for Sencity Antenna For In-Carriage Wireless Communication, Type: SOA 5600/360/3/20/V_1," Document No. 01.02.1358, May 2007.

[31] Mathworks, "Matlab Curve Fitting Toolbox, Version 1.2.2 (r2008b)," 2008.

[32] A. Bamba, W. Joseph, D. Plets, E. Tanghe, G. Vermeeren, L. Martens, J. Andersen, and J. Nielsen, "Assessment of reverberation time by two measurement systems for room electromagnetics analysis," in *Antennas and Propagation (APSURSI), 2011 IEEE International Symposium on*, Jul. 2011, pp. 3113–3116.

[33] J. Kunisch and J. Pamp, "An ultra-wideband space-variant multipath indoor radio channel model," *Proc. IEEE 2006 Int. Conf. on Ultra-Wideband*, pp. 290–294, 16-19 Nov. 2003.

[34] K. K. Talukdar and W. D. Lawing, "Estimation of the parameters of the Rice distribution," *J. Acoust. Soc. Am.*, vol. 89, no. 3, pp. 1193–1197, Mar. 1991.

A.3 In-room Reverberant Multi-link Channels: Preliminary Investigations

G. Steinböck, T. Pedersen, B.H. Fleury, W. Wang, and R. Raulefs In-room Reverberant Multi-link Channels: Preliminary Investigations. *IC1004 Temporary Document TD(12)03042, Barcelona, Spain, February 8-10, 2012.*

EUROPEAN COOPERATION
IN THE FIELD OF SCIENTIFIC
AND TECHNICAL RESEARCH

EURO-COST

SOURCE: Aalborg University

IC1004 TD(12)03042
Barcelona, Spain
February 8-10, 2012

In-room Reverberant Multi-link Channels: Preliminary Investigations

G. Steinböck, T. Pedersen, B.H. Fleury
Aalborg University
Dept. of Electronic Systems
Section NavCom
Fredrik Bajers Vej 7C
DK-9220 Aalborg East
DENMARK

W. Wang, R. Raulefs
German Aerospace Center (DLR)
Institute of Communications and Navigation
Oberpfaffenhofen
D-82234 Wessling
GERMANY

Phone: +45 9815 8615
Fax: +45 9815 1583
Email: gs@es.aau.dk

In-room Reverberant Multi-link Channels: Preliminary Investigations

Gerhard Steinböck, Troels Pedersen
and Bernard H. Fleury
Dept. of Electronic Systems,
Section Navigation and Communications,
Aalborg University
Fredrik Bajers Vej 7, DK-9220 Aalborg East, Denmark
Email: {gs, troels, bfl}@es.aau.dk

Wei Wang and Ronald Raulefs

Institute of Communications and Navigation,
German Aerospace Center (DLR)
Oberpfaffenhofen, 82234 Wessling, Germany
Email: {wei.wang, ronald.raulefs}@DLR.de

***Abstract*—We model the delay power spectrum of in-room reverberant multi-link radio channels. The model relies on the empirical observation that the delay power spectrum of each link measured in a closed room, consists of an early peak and a late exponential reverberation tail. The peak vanishes as the transmitter-receiver distance increases; the exponential decay of the reverberation tail is invariant with distances, while the onset of the tail is equal to the propagation time between the transmitter and the receiver. The proposed model allows for the prediction of path loss, mean delay, and rms delay spread versus distance for multiple links. These predictions are in good agreement with the estimates obtained from the multi-link measurements.**

I. Introduction

The field of indoor radio-localization has recently attracted significant interest. One approach for solving the localization problem is to rely on the measured power of the received signal [1] and to use a path loss model to infer the corresponding length of a radio link. Knowledge of the received power is often used for localization in already deployed systems (e.g. WiFi) where received signal strength is readily available or with cheap low power devices in sensor networks. To obtain an ambiguity free location estimate, multiple transmitter-receiver distance estimates are necessary. Thus multi-link models are of importance for radio-localization purposes.

In [2] we propose a distance dependent delay power spectrum model for in-room reverberant channels. This model builds on experimental observations of the behavior of the delay-power spectrum [3], [4] and on analogies to models used in room acoustics [5] and electromagnetic fields in cavities [6]. The model of the delay-power spectrum consists of a dominant and a reverberant component, which both depend on distance. This allows for the prediction of path gain (inverse of path loss), mean delay and rms delay spread versus distance. Thus, the model can be used to predict the transmitter-receiver distance based on measurement of one of these quantities, e.g. for localization purpose.

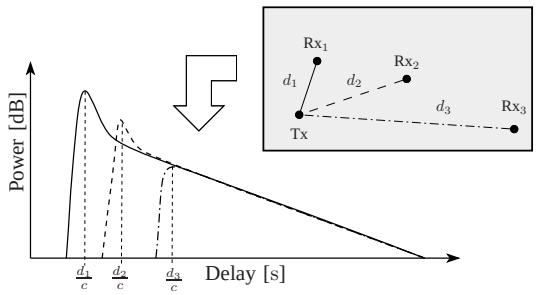

Fig. 1. Typical behavior of the bandlimited delay-power spectrum experimentally observed in an in-room environment at three different transmitter-receiver distances (schematically presented by the grey box).

In this contribution we present preliminary results on the delay power spectrum model used in a multi-link scenario. We summarize the model and validate it by comparing the predicted received power, mean delay and rms delay spread with estimates obtained from multi-link measurements.

II. Delay Power Spectrum Model

As in [2], we consider an in-room scenario as illustrated in Fig. 1. The delay-power spectrum is observed at different transmitter and receiver locations. A system bandwidth high enough to observe frequency fading (delay dispersion), but too low to separate single propagation paths in the environment is considered. The considered carrier frequencies are high enough, such that the smallest dimension of the room is large compared to the wavelength λ. The delay-power spectrum is the expectation of the squared magnitude of the impulse response $h(\tau, d)$:

$$G(\tau, d) = \mathrm{E}[|h(\tau, d)|^2]. \quad (1)$$

Here τ is the delay and d is the transmitter-receiver distance. In [4] it is observed that the delay-power spectrum in such an in-room scenario exhibits the typical

TABLE I
PARAMETERS OF THE PROPOSED MODEL.

Parameter	Meaning
G_0	Path gain at reference distance d_0.
d_0	Reference distance, typically 1 m.
n	Path gain decay exponent of the dominant component.
q	Ratio $G_{\mathrm{rev}}(d_0)/G_{\mathrm{dom}}(d_0)$.
T	Reverberation time of the reverberant component.

behavior depicted in Fig. 1. The tail of the delay-power spectrum exhibits the same constant exponential decay regardless of the transmitter-receiver distance. The early part is strong at short distance and gradually vanishes as the distance increases.

Based on these observations, we model the delay-power spectrum as a dominant component plus a reverberant component:

$$\begin{aligned} G(\tau, d) &= \mathrm{E}[|h_{\mathrm{dom}}(\tau, d)|^2] + \mathrm{E}[|h_{\mathrm{rev}}(\tau, d)|^2] \\ &= G_{\mathrm{dom}}(\tau, d) + G_{\mathrm{rev}}(\tau, d). \end{aligned} \tag{2}$$

Subscript dom indicates the dominant component and subscript rev denotes the reverberant component. The dominant component represents the early part of the delay-power spectrum consisting of a directly propagating component and possible first-order reflections from the floor, ceiling and walls. The reverberant component represents the multitude of higher order reflections in the room which yield the diffuse tail of the delay-power spectrum.

We model the delay-power spectrum of the dominant component as

$$G_{\mathrm{dom}}(\tau, d) = G_0 \left(\tfrac{d_0}{d}\right)^n \delta\left(\tau - \tfrac{d}{c}\right), \tag{3}$$

where n is the power decay exponent, $\delta(\,\cdot\,)$ is the Dirac delta function, c the speed of light, and $G_0 > 0$ is the gain at the reference distance d_0.

We model the reverberant delay-power spectrum as an exponentially decaying function with onset equal to the propagation time between the transmitter and the receiver:

$$G_{\mathrm{rev}}(\tau, d) = \begin{cases} G_{0,\mathrm{rev}}\, e^{-\frac{\tau}{T}}, & \tau > \frac{d}{c} \\ 0, & \text{otherwise} \end{cases} \tag{4}$$

where $G_{0,\mathrm{rev}}$ is the reference gain of the reverberant component. In analogy to acoustics [4], [5] we call T the reverberation time.

III. PREDICTIONS OF THE DELAY POWER SPECTRUM MODEL

Based on the model (2) we derived in [2] expressions for the path gain, mean delay, and rms delay spread as a function of the transmitter-receiver distance.

A. Path gain

The path gain at distance d is

$$\begin{aligned} G(d) &= \int G(\tau, d)\mathrm{d}\tau \\ &= \underbrace{G_0 \left(\tfrac{d_0}{d}\right)^n}_{G_{\mathrm{dom}}(d)} + \underbrace{G_{0,\mathrm{rev}}\, T\, e^{\frac{-d}{c\,T}}}_{G_{\mathrm{rev}}(d)}. \end{aligned} \tag{5}$$

The component $G_{\mathrm{dom}}(d)$ decays with d^{-n}, while $G_{\mathrm{rev}}(d)$ decays exponentially. Denoting by q the ratio of reverberant to dominant gain at reference distance d_0:

$$q = \frac{G_{\mathrm{rev}}(d_0)}{G_{\mathrm{dom}}(d_0)} = \frac{G_{0,\mathrm{rev}}}{G_0}\, T\, e^{\frac{-d_0}{c\,T}}, \tag{6}$$

the path gain can be recast as

$$G(d) = G_0 \left(\tfrac{d_0}{d}\right)^n + G_0\, q\, e^{\frac{d_0 - d}{c\,T}}. \tag{7}$$

The graph of $G(d)$ versus distance and q as parameter is depicted in Fig. 2a. At small distances $G_{\mathrm{dom}}(d)$ dominates and the path gain decays as d^{-n}. Beyond the reverberance distance d_r, the contribution of the reverberant component $G_{\mathrm{rev}}(d)$ in $G(d)$ leads to a deviation from $G_{\mathrm{dom}}(d)$.

The standard path gain model is a special case of (7) where the reverberant component is zero ($q = 0$). It reads

$$G_{\mathrm{std}}(d) = G_0 \left(\tfrac{d_0}{d}\right)^n. \tag{8}$$

We remark that the path loss is defined as the inverse of the path gain: $L(d) = G(d)^{-1}$. For notational convenience we consider only path gain in the sequel.

B. Mean Delay and Root Mean Squared Delay Spread

We derived the mean delay at distance d in [2] from (2) as

$$\mu_\tau(d) = \frac{1}{G(d)} \int \tau\, G(\tau, d)\mathrm{d}\tau \tag{9}$$

$$= \tfrac{d}{c} + T \frac{1}{1 + \left(\tfrac{d_0}{d}\right)^n \tfrac{1}{q}\, e^{\frac{d - d_0}{c\,T}}}. \tag{10}$$

In (10) the first term is the delay of a directly propagating component and the second term results from the reverberant component. Fig. 2b depicts the mean delay versus distance with the settings specified in the figure. The mean delay increases with distance. For distances larger than the reverberance distance, the curves approximately follow the straight line $\frac{d}{c} + T$.

Similarly the rms delay spread reads:

$$\sigma_\tau^2(d) = \frac{1}{G(d)} \int \tau^2\, G(\tau, d)\mathrm{d}\tau - \left(\mu_\tau(d)\right)^2, \tag{11}$$

$$= \frac{T^2}{1 + \left(\tfrac{d_0}{d}\right)^n \tfrac{1}{q}\, e^{\frac{d - d_0}{c\,T}}} \left(2 - \frac{1}{1 + \left(\tfrac{d_0}{d}\right)^n \tfrac{1}{q}\, e^{\frac{d - d_0}{c\,T}}}\right). \tag{12}$$

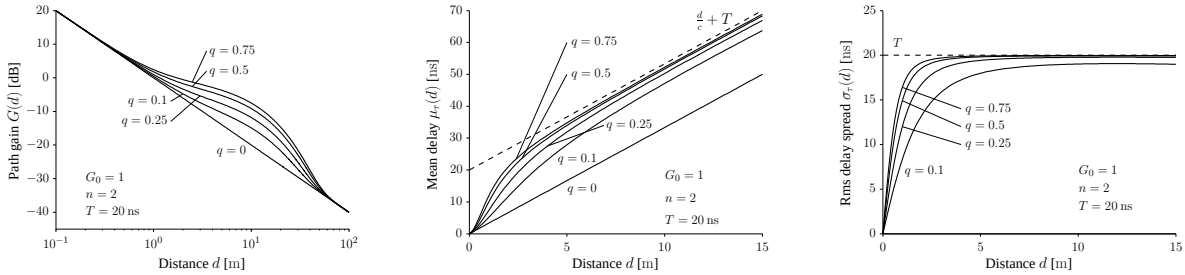

(a) (b) (c)

Fig. 2. Path gain (a), mean delay (b) and rms delay spread (c) versus distance predicted by the proposed model for $d_0 = 1$ m.

Fig. 2c depicts the rms delay spread versus distance. For distances larger than the reverberance distance $\sigma_\tau(d)$ approaches the reverberation time T.

C. Extension to the Multi-link Scenario

In the multi-link case we make use of the assumption that the delay power spectrum model and the corresponding model parameter settings are the same for all positions in the room. The dominant and reverberant component depend solely on the transmitter-receiver distance. Then for link k with transmitter-receiver distance d_k we have path gain $G(d_k)$, mean delay $\mu(d_k)$ and rms delay spread $\sigma(d_k)$.

IV. Measurement Setup

We validate the proposed model by means of measurement data from a campaign [7] conducted at DLR in Oberpfaffenhofen, Germany. The investigated room is sketched in Fig. 3. A panograph of it is depicted in Fig. 4. During the measurement process the environment was static and no one was in the room.

The room dimensions are $5.1 \times 5.25 \times 2.78\,\mathrm{m}^3$. The three inner walls are made of plaster boards. As visible in the panograph, the outer "wall" consists mainly of four windows (W1–W4) and two pillars made of concrete. The frames of the windows are metallic and the glass is metal coated. The height of the transmit and receive antenna was 1.26 m and 1.1 m, respectively.

The measurement data were collected using the Rusk-DLR channel sounder [8] operating at 5.2 GHz with a bandwidth of 120 MHz. The transmit antenna [9] was omni-directional with 3 dBi gain. A uniform circular array of eight monopoles with diameter 75.18 mm was used at the receiver. The transmitter and receiver were synchronized to a common clock via cables throughout the measurements.

The receive antenna array was placed at five fixed locations labeled as Rp1 to Rp5 respectively in Fig. 3. The transmit antenna was mounted on a model train which moved on two tracks labeled as T1 and T2. Frequency responses were measured for each receiver

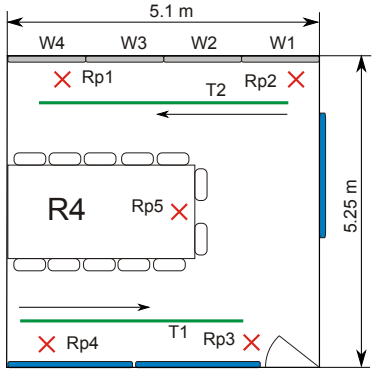

Fig. 3. Schematic of the investigated room. The arrows next to the tracks indicate the transmitter movement direction.

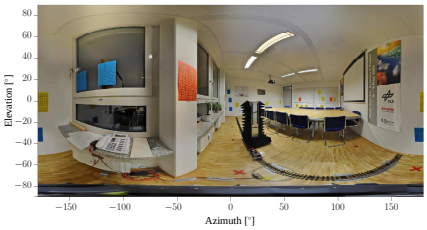

Fig. 4. Panograph (spherical panoramic photo) of the investigated room seen from Rp1 using an equi-rectangular projection.

position while the transmitter was moving along the two tracks.

The positions Rp1-Rp5 and the trajectories along the tracks were measured with a tachymeter. The odometer of the model train was connected to the channel sounder to record the traveled distance.

V. Model Fitting and Validation

A. Measurement Post Processing and Model Parameter Estimation

In this contribution we only consider the measurements obtained for receiver positions Rp1 to Rp4 and the transmitter moving on both, tracks T1 and T2. We compute the received power and the delay power spectrum at all pairs of transmitter-receiver positions as described

TABLE II
PARAMETER ESTIMATES FOR THE STANDARD AND PROPOSED MODELS.

Model	$\widehat{G}_0$	$\widehat{n}$	$\widehat{q}$	$\widehat{T}$ [ns]
Standard	$1.14 \cdot 10^{-5}$	1.13	—	—
Proposed	$6.85 \cdot 10^{-6}$	2.2	0.54	18.4

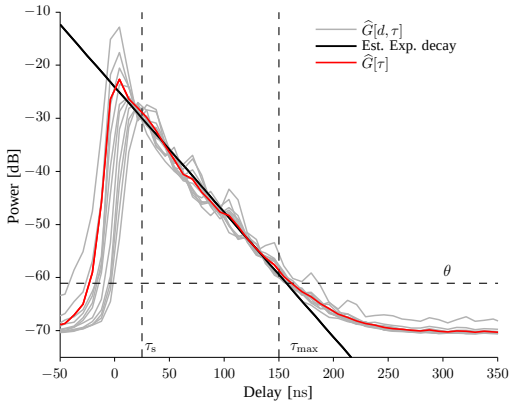

Fig. 5. Spatially averaged delay-power profiles obtained for transmitter-receiver distance intervals of 4λ for receiver positions Rp1 to Rp4 when the transmitter was moving along track T1 and T2. For clarity reasons only the delay power profiles of every second distance interval are shown. The straight line depicts an exponentially decaying function with decay factor $\widehat{T} = 18.4\,\text{ns}$. The dashed lines indicate the range $\tau_s = 25\,\text{ns} \leq \tau \leq \tau_{\max} = 150\,\text{ns}$ used for the estimation of $\widehat{T}$.

in detail in [2]. Fig. 6 reports the scatter plot of power values versus transmitter-receiver distance. As can be seen in Fig. 5 the underlying model assumption (4) holds true for the experimental delay-power spectra. Using the method, detailed in [2], to estimate the reverberation time in the range $25\,\text{ns} \leq \tau \leq 150\,\text{ns}$ yields $\widehat{T} = 18.4\,\text{ns}$.

We fit both the standard path loss model (8) and the proposed model as detailed in [2]. The estimates of the parameters of the models are reported in Table II and the path gains versus distance computed from the models with these parameter settings are shown in Fig. 6. For small distances the proposed model fits the estimated received power values better than the standard path gain model.

We compute the mean delay estimates $\widehat{\mu}_\tau$ and rms delay spread estimates $\widehat{\sigma}_\tau$ for each pair of transmitter-receiver positions from the estimates of the delay power spectra using (9) and (11), respectively. These estimates computed for all transmitter-receiver positions are reported for the multi-link scenario with the transmitter moving on track T1 in Fig. 9 and Fig. 10. These values are in accordance with values reported in [10] for office environments.

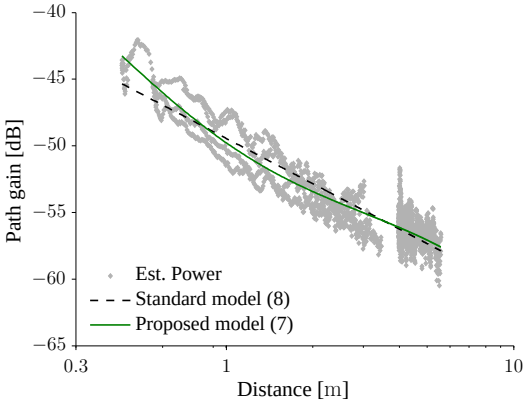

Fig. 6. Estimated received power versus distance with the predictions computed using the standard and the proposed path gain models.

B. Multi-link Preliminary Results

The transmitter-receiver distance between the multi-links and the model parameters reported in Table II are used to predict the path gain, mean delay and rms delay spread for the multi-links with (7), (10) and (12), respectively. Fig. 7 reports the transmitter-receiver distances when the transmitter is moving along track T1. We observe rather small changes in the transmitter-receiver distance for the receiver positions Rp1 and Rp2 (opposite T1). For Rp3 and Rp4 we observe a clear change in transmitter-receiver positions as in the one case the transmitter moves towards and in the other moves away from the receiver.

Fig. 8 shows model predictions of the received power together with the estimated receive power from the experimental data. The predictions of the standard and the proposed models are close to each other and follow well the trend of the received power estimates.

The proposed delay power spectrum model allows for the prediction of mean delay and rms delay spread. These predicted values are shown together with the estimates from the experimental results in Fig. 9 and 10. The trend of the obtained estimates from the experimental data follows closely the predictions. This is remarkable as for the model fitting we used only: i) an estimate of T from the exponential decay of the tail of the delay power spectrum and ii) the estimates of the received power versus transmitter-receiver distance.

VI. CONCLUSIONS

We propose a model for the delay power spectrum of in-room multi-link channels. The model is able to predict the received power, mean delay and rms delay spread in the multi-link case. We observe that the predictions of the model agree well with the trends observed in the estimates obtained from the measured data. These estimates

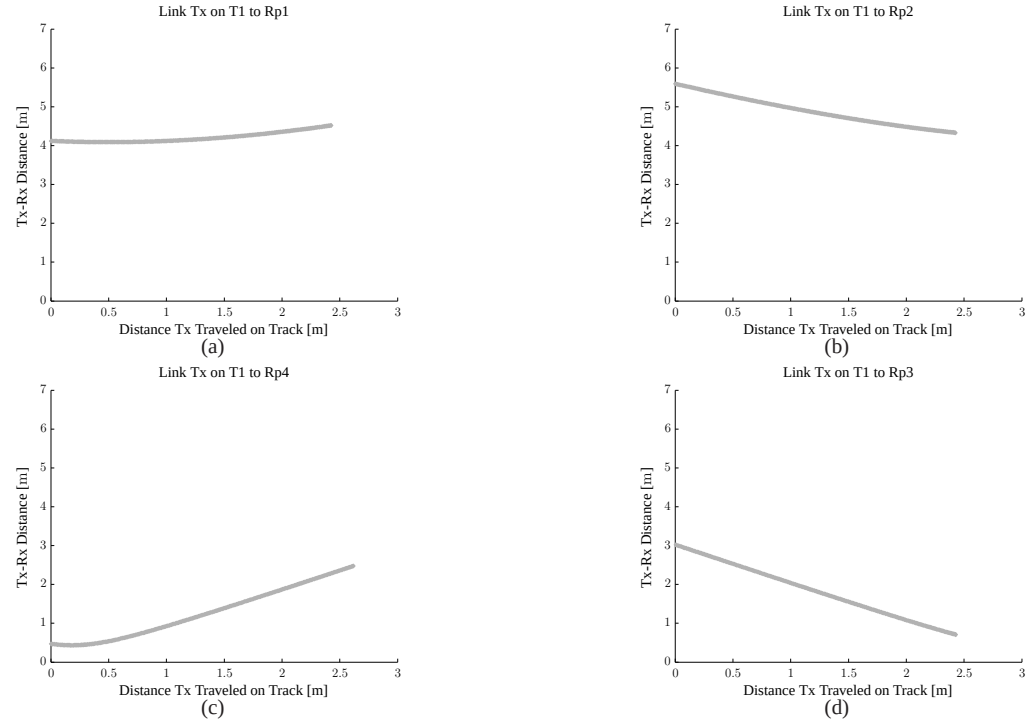

Fig. 7. Transmitter-receiver distance of the different links for the transmitter moving along track T1. The distance is obtained for the center of the receiver array.

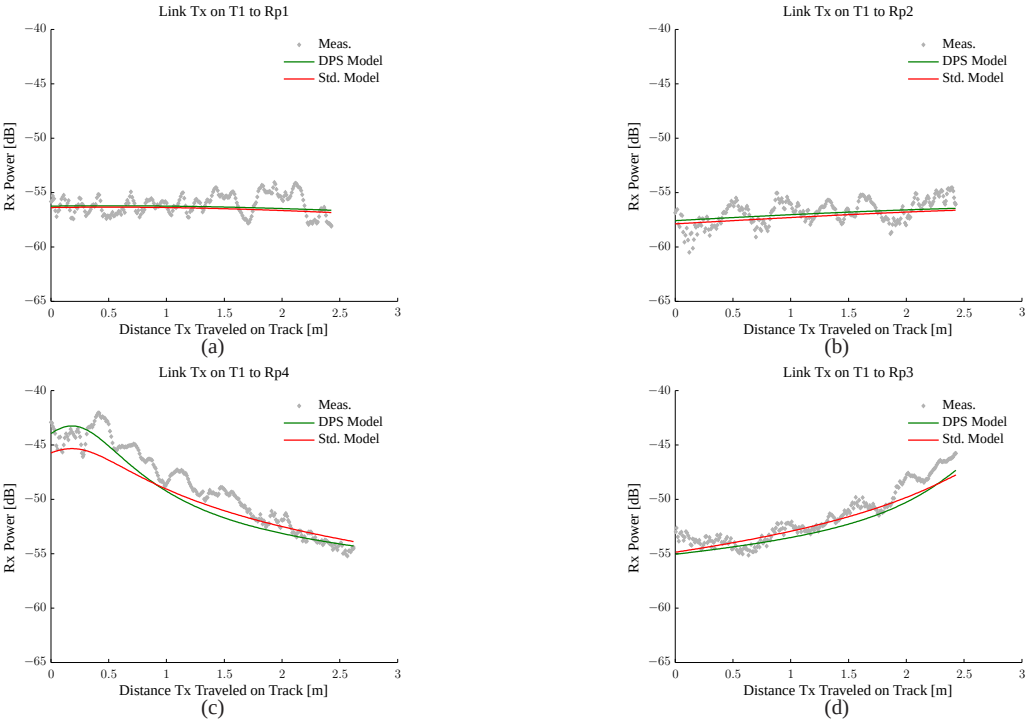

Fig. 8. Estimates of the received power from experimental data together with predictions for the multi-link scenario with the transmitter moving along track T1.

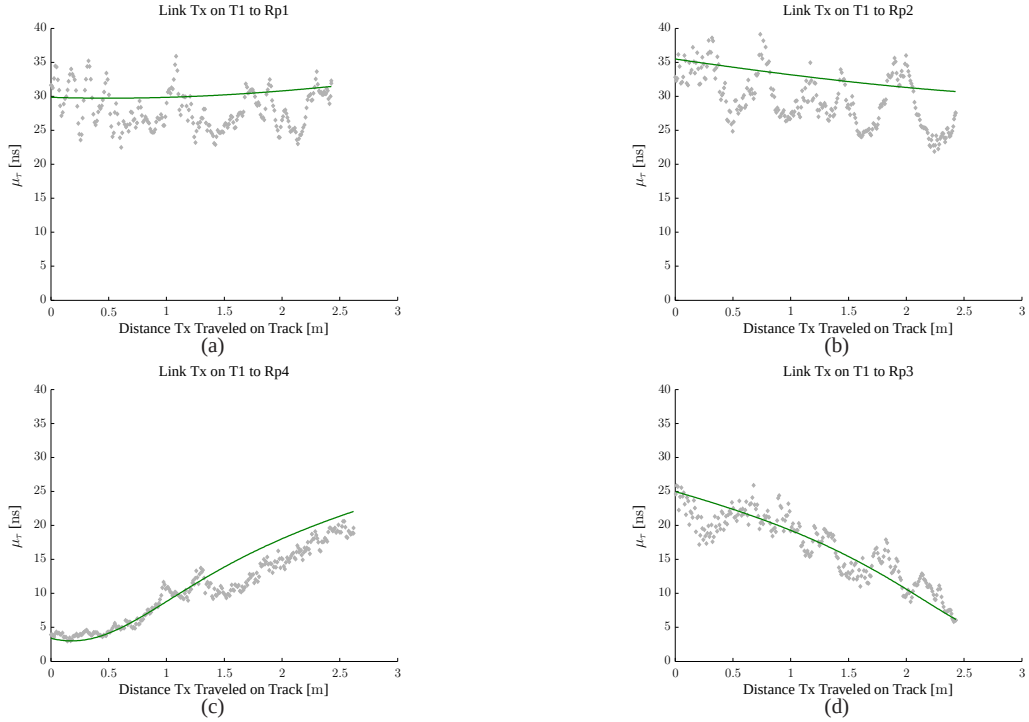

Fig. 9. Estimates of the mean delay from experimental data and the predictions in the multi-link case with the transmitter moving along track T1.

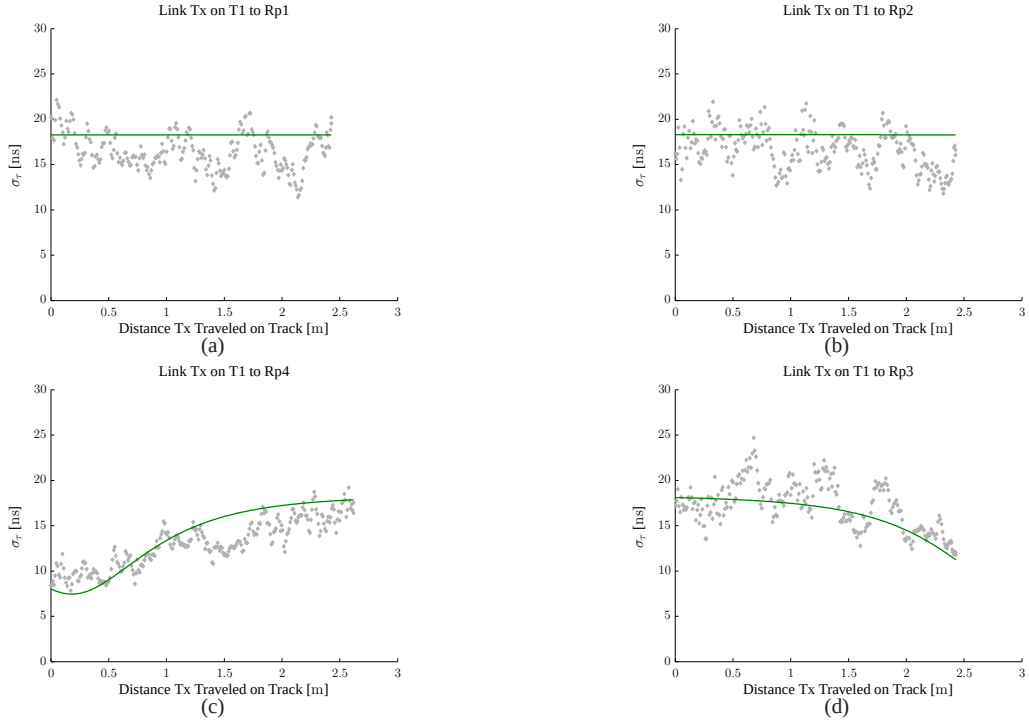

Fig. 10. Estimates of the rms delay spread from experimental data and the predictions in the multi-link case with the transmitter moving along track T1.

show a random fluctuation which can be attributed to small scale fading. In a next step we will include in the model these fluctuations. To that end the model should be extended to account for the correlation between the received power, mean delay and rms delay spread in both single and multi-link cases.

ACKNOWLEDGMENT

This work was supported by the project ICT-248894 Wireless Hybrid Enhanced Mobile Radio Estimators – Phase 2 (WHERE2).

REFERENCES

[1] H. Liu, H. Darabi, P. Banerjee, and J. Liu, "Survey of Wireless Indoor Positioning Techniques and Systems," *IEEE Trans. Syst., Man, Cybern. C*, vol. 37, no. 6, pp. 1067–1080, Nov. 2007.

[2] G. Steinböck, T. Pedersen, B. Fleury, W. Wang, T. Jost, and R. Raulefs, "Model for the Path Loss of In-room Reverberant Channels," in *Vehicular Technology Conference (VTC 2011-Spring), 2011 IEEE 73rd*, May 2011, pp. 1–5.

[3] C. Holloway, M. Cotton, and P. McKenna, "A model for predicting the power delay profile characteristics inside a room," *IEEE Trans. Veh. Technol.*, vol. 48, no. 4, pp. 1110–1120, 1999.

[4] J. B. Andersen, J. Ø. Nielsen, G. F. Pedersen, G. Bauch, and J. M. Herdin, "Room electromagnetics," *IEEE Antennas Propag. Mag.*, vol. 49, no. 2, pp. 27–33, 2007.

[5] H. Kuttruff, *Room Acoustics*, 4th ed. London: Taylor & Francis, 2000.

[6] D. A. Hill, *Electromagnetic Fields in Cavities: Deterministic and Statistical Theories*, ser. IEEE Press Series on Electromagnetic Wave Theory. Piscataway, NJ: Wiley/IEEE Press, 2009.

[7] G. Steinböck, T. Pedersen, and W. Wang, "AAU-DLR 2010 Indoor Measurement Campaign – Measurements for Validation of Models for Reverberant and Cooperative Channels," AAU and DLR, Report, 2011.

[8] J. Stephan, Y. Lostanlen, J. Keignart, W. Wang, D. Slock, and F. Kaltenberger, "Measurements of location-dependent channel features," ICT-217033 WHERE, Del. 4.1, Oct. 2008, http://www.ict-where.eu/.

[9] Huber+Suhner, "Datasheet for Sencity Antenna For In-Carriage Wireless Communication, Type: SOA 5600/360/3/20/V_1," Document No. 01.02.1358, May 2007.

[10] E. Damosso, Ed., *Digital mobile radio towards future generation systems: COST 231 Final Report*. Bruxelles, Belgium: European Commission, 1999.

A.4 Channel Measurements and Characteristics for Cooperative Positioning Applications

W. Wang, G. Steinböck, T. Jost, T. Pedersen, R. Raulefs and B.H. Fleury Channel Measurements and Characteristics for Cooperative Positioning Applications. In Proceedings of International Conference on Localization and GNSS, Munich, Germany, June 2012..

Channel Measurements and Characteristics for Cooperative Positioning Applications

Wei Wang*, Gerhard Steinböck‡, Thomas Jost*, Troels Pedersen‡, Ronald Raulefs* and Bernard Fleury‡

* German Aerospace Center (DLR)
Institute of Communications and Navigation
Oberpfaffenhofen, 82234 Wessling, Germany

‡Aalborg University
Dept. of Electronics Systems, Section Navigation and Communications,
Fredrik Bajers Vej 7, DK-9220 Aalborg East, Denmark

***Abstract*—We have conducted an indoor channel measurement campaign to characterize the propagation channel for the development of cooperative positioning algorithms. The campaign focused particularly on the characteristics of multi-link channels with applications to positioning. In this contribution we present the measurement campaign and preliminary results on correlation characteristics of the received power. It is observed that the link-pair log power is uncorrelated. Moreover, the received log power can be modeled by realizations of independent Gaussian distributions for each link, based on the measured results.**

I. Introduction

Cooperative positioning for indoor scenarios has gained much interest in past years. Such techniques rely on measuring and exchanging ranging and related information between terminals in cooperative communication networks [1] [2] [3]. In a cooperative network, anchor terminals at known positions are used to identify unknown positions of the mobile terminals given observations of ranges of a set of links as shown in Fig. 1. The estimated positions of mobile terminals are used to help and improve the position estimation of other mobile terminals. For each link, range observations can be obtained from different distance related channel features, e.g., the received signal strength indicator (RSSI) of the radio channel [4]. Thus knowledge of the relationship between range and radio channel features is a prerequisite for cooperative positioning in communication networks.

According to the survey [5], several works on channel characterization for cooperative communication scenarios have recently appeared. Models of the received power reported in [6], [7] consider large scale fading in cooperative networks. They may be used to study positioning methods relying on RSSI observations. However, these investigations of cooperative channels for communications focus on aspects where the relation to link ranges is less relevant. Consequently, many of these contributions lack the accuracy in the description of the link geometry necessary for indoor positioning purposes.

In the present contribution we characterize the received power for cooperative positioning. The characterization is obtained based on an indoor channel measurement campaign conducted at the German Aerospace Center (DLR) facilities. The measurements were performed with a purpose-built measurement platform allowing for accurate transceiver position information during the quasi-static measurement.

We introduce a multi-link signal model for the log power in Section II and present the measurement campaign in Section III. Post processing the measurements as outlined in Section IV provides the results in Section V. The results indicate that the log power values are Gaussian with low correlation between links. Based on these observations we propose to model the log power of the links as independent Gaussian random variables with the mean following a path loss model such as [4], [8].

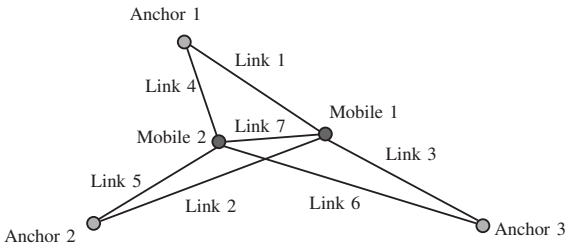

Fig. 1. The considered cooperative scenario with anchors and mobiles at known and unknown positions respectively. The position of each mobile is estimated based on range dependent radio channel observations of its links in the network.

II. Multi-link Model for Positioning

We consider the scenario in Fig. 1 with several anchor terminals and mobile terminals. Both anchor-to-mobile and mobile-to-mobile links are considered. Let P_ℓ denote the received log power of link ℓ after averaging out the fast fading due to multi-path propagation.[1] We consider P_ℓ as a random variable with mean μ_ℓ. We rewrite $P_\ell = \mu_\ell + R_\ell$ where the residual R_ℓ is a zero mean random variable. The observations from all L links can be expressed in vector form as

$$\mathbf{P} = \boldsymbol{\mu} + \mathbf{R}, \tag{1}$$

with $\mathbf{P} = [P_1, \ldots, P_\ell, \ldots, P_L]^T$ and vectors $\boldsymbol{\mu}$ and $\mathbf{R}$ defined similarly. The mean power $\boldsymbol{\mu}$ can be expressed via an appropriate path loss model [4], [8]. However, in this work we do not consider a specific path loss model. The residual may include deviations from the mean power due to the environment and the locations of the anchors and mobile nodes in the environment. In practical settings, $\mathbf{R}$ also includes estimation errors of an RSSI estimator. In this contribution

[1]This averaging can be done in practical implementations in the spatial and/or frequency domain.

TABLE I
CHANNEL SOUNDER SETTINGS.

Parameter	Value
RF centre frequency	5.2 GHz
Bandwidth	120 MHz
Number of sub-carriers	1537
Sub-carrier spacing Δf	78.125 kHz
Transmit power	1 mW
Signal period	12.8 μs
Number of snapshots per block	20
Block repetition rate	131.072 ms
Transmitter antenna	Omni-directional (V-polarized)
Receiver antenna	8-element UCA (V-polarized)
Train speed	0.074 ± 0.01 m/s

we do not consider the mean power but focus on the second order characterization of $\mathbf{R}$ jointly for all links. The covariance matrix of $\mathbf{R}$ and thus of $\mathbf{P}$ is denoted as

$$\mathbf{\Sigma} = \mathrm{cov}(\mathbf{R}) = E\{\mathbf{R}\mathbf{R}^T\}, \tag{2}$$

where $E\{\cdot\}$ is the expectation operator. The correlation coefficient matrix obtained by normalizing $\mathbf{\Sigma}$ as

$$\boldsymbol{\rho} = \boldsymbol{D}_{\mathbf{\Sigma}}{}^{-1/2}\, \mathbf{\Sigma}\, \boldsymbol{D}_{\mathbf{\Sigma}}{}^{-1/2}, \tag{3}$$

where $\boldsymbol{D}_{\mathbf{\Sigma}}$ is a diagonal matrix with the same diagonal entries as $\mathbf{\Sigma}$. It is worth to note that $\mathbf{\Sigma}$ can be recovered if $\boldsymbol{D}_{\mathbf{\Sigma}}$ and $\boldsymbol{\rho}$ are known.

III. CHANNEL MEASUREMENT CAMPAIGN

The measurements were conducted with a MEDAV RUSK broadband channel sounder at the premises of the German Aerospace Center (DLR). The parameter setup of the channel sounder is summarized in Table I. A wideband signal, more specifically a multitone, was sent by the transmitter. The single transmit antenna depicted on the left side of Fig. 2 was mounted on the top of a railway model which was running along a track, see Fig. 3. The receiver was equipped with an 8-element uniform circular array (UCA) as visualized on the right side of Fig. 2. Both the transmit and receive antennas were vertically polarized. In a snapshot all eight channel frequency responses are sequentially measured. The sounder was operating in "block" mode. In each block 20 consecutive snapshots are performed. The block period is 131.072 ms. The transmitting antenna mounted on the model train shown on the left side of Fig. 2 moved with a speed of about 0.074 m/s. Thus from block to block the transmitter moved approximately 7.8 mm or 0.14 wavelengths. From snapshot to snapshot within a block the transmitter moved approximately 2×10^{-4} wavelengths.

The center position of the receiver array was precisely determined using a tachymeter giving a nominal accuracy in the sub-cm domain. To get a similar accuracy for the transmitter antenna, we run the model train by a cogwheel. The motor of the train is equipped with a rotary encoder which generates 500 impulses per motor turn. This results in a precise measurement of the traveled distance along the track for each captured channel transfer function. More details of the hardware setup can be found in [9].

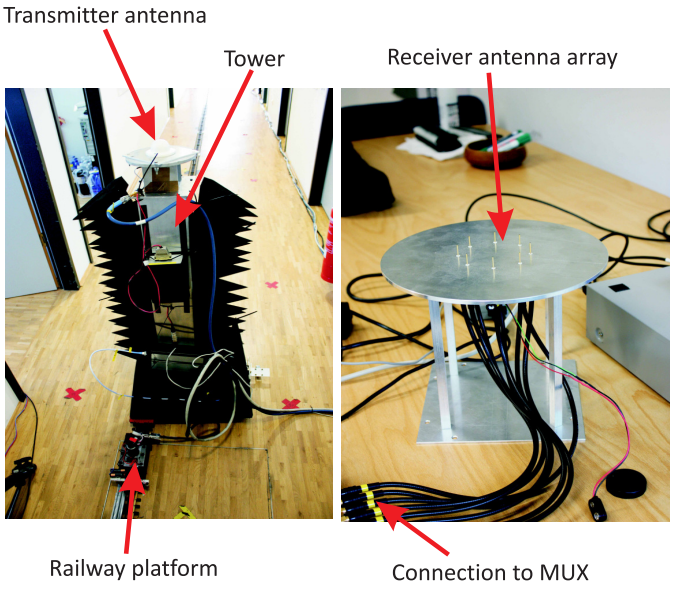

Fig. 2. Measurement setup with the used antennas.

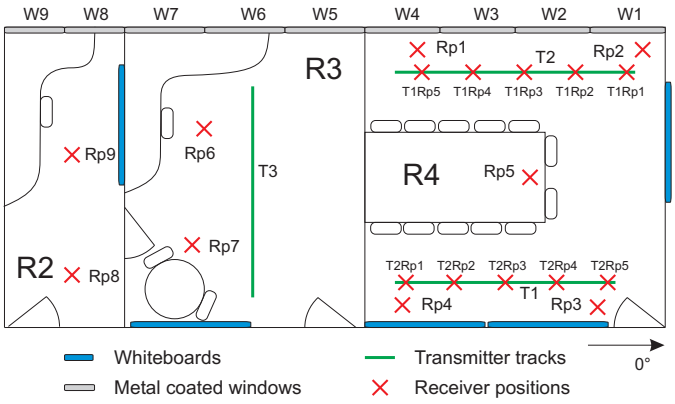

Fig. 3. Overview of the measured indoor environment.

The experimentally investigated indoor environment is depicted in Fig. 3 and described in [10]. The receiver array was placed at positions labeled from Rp1 to Rp9. The receivers at those locations may act as anchor nodes and/or mobile nodes while the transmitter was running on tracks T1, T2 and T3. Moreover, the receiver array was also located at 5 positions on track T1 and T2 while the transmitter was running on track T2 and T1 respectively. The corresponding locations are labeled from T1Rp1 to T1Rp5 and T2Rp1 to T2Rp5. In this contribution we only focus on the measurements with the transmitter moving on track T1 and the receivers located in room R4.

As the hardware setup allows only single link measurements, we alternatively measure the links sequentially, one by one. By using the high positioning accuracy of the measurement platform, we are able to associate and group the measured channel transfer functions to link-pairs. This data association is addressed in Section IV in more details. During the measurement time, no persons were inside the room and the door was closed to keep the environment as stable as possible.

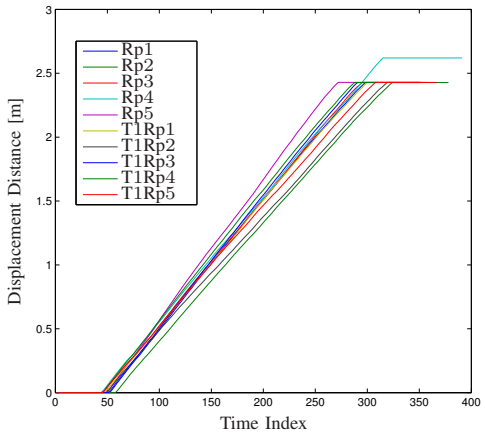

Fig. 4. Displacement along track T1 for the measurements.

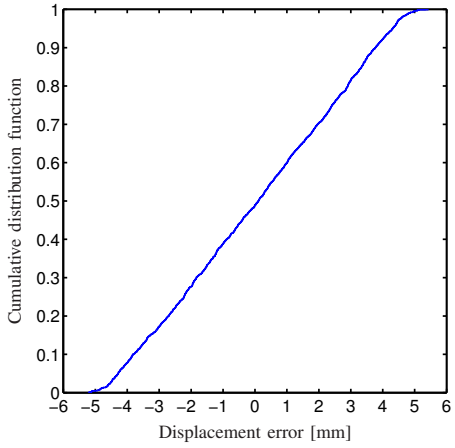

Fig. 5. Cumulative distribution function of displacement errors.

IV. Data Processing

The channel transfer function can be assumed as constant within each block due to the high measurement rate. This allows to reduce the noise floor by averaging the measured transfer functions within a block. The average channel transfer function recorded from link ℓ with receive antenna m at subcarrier f within block b is denoted by $H_{\ell,m}(b,f)$, where $f = 0,\ldots,N-1$.

A. Data Association

The experimental data was obtained by sequentially measuring the links one by one in a quasi-static environment. Thus, to emulate a multi-link scenario for a particular transmitter position we would consider the single link data obtained at that position. This, however, can be done only approximately, because the measurements were taken with a fixed time grid and a varying train velocity. In this work we consider the displacement along the track of the transmitter. Fig. 4 visualizes the transmitter displacement as a function of the block time index. We only consider the measurement data collected when the train was moving and discard the measurement data collected in the beginning and end of the track when the train was stationary. We observe different slopes of the lines, indicating a difference in the train velocity for each measured link. The displacement along track T1 for adjacent time indices is approximately 1 cm.

For each link ℓ we measured B_ℓ blocks of channel transfer functions at the corresponding displacement distances $d_{1,\ell},\ldots,d_{B_\ell,\ell}$. We choose as the displacement reference for a given track the displacement of link $\widehat{\ell}$ where the train was moving the fastest on this track. This fastest run results in a minimum number of measured blocks. For block $i \in \{1,\ldots,B_{\widehat{\ell}}\}$ with the reference displacement $d_{i,\widehat{\ell}}$ we seek the block with index $b_\ell(i)$ which is recorded closest to the reference displacement; ie.

$$b_\ell(i) = \arg\min_j ||d_{i,\widehat{\ell}} - d_{j,\ell}||, \qquad \ell = 1,\ldots,L. \tag{4}$$

For block index i we assign the average displacement d_i calculated as

$$d_i = \frac{1}{L}\sum_{\ell=1}^{L} d_{b_\ell(i),\ell}. \tag{5}$$

The displacement d_i corresponds to the average of matched displacement distances of the links between a transmitter position and all L receiver antenna array positions. The cumulative distribution of the displacement errors $(d_i - d_{b_\ell(i),\ell})$ are shown in Fig. 5. The error is almost uniformly distributed over ± 5 mm.

B. Estimation of Power, Residual and Correlation Coefficients

The log of the averaged received power at the ℓ-th link and position d is obtained by averaging in the frequency domain and spatial domain (8-elements of the receiver array) as

$$\widehat{P}_\ell(d) = 10\log_{10}\left(\frac{1}{8\,N}\sum_{m=1}^{8}\sum_{f=0}^{N-1}|H_{\ell,m}(d,f)|^2\right)\ [\mathrm{dB}]\,. \tag{6}$$

In this contribution the estimate of the mean power $\widehat{\mu}_\ell(d)$ at d is obtained by averaging the corresponding $\widehat{P}_\ell(d)$ within a sliding window size of approximately 42 cm. This window size corresponds to estimates of 41 blocks, centered at position d. We collect the estimates $\widehat{P}_\ell(d)$ and $\widehat{\mu}_\ell(d)$ for all links and positions in matrices $\widehat{\mathbf{P}} \in \mathbb{R}^{L\times B_{\widehat{\ell}}}$ and $\widehat{\boldsymbol{\mu}} \in \mathbb{R}^{L\times B_{\widehat{\ell}}}$ respectively. The estimated residual reads

$$\widehat{\mathbf{R}} = \widehat{\mathbf{P}} - \widehat{\boldsymbol{\mu}}. \tag{7}$$

The covariance matrix is estimated from $\widehat{\mathbf{R}}$ by averaging over all positions d as

$$\widehat{\boldsymbol{\Sigma}} = \frac{1}{B_{\widehat{\ell}}}\widehat{\mathbf{R}}\widehat{\mathbf{R}}^T. \tag{8}$$

By insertion of $\widehat{\boldsymbol{\Sigma}}$ in Eq. (3) we obtain the estimate of $\widehat{\boldsymbol{\rho}}$.

V. Results

We make the assumption that the displacement errors after the data association do not effect the evaluation of $\widehat{\boldsymbol{\Sigma}}$. To validate this, we evaluate the correlation coefficient of the residual

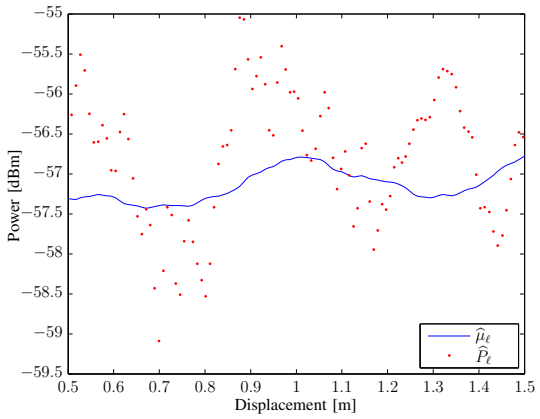

Fig. 6. Measured power at Rp2 versus displacement. The mean power computed using the sliding window of length 42 cm is also reported.

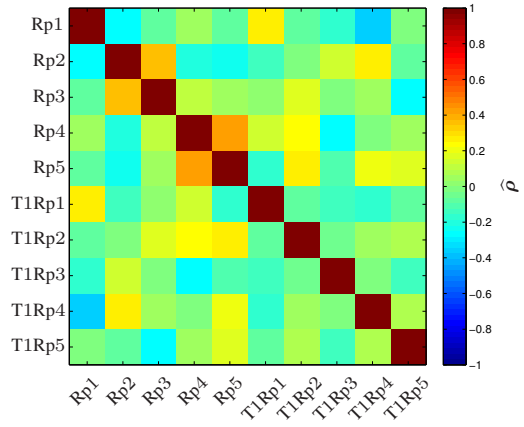

Fig. 7. Link-pair correlation coefficient $\widehat{\boldsymbol{\rho}}$. The values along the main diagonal of $\widehat{\boldsymbol{\Sigma}}$ are 0.67, 0.72, 0.43, 0.72, 0.69, 0.67, 0.52, 0.53, 0.54, and 0.43.

from adjacent blocks which are approximately 1 cm spaced. The calculation is performed similar as Eq. (8) except that the correlation coefficients are computed for adjacent blocks instead of different links. The estimates of the adjacent block correlation coefficients range from 0.7 to 0.9 for the different links and the average is 0.82. Fig. 6 shows an example of the power measured at Rp2 versus the displacement. The appearance of this plot once more confirms the assumption of highly correlated neighboring samples.

The correlation coefficients of the experimental residual log power values of any two links are reported in Fig. 7. The magnitude of the correlation coefficients ranges from 0.0 to 0.4 with an average of 0.14. This result confirms the weak correlation of large scale fading observed in a cooperative communication setting in [7]. The standard deviations of the log power residuals for the different links obtained as the square root of the diagonal entries (listed in Fig. 7) of $\widehat{\boldsymbol{\Sigma}}$ range from 0.65 to 0.85. Further investigation of the correlation coefficients can be performed with scatter plots of the residuals from different links as shown in Fig. 9. The figure shows only the results of link-pairs among T1Rp1 to T1Rp5. The other link-pairs have similar scatter plots. These scatter plots confirm

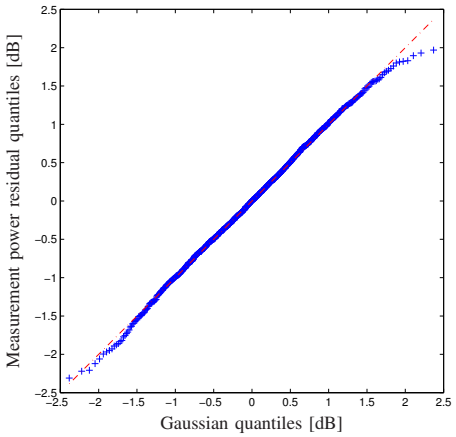

Fig. 8. Quantile-Quantile plot of the measured residual samples versus the Gaussian quantiles.

that there is no strong link-level correlation. We remark that the adjacent spacing of points from T1Rp1 to T1Rp5 is 0.5 m. Even those rather closely spaced receivers show no correlation of the power residual.

The Quantile-Quantile plot of the power residual $\widehat{\mathbf{R}}$ versus a Gaussian probability density function with mean of -0.01 and standard deviation of 0.77 estimated from $\widehat{\mathbf{R}}$ is presented in Fig. 8. The good fit in Fig. 8 suggests to model the residuals as Gaussian random variables.

The scatter plot of residuals versus the true range is shown in Fig. 10. We observe no range dependency of the residuals variance obtained along track T1. However, the residuals variance obtained along track T2, not shown here, indicates a distance dependency for ranges below 1.5 m but similarly as in track T1 no range dependency above 1.5 m.

Based on our signal model we propose an interim model for the received log power as

$$\mathbf{P} \sim \mathcal{N}(\boldsymbol{\mu}, \boldsymbol{\Sigma}), \tag{9}$$

where $\boldsymbol{\mu}$ can be obtained from a path loss model [4], [8] and the covariance matrix $\boldsymbol{\Sigma}$ is diagonal:

$$\boldsymbol{\Sigma} = \begin{bmatrix} \sigma_1^2 & & 0 \\ & \ddots & \\ 0 & & \sigma_L^2 \end{bmatrix}. \tag{10}$$

Due to the small observed variations in $\widehat{\boldsymbol{\Sigma}}$ for σ_1^2 to σ_L^2 we propose the approximation $\boldsymbol{\Sigma} \approx \sigma^2\,\mathbf{I}$, where $\mathbf{I}$ is the identity matrix and σ is the sample mean of σ_1^2 to σ_L^2 of $\widehat{\boldsymbol{\Sigma}}$. Thus $R_1, \ldots, R_L$ are approximated as i.i.d. Gaussian random variables.

VI. Conclusion and Outlook

The proposed data association method allows to convert the single link measurements into virtual multi-link measurements. We show that for the used measurement platform, the conversion approach is accurate enough to characterize the received powers of multi-link channels.

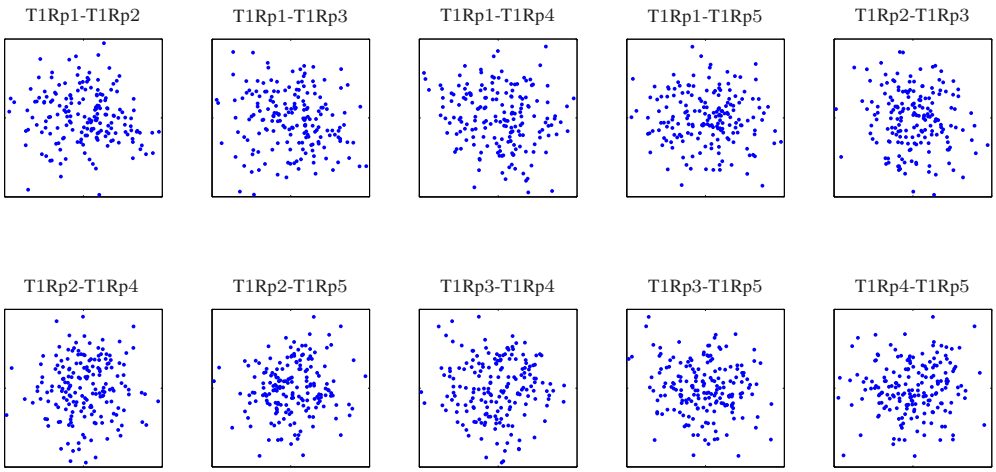

Fig. 9. Scatter plot of link-pair power residuals. The horizontal (vertical) component of any point represents the residual of the first (second) link given by the title and measured at the same displacement. The considered range is $[-2, 2]$ dB.

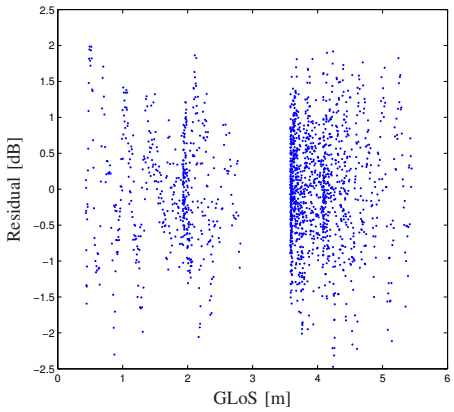

Fig. 10. Scatter plot of power residuals versus the geometric line of sight (GLoS).

The presented results obtained from measurements collected in an in-room environment show only insignificant correlation between the log power values of different links. This is in accordance with the observations in [7]. We observe the log power values to be Gaussian distributed with a range dependent mean. The behavior of the mean versus range can be described according to a path loss model. In the presented results the variance of the log power values appeared to be constant with range. However, preliminary results of another measurement, exhibited an increasing variance with range up to 1.5 m and appeared to be constant above. Further investigations are needed to provide a deeper insight into this phenomenon and to characterize the typical behavior of the variance.

ACKNOWLEDGMENT

This work was founded by the European Community's project Wireless Hybrid Enhanced Mobile Radio Estimators 2 (WHERE2). It was also conducted within the frame work of COST IC1004. The authors would like to thank Siwei Zhang for his support during the measurement campaign.

REFERENCES

[1] S. Zhang and R. Raulefs, "Improved Particle Filtering by Exploring Nodamic Movements," in *5th International Symposium on Communications, Control, and Signal Processing*, Rome, Italy, May 2012.

[2] H. Wymeersch, J. Lien, and M. Win, "Cooperative Localization in Wireless Networks," *Proceedings of the IEEE*, vol. 97, no. 2, pp. 427–450, Feb. 2009.

[3] Patwari, N. and Ash, J.N. and Kyperountas, S. and Hero, A.O., III and Moses, R.L. and Correal, N.S., "Locating the Nodes: Cooperative Localization in Wireless Sensor Networks," *IEEE Signal Processing Magazine*, vol. 22, no. 4, pp. 54–69, July 2005.

[4] ICT-WHERE Deliverable, "Estimation of location-dependent channel information (Final Report)," 2010.

[5] C. Oestges, "Multi-link propagation modeling for beyond next generation wireless," in *Antennas and Propagation Conference (LAPC), 2011 Loughborough*, Nov. 2011.

[6] K. Butterworth, K. Sowerby, and A. Williamson, "Base station placement for in-building mobile communication systems to yield high capacity and efficiency," *IEEE Transactions on Communications*, vol. 48, no. 4, pp. 658–669, April 2000.

[7] N. Jalden, P. Zetterberg, B. Ottersten, A. Hong, and R. Thomä, "Correlation Properties of Large Scale Fading Based on Indoor Measurements," in *Wireless Communications and Networking Conference (WCNC)*, March 2007.

[8] G. Steinboeck, T. Pedersen, B. Fleury, W. Wang, T. Jost, and R. Raulefs, "Model for the path loss of in-room reverberant channels," in *Proceedings of the IEEE 73rd Vehicular Technology Conference (VTC-Spring)*, Budapest, Hungary, May 2011.

[9] W. Wang and T. Jost, "A Low-Cost Platform for Time-Variant Wireless Channel Measurements with Applications to Positioning," *IEEE Transactions on Instrumentation and Measurement*, to appear in 2012.

[10] G. Steinboeck, T. Pedersen, and W. Wang, "AAU-DLR 2010 Indoor Measurement Campaign : Measurements for Validation of Models for Reverberant and Cooperative Channels," 2011.

A.5 Time-variant Channel Modeling Related to Indoor Human Crowd Activity

J. Stéphan, A. Cordonnier and Y. Corre Time-variant Channel Modeling Related to Indoor Human Crowd Activity. *Internal Report.*, June , 2012, Rennes, France.

WHERE2

Wireless Time-variant Channel Modeling Related to Indoor Human Crowd Activity

Julien Stéphan, Antoine Cordonnier, Yoann Corre
Radio Department
SIRADEL S.A.S.

I. INTRODUCTION

In the frame of the WHERE2 project, SIRADEL extended a stochastic (GSCM) and a deterministic (ray-tracing) channel model (respectively WINNER [1] and SIRADEL indoor ray-tracing model [2]) to simulate indoor time-variant channel properties related to human crowd activity. Both models aim at feeding the design and assessment of indoor wireless communication based geolocation algorithms with realistic non-stationary channels. This report presents the general principle leading the channel models elaboration as well as some evaluation results obtained by comparison to time-variant narrowband CW measurements. These measurements have been collected on a static radio link in line-of-sight (LOS) set in an open space of a typical corporate building , in which a large set of controlled or monitored Human Crowd Activity (HCA) scenarios have been tested.

Two scenarios have been first collected respectively without any HCA (i.e. during the night) and with uncontrolled but monitored HCA. This allows to get reference statistics for characterization of the radio channel dynamic in the measurement area. Analysis of these scenarios is respectively based on global statistics (mean power over the whole measurement duration and standard deviation) and local statistics computed over 1 second-long intervals. Three metrics of interest (mean and standard deviation of the power, and an estimated K-factor) are notably associated to variations in the monitored HCA along a timeslot of approximately 10min.

A second set of scenarios has been then collected considering a fully controlled movement of a single person within the measurement area. Objective is to finely characterize the fading caused by this person in order to validate and refine the proposed simulation methods. Six sub-scenarios are addressed where trajectory, walking speed or the location of the AP (Access Point) differs. A shadowing pattern has been extracted from each scenario, obtained from a 70ms-long sliding window filtering plus an averaging of all reproductions of the same measurement. These patterns have been analyzed and then compared to the ones simulated by the deterministic simulation method.

The report is organized as follows. Section II describes the elaborated solution. Section III presents the measurement setup and some of the measurement characteristics. Section IV gives results from the deterministic ray-tracing evaluation. Finally, Section V summarizes the main conclusions and gives some perspective.

II. TIME-VARYING CHANNEL PREDICTION

The solution described in this section predicts multi-path channel properties for a static radio link that undergoes variations due to human body obstructions. The process depicted in Figure 1 generates continuous channel realizations either for a geometry-based stochastic channel model (i.e. WINNER2) or an indoor ray-tracing solution. The prediction scenario (first step) is composed of two elements: the definition of the static radio link and definition of the continuous human crowd activity (from a random model or a controlled description of human body movements).

The static multi-path channel is predicted in the second step, using either an indoor ray-tracing [2] or the WINNER 2 stochastic model, while the HCA prediction leads to successive and correlated snapshots of human body locations, separated by a constant user-defined time interval.

Both predictions (respectively channel and HCA) are combined in the third step in order to determine the list of obstructing bodies for each path and at each snapshot, i.e. the so-called "obstruction state". Fourth step determines the shadowing loss and Doppler shift to be affected to each obstructed path. Lastly, the time-variant channel prediction is obtained by gathering modified multi-path predictions obtained at each snapshot.

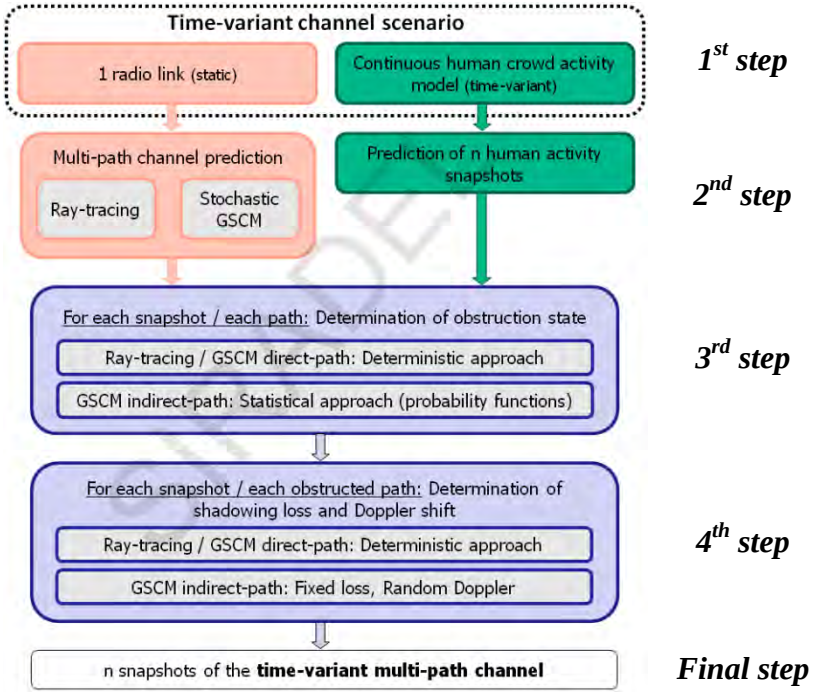

Figure 1: Time-variant channel models – Generic process.

The exact trajectory of indirect paths (i.e. paths that undergo at least one interaction with the environment) for the WINNER 2 model is unknown. Thus, the determination of their "obstruction state" (third step) as well as their shadowing loss and Doppler shift (fourth step) is obtained from a stochastic approach. For the first snapshot, the obstruction of an indirect path by a given person is determined randomly by the following obstruction probability function:

$$p(PE_{I,K}, PT_J) = f(\Delta l, dh_1, dv_1, \phi_1, \theta_1, dh_2, dv_2, \phi_2, \theta_2) \qquad (1)$$

Where $p(PE_{I,K}, PT_J)$ is the probability that the person $PE_{I,K}$ obstructs the path PT_J. Δl is the excess path-length defined as the difference between the path-length and the AP - $PE_{I,K}$ – MD (Mobile Device) length; dh_1 (resp. dh_2) is the horizontal distance between AP (resp. MD) antenna and the person location; dv_1 (resp. dv_2) is the minimum vertical distance between AP (resp. MD) antenna and the person location; ϕ_1 (resp. ϕ_2) is the horizontal angle difference between the AP path direction and the direction from AP to the person location; and θ_1 (resp. θ_2) is the minimum vertical angular difference between the AP path direction and the direction from AP to the person location. Remark that $p(PE_{I,K}, PT_J) = 0$ when $\Delta l < 0$m. The obstruction of the path PT_J by the person $PE_{I,K}$ is simulated from the two-state random variable $S_{I,J,K}$ with obstruction probability $p(PE_{I,K}, PT_J)$. At following snapshots, each probability that a person obstructs an indirect path is obtained by probability function depending on the previous obstruction state and state duration. A unique attenuation (which depends on the frequency band, see [3] for instance) and a random non-zero Doppler shift (which has a probability density function similar to the Bell-shaped Doppler power spectrum given at 2.4GHz in [4]) is then considered for each obstructed indirect path.

The 3D geometry of the WINNER 2 direct path and ray-tracing multi-path is fully known. Thus, determination of the "obstruction state" of each path (third step) results from a simple geometry analysis. Furthermore, a specific method is used to calculate LOS direct-path contribution for both models. This method, inspired from [5] with some enhancements, considers different situations.

1) The person is not in the vicinity of the LOS direct path. The propagation loss remains unchanged.

2) The person is approaching the LOS direct path, but does not yet obstruct the line-of-sight. Propagation loss considers two new contributions: a weighted direct path and one diffracted path (diffraction at the interior edge of the person). Both take into account additional knife-edge diffraction losses at the interior edge and the exterior edge of the person as well as a phase shift geometrically determined (by taking into account the excess path-length).

3) The person is crossing the horizontal projection of the line-of-sight, but the line-of-sight passes above the person head. Propagation loss considers three new contributions: the weighted direct path and two paths diffracted at the edges of the person. All these paths take into account specific additional knife-edge diffraction losses at the interior edge, the exterior edge and on the head of the person as well as a phase shift geometrically determined.

4) The person is crossing the line-of-sight. The direct path is assumed to be negligible. It is replaced by three contributions that correspond to paths diffracted at the interior edge, the exterior edge and on the head of the person.

For simplicity at this stage, a constant attenuation and a random non-zero Doppler shift is considered for indirect ray-tracing obstructed paths, as for indirect GSCM paths. At the end, this approach allows generating time-variant channel realizations with correlation: correlation in time, but also cross-correlation between different wireless links affected by the same spatial distribution of human bodies at a given time.

III. MEASUREMENT SETUP AND ANALYSIS

A. Overview

The evaluation of presented models relies on CW power measurements collected at frequency 2.1GHz in the first floor of a typical recent office building. The measurement area is limited to one large open-space that is mainly composed of large desks organized in four separate islands. All measurements have been collected from a unique 6m-long LOS static radio link. This radio link has been set such that the direct-path is crossed at its middle by the privileged HCA trajectory in the open-space (actually in the continuation of a corridor). Table 1 summarizes main measurement characteristics and Figure 2 illustrates the measurement setup.

Table 1: Main measurement characteristics.

Type of measurement	Narrow-band (CW) time-domain measurements. 1 LOS radio link
Environment	An open space in typical office building (i.e. SIRADEL premises)
Central frequency	2.1GHz
Bandwidth	10KHz
Antenna type	Same omni-directional antennas for AP and MS
Antenna height	102.5cm (from floor to base of the antenna)
Transmitted power	10dBm
Receiver sensitivity	< -110dBm
Time resolution	1ms (scenario M1) or 0.1ms (scenario M2)

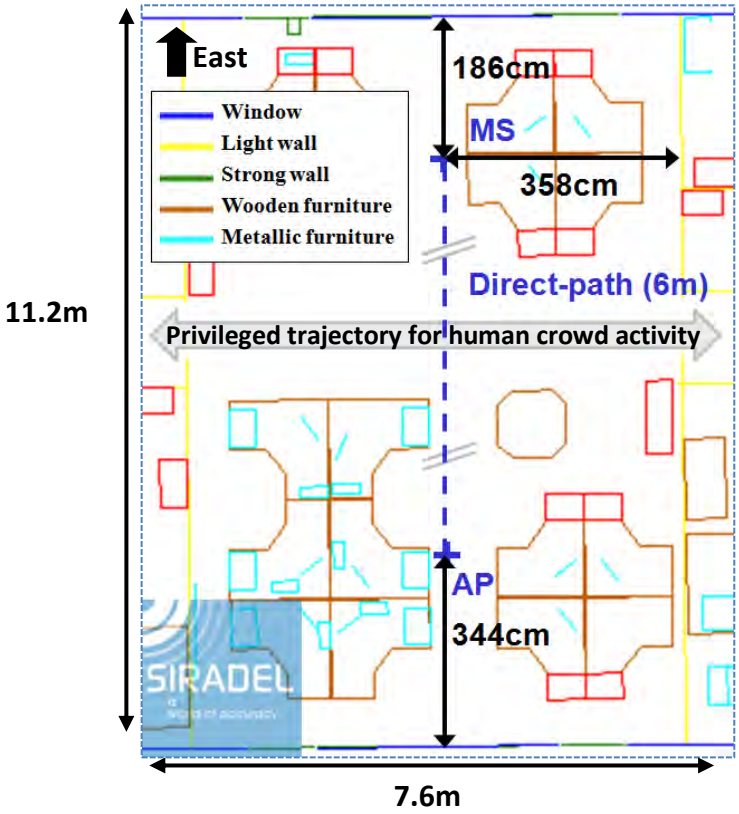

Figure 2: Measurement setup.

Two different HCA scenarios are addressed:

- **Scenario M1:** Measurements collected during several long periods of time, without any human activity or with uncontrolled but monitored HCA.
- **Scenario M2:** Characterization of time variations from the controlled movement of one single person.

Scenario M1 aims at collecting some reference statistics for characterization of the radio channel dynamic in the measurement area, whereas scenario M2 is used to validate and refine the simulation methods as well as to provide a precise characterisation of the fading (on large and small scale components).

B. Scenario M1

Scenario M1 is divided in two sub-scenarios:

- **Scenario M1.1:** Measurements collected during the night (i.e. out of working hours) without any HCA.
- **Scenario M1.2:** Measurements collected with monitored (but uncontrolled) HCA during a common working day.

As expected, received power collected during scenario M1.1 is very stable over the whole measurement duration. The standard deviation is 0.013dB only, which makes certain that variations observed from other scenarios come from human activity.

Measurements M1.2 have been collected mainly early in the morning (i.e. 8:15 AM – 9:45 AM) and after lunch break when the number of person crossing the open space or going to the desks is growing up during the data collection. Jointly with the received power measurement, the HCA was monitored based on the two following observations: number of persons moving or standing up and number of persons crossing the direct-path.

Power measurements have been processed to provide statistics on 1 second-long intervals: the mean of the received power; its standard deviation; and an estimate of the Ricean K-factor from Greenstein [6] method. Figure 3 to Figure 5 plot together these statistics and the monitored HCA along a timeslot of approximately 10min. The dotted lines represent raw statistics (computed every 0.5 s with a sliding window) whereas the plain lines represents smoothed statistics (average over a 5s interval).

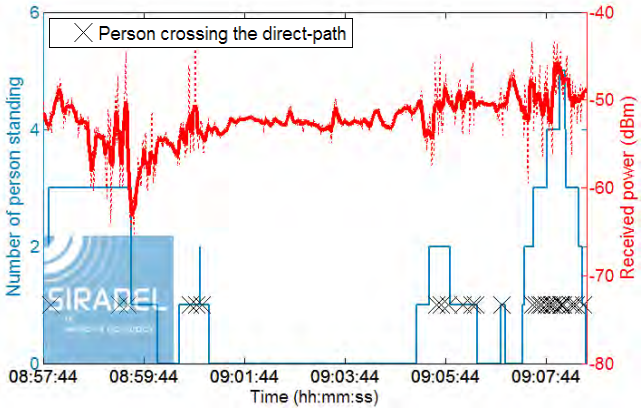

Figure 3: Mean received power versus human crowd activity.

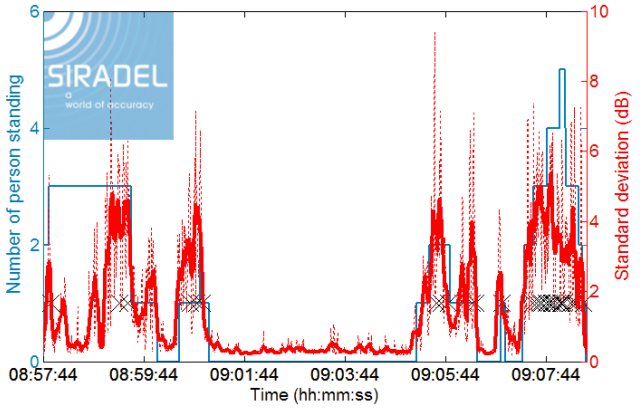

Figure 4: Standard deviation of received power versus human crowd activity.

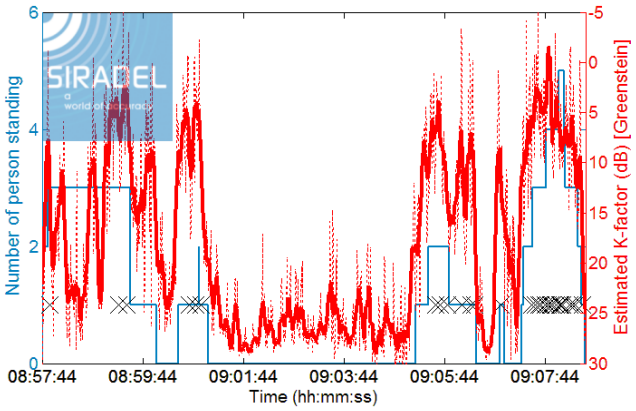

Figure 5: Estimated K-factor versus human crowd activity.

We observe that the mean received power globally increases and is more dispersive when there are several moving or static standing persons in the open space. Standard deviation is maximized when several persons crossed successively or simultaneously the direct path (reaching 5.5dB in the illustrated timeslot). The analysis stresses that the Ricean K-factor sensibly decreases as soon as a person moves near the radio link. An estimated K-factor of approximately 10dB is obtained when a single person is standing up or moving in the open space whereas it is lower than 5dB as soon as there are more than 3 persons in motion. An estimated K-factor close or equal to 0dB has been even obtained during repetitive or strong obstructions of the direct path. This range reveals that, for a LOS radio link in such configuration (low height antennas and populated indoor environment), the distribution of the fading depends on how dense and how the HCA is distributed.

C. Scenario M2

Scenario M2 is divided in 6 sub-scenarios:

- **Scenario M2.1**: A person crosses perpendicularly the direct-path in the middle.
- **Scenario M2.2**: A person moves along the direct-path.
- **Scenario M2.3**: A person moves in parallel of the direct-path (2.5m away to the East).
- **Scenario M2.4**: A person crosses perpendicularly the direct-path at different distances from the AP.
- **Scenario M2.5**: Same scenario than M2.1 with two different walking speeds.
- **Scenario M2.6**: Same scenario than M2.1 for 16 different AP locations (4x4 grid with 5-cm resolution).

For all scenarios, the person walks at a constant speed (i.e. 3.6km/h for all scenarios except for scenario M2.5 where the walking speeds are respectively at 2.1 and 5.1km/h). The reproducibility of scenarios has been checked by repeating several times the measurements, with the same controlled HCA, or after changing the direction of the person movement to the opposite. It was observed to be really good: for instance, the maximum standard deviation (computed over a 70 ms-long sliding window) between all reproductions of scenario M2.1 is lower than 2.5dB. One shadowing pattern has been extracted from each scenario M2.1 to M2.5 and 16 patterns have been extracted from scenario M2.6.

This shadowing pattern is obtained from averaging the received power by 70 ms-long (i.e. half-wavelength for a walking speed of 1 m/s) sliding window and an averaging over all reproductions of the same scenario. This methodology has been defined after evaluation of different averaging methods. Several window lengths have been notably evaluated but only characteristics of the small-scale component, which are not detailed in this report, are impacted. Figure 6 illustrates some of the extracted shadowing patterns.

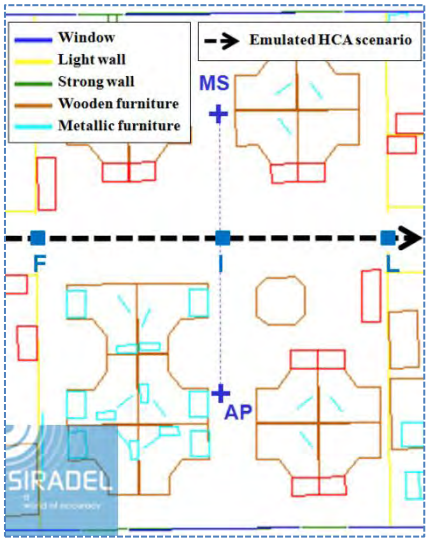

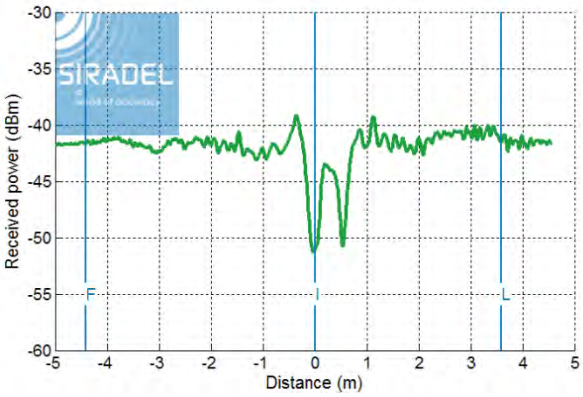

(a) Scenario M2.1

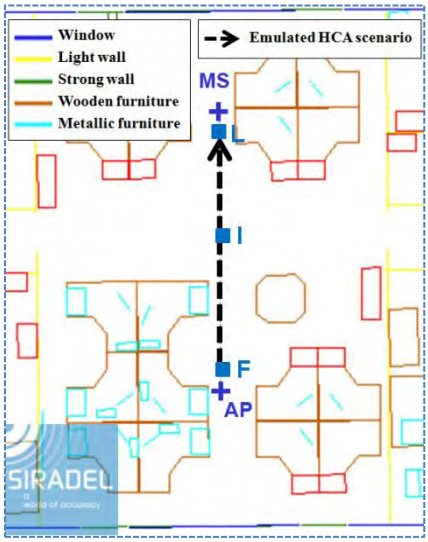

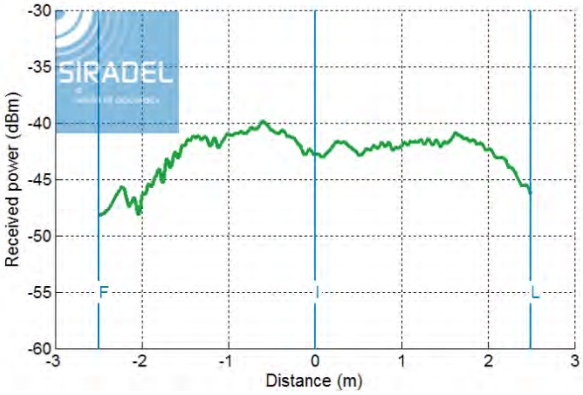

(b) Scenario M2.2

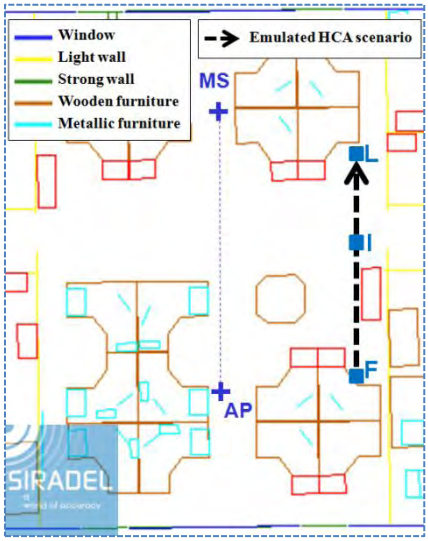

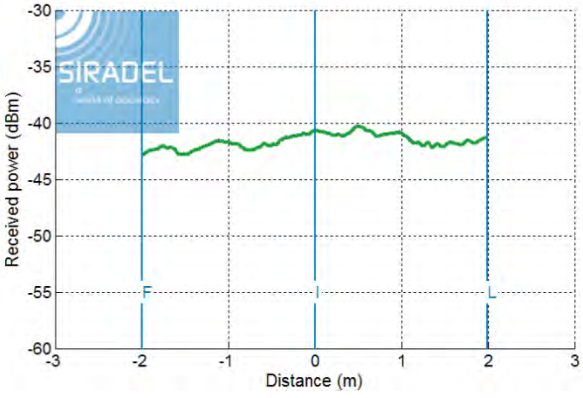

(c) Scenario M2.3

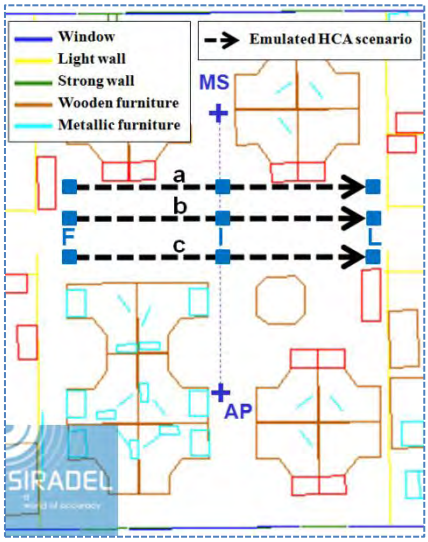

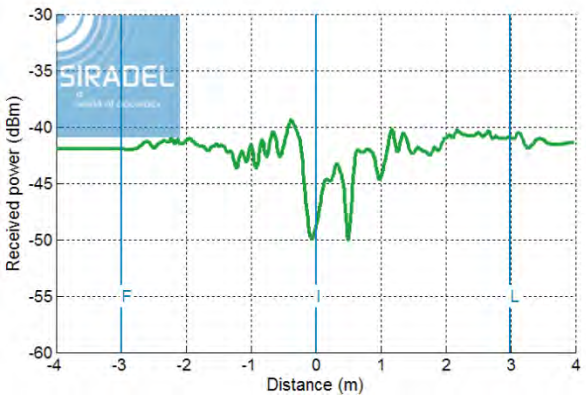

M2.4a : +1m

Relative distance from the intersection point between the direct-path and the HCA trajectory of M2.1 scenario. Positive if closer to the MS.

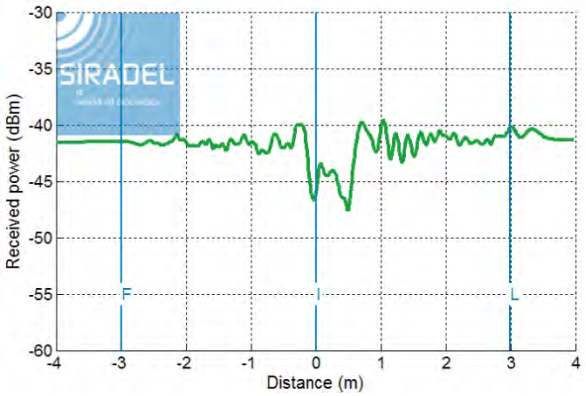

M2.4b : +0.5m

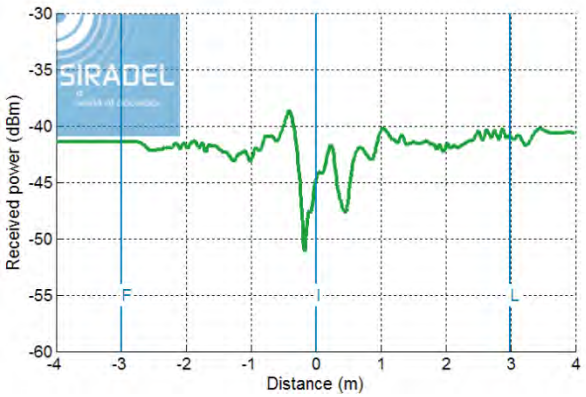

M2.4c : -0.5m

(d) Scenario M2.4

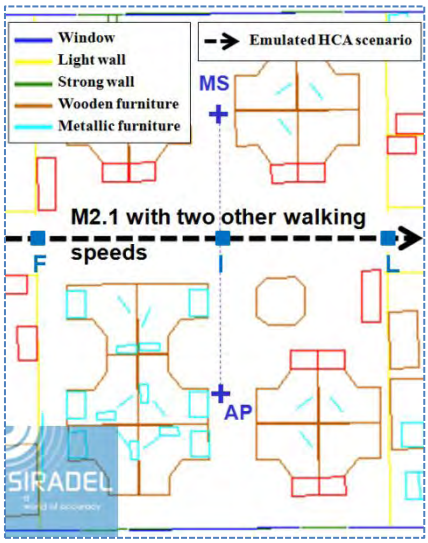

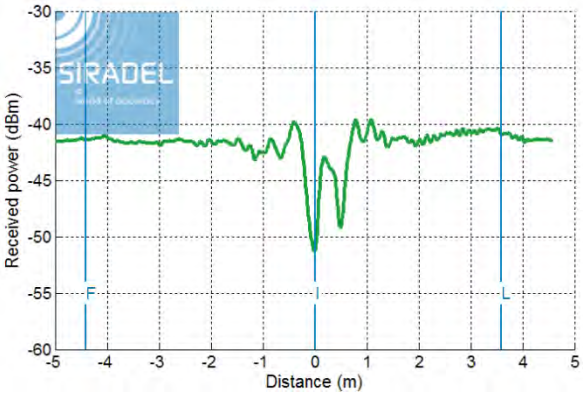

M2.5a: 2.1 km/h

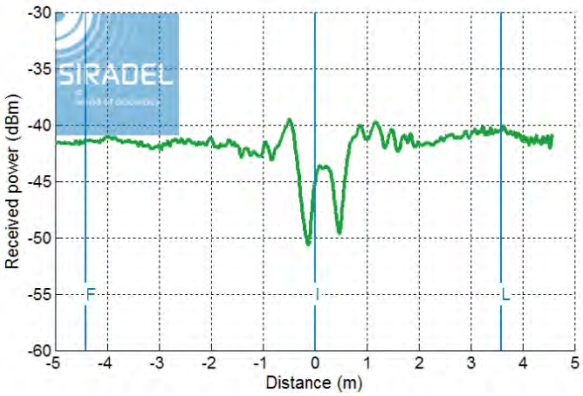

M2.5b: 5.1 km/h

(e) Scenario M2.5

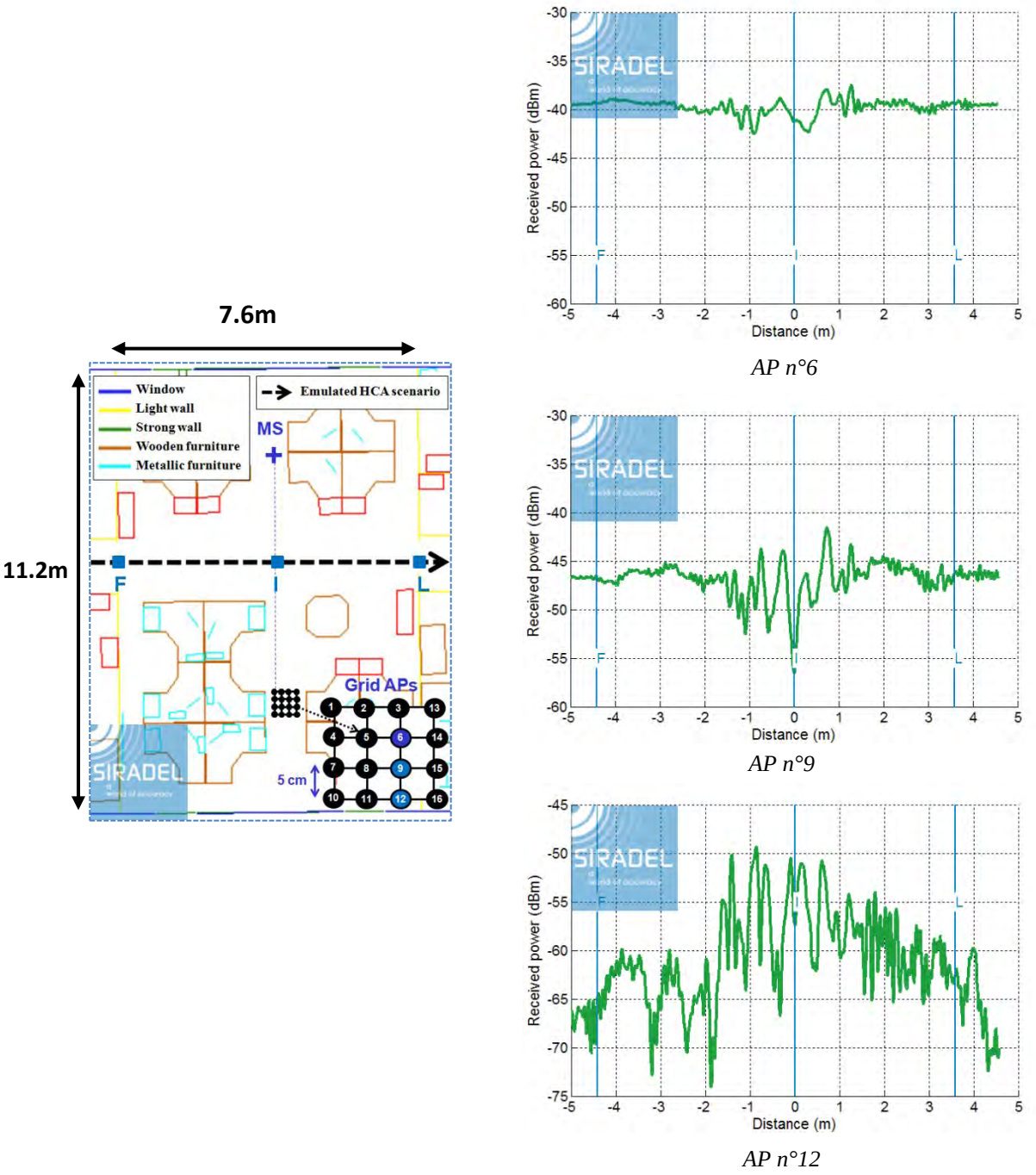

(f) Scenario M2.6

Figure 6: Shadowing pattern for scenarios M2.1 to M2.5 and for three sub-scenarios M2.6.

We observe that each kind of HCA scenario leads to different shadowing pattern whereas a same HCA scenario reproduced at different speed (i.e. scenarios M2.5) leads to quasi-identical patterns. Thereby, for a single person movement, only the trajectory of the HCA has an influence on shadowing pattern. This observation is notably confirmed by comparing scenarios M2.1 and M2.4 for which the extracted shadowing patterns are sensibly different whereas the emulated HCA scenarios are close.

We also observe that the maximum fade is always caused by the partial or total obstruction of the direct path. In all scenarios where the person crosses perpendicularly the direct-path (i.e. scenario M2.1, and M2.4 to M2.6), the minimum or maximum received power are collected over a very short-distance (few centimeters) around the waypoint "I" (which symbolizes, for these scenarios, the moment where the direct path is the most obstructed by the person). Besides, scenario M2.2 confirms that the shadowing loss due to direct-path obstruction depends on

the exact location of the person. It is thus necessary to have a model capable of reproducing the wide diversity of situations. We are aiming to address this objective by a deterministic and a stochastic channel models.

Furthermore, scenario M2.6 put forward that the radio link configuration (i.e. fading condition: constructive, intermediate or destructive) has a strong influence on the obtained pattern. This scenario highlights that the fading caused by a single person movement can be weak (lower than -2dB) when the initial recombination of the radio wave are constructive or very strong (higher than +20dB) and even positive when the initial recombination is destructive. M2.1 to M2.5 scenarios have been collected for an intermediate initial fading condition.

IV. SIMULATION RESULTS

The ray-tracing simulations are compared to all measurement scenarios presented in the previous section. A first set of predictions used a full deterministic method including geometric determination of the phase of the field of each ray path (i.e. before adding impact of the human body). Nevertheless, this calculation method is very sensitive to inaccuracies in the scenario description: building layout, radio terminal locations, material properties, etc. Predicting real phases is not possible. And, as observed from the measurements, the initial state of the channel has a strong impact on the shadowing pattern.

Therefore another approach was followed, where the set of initial phases are tuned by comparison to the measurements. The average error in the power level and the correlation between the predicted and measured shadowing patterns were the two metrics to be optimized in this tuning process. Figure 7 shows the comparison between measured and simulated shadowing patterns for the scenario M2.1.

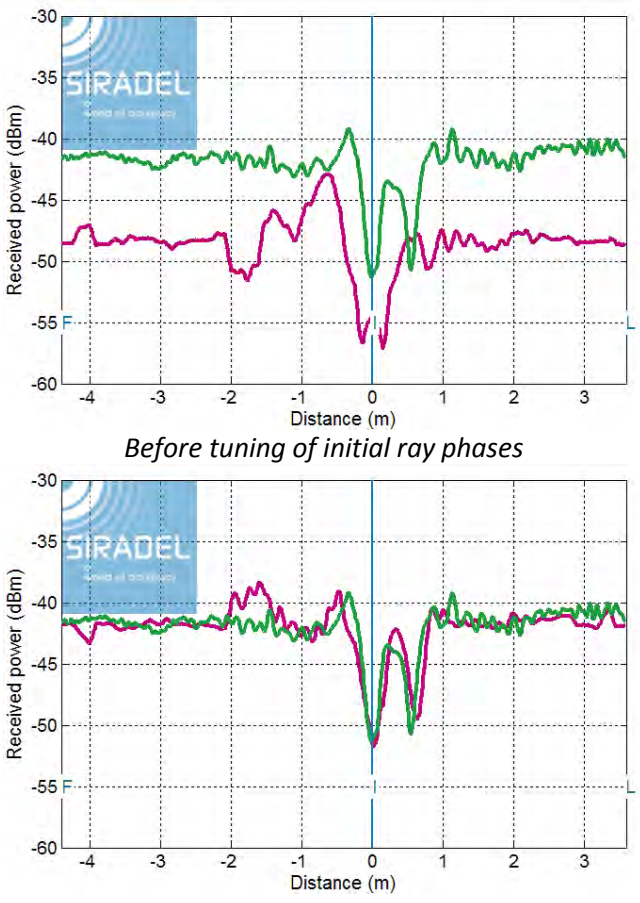

Figure 7: Comparison between measured and simulated shadowing pattern for scenario M2.1.

Table 2 gives statistics on measurement-prediction differences for each scenario.

Table 2 : Measurement-prediction difference statistics by scenario.

	Mean Difference [dB]	RMS Difference [dB]	Standard deviation [dB]	Correlation
Scenario M2.1	0.10	1.33	1.33	0.8
Scenario M2.2	-0.10	1.00	1	0.88
Scenario M2.3	-0.03	0.47	0.47	0.76
Scenario M2.4a	-0.03	1.08	1.08	0.85
Scenario M2.4b	0.15	0.97	0.96	0.77
Scenario M2.4c	0.43	1.14	1.05	0.82
Scenario M2.5a	0.13	1.12	1.12	0.80
Scenario M2.5b	0.37	1.28	1.23	0.77
Scenario M2.6: APn°6	0.13	1.94	1.94	0.51*
Scenario M2.6: APn°9	0.17	2.20	2.19	0.40*
Scenario M2.6: APn°12	-2.16	5.53	5.09	0.52*

Mean difference and standard deviation are respectively lower than 0.5dB and 2.2dB for all scenarios except for the scenario M2.6 for which the initial fading is destructive. This specific case seems the most complicated to reproduce by simulation. Besides, correlations for all scenarios M2.6 (those highlighted with an asterisk in Table 2) are not satisfactory and will require further analysis.

We confirm that in most configurations the measured patterns may be reproduced by the deterministic approach once the initial phases are tuned. This validation is also a first step to confirm relevance of the stochastic approach, which is based on an identical process for the direct-path calculation.

V. CONCLUSION

Elaboration of a stochastic and a deterministic model accounting for time-variant channel properties related to human crowd activity has been presented. The purpose is to provide realistic channel realizations for indoor geolocation algorithms as well as for system-level simulations of indoor wireless systems. The deterministic model has been evaluated and refined from the analysis of a time-variant CW campaign. Two different scenarios (M1 and M2) have been addressed for the same static LOS radio link.

Scenario M1 allows getting reference statistics for characterization of the radio channel dynamic in the measurement area. It has been demonstrated that the channel is stable without any HCA as well as that the mean received power becomes more dispersive when there are several moving or static standing persons. Moreover, an analysis based on an estimated K-factor shows that characteristics of fading changes once one person is standing up or moving in the open space.

Scenario M2 has been divided in 6 sub-scenarios. Each one considers a specific movement of one single person or an AP location slightly modified. The reproducibility of each sub-scenario has been first confirmed. A measured shadowing pattern from each sub-scenario has been then extracted and analyzed. We observe that, for a single person movement, both the trajectory of the HCA and the initial state of fading have an influence on the shadowing pattern (impact of walking speed is negligible if shadowing pattern is considered according distance).

Lastly, the measured shadowing pattern has been compared to the simulated ones. We demonstrate that measured patterns may be reproduced by the deterministic prediction approach with good accuracy (global mean error < 0.1dB and standard deviation = 2.05dB). However the shadowing pattern is highly sensitive to the exact state of the unobstructed channel, in particular to the phases of the multi-path field contributions as observed by small changes in the AP locations. Therefore the initial phases of the predicted ray fields had to be tuned for relevant comparison to the measurements.

Current version of the models have been designed and parameterized to simulate a static radio link in LOS at 2.1GHz. Parameterization must be extended to a wider range of configurations including for instance mobile terminals and NLOS situations. The simulation of MIMO radio links with human activity is also envisaged. MIMO sub-channels undergo a correlated but slightly different impact of the human activity. One key perspective of this work is then to characterize the evolution of the MIMO capacity in presence of human crowd activity in a very realistic way.

REFERENCES

[1] WINNER II IST project, WINNER II channel models - Channel models, Delivery D1.1.2 part I v1.2, Sept. 2007.

[2] Y. Lostanlen, G. Gougeon, "Introduction of diffuse scattering to enhance ray-tracing methods for the analysis of deterministic indoor UWB radio channels", International Conference on Electromagnetics in Advanced Applications (ICEAA), September 2007

[3] ITU, "Propagation data and prediction methods for the planning of indoor radiocommunication systems and radio local area networks in the frequency range 900 MHz to 100 GHz", ITU-R P.1238-6, 2009.

[4] IEEE 802.11, TGn channel models, IEEE 802.11-03/940r0, 2003.

[5] M. Varshney, Z. Ji, M. Takai and R. Bagrodia, "Modeling environmental mobility and its effect on network protocol stack", Proceedings of the IEEE Wireless Communications and Networking Conference (WCNC), April 2006.

[6] L.J. Greenstein, V. Erceg, "Ricean K-Factors in Narrow-Band Fixed Wireless Channels: Theory, Experiments, and Statistical Models", IEEE Transaction on vehicular technology, November 2009.

A.6 Exploiting the Graph Description of Indoor Layout for Ray Persistency Modeling in Moving Channel

Bernard Uguen, Nicolas Amiot, Mohamed Laaraiedh Exploiting the Graph Description of Indoor Layout for Ray Persistency Modeling in Moving Channel. In Proceedings of the 6th European Conference on Antennas and Propagation (EuCAP 2012), Prague, Czech Republic, Mar. 2012..

Exploiting the Graph Description of Indoor Layout for Ray Persistency Modeling in Moving Channel

Bernard Uguen, Nicolas Amiot, Mohamed Laaraiedh
IETR UMR CNRS 6164 - University of Rennes 1
Email: {bernard.uguen, nicolas.amiot, mohamed.laaraiedh}@univ-rennes1.fr

***Abstract*—This paper proposes a technique based on description of the layout using different graphs to obtain a ray signature which is associated with path persistency observed for small displacement of radio link termination of a mobile channel. The algorithm used to derive the signature from the layout graph description and the position of $\mathbf{T}_x$ and $\mathbf{R}_x$ is described. The mathematical relationship between signature and rays is also presented. A comparison of simulated and measured IR-UWB channel impulse response over a pedestrian trajectory is shown.**

I. Introduction

There is today a significant research effort in localization and tracking community for measuring and modeling the features of the channel [1] for indoor human mobility. In particular, there is a growing interest for introducing channel modeling tools which respect spatial coherence of the channel w.r.t human mobility. For example semi deterministic model derived from the statistical model IEEE 802.15.4a have been proposed as e.g in [2].

The propagation channel parameters are time varying due to the motion of the extremities of the radio link or because of motion of human or objects in the propagation environment. The human motion introduces small scale and large scale variations. This paper focuses on large scale variations that remain coherent over significant distances.

Path persistency has been defined in [1] as the evolution of a particular path of the channel impulse response which exhibits a differential change of a given feature in accordance with its differential motion. In [3] the path persistency has been exploited in the context of indoor positioning systems employing high bandwidth time-of-arrival methods.

Otherwise, the graph structure has proven its relevance in describing the inner nature of the propagation channel. Stochastic propagation graphs have been introduced and developed in [4] for describing the reverberant nature of the channel and for explaining the exponential decay of the Power Delay Profile (PDP) as a function of delay.

This contribution aims at exploiting graph structure in order to determine in the channel impulse response, the part which remains persistent when the terminal is moving and can thus be exploited as a valuable observable for positioning and tracking.

All site specific tools have their own approach to describe the layout. This paper presents an approach based on a graph description of the layout which allows to capture the path persistency under the form of what is here defined as ray signature. The ray signature can remain stationary over short distances and consequently its knowledge can be exploited for accelerating the determination of rays when modeling the channel impulse response over pedestrian trajectories.

The first section introduces the proposed graph description of the layout suitable for the determination of ray signatures. The second section introduces the concept of ray signatures and describes how to derive the signature from the layout graphs. The third section provides the mathematical relationship between a ray and its signature which is used in an incremental ray tracing tool. The last section presents a comparison between channel impulse responses measured and simulated along a synthetic pedestrian trajectory in an office environment.

II. Multigraph description of the layout

The data structure of the indoor layout is described through the definition of the following graphs.

- The structure graph $\mathcal{G}_s$
- The visibility graph $\mathcal{G}_v$
- The topological graph $\mathcal{G}_t$
- The graph of rooms $\mathcal{G}_r$

The adopted multi graph description contains meta information from the layout which can be exploited for both incremental identification of rays and simulation of indoor pedestrian mobility.

A. The structure graph $\mathcal{G}_s$

The first graph describing the layout is $\mathcal{G}_s(\mathcal{V}_s, \mathcal{E}_s)$. $\mathcal{V}_s$ is the set of nodes and $\mathcal{E}_s$ is the set of edges. This is illustrated in figure 1 for 4 vertices and 4 walls room. In this example:

$$\mathcal{V}_s = \{-1, -2, -3, -4, 1, 2, 3, 4\}$$

$$\text{card}(\mathcal{V}_s) = 8$$

Vertices can be associated with a diffraction interaction whereas the edge (positive index) are associated either with transmission or diffraction.

- A positive node (wall) is necessarily connected to a negative node (vertex)
- For a vertex to be a potential diffracting node, its degree has to be lower or equal to 2

Each node index allows to retrieve the associated constitutive properties of the wall.

Figure 2 shows the $\mathcal{G}_s$ graph of an indoor environment. Only edges are displayed, black lines are associated with doors and windows.

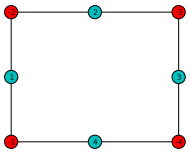

Fig. 1. $\mathcal{G}_s$ representation of a 4 walls layout (nodes in red: vertices, nodes in blue: walls)

Fig. 2. The structure graph $\mathcal{G}_s$

B. The visibility graph $\mathcal{G}_v$

The second defined graph of the layout is the visibility graph $\mathcal{G}_v$. Nodes of this graph are the same as those of $\mathcal{G}_s$. Only edges are defined differently from $\mathcal{G}_s$. Two nodes are connected if they share an "optical" visibility relationship. A wall ($id > 0$) can be connected to a vertex ($id < 0$). Optical visibility means that the electromagnetic energy can flow from one node to another. The $\mathcal{G}_v$ graph structure is sparse and well adapted to describe visibility relationships between layout and edges.

Fig. 3. Visibility graph $\mathcal{G}_v$

C. The topological (cycles) graph $\mathcal{G}_t$

The third defined graph of the Layout is the topological graph $\mathcal{G}_t$. It results from the determination of all cycles of the graph $\mathcal{G}_s$. $\mathcal{G}_t$ contains a valuable topological information. Each cycle contains various attributes as for example the set of nodes and edges of the cycle. This information is exploited once the position of $\mathbf{T}_x$ or $\mathbf{R}_x$ is known in order to connect directly leaves of $\mathcal{G}_v$ which are associated with a given cycle. This data organization accelerates search of walls and vertices to connect with. Graph $\mathcal{G}_t$ is shown in Figure 4.

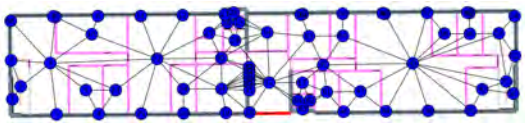

Fig. 4. Topological (cycles) graph $\mathcal{G}_t$

D. The graph of rooms $\mathcal{G}_r$

The fourth defined graph is the graph of rooms $\mathcal{G}_r$. It is the subgraph of $\mathcal{G}_t$ retaining only cycles which possess at least one door. An example of a graph of rooms is shown in Figure 5. This graph is used for fast extraction of the list of edges which belongs to a given room. This graph can also been used to build a state machine for inter-room mobility of pedestrian agents.

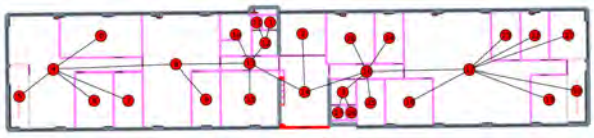

Fig. 5. Graph of rooms $\mathcal{G}_r$

III. Defining a ray signature

A. Definition

Let first define a ray with N_i interactions as an ordered list of $N_i + 2$ points starting at $\mathbf{t}_x$ and ending at $\mathbf{r}_x$.

$$\mathcal{R} = \{\mathbf{t_x}, \mathbf{p}_0, \cdots, \mathbf{p}_{N_i-1}, \mathbf{r}_x\} = \{\mathbf{t}_x, \mathcal{P}, \mathbf{r}_x\} \quad (1)$$

where $\mathbf{t}_x$ and $\mathbf{r}_x$ are points associated with transmitter and receiver and the ordered list of N_i interaction points is $\mathcal{P} = \{\mathbf{p}_0, \cdots, \mathbf{p}_{N_i-1}\}$. The signature of $\mathcal{R}$ is defined as the sequence of structure ids of $\mathcal{P}$. The structure id of a point is simply the identification number either of the diffraction point ($id < 0$) ot the segment number ($id > 0$), this is directly a node number from graph $\mathcal{G}_s$ or $\mathcal{G}_v$ defined previously. $\mathrm{Id}(\mathbf{p})$ is a function which returns the layout index number of $\mathbf{p}$.

$$\mathcal{S}(\mathcal{R}) = \mathcal{S}(\mathcal{P}) = \{\mathrm{Id}(\mathbf{p}_0), \cdots, \mathrm{Id}(\mathbf{p}_{N_i-1})\} \quad (2)$$

Conventionally, the signature of the LOS path is the empty set, $\mathcal{S}(\{\mathbf{t}_x, \mathbf{r}_x\}) = \emptyset$. Notice that when at least one ending point of the radio link is moving, all the points of $\mathcal{P}$ are moving correspondingly. This is not the case of the signature $\mathcal{S}$ which can remain stationary in the vicinity region of the moving point.

B. Algorithm to Determine Signature from $\mathcal{G}_v$

In a first step the algorithm seeks for the nodes $\mathcal{V}_{tx}$ of $\mathcal{G}_s$ which are visible from $\mathbf{T}_x$, and the set of nodes $\mathcal{V}_{rx}$ of $\mathcal{G}_s$ which are visible both from $\mathbf{R}_x$. This is a fast operation if the information of the room numbers where are lying $\mathbf{T}_x$ and $\mathbf{R}_x$ are maintained available along the simulated trajectory. The second step consists in exploiting the 2 subsets $\mathcal{V}_{tx}$ and $\mathcal{V}_{rx}$ for

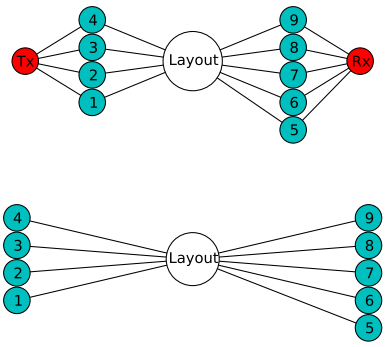

Fig. 6. Principle of signature determination, nodes subset $\mathcal{V}_{tx}$ (left) and $\mathcal{V}_{rx}$ (right)

determining $N_t \times N_r$ first order signatures where card$(\mathcal{V}_{tx}) = N_t$ and card$(\mathcal{V}_{rx}) = N_r$. The algorithm exploits the Dijkstra algorithm to determine the shortest path between 2 nodes in the graph $\mathcal{G}_v$. If a keyhole is detected, i.e a central node which is present in many discovered signatures, it is possible to remove this node and to iterate the algorithm in order to get new signatures which explore less direct paths. In scenarios where one extremity is moving continuously along a trajectory the set of signature $\mathcal{L}$ calculated at one point can be exploited for determining rays in its vicinity. $\mathcal{L}$ can be incrementally updated. Figure 6 and Algorithm 1 describe the principle of rays signatures determination.

Algorithm 1 Determination of signatures list

Require: $\mathbf{t}_x$,$\mathbf{r}_x$
Require: $\mathcal{G}_s$,$\mathcal{G}_v$,$\mathcal{G}_r$
  $\mathcal{L} = \emptyset$ Initialize a list of signatures
  $\mathcal{V}_t \leftarrow$ get visible nodes$(\mathcal{G}_r, \mathbf{t}_x)$
  $\mathcal{V}_r \leftarrow$ get visible nodes$(\mathcal{G}_r, \mathbf{r}_x)$
  for $nt \in \mathcal{V}_t$ **do**
    for $nr \in \mathcal{V}_t$ **do**
      $\mathcal{S}_{it,ir} =$ Dijkstra$(\mathcal{G}_v, n_t, n_r)$
      $\mathcal{L} \leftarrow \mathcal{L}$.append$(\mathcal{S}_{it,ir})$
    end for
  end for

IV. Ray Determination From Ray Signature

The determination of a ray from its signature is a two steps process. The fist step consists in calculating a set of intermediate points starting from the transmitter. Once calculated those intermediate points can be used for any receiver position with the same signature. The signature can be either valid or not valid for a given receiver depending on its coordinates.

A. Determination of Image points

The transmitter is defined as

$$\mathbf{t}_x = [x_t, y_t]^T \tag{3}$$

We consider a signature of length N which can contain three types of interaction: diffraction (D), reflection (R), transmission (T). From this signature, 2 ordered lists of points are retrieved.

$$\mathbf{p}_a = [\mathbf{a}_0, ..., \mathbf{a}_{N-1}] \tag{4}$$

$$\mathbf{p}_b = [\mathbf{b}_0, ..., \mathbf{b}_{N-1}] \tag{5}$$

$$\mathbf{a}_k = [x_{Ak}, y_{Ak}]^T,\ \mathbf{b}_k = [x_{Bk}, y_{Bk}]^T \tag{6}$$

In the case of a diffraction the point appears identical in each list otherwise $\mathbf{p}_a$ and $\mathbf{p}_b$ contains respectively tail points and head points of the signature segments.

The sequence of intermediate points can be determined from the knowledge of the transmitter point, the sequence of segments and also importantly the type of interaction $(R|T|D)$. This sequence of intermediate points is:

$$\mathbf{m} = [\mathbf{m}_0, ..., \mathbf{m}_{N-1}] \tag{7}$$

with:

$$\mathbf{m}_k = [x_k, y_k]^T \tag{8}$$

Depending on the nature of the interaction the intermediate point is either the image of the current point w.r.t the segment (Reflection), the current point itself (Transmission), the diffraction (interaction) point itself (Diffraction).

$\mathbf{m}_0$ depends on the type of the first interaction as:

- (R): $\mathbf{m}_0 = \mathbf{S}_0\mathbf{t}_x + \mathbf{v}_0$
- (T): $\mathbf{m}_0 = \mathbf{t}_x$
- (D): $\mathbf{m}_0 = \mathbf{a}_0$

and similarly, $\mathbf{m}_k$ depends on the type of the k^{th} interaction:

- (R): $\mathbf{m}_k = \mathbf{S}_k\mathbf{m}_{k-1} + \mathbf{v}_k$
- (T): $\mathbf{m}_k = \mathbf{m}_{k-1}$
- (D): $\mathbf{m}_k = \mathbf{a}_k$

where $\mathbf{S}_k$ (reflection matrix) and $\mathbf{v}_k$ are defined as:

$$\mathbf{S}_k = \begin{bmatrix} a_k & -b_k \\ -b_k & -a_k \end{bmatrix} \tag{9}$$

the translation vector is defined as

$$\mathbf{v}_k = \begin{bmatrix} c_k \\ b_k \end{bmatrix} \tag{10}$$

with

$$a_k = \frac{(x_{Ak}-x_{Bk})^2-(y_{Ak}-y_{Bk})^2}{(x_{Ak}-x_{Bk})^2+(y_{Ak}-y_{Bk})^2} \tag{11}$$

$$b_k = \frac{2(x_{Bk}-x_{Ak})(y_{Ak}-y_{Bk})}{(x_{Ak}-x_{Bk})^2+(y_{Ak}-y_{Bk})^2} \tag{12}$$

$$c_k = 2\frac{x_{Ak}(y_{Ak}-y_{Bk})^2+y_{Ak}(x_{Bk}-x_{Ak})(y_{Ak}-y_{Bk})}{(x_{Ak}-x_{Bk})^2+(y_{Ak}-y_{Bk})^2} \tag{13}$$

$$d_k = 2\frac{x_{Ak}(y_{Ak}-y_{Bk})(x_{Bk}-x_{Ak})+y_{Ak}(x_{Bk}-x_{Ak})^2}{(x_{Ak}-x_{Bk})^2+(y_{Ak}-y_{Bk})^2} \tag{14}$$

The coordinates of intermediates points are obtained by solving

$$\mathbf{A}\mathbf{m} = \mathbf{y} \tag{15}$$

$$\mathbf{A} = \begin{bmatrix} \mathbf{I}_2 & & & \\ \{-\mathbf{S}_1|\mathbf{O}_2|\mathbf{O}_2\} & \mathbf{I}_2 & & \\ & \ddots & \ddots & \\ & & \{-\mathbf{S}_{N-1}|\mathbf{O}_2|\mathbf{O}_2\} & \mathbf{I}_2 \end{bmatrix} \tag{16}$$

$$\mathbf{y} = \begin{bmatrix} \{\mathbf{S}_0\mathbf{t}_x + \mathbf{v_0}|\mathbf{t}_x\}|\mathbf{a}_0\} \\ \{\mathbf{v_1}|\mathbf{z}_2|\mathbf{d}_1\} \\ \vdots \\ \{\mathbf{v_{N-1}}|\mathbf{z}_2|\mathbf{d}_{N-1}\} \end{bmatrix} \tag{17}$$

where $\mathbf{I}_2$ and $\mathbf{O}_2$ are respectively identity matrix and zero matrix of dimension 2, $\mathbf{z}_2$ is 2×1 zero column vector. The notation $\{R|T|D\}$ stands for the possible matrix entries depending on the interaction type.

B. Determination of interaction points

The receiver is given by:

$$\mathbf{r_x} = [x_r, y_r]^T \tag{18}$$

Interaction points are points which belong to the layout segments. They are obtained from the intersection between the segments indicated by the signature and the segments joining successively the previously obtained intermediate points $\mathbf{m}$. The unknown interaction points are

$$\mathbf{p}_k = [x_k^{'}, y_k^{'}]^T \tag{19}$$

By introducing a parameterisation on both the unknown 4×1 column vector is:

$$\mathbf{x}_k^{'} = \left[\mathbf{p}_k^T, \mathbf{\Gamma}_k^T\right]^T \tag{20}$$

with

$$\mathbf{\Gamma}_k = [\alpha_k, \beta_k]^T \tag{21}$$

Starting from the receiver and joining the last intermediate point $\mathbf{m}_{N-1}$

$$\mathbf{p}_0 + \alpha_0(\mathbf{r_x} - \mathbf{m}_{N-1}) = \mathbf{r_x} \tag{22}$$

$$\mathbf{p}_0 + \beta_0(\mathbf{a}_{N-1} - \mathbf{b}_{N-1}) = \mathbf{a}_{N-1} \tag{23}$$

We solve successively the following linear systems

$$\mathbf{T}_0\mathbf{x}_0^{'} = \mathbf{y}_0^{'} \tag{24}$$

with:

$$\mathbf{T}_0 = \begin{bmatrix} \mathbf{I}_2 & \mathbf{r_x} - \mathbf{m}_{N-1} & \mathbf{0}_{2\times 1} \\ \mathbf{I}_2 & \mathbf{0}_{2\times 1} & \mathbf{a}_{N-1} - \mathbf{b}_{N-1} \end{bmatrix} \tag{25}$$

and

$$\mathbf{y}_0^{'} = \left[\mathbf{r_x}^T, \mathbf{a}_{N-1}^T\right]^T \tag{26}$$

For determination of interaction point $\mathbf{p}_k$ it proceeds identically taking advantage of the knowledge of point $\mathbf{p}_{k-1}$:

$$\mathbf{p}_k + \alpha_k(\mathbf{p}_{k-1} - \mathbf{m}_{N-(k+1)}) = \mathbf{p}_{k-1} \tag{27}$$

$$\mathbf{p}_k + \beta_k(\mathbf{a}_{N-(k+1)} - \mathbf{b}_{N-(k+1)}) = \mathbf{a}_{N-(k+1)} \tag{28}$$

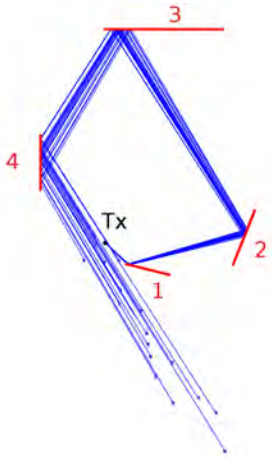

Fig. 7. Rays in blue share the same signature

This takes the forme of the linear equation:

$$\mathbf{T}_k\mathbf{x}_k^{'} = \mathbf{y}_k^{'} \tag{29}$$

with

$$\mathbf{T}_k = \begin{bmatrix} \mathbf{I}_2 & \mathbf{p}_{k-1} - \mathbf{m}_{N-(k+1)} & \mathbf{0}_{2\times 1} \\ \mathbf{I}_2 & \mathbf{0}_{2\times 1} & \mathbf{a}_{N-(k+1)} - \mathbf{b}_{N-(k+1)} \end{bmatrix} \tag{30}$$

and

$$\mathbf{y}_k^{'} = \left[\mathbf{p}_{k-1}^T, \mathbf{a}_{N-(k+1)}^T\right]^T \tag{31}$$

The parameterization of the signature segment β_k plays a very important role, if $0 < \beta_k < 1$ the interaction point $\mathbf{p}_k$ is valid and the calculation can proceed otherwise the interaction point is out of the segment and the signature is rejected for the current receiver coordinates.

As an example Figure 7 shows a set of rays (in blue) which are all sharing the same signature, which contains 4 reflections. $\mathbf{T}_x$ is static and is placed above-left the first segment.

The signature for all blue rays is $\mathcal{S} = \{1, 2, 3, 4\}$. The figure has been produced by drawing randomly $\mathbf{R}_x$ in the plane. There exists a validity region for $\mathbf{R}_x$ for a ray being associated with the signature. It means that if one termination of the signature is static (e.g. an access point), either $\mathbf{T}_x$ or $\mathbf{R}_x$, one can associate the couple (access point, signature) to a validity region where the signature is associated to valid rays.

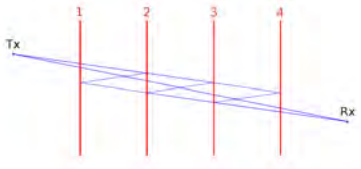

Fig. 8. Illustration of deriving higher order signatures from a signature containing at least a double transmission (TT)

One other interesting features of ray signature which is illustrated in Figure 8, is that it is possible to derive higher

order signatures from a lower order signature. The order of a signature being defined as the number of interactions N_i involved in the signature. For example if we have a signature of order 4: $\mathcal{S}_0 = \{1, 2, 3, 4\}$ corresponding for example to the transmission through of 4 successive walls placed between $\mathbf{T}_x$ and $\mathbf{R}_x$, one can derive those 3 new signatures of order 6, $\mathcal{S}_1 = \{1, 2, 1, 2, 3, 4\}$, $\mathcal{S}_2 = \{1, 2, 3, 2, 3, 4\}$, $\mathcal{S}_3 = \{1, 2, 3, 4, 3, 4\}$

V. Relating Ray Persistency to Ray Signature

Figure 9 presents the synthetic trajectory selected on the available measured link of an IR-UWB measurement campaign realized in the FP7-WHERE project [5]. Each transmitter position Tx_k along the trajectory is numbered from $k = 0$ to $k = 81$. The trajectory starts on the right and the node moves from right to left. 4 Receivers are placed in the environment (Rx_1 bottom right to Rx_4 up left). In figure 10, the Channel Impulse Response (CIR) of 4 links $\{Tx_kRx_1$,Tx_kRx_2,Tx_kRx_3,$Tx_kRx_4\}$ are shown. The horizontal axis is the delay expressed in nanoseconds of the CIR and the vertical axis corresponds to the synthetic trajectory index. Figure 11 is the noise free simulated CIR along the same trajectory with the ray tracing tool exploiting signatures. One can observe that there exist diagonal NLOS paths, meaning spatially coherent NLOS contributors which are often correctly predicted through RT simulation. An other interesting aspect is when one considers room transitions (e.g $Rx3$ $Tx53$) which are critical events regarding the CIR structure.

Fig. 9. Measured CIR along indoor selected trajectory, (red points) 4 Tx (1 is bottom right), (blue points) 81 Rx (0 right - 81 right)

VI. Conclusion

This paper has presented a technique for fast retrieving the ray signature from a graph description of the indoor layout. This signature is a precursor of rays and can be exploited to save computational time when evaluating the channel impulse response for example when studying indoor pedestrian localization or tracking scenario. In the last section ray persistency has been well observed in measurements data and well retrieved using an incremental ray tracing tool. A current line of investigation in tracking applications is to consider how to identify a ray signature from a sequential accumulation of channel impulse responses. This should be helpful in the context of map aided positioning and tracking scenarios.

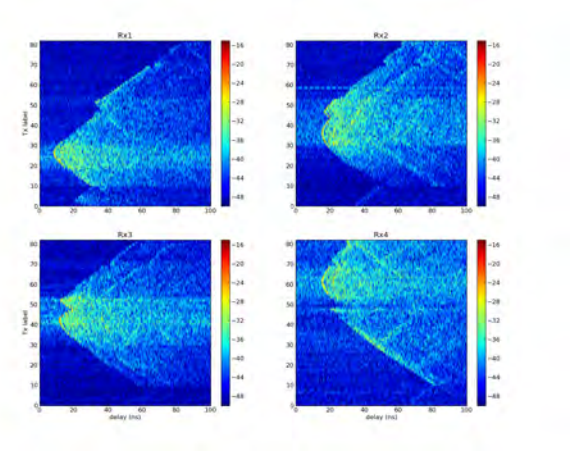

Fig. 10. Measured CIR along an indoor selected trajectory

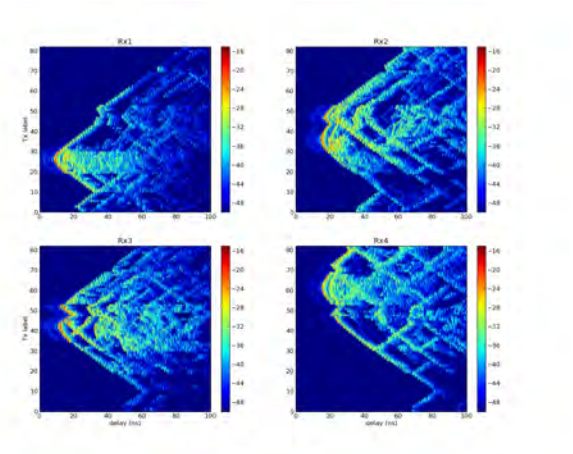

Fig. 11. Ray tracing simulated CIR along an indoor selected trajectory

Acknowledgment

The work has been performed in the FP7 project ICT-248894 WHERE2, which is funded by the European Union

References

[1] C.-C. Chong, C.-M. Tan, D. Laurenson, S. McLaughlin, M. Beach, and A. Nix, "A novel wideband dynamic directional indoor channel model based on a markov process," *Wireless Communications, IEEE Transactions on* **4** no. 4, (July, 2005) 1539 – 1552.

[2] J. Youssef, B. Denis, C. Godin, and S. Lesecq, "Dynamic ir-uwb channel model preserving ieee 802.15.4a statistics over large-scale trajectories," *Personal, Indoor and Mobile Radio Communications, 2009 IEEE 20th International Symposium on* (Sept., 2009) 1737–1741.

[3] F. Akgul and K. Pahlavan, "Path persistency for high precision ranging in different building architectures," in *Personal, Indoor and Mobile Radio Communications, 2007. PIMRC 2007. IEEE 18th International Symposium on*, pp. 1 –5. Sept., 2007.

[4] T. Pedersen and B. H. Fleury, "Radio channel modelling using stochastic propagation graphs," in *Communications, 2007. ICC '07. IEEE International Conference on*, pp. 2733–2738. 24-28 june, 2007.

[5] ICT-217033-WHERE-Project, "Deliverable 4.1: Measurements of location-dependent channel features,".

A.7 Technical Report on UWB Simulations of the WHERE2 Synthetic Environment

M.Laaraiedh, B. Uguen, N. Amiot and M. Mhedhbi Technical report on UWB simulations of the WHERE2 synthetic environment. *Internal Simulation Report.*, June , 2012, Rennes, France.

Technical report on UWB simulations of the WHERE2 synthetic environment

June, 2012

Contents

1 Introduction

This report provides a technical presentation of UWB simulations of the indoor synthetic environment defined within WHERE2 project. The main goal of these simulations is the modeling of UWB channel propagation from the very perspective of localization techniques.

The results presented in this technical report are carried out and developed by the following members from University of Rennes 1 (UR1):

- Prof. Bernard Uguen
- Assistant Prof. Mohamed Laaraiedh
- PhD Student Nicolas Amiot
- PhD Student Meriem Mhedhbi

2 UR1 Ray Tracing Tool: PyRay

Ray tracing (RT) tools have been developed for accurate radio propagation predictions. Those RT tools are based on geometrical optics (GO) and geometric/uniform theory of diffraction (GTD/UTD) which allow to define the optical paths from a transmitter to a receiver using an electromagnetic formulation of propagation phenomena such as reflection, transmission, and diffraction. In order to perform simulation with RT tools, a detailed 3D site geometry, material properties, transmitter/receiver locations, and antenna properties are required. Once this complete information is given, a RT task is executed. Then, after the identification of rays that are captured by the receiver antenna, the channel transfer function is calculated. In some tools the tracing task is preceded by a ray launching step where rays are uniformly propagated in all directions.

PyRay is mainly an UWB indoor RT tool developed in Python by UR1. A generic digram of PyRay architecture is given in Figure 1. In order to simulate UWB antennas, PyRay uses vector spherical harmonics (VSH) to compactly

describe the antenna radiation pattern within the entire frequency band [1]. VSH expansion of antenna radiation function simplifies data storage, process and analysis. Hence, the amount of data necessary to describe antennas is drastically reduced, the vector radiation functions are quickly reconstructed for different directions, and antenna radiation pattern is properly reconstructed [1]. PyRay is reinforced by a graph-based description of indoor channels based on four types of graphs: the structure graph, the visibility graph, the topological graph and the graph of rooms [2]. Based on this graph representation and using Dijkstra's algorithm, the signature of a ray is determined as the sequence of interactions of the ray from the transmitter to the receiver. In addition, a two-step process is developed in order to determine rays from their signatures. This ray determining process is used together with the graph-based representation of the radio channel to make the simulation of radio propagation channels faster [2].

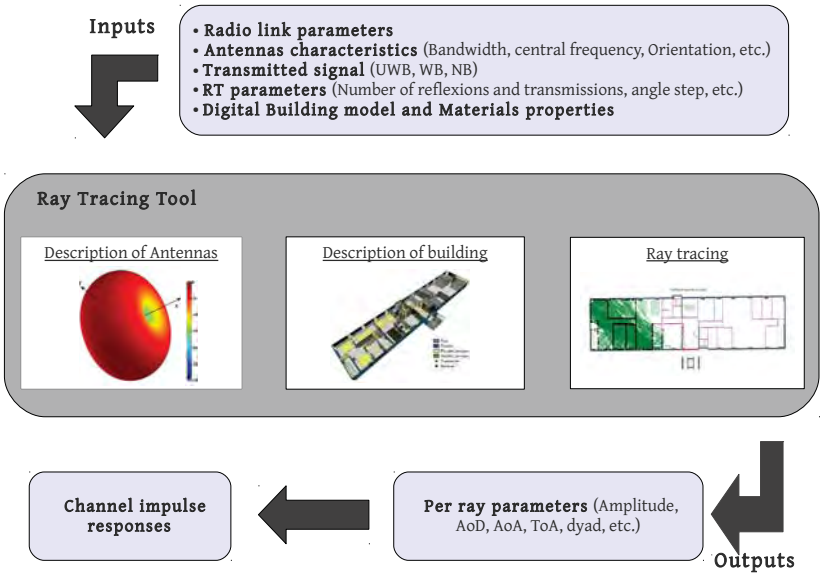

Figure 1: Generic architecture of ray tracing tools.

3 WHERE2 indoor synthetic environment

Within WHERE2 project, a synthetic indoor environment has been defined [3] in order to assess the performances of proposed localization techniques. This synthetic environment has been simulated using PyRay tool in order to get CIR from which location dependent parameters (LDPs) can be extracted and exploited in localization algorithms. The figures 2 and 3 plot the visualization of the synthetic environment using PyRay in respectively 2D and 3D landmarks. The points represent the grid chosen for performing simulations: the red points represent the transmitters while the blue points represent the receivers. The different components of the environments (i.g. doors, walls, etc.) are represented in different colors to highlight the difference between materials. The properties of these materials are taken into consideration by PyRay in order to perform realistic simulations. Notice that the simulations presented in this report does not consider furniture pieces in the environment such as tables, metallic cabinets, etc. We are still aware about the importance of consider all these pieces in order to obtain more realistic and proper simulations.

In addition to these points, we have carried out simulations on the same points defined during the WHERE M1 measurement campaign [3]. The simulated points are shown in Figure 12. Simulating these points is of great importance to compare measurements and simulations especially from the very localization perspective (see Section 5).

4 Simulation results

For each Tx-Rx pair, PyRay is applied in order to compute rays propagating between the transmitter and the receiver while taking into account the layout description and the different interactions between these rays and the different components of this layout. Furthermore, a refined description of antennas (those used during the M1 measurement campaign) is performed using VSH technique. The transmitted pulse used for simulations is the same used during M1 measurement campaign. This pulse is plotted in Figure 5 for both time and frequency domains, respectively.

Figure 2: 2D description of the synthetic environment.

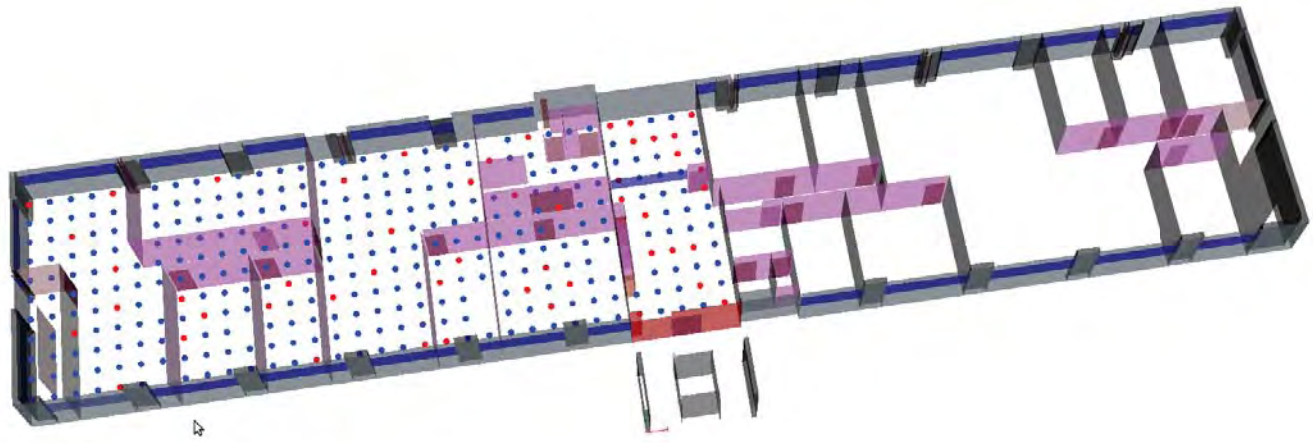

Figure 3: 3D description of the synthetic environment.

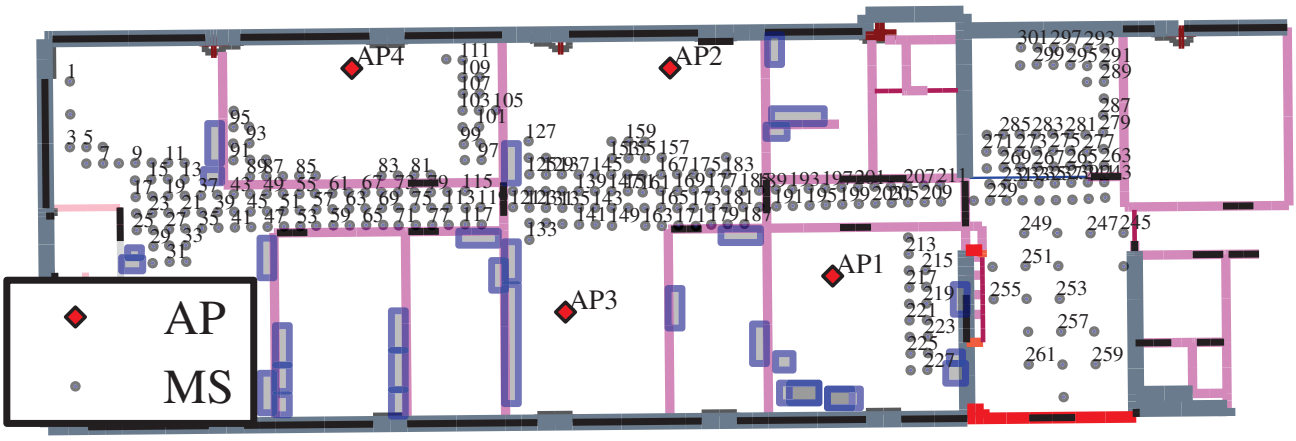

Figure 4: APs and MSs locations during the *WHERE* measurement campaign.

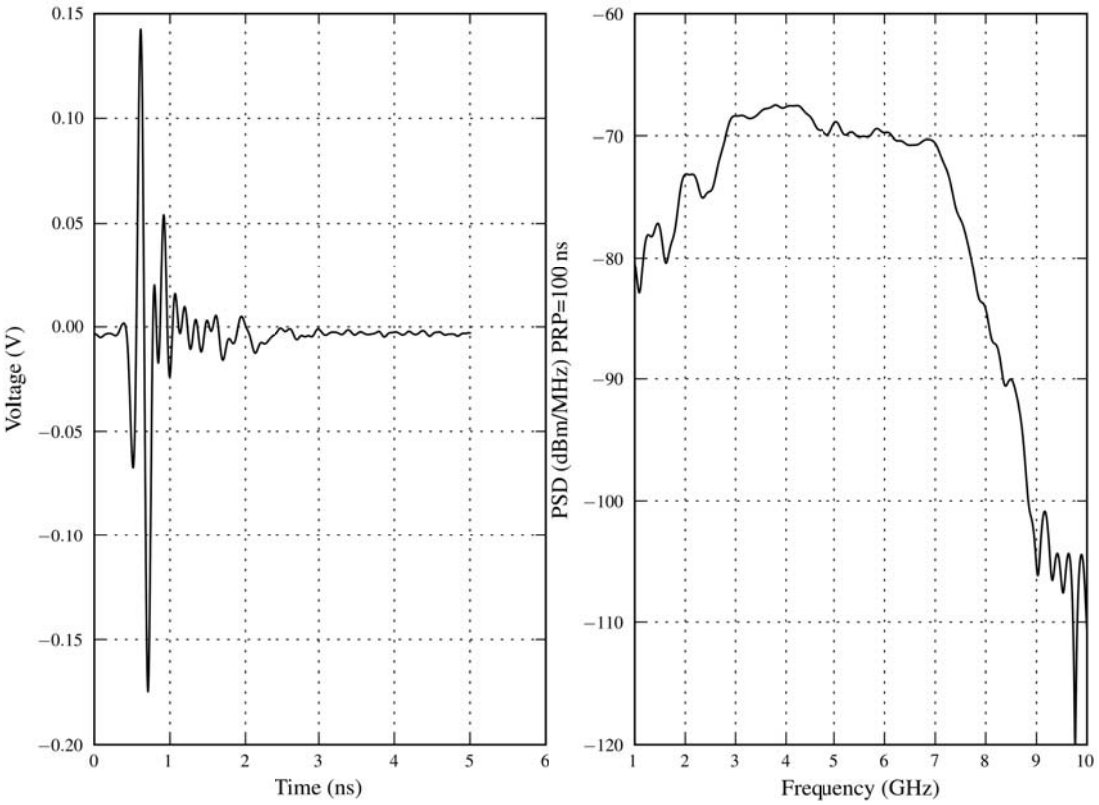

Figure 5: UWB impulse feeding the Tx antenna in time and frequency domains respectively.

4.1 Simulation format

The obtained simulations are a set of Matlab files which store the different channel impulse responses (CIR) of all the defined links between transmitters and receivers in Figure 2. In addition to the CIR, the coordinates of Tx and Rx are also available. Figure 6 plots an example of obtained CIRs.From these CIRs, different radio parameters can be extracted such as RSSI, TOA, τ_{RMS}, τ_{mean}, etc.

In many simultaneous localization and mapping (SLAM) algorithms, it is necessary to identify the rays reflected on or transmitted across the wall which is to be reconstructed. The UWB simulations provide, in addition to the radio-parameters mentioned before, the possibility to identify one, a set, or all the rays which are implicated in the CIR. Figure 7 plots all the obtained rays between two points. As an example, the 5^{th} strongest ray is plotted in Figure 8. Furthermore, for each ray different information are available and can be exploited within T2.3 and WHERE2 project.

The simulation results are presented into Matlab files (.mat Format) and put on the BSCW server (Figure 9) for further exploitation by the partners. The results are saved as follows:

- For each transmitter (idtx from 001 to 051), a zipped file (Tx[idtx].zip) is created which contains the simulations results of all radio links between the current transmitter and all the receivers (idrx from 001 to 343).
- Inside each zipped file, 343 matlab files contain the simulations of all the radio links, the format of these matlab files is: cir-tx[idtx]-rx[idrx].mat
- Each matlab file contains the following informations:
  - The coordinates of the Tx
  - The coordinates of the Rx
  - The CIR between the Tx and the Rx3 without taking into consideration the antenna
  - The time base of the CIR without taking into consideration the antenna
  - The CIR when taking into consideration the antenna (the antenna used in M1 measurements, see D4.1 from WHERE1 [3])
  - The time base of the CIR when taking into consideration the antenna

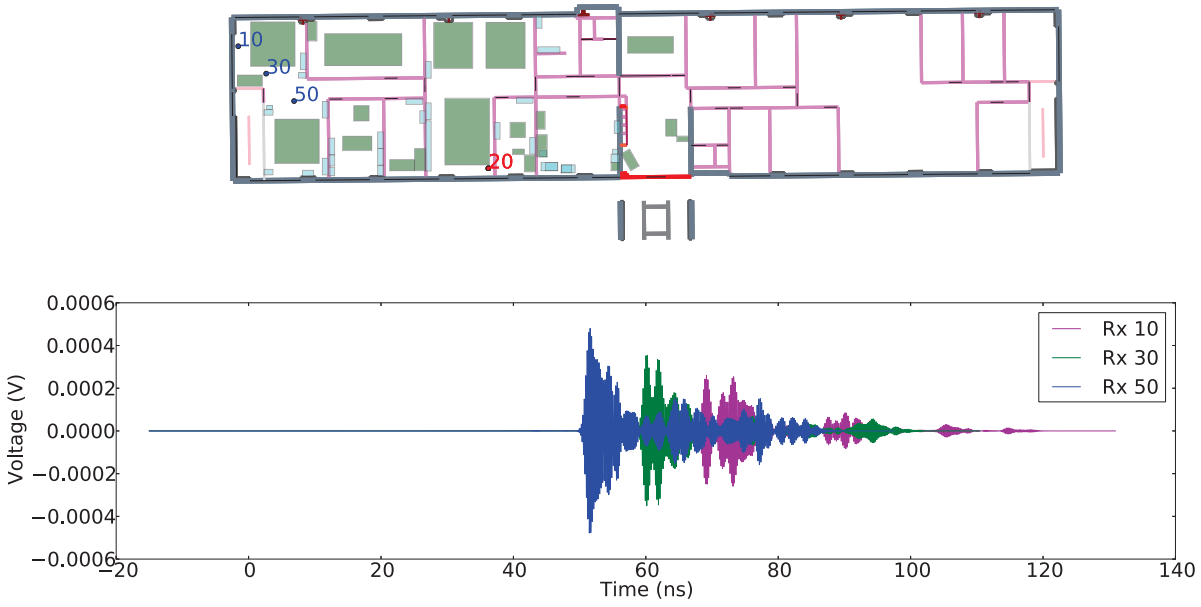

Figure 6: Examples of CIR obtained in the synthetic environment.

Figure 7: Examples of obtained rays in the synthetic environment.

Figure 8: Each ray can be identified and exploited individually.

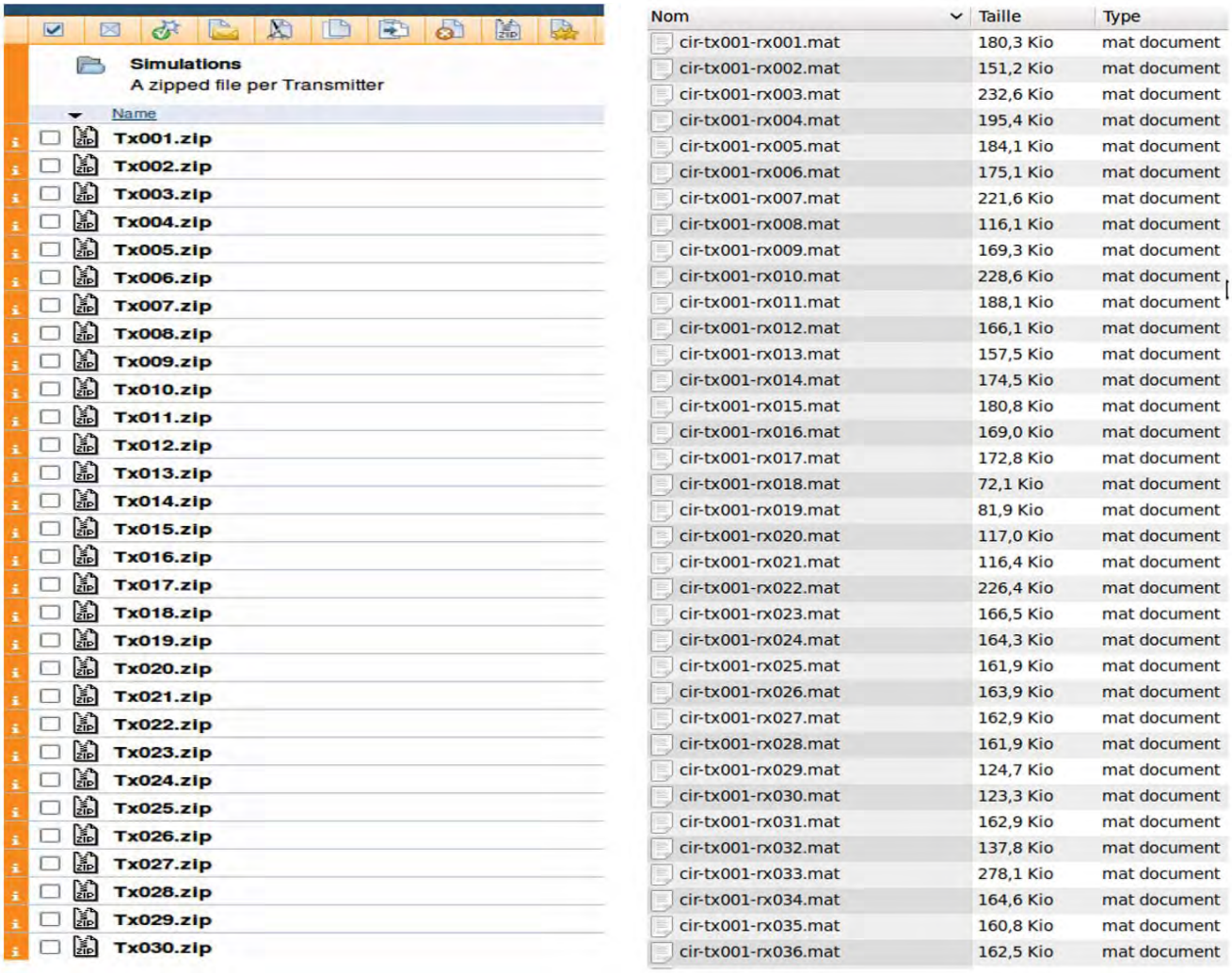

Figure 9: Simulation files on the BSCW server.

4.2 Post Processing of simulations

An example of processing of a matlab file is given in Figure 10. Different parameters can be extracted from the obtained CIR. Among these parameters, the following are the most important:

- Distance between Tx and Rx

$$d = \sqrt{(x_{Tx} - x_{Rx})^2 + (y_{Tx} - y_{Rx})^2 + (z_{Tx} - z_{Rx})^2}$$

  where (x_{Tx}, y_{Tx}, z_{Tx}) and (x_{Rx}, y_{Rx}, z_{Rx}) are respectively the coordinates of the Tx and the Rx.

- Time of flight

$$\tau_0 = d/c$$

- Transmitted power

$$E_t = 10 \log_{10} \int_0^T \delta^2(t) dt$$

  where $\delta(t)$ is the transmitted pulse and t is the time base

- RSSI: total received energy (E_{tot}) and the energy integrated over the strongest received path (E_{max})

$$E_{tot} = 10 \log_{10} \int_0^T r^2(t) dt$$

$$E_{max} = 10 \log_{10} \int_{\tau_M - \alpha T_s}^{\tau_M + (1-\alpha) T_s} r^2(t) dt$$

  where $r(t)$ is the CIR

- The Mean excess delay

$$\tau_{mean} = \frac{\int_0^T t r^2(t) dt}{\int_0^T r^2(t) dt}$$

- The Delay spread

$$\tau_{rms} = \sqrt{\frac{\int_0^T (t - \tau_{mean})^2 r^2(t) dt}{\int_0^T r^2(t) dt}}$$

- Time of arrival of the first path (TOA) can be estimated using different techniques [4].

- Angle of arrival

$$\alpha_{tr} = \arctan 2(\frac{y_{Tx} - y_{Rx}}{x_{Tx} - x_{Rx}})$$

5 Application to localization techniques

In addition to the evaluation of localization techniques, two main applications of ray tracing simulations in localization techniques are identified: the establishment of fingerprinting databases and the modeling of LDPs.

5.1 Application to fingerprinting techniques

Fingerprinting localization techniques are based on the off-line construction of a LDP database. In this database, one or more LDPs are saved over a grid defined within the targeted environment. The problem with those techniques is the need to carry out laborious measurement campaigns in order to construct and update these databases. Ray tracing tools present an alternative to those measurement campaigns. Calibrated ray tracing tools may help to construct realistic fingerprinting databases once a proper description of environment layout and antennas is performed. In addition, ray tracing tools can update the environment and/or antennas description to track environment changes in order to avoid laborious measurement campaigns at each time the environment changes.

example.m

```
% go to the folder "Tx001" in which you find 343 .mat files corresponding to the 343 links between the Tx 1 and all the Rx. example:

load cir-tx001-rx003.mat
load cir-tx001-rx004.mat

Tx                  % coordinates of the current Tx (here Tx1)

Rx3                 % coordinates of the Rx 3
Rx4                 % coordinates of the Rx 4

ciro3               % the CIR between the Tx (here Tx1) and the Rx3 without taking into consideration the antenna (the antenna used in M1 measurements, see D4.1 from WHERE1)
to3                 % time base of ciro3
cira3               % the CIR when taking into consideration the antenna
ta3                 % time base of cira3

ciro4               % the CIR between the Tx (here Tx1) and the Rx4 without taking into consideration the antenna (the antenna used in M1 measurements, see D4.1 from WHERE1)
to4                 % time base of ciro4
cira4               % the CIR when taking into consideration the antenna
ta4                 % time base of cira4



tau3 = sqrt((Rx3-Tx)'*(Rx3-Tx))/0.3   % Compute the actual TOA between the current Tx (here Tx1) and the Rx3
tau4 = sqrt((Rx4-Tx)'*(Rx4-Tx))/0.3   % Compute the actual TOA between the current Tx (here Tx1) and the Rx4

plot(to3, ciro3)        % plot the channel impulse response between the current Tx (here Tx1) and the Rx3, without antenna
plot(to4, ciro4)        % plot the channel impulse response between the current Tx (here Tx1) and the Rx4, without antenna



plot(ta3, cira3)        % plot the channel impulse response between the current Tx (here Tx1) and the Rx3, with antenna
plot(ta4, cira4)        % plot the channel impulse response between the current Tx (here Tx1) and the Rx4, with antenna
```

Figure 10: Example of processing of simulation files.

In this section, we apply fingerprinting technique to both M1 measurement campaign and PyRay simulations in order to compare performances. In Fig.11, we plot the CDF of absolute positioning error obtained by applying a neural networks-based fingerprinting technique respectively on measurements and RT simulations obtained using PyRay tool. The technique applies feedforward neural networks to learn the 302 MS positions using four RSSIs measured (respectively estimated) with four APs as shown in Fig.12 which plots the MSs and APs positions defined during the WHERE measurement campaign carried in the same environment described in section 3. Fig.11 shows that RT simulations give similar fingerprinting accuracy to that obtained using measurements which proves that RT tools can be reliable in such localization techniques. Nevertheless, this reliability is dependent on the capacity of the ray tracing tool to properly describe environment and antennas.

5.2 Modeling of location-dependent parameters

Modeling of LDPs is very useful in evaluating localization techniques performances. Thus, LDPs models should be as accurate as possible. Since RT tools are able to reproduce radio channel and propagation phenomena with higher accuracy, models extracted from RT simulations would be rather accurate for realistic evaluation of localization techniques. In order to assess the RT tool accuracy in LDPs modeling, we compare the RSSI and TOA values obtained using the PyRay tool and those obtained during the M1 measurement campaign (Fig.12).

In Fig. 13 we plot for AP3 and AP4 the evolution of measured and simulated RSSIs along the trajectory defined during the measurement campaign (Figure 12). Although the general patterns of measured and simulated RSSI look the same, some large differences occurs at some points. This is particularly explained by the fact that many pieces of furniture have not been included in the environment description. In particular, metallic cabinets (plotted in grey in Fig.12) have strong effects on radio-propagation and thus on the RSSI values. In order to reduce the gap between simulations and measurements, these pieces of furniture must be properly included in the description of the environment.

As for TOA, we apply on both simulated and measured CR the *Thresholded dichotomous left interval selection* technique put forward in [4]. In the same way as for RSSI, we plot in Fig.14 the evolution of estimated ranging errors along the same trajectory for both simulations and measurements. These figures show that the regions with large RSSI simulation errors (in Fig.13) coincide with the regions where the ranging error obtained using measurements is very large. This is explained by the presence of metallic cabinets which obstruct the direct path. These metallic cabinets are in fact taken

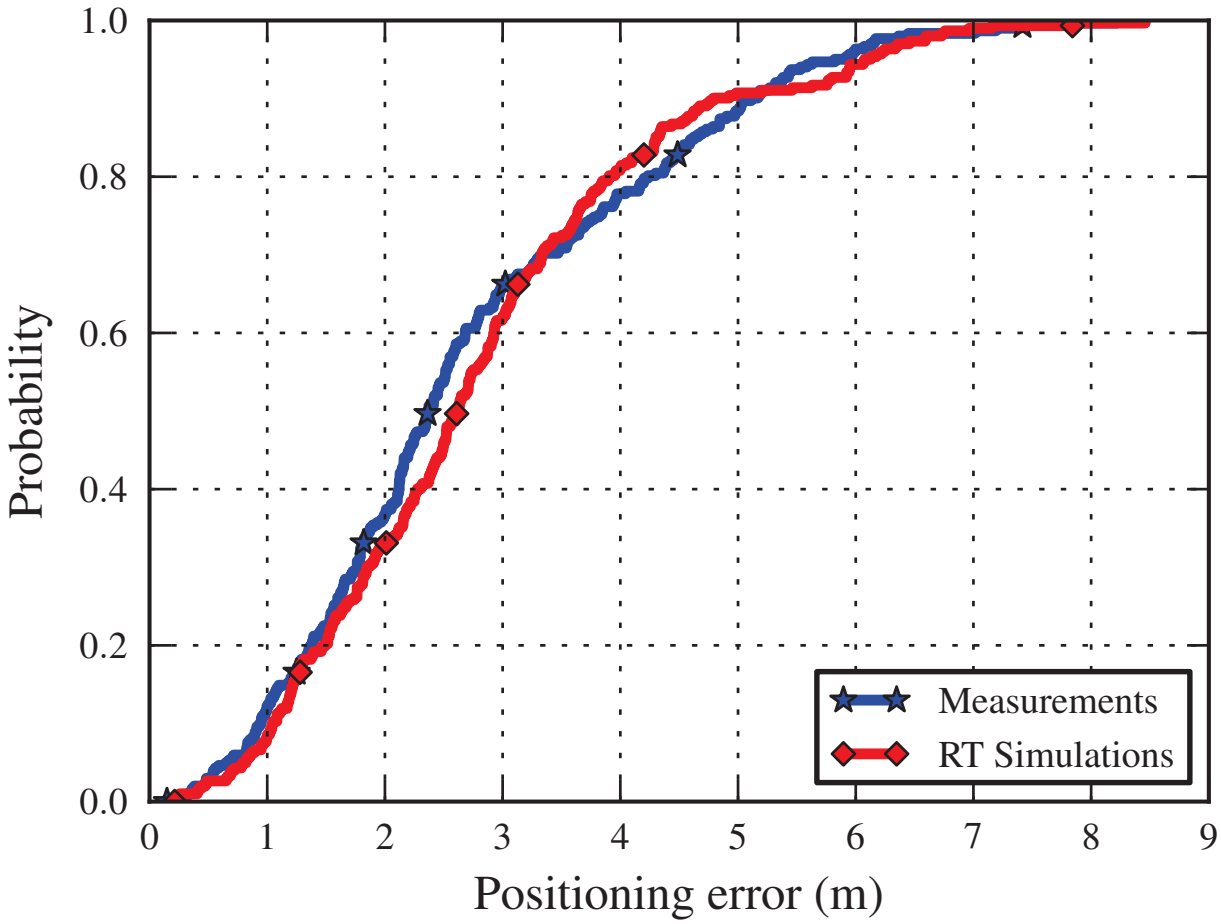

Figure 11: Fingerprinting-based positioning accuracy using measurements and RT simulations respectively.

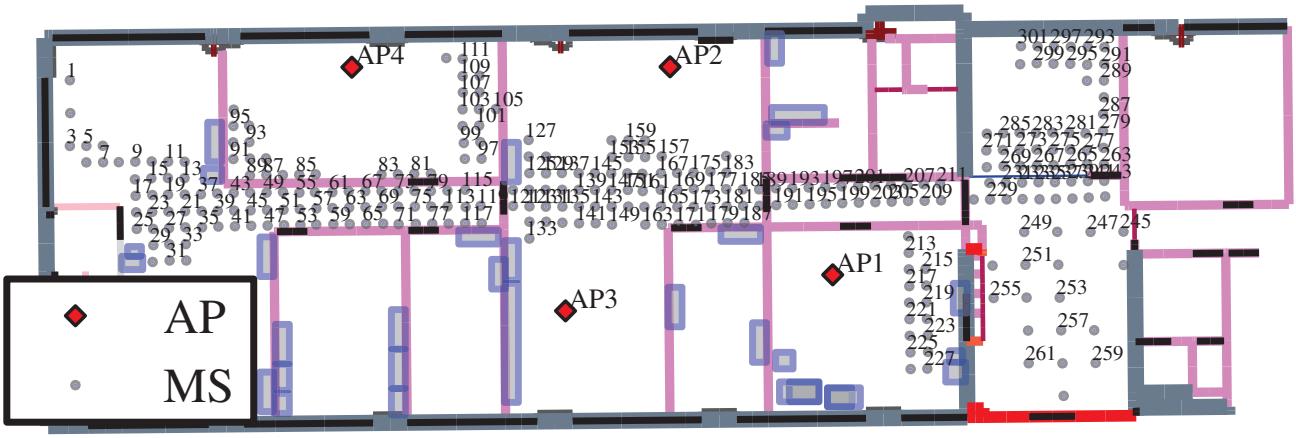

Figure 12: APs and MSs locations during the *WHERE* measurement campaign.

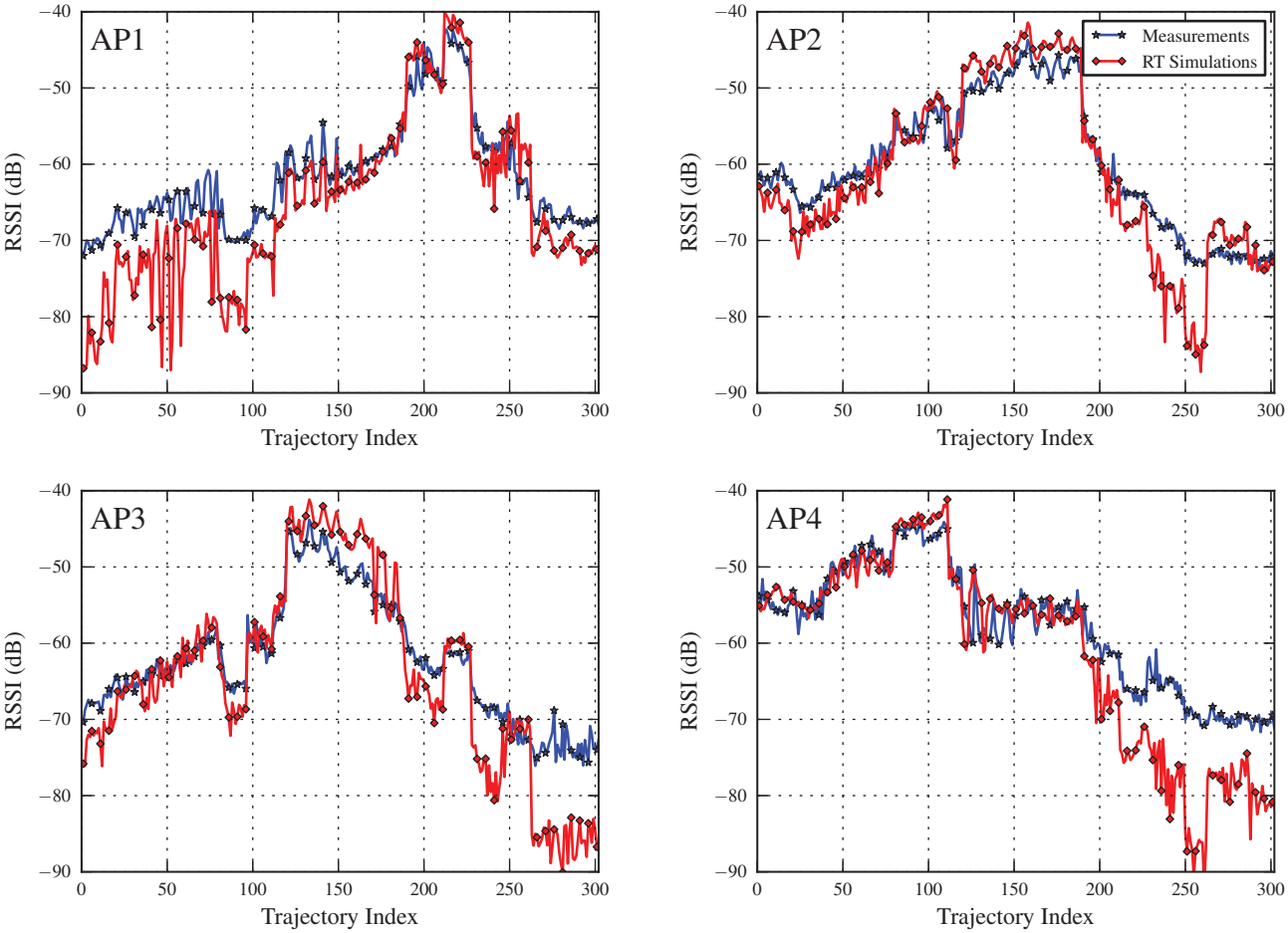

Figure 13: Measured versus Simulated RSSI values for AP3 and AP4.

into consideration by the measurement process when calculating the CIR unlike in simulations where the environment description is limited to walls, doors and windows.

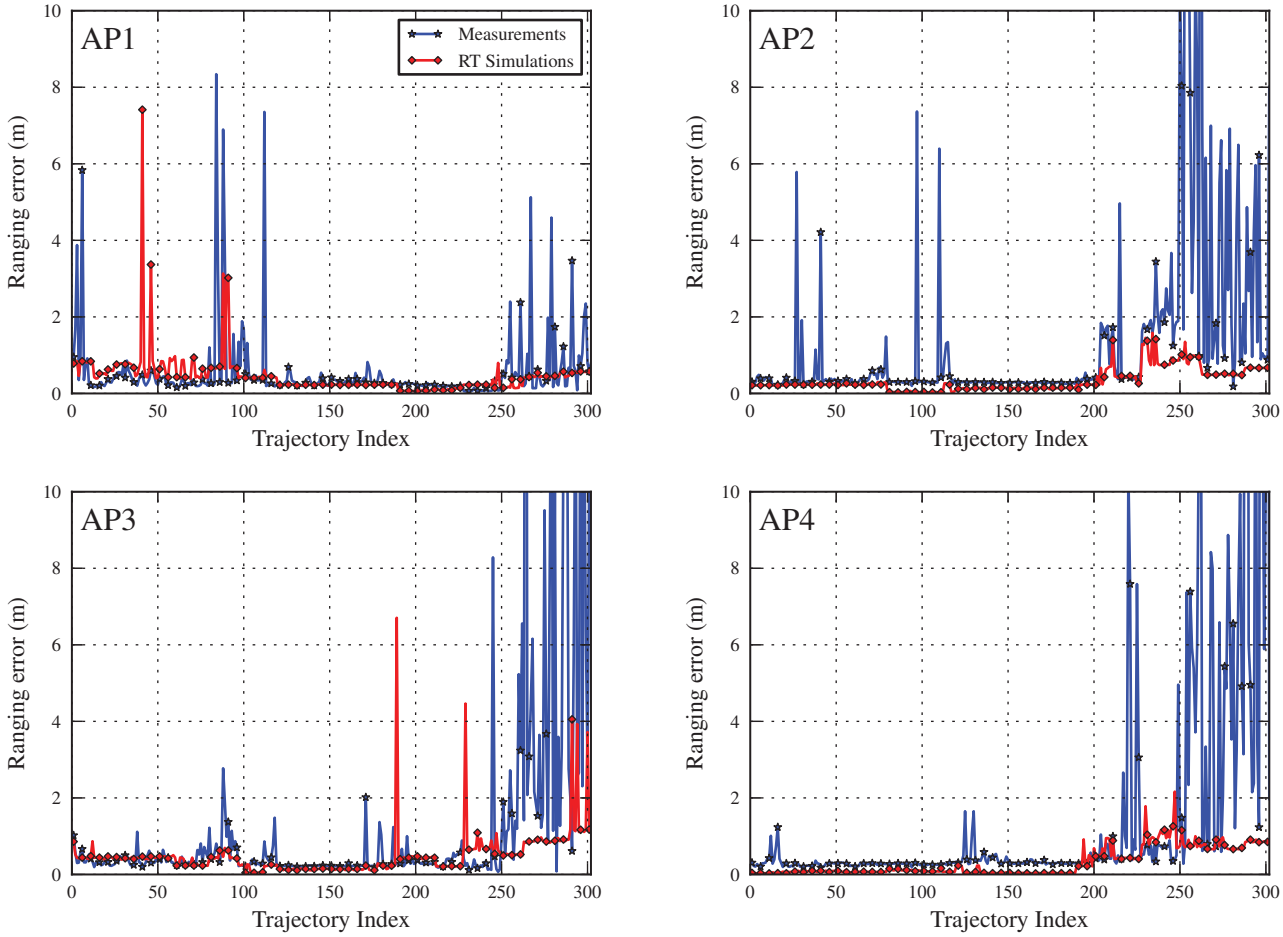

Figure 14: Measured versus Simulated TOA ranging values for AP3 and AP4.

Figure 15 shows how the absolute ratio (in dB) between the simulated and the measured RSSIs. As aforementioned, this difference is justified by the fact that furniture pieces have not been included in the PyRay description of the synthetic environment. The same conclusion is shown by Figure 16 which plots the CDF of absolute ranging error using the *Thresholded dichotomous left interval selection* technique applied respectively on measurements and simulations.

As outcome in section 5.1, the reliability of a RT tool in LDPs modeling depends on the precision and the depth of environment description. A complete environment description in which walls, doors, windows, and furnitures are considered and properly described would lead to better simulation accuracy and avoid hence carrying laborious measurements.

References

[1] R. Burghelea, S. Avrillon, and B. Uguen. Vector spherical harmonics antenna description for IR-UWB ray tracing simulator. In *Electromagnetics in Advanced Applications, 2009. ICEAA '09. International Conference on*, pages 303 –306, sept. 2009.

[2] Bernard Uguen, Nicolas Amiot, and Mohamed Laaraiedh. Exploiting the Graph Description of Indoor Layout for Ray Persistency Modeling in Moving Channel. In *Proceedings of the 6th European Conference on Antennas and Propagation (EuCAP 2012)*. Prague, Czech Republic, March 2012.

[3] Y. Lostanlen, J. Stephan, J. Keignart, W. Wang, D. Slock, and F. Kaltenberger. D4.1: Measurements of location-dependent channel features. Deliverable, October 2008.

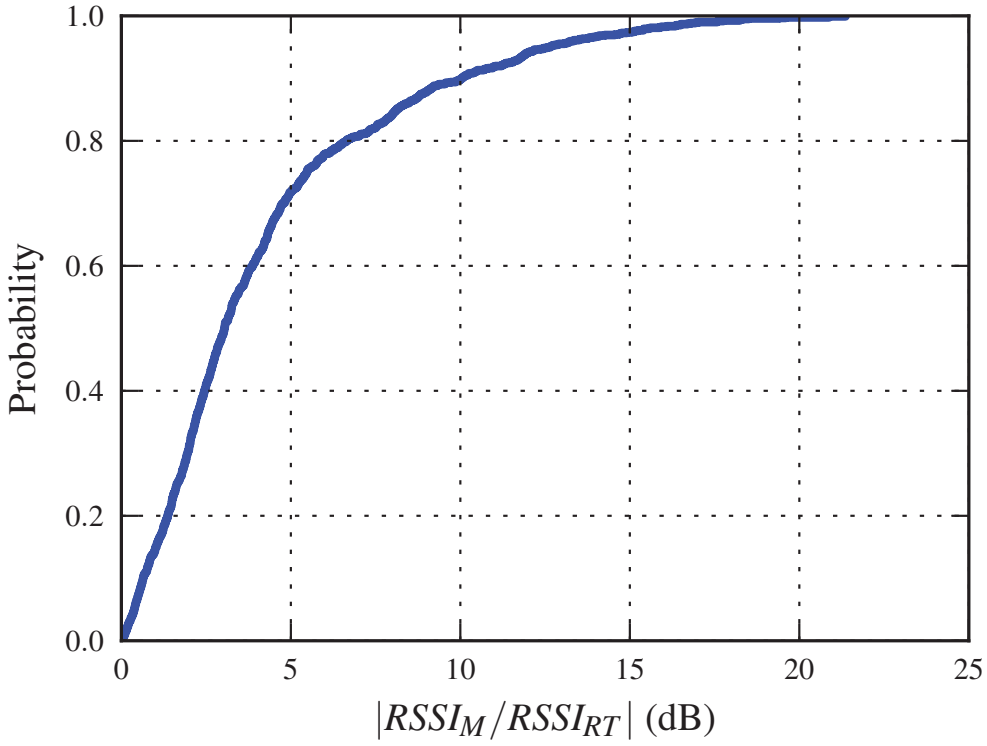

Figure 15: CDF of measured vs. simulated RSSI ratio for all receivers

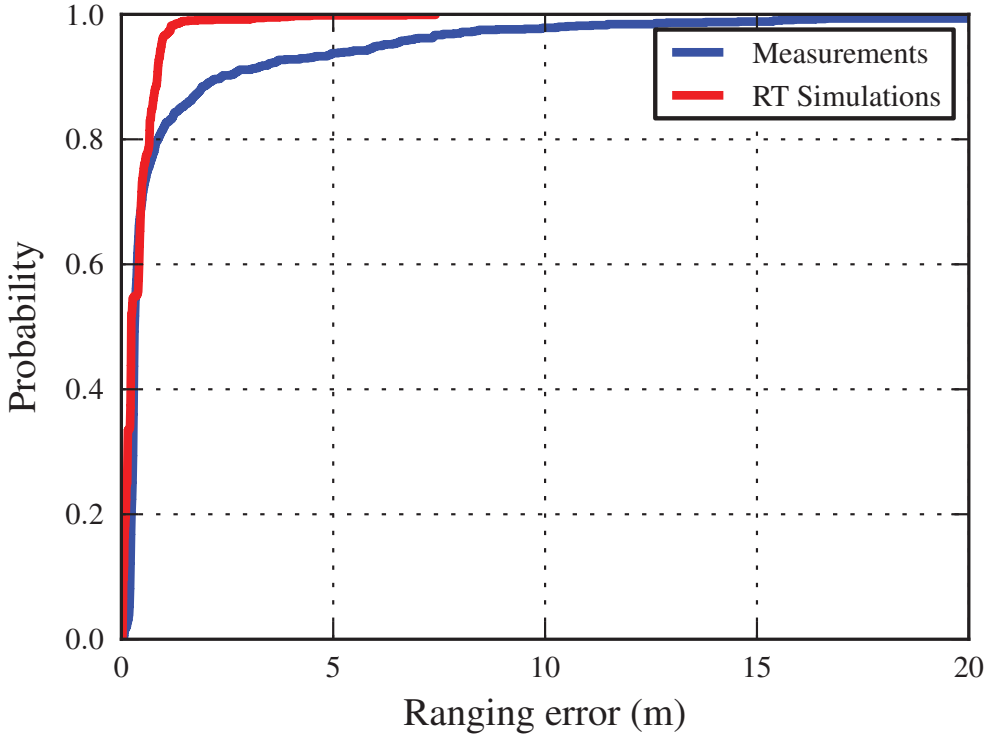

Figure 16: TOA based ranging error using simulations and measurements respectively

[4] L. Yu, M. Laaraiedh, S. Avrillon, B. Uguen, J. Keignart, and J. Stephan. Performance Evaluation of Threshold-Based TOA Estimation Techniques Using IR-UWB Indoor Measurements. In *Proc. of 18th European Wireless Conference (EW2012)*. Poznan, Poland, April 2012.

A.8 Application of Bayesian Hierarchical Prior Modeling to Sparse Channel Estimation

N. L. Pedersen, C. N. Manchón, D. Shutin and B.H. Fleury Application of Bayesian Hierarchical Prior Modeling to Sparse Channel Estimation. *IEEE International Conference on Communications (ICC).*, June 10-15, 2012, Ottawa, Canada.

Application of Bayesian Hierarchical Prior Modeling to Sparse Channel Estimation

Niels Lovmand Pedersen*, Carles Navarro Manchón*, Dmitriy Shutin† and Bernard Henri Fleury*
*Department of Electronic Systems, Aalborg University
Niels Jernes Vej 12, DK-9220 Aalborg, Denmark, Email: {nlp,cnm,bfl}@es.aau.dk
†Institute of Communications and Navigation, German Aerospace Center
Oberpfaffenhofen, D-82234 Wessling, Germany, Email: dmitriy.shutin@dlr.de

***Abstract*—Existing methods for sparse channel estimation typically provide an estimate computed as the solution maximizing an objective function defined as the sum of the log-likelihood function and a penalization term proportional to the ℓ_1-norm of the parameter of interest. However, other penalization terms have proven to have strong sparsity-inducing properties. In this work, we design pilot-assisted channel estimators for OFDM wireless receivers within the framework of sparse Bayesian learning by defining hierarchical Bayesian prior models that lead to sparsity-inducing penalization terms. The estimators result as an application of the variational message-passing algorithm on the factor graph representing the signal model extended with the hierarchical prior models. Numerical results demonstrate the superior performance of our channel estimators as compared to traditional and state-of-the-art sparse methods.**

I. Introduction

During the last few years the research on compressive sensing techniques and sparse signal representations [1], [2] applied to channel estimation has received considerable attention, see e.g., [3]–[7]. The reason is that, typically, the impulse response of the wireless channel has a few dominant multipath components. A channel exhibiting this property is said to be sparse [3].

The general goal of sparse signal representations from overcomplete dictionaries is to estimate the sparse vector $\boldsymbol{\alpha}$ in the following system model:

$$\boldsymbol{y} = \boldsymbol{\Phi}\boldsymbol{\alpha} + \boldsymbol{w}. \tag{1}$$

In this expression $\boldsymbol{y} \in \mathbb{C}^M$ is the vector of measurement samples and $\boldsymbol{w} \in \mathbb{C}^M$ represents the samples of the additive white Gaussian random noise with covariance matrix $\lambda^{-1}\boldsymbol{I}$ and precision parameter $\lambda > 0$. The matrix $\boldsymbol{\Phi} = [\boldsymbol{\phi}_1, \ldots, \boldsymbol{\phi}_L] \in \mathbb{C}^{M\times L}$ is the overcomplete dictionary with more columns than rows ($L > M$) and $\boldsymbol{\alpha} = [\alpha_1, \ldots, \alpha_L]^{\mathrm{T}} \in \mathbb{C}^L$ is an unknown sparse vector, i.e., $\boldsymbol{\alpha}$ has few nonzero elements at unknown locations.

Often, a sparse channel estimator is constructed by solving the ℓ_1-norm constrained quadratic optimization problem, see among others [4]–[6]:

$$\widehat{\boldsymbol{\alpha}} = \underset{\boldsymbol{\alpha}}{\operatorname{argmin}} \left\{ \|\boldsymbol{y} - \boldsymbol{\Phi}\boldsymbol{\alpha}\|_2^2 + \kappa\|\boldsymbol{\alpha}\|_1 \right\} \tag{2}$$

with $\kappa > 0$ and $\|\cdot\|_p$, $p \geq 1$, denoting the ℓ_p vector norm. This method is also known as Least Absolute Shrinkage and Selection Operator (LASSO) regression [8] or Basis Pursuit Denoising [9]. The popularity of the LASSO regression is mainly attributed to the convexity of the cost function, as well as to its provable sparsity-inducing properties (see [2]). In [4]–[6] the LASSO regression is applied to *orthogonal frequency-division multiplexing* (OFDM) pilot-assisted channel estimation. Various channel estimation algorithms that minimize the LASSO cost function using convex optimization are compared in [6].

Another approach to sparse channel estimation is sparse Bayesian learning (SBL) [7], [10]–[12]. Specifically, SBL aims at finding a sparse *maximum a posteriori* (MAP) estimate of $\boldsymbol{\alpha}$

$$\widehat{\boldsymbol{\alpha}} = \underset{\boldsymbol{\alpha}}{\operatorname{argmin}} \left\{ \|\boldsymbol{y} - \boldsymbol{\Phi}\boldsymbol{\alpha}\|_2^2 + \lambda^{-1}Q(\boldsymbol{\alpha}) \right\} \tag{3}$$

by specifying a prior $p(\boldsymbol{\alpha})$ such that the penalty term $Q(\boldsymbol{\alpha}) \propto^e -\log p(\boldsymbol{\alpha})$ induces a sparse estimate $\widehat{\boldsymbol{\alpha}}$.[1]

Obviously, by comparing (2) and (3) the SBL framework realizes the LASSO cost function by choosing the Laplace prior $p(\boldsymbol{\alpha}) \propto \exp(-a\|\boldsymbol{\alpha}\|_1)$ with $\kappa = \lambda^{-1}a$. However, instead of working directly with the prior $p(\boldsymbol{\alpha})$, SBL models this using a two-layer (2-L) hierarchical structure. This involves specifying a conditional prior $p(\boldsymbol{\alpha}|\boldsymbol{\gamma})$ and a hyperprior $p(\boldsymbol{\gamma})$ such that $p(\boldsymbol{\alpha}) = \int p(\boldsymbol{\alpha}|\boldsymbol{\gamma})p(\boldsymbol{\gamma})\mathrm{d}\boldsymbol{\gamma}$ has a sparsity-inducing nature. The hierarchical approach to the representation of $p(\boldsymbol{\alpha})$ has several important advantages. First of all, one is free to choose simple and analytically tractable probability density functions (pdfs). Second, when carefully chosen, the resulting hierarchical structure allows for the construction of efficient yet computationally tractable iterative inference algorithms with analytical derivation of the inference expressions.

In [13] we propose a 2-L and a three-layer (3-L) prior model for $\boldsymbol{\alpha}$. These hierarchical prior models lead to novel sparsity-inducing priors that include the Laplace prior for complex variables as a special case. This paper adapts the Bayesian probabilistic framework introduced in [13] to OFDM pilot-assisted sparse channel estimation. We then propose a variational message passing (VMP) algorithm that effectively exploits the hierarchical structure of the prior models. This approach leads to novel channel estimators that make use

[1]Here $x \propto^e y$ denotes $\exp(x) = \exp(v)\exp(y)$, and thus $x = v + y$, for some arbitrary constant v. We will also make use of $x \propto y$ which denotes $x = vy$ for some positive constant v.

of various priors with strong sparsity-inducing properties. The numerical results reveal the promising potential of our estimators with improved performance as compared to state-of-the-art methods. In particular, the estimators outperform LASSO.

Throughout the paper we shall make use of the following notation: $(\cdot)^{\mathrm{T}}$ and $(\cdot)^{\mathrm{H}}$ denote respectively the transpose and the Hermitian transpose; the expression $\langle f(\boldsymbol{x})\rangle_{q(\boldsymbol{x})}$ denotes the expectation of the function $f(\boldsymbol{x})$ with respect to the density $q(\boldsymbol{x})$; $\mathrm{CN}(\boldsymbol{x}|\boldsymbol{a},\boldsymbol{B})$ denotes a multivariate complex Gaussian pdf with mean $\boldsymbol{a}$ and covariance matrix $\boldsymbol{B}$; similarly, $\mathrm{Ga}(x|a,b) = \frac{b^a}{\Gamma(a)}x^{a-1}\exp(-bx)$ denotes a Gamma pdf with shape parameter a and rate parameter b.

II. Signal Model

We consider a single-input single-output OFDM system with N subcarriers. A cyclic prefix (CP) is added to preserve orthogonality between subcarriers and to eliminate inter-symbol interference between consecutive OFDM symbols. The channel is assumed static during the transmission of each OFDM symbol. The received (baseband) OFDM signal $\boldsymbol{r} \in \mathbb{C}^N$ reads in matrix-vector notation

$$\boldsymbol{r} = \boldsymbol{X}\boldsymbol{h} + \boldsymbol{n}. \tag{4}$$

The diagonal matrix $\boldsymbol{X} = \mathrm{diag}(x_1, x_2, \ldots, x_N)$ contains the transmitted symbols. The components of the vector $\boldsymbol{h} \in \mathbb{C}^N$ are the samples of the channel frequency response at the N subcarriers. Finally, $\boldsymbol{n} \in \mathbb{C}^N$ is a zero-mean complex symmetric Gaussian random vector of independent components with variance λ^{-1}.

To estimate the vector $\boldsymbol{h}$ in (4), a total of M pilot symbols are transmitted at selected subcarriers. The pilot pattern $\mathcal{P} \subseteq \{1, \ldots, N\}$ denotes the set of indices of the pilot subcarriers. The received signals observed at the pilot positions $\boldsymbol{r}_{\mathcal{P}}$ are then divided each by the corresponding pilot symbol $\boldsymbol{X}_{\mathcal{P}} = \mathrm{diag}(x_n : n \in \mathcal{P})$ to produce the vector of observations:

$$\boldsymbol{y} \triangleq (\boldsymbol{X}_{\mathcal{P}})^{-1}\boldsymbol{r}_{\mathcal{P}} = \boldsymbol{h}_{\mathcal{P}} + (\boldsymbol{X}_{\mathcal{P}})^{-1}\boldsymbol{n}_{\mathcal{P}}. \tag{5}$$

We assume that all pilot symbols hold unit power such that the statistics of the noise term $(\boldsymbol{X}_{\mathcal{P}})^{-1}\boldsymbol{n}_{\mathcal{P}}$ remain unchanged, i.e., $\boldsymbol{y} \in \mathbb{C}^M$ yields the samples of the true channel frequency response (at the pilot subcarriers) corrupted by additive complex white Gaussian noise with component variance λ^{-1}.

In this work, we consider a frequency-selective wireless channel that remains constant during the transmission of each OFDM symbol. The maximum relative delay $\tau_{\max}$ is assumed to be large compared to the sampling time T_{s}, i.e., $\tau_{\max}/T_{\mathrm{s}} \gg 1$ [3]. The impulse response of the wireless channel is modeled as a sum of multipath components:

$$g(\tau) = \sum_{k=1}^{K} \beta_k \delta(\tau - \tau_k). \tag{6}$$

In this expression, β_k and τ_k are respectively the complex weight and the continuous delay of the kth multipath component, and $\delta(\cdot)$ is the Dirac delta function. The parameter K is the total number of multipath components. The channel parameters K, β_k, and τ_k, $k = 1, \ldots, K$, are random variables. Specifically, the weights β_k, $k = 1, \ldots, K$, are mutually uncorrelated zero-mean with the sum of their variances normalized to one. Additional details regarding the assumptions on the model (6) are provided in Section VI.

III. The Dictionary Matrix

Our goal is to estimate $\boldsymbol{h}$ in (4) by applying the general optimization problem (3) to the observation model (5). For doing so, we must define a proper dictionary matrix $\boldsymbol{\Phi}$. In this section we give an example of such a matrix. As a starting point, we invoke the parametric model (6) of the channel. Making use of this model, (5) can be written as

$$\boldsymbol{y} = \boldsymbol{T}(\boldsymbol{\tau})\boldsymbol{\beta} + \boldsymbol{w} \tag{7}$$

with $\boldsymbol{h}_{\mathcal{P}} = \boldsymbol{T}(\boldsymbol{\tau})\boldsymbol{\beta}$, $\boldsymbol{w} = (\boldsymbol{X}_{\mathcal{P}})^{-1}\boldsymbol{n}_{\mathcal{P}}$, $\boldsymbol{\beta} = [\beta_1, \ldots, \beta_K]^{\mathrm{T}}$, $\boldsymbol{\tau} = [\tau_1, \ldots, \tau_K]^{\mathrm{T}}$, and $\boldsymbol{T}(\boldsymbol{\tau}) \in \mathbb{C}^{M\times K}$ depending on the pilot pattern $\mathcal{P}$ as well as the unknown delays in $\boldsymbol{\tau}$. Specifically, the (m,k)th entry of $\boldsymbol{T}(\boldsymbol{\tau})$ reads

$$\boldsymbol{T}(\boldsymbol{\tau})_{m,k} \triangleq \exp(-j2\pi f_m \tau_k), \quad \begin{matrix} m = 1, 2, \ldots, M \\ k = 1, 2, \ldots, K \end{matrix} \tag{8}$$

with f_m denoting the frequency of the mth pilot subcarrier. In the general optimization problem (3) the columns of $\boldsymbol{\Phi}$ are known. However, the columns of $\boldsymbol{T}(\boldsymbol{\tau})$ in (7) depend on the unknown delays in $\boldsymbol{\tau}$. To circumvent this discrepancy we follow the same approach as in [5] and consider a grid of uniformly-spaced delay samples in the interval $[0, \tau_{\max}]$:

$$\boldsymbol{\tau}_d = \left[0, \frac{T_{\mathrm{s}}}{\zeta}, \frac{2T_{\mathrm{s}}}{\zeta}, \ldots, \tau_{\max}\right]^{\mathrm{T}} \tag{9}$$

with $\zeta > 0$ such that $\zeta\tau_{\max}/T_{\mathrm{s}}$ is an integer. We now define the dictionary $\boldsymbol{\Phi} \in \mathbb{C}^{M\times L}$ as $\boldsymbol{\Phi} = \boldsymbol{T}(\boldsymbol{\tau}_d)$. Thus, the entries of $\boldsymbol{\Phi}$ are of the form (8) with delay vector $\boldsymbol{\tau}_d$. The number of columns $L = \zeta\tau_{\max}/T_{\mathrm{s}} + 1$ in $\boldsymbol{\Phi}$ is thereby inversely proportional to the selected delay resolution T_{s}/ζ.

It is important to notice that the system model (1) with $\boldsymbol{\Phi}$ defined using discretized delay components is an approximation of the true system model (7). This approximation model is introduced so that (3) can be applied to solve the channel estimation task. The estimate of the channel vector at the pilot subcarriers is then $\widehat{\boldsymbol{h}}_{\mathcal{P}} = \boldsymbol{\Phi}\widehat{\boldsymbol{\alpha}}$. In order to estimate the channel $\boldsymbol{h}$ in (4) the dictionary $\boldsymbol{\Phi}$ is appropriately expanded (row-wise) to include all N subcarrier frequencies.

IV. Bayesian Prior Modeling

In this section we specify the joint pdf of the system model (1) when it is augmented with the 2-L and the 3-L hierarchical prior model. The joint pdf of (1) augmented with the 2-L hierarchical prior model reads

$$p(\boldsymbol{y}, \boldsymbol{\alpha}, \boldsymbol{\gamma}, \lambda) = p(\boldsymbol{y}|\boldsymbol{\alpha}, \lambda)p(\lambda)p(\boldsymbol{\alpha}|\boldsymbol{\gamma})p(\boldsymbol{\gamma}; \boldsymbol{\eta}). \tag{10}$$

The 3-L prior model considers the parameter $\boldsymbol{\eta}$ specifying the prior of $\boldsymbol{\gamma}$ in (10) as random. Thus, the joint pdf of (1)

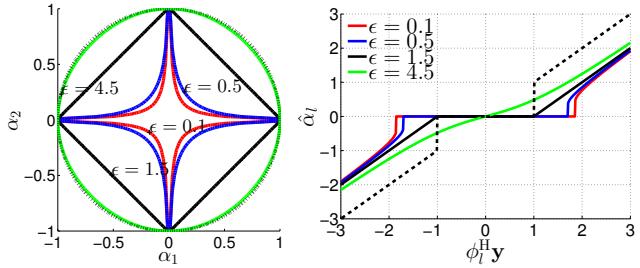

(a) (b)

Fig. 1. 2-L hierarchical prior pdf for $\boldsymbol{\alpha} \in \mathbb{C}^2$: (a) Contour plot of the restriction to the $\mathrm{Im}\{\alpha_1\} = \mathrm{Im}\{\alpha_2\} = 0$ – plane of the penalty term $Q(\alpha_1, \alpha_2; \epsilon, \eta) \propto^e -\log(p(\alpha_1; \epsilon, \eta)p(\alpha_2; \epsilon, \eta))$. (b) Restriction to $\mathrm{Im}\{\boldsymbol{\phi}_l^{\mathrm{H}}\boldsymbol{y}\} = 0$ of the resulting MAP estimation rule (3) with ϵ as a parameter in the case when $\boldsymbol{\Phi}$ is orthonormal. The black dashed line indicates the hard-threshold rule and the black solid line the soft-threshold rule (obtained with $\epsilon = 3/2$). The black dashed line indicates the penalty term resulting when the prior pdf is a circular symmetric Gaussian pdf.

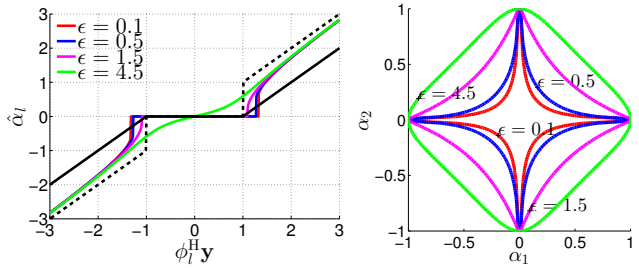

(a) (b)

Fig. 2. Three-layer hierarchical prior pdf for $\boldsymbol{\alpha} \in \mathbb{C}^2$ with the setting $a = 1$, $b = 0.1$: (a) Restriction to $\mathrm{Im}\{\boldsymbol{\phi}_l^{\mathrm{H}}\boldsymbol{y}\} = 0$ of the resulting MAP estimation rule (3) with ϵ as a parameter in the case when $\boldsymbol{\Phi}$ is orthonormal. The black dashed line indicates the hard-threshold rule and the black solid line the soft-threshold rule. (b) Contour plot of the restriction to the $\mathrm{Im}\{\alpha_1\} = \mathrm{Im}\{\alpha_2\} = 0$ – plane of the penalty term $Q(\alpha_1, \alpha_2; \epsilon, a, b) \propto^e -\log(p(\alpha_1; \epsilon, a, b)p(\alpha_2; \epsilon, a, b))$.

augmented with this hierarchical prior model is of the form

$$p(\boldsymbol{y}, \boldsymbol{\alpha}, \boldsymbol{\gamma}, \boldsymbol{\eta}, \lambda) = p(\boldsymbol{y}|\boldsymbol{\alpha}, \lambda)p(\lambda)p(\boldsymbol{\alpha}|\boldsymbol{\gamma})p(\boldsymbol{\gamma}|\boldsymbol{\eta})p(\boldsymbol{\eta}). \quad (11)$$

In (10) and (11) we have $p(\boldsymbol{y}|\boldsymbol{\alpha}, \lambda) = \mathrm{CN}(\boldsymbol{y}|\boldsymbol{\Phi}\boldsymbol{\alpha}, \lambda^{-1}\boldsymbol{I})$ due to (1). Furthermore, we select the conjugate prior $p(\lambda) = p(\lambda; c, d) \triangleq \mathrm{Ga}(\lambda|c, d)$. Finally, we let $p(\boldsymbol{\alpha}|\boldsymbol{\gamma}) = \prod_{l=1}^{L} p(\alpha_l|\gamma_l)$ with $p(\alpha_l|\gamma_l) \triangleq \mathrm{CN}(\alpha_l|0, \gamma_l)$. In the following we show the main results and properties of these prior models. We refer to [13] for a more detailed analysis.

A. Two-Layer Hierarchical Prior Model

The 2-L prior model assumes that $p(\boldsymbol{\gamma}) = \prod_{l=1}^{L} p(\gamma_l)$ with $p(\gamma_l) = p(\gamma_l; \epsilon, \eta_l) \triangleq \mathrm{Ga}(\gamma_l|\epsilon, \eta_l)$. We compute the prior of $\boldsymbol{\alpha}$ to be

$$p(\boldsymbol{\alpha}; \epsilon, \boldsymbol{\eta}) = \int_0^\infty p(\boldsymbol{\alpha}|\boldsymbol{\gamma})p(\boldsymbol{\gamma}; \epsilon, \boldsymbol{\eta})\mathrm{d}\boldsymbol{\gamma} = \prod_{l=1}^{L} p(\alpha_l; \epsilon, \eta_l) \quad (12)$$

with

$$p(\alpha_l; \epsilon, \eta_l) = \frac{2}{\pi\Gamma(\epsilon)}\eta_l^{\frac{(\epsilon+1)}{2}}|\alpha_l|^{\epsilon-1}K_{\epsilon-1}(2\sqrt{\eta_l}|\alpha_l|). \quad (13)$$

In this expression, $K_\nu(\cdot)$ is the modified Bessel function of the second kind with order $\nu \in \mathbb{R}$. The prior (13) leads to the general optimization problem (3) with penalty term

$$Q(\boldsymbol{\alpha}; \epsilon, \boldsymbol{\eta}) = \sum_{l=1}^{L} \log\left(|\alpha_l|^{\epsilon-1}K_{\epsilon-1}\left(2\sqrt{\eta_l}|\alpha_l|\right)\right). \quad (14)$$

We now show that the 2-L prior model induces the ℓ_1-norm penalty term and thereby the LASSO cost function as a special case. Selecting $\epsilon = 3/2$ and using the identity $K_{\frac{1}{2}}(z) = \sqrt{\frac{\pi}{2z}}\exp(-z)$ [14], (13) yields the Laplace prior

$$p(\alpha_l; \epsilon = 3/2, \eta_l) = \frac{2\eta_l}{\pi}\exp(-2\sqrt{\eta_l}|\alpha_l|). \quad (15)$$

With the selection $\eta_l = \eta$, $l = 1, \ldots, L$, we obtain $Q(\boldsymbol{\alpha}; \eta) = 2\sqrt{\eta}\|\boldsymbol{\alpha}\|_1$.

The prior pdf (13) is specified by ϵ and the regularization parameter $\boldsymbol{\eta}$. In order to get insight into the impact of ϵ on the properties of this prior pdf we consider the case $\boldsymbol{\alpha} \in \mathbb{C}^2$. In Fig. 1(a) the contour lines of the restriction to $\mathbb{R}^2$ of $Q(\alpha_1, \alpha_2; \epsilon, \eta) \propto^e -\log(p(\alpha_1; \epsilon, \eta)p(\alpha_2; \epsilon, \eta))$ are visualized;[2] each contour line is computed for a specific choice of ϵ. Notice that as ϵ decreases towards 0 more probability mass accumulates along the $\boldsymbol{\alpha}$-axes; as a consequence, the mode of the resulting posterior is more likely to be located close to the axes, thus promoting a sparse solution. The behavior of the classical ℓ_1 penalty term obtained for $\epsilon = 3/2$ can also be clearly recognized. In Fig. 1(b) we consider the case when $\boldsymbol{\Phi}$ is orthonormal and compute the MAP estimator (3) with penalty term (14) for different values of ϵ. Note the typical soft-threshold-like behavior of the estimators. As $\epsilon \to 0$, more components of $\widehat{\boldsymbol{\alpha}}$ are pulled towards zero since the threshold value increases, thus encouraging a sparser solution.

B. Three-Layer Hierarchical Prior Model

We now turn to the SBL problem with a 3-L prior model for $\boldsymbol{\alpha}$ leading to the joint pdf in (11). Specifically, the goal is to incorporate the regularization parameter $\boldsymbol{\eta}$ into the inference framework. To that end, we define $p(\boldsymbol{\eta}) = \prod_l^L p(\eta_l)$ with $p(\eta_l) = p(\eta_l; a_l, b_l) \triangleq \mathrm{Ga}(\eta_l|a_l, b_l)$ and compute the prior $p(\boldsymbol{\alpha})$. Defining $\boldsymbol{a} \triangleq [a_1, \ldots, a_l]^{\mathrm{T}}$ and $\boldsymbol{b} \triangleq [b_1, \ldots, b_L]^{\mathrm{T}}$ we obtain $p(\boldsymbol{\alpha}; \epsilon, \boldsymbol{a}, \boldsymbol{b}) = \prod_l^L p(\alpha_l; \epsilon, a_l, b_l)$ with

$$\begin{aligned} p(\alpha_l; \epsilon, a_l, b_l) &= \int_0^\infty p(\alpha_l|\gamma_l)p(\gamma_l)\mathrm{d}\gamma_l \\ &= \frac{\Gamma(\epsilon + a_l)\Gamma(a_l + 1)}{\pi b_l\Gamma(\epsilon)\Gamma(a_l)}\left(\frac{|\alpha_l|^2}{b_l}\right)^{\epsilon-1}U\left(\epsilon + a_l; \epsilon; \frac{|\alpha_l|^2}{b_l}\right). \end{aligned} \quad (16)$$

In this expression, $U(\cdot;\cdot;\cdot)$ is the confluent hypergeometric function [14]. In Fig. 2(a) we show the estimation rules produced by the MAP solver for different values of ϵ and fixed parameters a_l and b_l when $\boldsymbol{\Phi}$ is orthonormal. It can

[2]Let f denote a function defined on a set A. The restriction of f to a subset $B \subset A$ is the function defined on B that coincides with f on this subset.

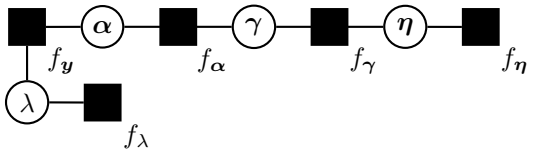

Fig. 3. A factor graph that represents the joint pdf (11). In this figure $f_{\boldsymbol{y}} \equiv p(\boldsymbol{y}|\boldsymbol{\alpha}, \lambda)$, $f_{\boldsymbol{\alpha}} \equiv p(\boldsymbol{\alpha}|\boldsymbol{\gamma})$, $f_{\boldsymbol{\gamma}} \equiv p(\boldsymbol{\gamma}|\boldsymbol{\eta})$, $f_{\boldsymbol{\eta}} \equiv p(\boldsymbol{\eta})$, and $f_\lambda \equiv p(\lambda)$.

be seen that the estimation rules obtained with the 3-L prior model approximate the hard-thresholding rule. In Fig. 2(b), we depict the contour lines of the restriction to $\mathbb{R}^2$ of $Q(\alpha_1, \alpha_2; \epsilon, a, b) \ \propto^e \ -\log(p(\alpha_1; \epsilon, a, b)p(\alpha_2; \epsilon, a, b))$. Observe that although the contours behave qualitatively similarly to those shown in Fig. 1(a) for the 2-L prior model, the estimation rules in Fig. 2(a) and Fig. 1(b) are different.

Naturally, the 3-L prior model encompasses three free parameters, ϵ, $\boldsymbol{a}$, and $\boldsymbol{b}$. The choice $\epsilon = 0$ and b_l small (practically we let $b_l = 10^{-6}$, $l = 1, \ldots, L$) induces a weighted log-sum penalization term. This term is known to strongly promote a sparse estimate [10], [11]. Later in the text we will also adopt this parameter setting.

V. Variational Message Passing

In this section we present a VMP algorithm for estimating $\boldsymbol{h}$ in (4) given the observation $\boldsymbol{y}$ in (5). Let $\boldsymbol{\Theta} = \{\boldsymbol{\alpha}, \boldsymbol{\gamma}, \boldsymbol{\eta}, \lambda\}$ be the set of unknown parameters and $p(\boldsymbol{y}, \boldsymbol{\Theta})$ be the joint pdf specified in (11). The factor graph [15] that encodes the factorization of $p(\boldsymbol{y}, \boldsymbol{\Theta})$ is shown in Fig. 3. Consider an auxiliary pdf $q(\boldsymbol{\Theta})$ for the unknown parameters that factorizes according to $q(\boldsymbol{\Theta}) = q(\boldsymbol{\alpha})q(\boldsymbol{\gamma})q(\boldsymbol{\eta})q(\lambda)$. The VMP algorithm is an iterative scheme that attempts to compute the auxiliary pdf that minimizes the Kullback-Leibler (KL) divergence $\mathrm{KL}(q(\boldsymbol{\Theta})\|p(\boldsymbol{\Theta}|\boldsymbol{y}))$. In the following we summarize the key steps of the algorithm; the reader is referred to [16] for more information on VMP.

From [16] the auxiliary function $q(\boldsymbol{\theta}_i)$, $\boldsymbol{\theta}_i \in \boldsymbol{\Theta}$, is updated as the product of incoming messages from the neighboring factor nodes f_n to the variable node $\boldsymbol{\theta}_i$:

$$q(\boldsymbol{\theta}_i) \propto \prod_{f_n \in \mathcal{N}_{\boldsymbol{\theta}_i}} m_{f_n \to \boldsymbol{\theta}_i}. \tag{17}$$

In (17) $\mathcal{N}_{\boldsymbol{\theta}_i}$ is the set of factor nodes neighboring the variable node $\boldsymbol{\theta}_i$ and $m_{f_n \to \boldsymbol{\theta}_i}$ denotes the message from factor node f_n to variable node $\boldsymbol{\theta}_i$. This message is computed as

$$m_{f_n \to \boldsymbol{\theta}_i} = \exp\left(\langle \ln f_n \rangle_{\prod_j q(\boldsymbol{\theta}_j),\, \boldsymbol{\theta}_j \in \mathcal{N}_{f_n} \setminus \{\boldsymbol{\theta}_i\}} \right), \tag{18}$$

where $\mathcal{N}_{f_n}$ is the set of variable nodes neighboring the factor node f_n. After an initialization procedure, the individual factors of $q(\boldsymbol{\Theta})$ are then updated iteratively in a round-robin fashion using (17) and (18).

We provide two versions of the VMP algorithm: one applied to the 2-L prior model (referred to as VMP-2L) and another one applied to the 3-L model (VMP-3L). The messages corresponding to VMP-2L are easily obtained as a special case of the messages computed for VMP-3L by assuming $q(\eta_l) = \delta(\eta_l - \hat{\eta}_l)$, where $\hat{\eta}_l$ is some fixed real number.

1) Update of $q(\boldsymbol{\alpha})$: According to (17) and Fig. 3 the computation of the update of $q(\boldsymbol{\alpha})$ requires evaluating the product of messages $m_{f_{\boldsymbol{y}} \to \boldsymbol{\alpha}}$ and $m_{f_{\boldsymbol{\alpha}} \to \boldsymbol{\alpha}}$. Multiplying these two messages yields the Gaussian auxiliary pdf $q(\boldsymbol{\alpha}) = \mathrm{CN}\left(\boldsymbol{\alpha}|\hat{\boldsymbol{\alpha}}, \hat{\boldsymbol{\Sigma}}_{\boldsymbol{\alpha}}\right)$ with covariance matrix and mean given by

$$\hat{\boldsymbol{\Sigma}}_{\boldsymbol{\alpha}} = (\langle \lambda \rangle_{q(\lambda)} \boldsymbol{\Phi}^{\mathrm{H}} \boldsymbol{\Phi} + \boldsymbol{V}(\boldsymbol{\gamma}))^{-1}, \tag{19}$$

$$\hat{\boldsymbol{\alpha}} = \langle \boldsymbol{\alpha} \rangle_{q(\boldsymbol{\alpha})} = \langle \lambda \rangle_{q(\lambda)} \hat{\boldsymbol{\Sigma}}_{\boldsymbol{\alpha}} \boldsymbol{\Phi}^{\mathrm{H}} \boldsymbol{y}. \tag{20}$$

In the above expression we have defined $\boldsymbol{V}(\boldsymbol{\gamma}) = \mathrm{diag}(\langle \gamma_1^{-1} \rangle_{q(\boldsymbol{\gamma})}, \ldots, \langle \gamma_L^{-1} \rangle_{q(\boldsymbol{\gamma})})$.

2) Update of $q(\boldsymbol{\gamma})$: The update of $q(\boldsymbol{\gamma})$ is proportional to the product of the messages $m_{f_{\boldsymbol{\alpha}} \to \boldsymbol{\gamma}}$ and $m_{f_{\boldsymbol{\gamma}} \to \boldsymbol{\gamma}}$:

$$q(\boldsymbol{\gamma}) \propto \prod_{l=1}^{L} \gamma_l^{\epsilon - 2} \exp\left(-\gamma_l^{-1} \langle |\alpha_l|^2 \rangle_{q(\boldsymbol{\alpha})} - \gamma_l \langle \eta_l \rangle_{q(\boldsymbol{\eta})} \right). \tag{21}$$

The right-hand side expression in (21) is recognized as the product of Generalized Inverse Gaussian (GIG) pdfs [17] with order $p = \epsilon - 1$. Observe that the computation of $\boldsymbol{V}(\boldsymbol{\gamma})$ in (19) requires evaluating $\langle \gamma_l^{-1} \rangle_{q(\boldsymbol{\gamma})}$ for all $l = 1, \ldots, L$. Luckily, the moments of the GIG distribution are given in closed form for any $n \in \mathbb{R}$ [17]:

$$\langle \gamma_l^n \rangle_{q(\boldsymbol{\gamma})} = \left(\frac{\langle |\alpha_l|^2 \rangle_{q(\boldsymbol{\alpha})}}{\langle \eta_l \rangle_{q(\boldsymbol{\eta})}} \right)^{\frac{n}{2}} \frac{K_{p+n}\left(2\sqrt{\langle \eta_l \rangle_{q(\boldsymbol{\eta})} \langle |\alpha_l|^2 \rangle_{q(\boldsymbol{\alpha})}}\right)}{K_p\left(2\sqrt{\langle \eta_l \rangle_{q(\boldsymbol{\eta})} \langle |\alpha_l|^2 \rangle_{q(\boldsymbol{\alpha})}}\right)}. \tag{22}$$

3) Update of $q(\boldsymbol{\eta})$: The update of $q(\boldsymbol{\eta})$ is proportional to the product of messages $m_{f_{\boldsymbol{\eta}} \to \boldsymbol{\eta}}$ and $m_{f_{\boldsymbol{\gamma}} \to \boldsymbol{\eta}}$:

$$q(\boldsymbol{\eta}) \propto \prod_{l=1}^{L} \eta_l^{\epsilon + a_l - 1} \exp\left(-(\langle \gamma_l \rangle_{q(\boldsymbol{\gamma})} + b_l) \eta_l \right). \tag{23}$$

Clearly, $q(\boldsymbol{\eta})$ factorizes as a product of L gamma pdfs, one for each individual entry in $\boldsymbol{\eta}$. The first moment of η_l used in (22) is easily computed as

$$\langle \eta_l \rangle_{q(\boldsymbol{\eta})} = \frac{\epsilon + a_l}{\langle \gamma_l \rangle_{q(\boldsymbol{\gamma})} + b_l}. \tag{24}$$

Naturally, $q(\boldsymbol{\eta})$ is only computed for VMP-3L.

4) Update of $q(\lambda)$: It can be shown that $q(\lambda) = \mathrm{Ga}(\lambda | M + c, \langle \|\boldsymbol{y} - \boldsymbol{\Phi}\boldsymbol{\alpha}\|_2^2 \rangle_{q(\boldsymbol{\alpha})} + d)$. The first moment of λ used in (19) and (20) is therefore

$$\langle \lambda \rangle_{q(\lambda)} = \frac{M + c}{\langle \|\boldsymbol{y} - \boldsymbol{\Phi}\boldsymbol{\alpha}\|_2^2 \rangle_{q(\boldsymbol{\alpha})} + d}. \tag{25}$$

VI. Numerical Results

We perform Monte Carlo simulations to evaluate the performance of the two versions of the derived VMP algorithm in Section V. We consider a scenario inspired by the 3GPP LTE standard [20] with the settings specified in Table I. The multipath channel (6) is based on the model used in [21] where, for each realization of the channel, the total number of multipath components K is Poisson distributed with mean of $\langle K \rangle_{p(K)} = 10$ and the delays τ_k, $k = 1, \ldots, K$, are

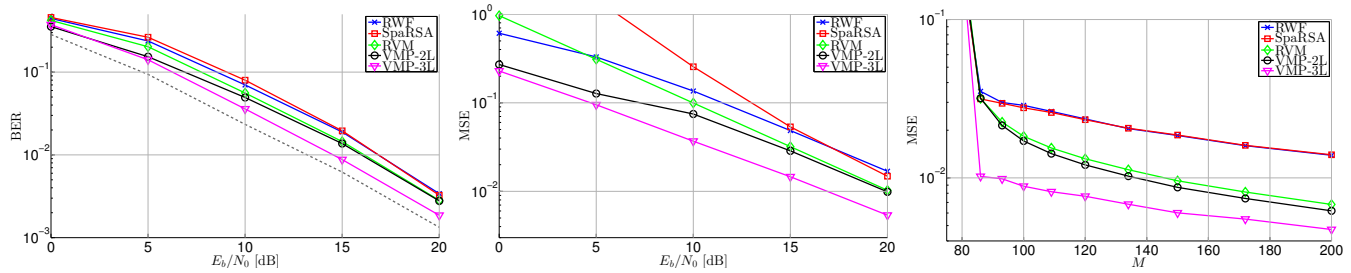

(a) (b) (c)

Fig. 4. Comparison of the performance of the VMP-2L, VMP-3L, RWF, RVM, and SparseRSA algorithms: (a) BER versus E_b/N_0, (b) MSE versus E_b/N_0, (c) MSE versus number of available pilots M with fixed $L = 200$ and the ratio between received symbol power and noise variance set to 15 dB. In (a,b) we have $M = 100$ and $L = 200$. In (a) the dashed line shows the BER performance when the true channel vector $\boldsymbol{h}$ in (4) is known.

TABLE I
PARAMETER SETTINGS FOR THE SIMULATIONS. THE CONVOLUTIONAL CODE AND DECODER HAS BEEN IMPLEMENTED USING [18].

Sampling time, $T_{\rm s}$	32.55 ns
CP length	4.69 μs / 144 $T_{\rm s}$
Subcarrier spacing	15 kHz
Pilot pattern	Equally spaced, QPSK
Modulation	QPSK
Subcarriers, N	1200
Pilots, M	100
OFDM symbols	1
Information bits	727
Channel interleaver	Random
Convolutional code	$(133, 171, 165)_8$
Decoder	BCJR algorithm [19]

independent and uniformly distributed random variables drawn from the continuous interval [0, 144 $T_{\rm s}$] (corresponding to the CP length). The kth nonzero component β_k conditioned on the delay τ_k has a zero-mean complex circular symmetric Gaussian distribution with variance $\sigma^2(\tau_k) = \langle|\beta_k|^2\rangle_{p(\beta_k|\tau_k)} = u\exp(-\tau_k/v)$ and parameters $u, v > 0$.[3]

To initialize the VMP algorithm we set $\langle\lambda\rangle_{q(\lambda)}$ and $\langle\gamma_l^{-1}\rangle_{q(\boldsymbol{\gamma})}$ equal to the inverse of the sample variance of $\boldsymbol{y}$ and the inverse number of columns L respectively. Furthermore, we let $c = d = 0$ in (25), which corresponds to the Jeffreys noninformative prior for λ. Once the initialization is completed, the algorithm sequentially updates the auxiliary pdfs $q(\boldsymbol{\alpha})$, $q(\boldsymbol{\gamma})$, $q(\boldsymbol{\eta})$, and $q(\lambda)$ until convergence is achieved. Obviously, $q(\boldsymbol{\eta})$ is only updated for VMP-3L, whereas for VMP-2L the entries in $\boldsymbol{\eta}$ are set to M. For both versions we select $\epsilon = 0$ and for VMP-3L we set $a_l = 1$ and $b_l = 10^{-6}$, $l = 1, \ldots, L$. Finally, the dictionary $\boldsymbol{\Phi}$ is specified by M pilot subcarriers and a total of $L = 200$ columns (corresponding to the choice $\tau_{\max} = 144\ T_{\rm s}$ and $\zeta \approx 1.4$ in (9)).

The VMP is compared to a classical OFDM channel estimator and two state-of-the-art sparse estimation schemes. Specifically, we use as benchmark the robustly-designed Wiener Filter (RWF) [22], the relevance vector machine (RVM) [10], [11],[4] and the *sparse reconstruction by separable approximation* (SpaRSA) algorithm [23].[5] The RVM is an EM algorithm based on the 2-L prior model of the student-t pdf over each α_l, whereas SpaRSA is a proximal gradient method for solving (2). In case of the SpaRSA algorithm the regularization parameter κ needs to be set. In all simulations, we let $\kappa = 2$, which leads to good performance in high signal-to-noise ratio (SNR) regime.

The performance is compared with respect to the resulting bit-error-rate (BER) and mean-squared error (MSE) of the estimate $\widehat{\boldsymbol{h}}$ versus the SNR (E_b/N_0). In addition, in order to quantify the necessary pilot overhead, we evaluate the MSE versus the number of available pilots M. Hence, in this setup M is no longer fixed as in Table I.

In Fig. 4(a) we compare the BER performance of the different schemes. We see that VMP-3L outperforms the other schemes across all the SNR range considered. Specifically, at 1 % BER the gain is approximately 2 dB compared to VMP-2L and RVM and 3 dB compared to SpaRSA and RWF. Also VMP-2L achieves lower BER in the SNR range 0 - 12 dB compared to RVM and across the whole SNR range compared to SpaRSA and RWF.

The superior BER performance of the VMP algorithm is well reflected in the MSE performance shown in Fig. 4(b). Again VMP-3L is a clear winner followed by VMP-2L. The bad MSE performance of the SpaRSA for low SNR is due to the difficulty in specifying a suitable regularization parameter κ across a large SNR range.

We next fix the ratio between received symbol power and noise variance to 15 dB[6] and evaluate the MSE versus number of available pilots M. The results are depicted in Fig. 4(c). Observe a noticeable performance gain obtained with VMP-3L. In particular, VMP-3L exhibits the same MSE performance as VMP-2L and RVM using only approximately 85 pilots, roughly half as many as VMP-2L and RVM. Fur-

[3]The parameter u is computed such that $\langle\sum_{k=1}^{K}|\beta_k(t)|^2\rangle_{p(\boldsymbol{\beta},\boldsymbol{\tau},K)} = 1$, where $p(\boldsymbol{\beta},\boldsymbol{\tau},K)$ is the joint pdf of the parameters of the channel model. In the considered simulation scenario, $\langle K\rangle_{p(K)} = 10$, $\tau_{\max} = 144\ T_{\rm s}$, and $v = 20\ T_{\rm s}$ (the decay rate).

[4]The software is available on-line at http://dsp.ucsd.edu/~dwipf/.

[5]The software is available on-line at http://www.lx.it.pt/~mtf/SpaRSA/

[6]Note that this value does not correspond with E_b/N_0 as represented in Fig. 4(a) and 4(b). The specific E_b/N_0 depends on the number of bits in an OFDM block, which in turn depends on the number of pilot symbols M.

thermore, VMP-3L, using this number of pilots, significantly outperforms SpaRSA and RWF using 200 pilots.

VII. Conclusion

In this paper, we proposed channel estimators based on sparse Bayesian learning. The estimators rely on Bayesian hierarchical prior modeling and variational message passing (VMP). The VMP algorithm effectively exploits the probabilistic structure of the hierarchical prior models and the resulting sparsity-inducing priors. Our numerical results show that the proposed channel estimators yield superior performance in terms of bit-error-rate and mean-squared error as compared to other existing estimators, including the estimator based on the ℓ_1-norm constraint. They also allow for a significant reduction of the amount of pilot subcarriers needed for estimating a given channel.

Acknowledgment

This work was supported in part by the 4GMCT cooperative research project funded by Intel Mobile Communications, Agilent Technologies, Aalborg University and the Danish National Advanced Technology Foundation. This research was also supported in part by the project ICT- 248894 Wireless Hybrid Enhanced Mobile Radio Estimators (WHERE2).

References

[1] R. Baraniuk, "Compressive sensing," *IEEE Signal Processing Magazine*, vol. 24, no. 4, pp. 118–121, July 2007.

[2] E. J. Candes and M. B. Wakin, "An introduction to compressive sampling," *IEEE Signal Process. Mag.*, vol. 25, no. 2, pp. 21–30, Mar. 2008.

[3] W. Bajwa, J. Haupt, A. Sayeed, and R. Nowak, "Compressed channel sensing: A new approach to estimating sparse multipath channels," *Proceedings of the IEEE*, vol. 98, no. 6, pp. 1058–1076, Jun. 2010.

[4] G. Taubock and F. Hlawatsch, "A compressed sensing technique for OFDM channel estimation in mobile environments: Exploiting channel sparsity for reducing pilots," in *Proc. IEEE Int. Conf. Acoustics, Speech and Signal Processing ICASSP 2008*, 2008, pp. 2885–2888.

[5] C. R. Berger, S. Zhou, J. C. Preisig, and P. Willett, "Sparse channel estimation for multicarrier underwater acoustic communication: From subspace methods to compressed sensing," *IEEE Trans. on Sig. Proc.*, vol. 58, no. 3, pp. 1708–1721, 2010.

[6] J. Huang, C. R. Berger, S. Zhou, and J. Huang, "Comparison of basis pursuit algorithms for sparse channel estimation in underwater acoustic OFDM," in *Proc. OCEANS 2010 IEEE - Sydney*, 2010, pp. 1–6.

[7] D. Shutin and B. H. Fleury, "Sparse variational Bayesian SAGE algorithm with application to the estimation of multipath wireless channels," *IEEE Trans. on Sig. Proc.*, vol. 59, pp. 3609–3623, 2011.

[8] R. Tibshirani, "Regression shrinkage and selection via the LASSO," *J. R. Statist. Soc.*, vol. 58, pp. 267–288, 1994.

[9] S. S. Chen, D. L. Donoho, Michael, and A. Saunders, "Atomic decomposition by basis pursuit," *SIAM Journal on Scientific Computing*, vol. 20, pp. 33–61, 1998.

[10] M. Tipping, "Sparse Bayesian learning and the relevance vector machine," *J. of Machine Learning Res.*, vol. 1, pp. 211–244, June 2001.

[11] D. Wipf and B. Rao, "Sparse Bayesian learning for basis selection," *IEEE Trans. on Sig. Proc.*, vol. 52, no. 8, pp. 2153 – 2164, aug. 2004.

[12] D. G. Tzikas, A. C. Likas, and N. P. Galatsanos, "The variational approximation for Bayesian inference," *IEEE Signal Process. Mag.*, vol. 25, no. 6, pp. 131–146, November 2008.

[13] N. L. Pedersen, D. Shutin, C. N. Manchón, and B. H. Fleury, "Sparse estimation using Bayesian hierarchical prior modeling for real and complex models," *submitted to IEEE Trans. on Sig. Proc.*, 2012, arXiv:1108.4324v1.

[14] M. Abramowitz and I. A. Stegun, *Handbook of Mathematical Functions with Formulas, Graphs, and Mathematical Tables*. Dover, 1972.

[15] F. R. Kschischang, B. J. Frey, and H. A. Loeliger, "Factor graphs and the sum-product algorithm," *IEEE Trans. on Information Theory*, vol. 47, no. 2, pp. 498–519, Feb 2001.

[16] J. Winn and C. M. Bishop, "Variational message passing," *J. Mach. Learn. Res.*, vol. 6, pp. 661–694, 2005.

[17] B. Jorgensen, *Statistical Properties of the Generalized Inverse Gaussian Distribution (Lecture Notes in Statistics 9)*. Springer-Verlag New York Inc, 1982.

[18] The iterative solutions coded modulation library. [Online]. Available: http://www.iterativesolutions.com

[19] L. Bahl, J. Cocke, F. Jelinek, and J. Raviv, "Optimal decoding of linear codes for minimizing symbol error rate," *IEEE Trans. on Inform. Theory*, vol. 20, no. 2, pp. 284–287, 1974.

[20] 3rd Generation Partnership Project (3GPP) Technical Specification, "Evolved universal terrestrial radio access (e-utra); base station (bs) radio transmission and reception," TS 36.104 V8.4.0, Tech. Rep., 2008.

[21] M. L. Jakobsen, K. Laugesen, C. Navarro Manchón, G. E. Kirkelund, C. Rom, and B. Fleury, "Parametric modeling and pilot-aided estimation of the wireless multipath channel in OFDM systems," in *Proc. IEEE Int Communications (ICC) Conf*, 2010, pp. 1–6.

[22] O. Edfors, M. Sandell, J.-J. van de Beek, S. K. Wilson, and P. O. Börjesson, "OFDM channel estimation by singular value decomposition," *IEEE Trans. on Communications*, vol. 46, no. 7, pp. 931–939, 1998.

[23] S. J. Wright, R. D. Nowak, and M. A. T. Figueiredo, "Sparse reconstruction by separable approximation," *IEEE Trans. on Sig. Proc.*, vol. 57, no. 7, pp. 2479–2493, 2009.

A.9 UWB Antenna Measurement Report

T. Pedersen, B. Uguen and M. Laaraiedh UWB Antenna Measurement Report. *Internal Measurement Report.*, June , 2012, Aalborg, Denmark.

Antenna Measurement Campaign at IETR, April, 2012

Troels Pedersen, Bernard Uguen, Stephane Avrillon,
Mohamed Laaraiedh, and Meriem Mhedhbi

June 28, 2012

Contents

1 Introduction

This report documents a two-day antenna measurement campaign performed at the IETR using the near field measurement chamber at INSA, Rennes, France, April 12&13, 2012. The objective of the campaign is to collect data for characterizing the variability of the radiation pattern of ultra wideband (UWB) antennas due to antenna structure and vicinity of the human body. In the measurement the human body is represented by a phantom of an arm.

The measurement campaign was planned and carried out by a team consisting of

- Prof. Bernard Uguen (IETR, University Rennes 1, France)
- Associate Prof Stephane Avrillon (IETR, University Rennes 1, France)
- Assistant Prof. Mohamed Laaraiedh (IETR, University Rennes 1, France)
- PhD Student Meriem Mhedhbi (IETR, University Rennes 1, France)
- Associate Prof. Troels Pedersen (NavCom, Aalborg University, Denmark)

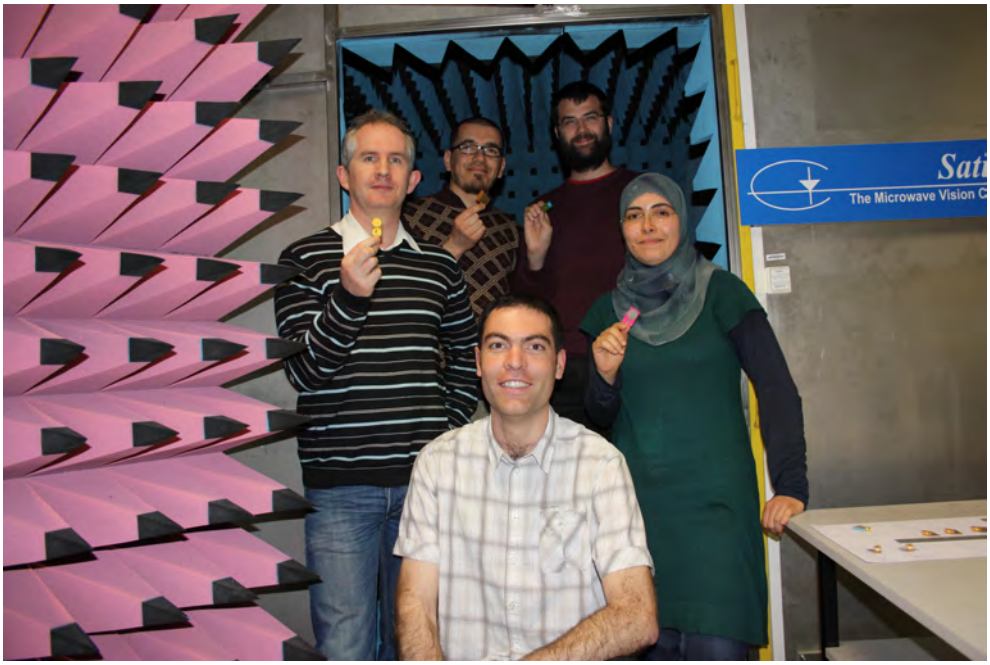

Figure 1.1: Measurement team after the completed measurement campaign.

2 Measurement Setup

The measurement campaign was carried out in the Satimo StarGate SG32 near field antenna measurement chamber at INSA. Information on Satimo equipment can be found in [1]. The measurement process is controlled by the Satimo equipent in an automized fashion: After mounting the antenna in the positioner, closing the chamber door, the antenna measurement data is collected automatically when started from the control computer.

2.1 Measurement Platform

The antennas and phantom were mounted on a platform custom-built for the measurement campaign (see Figure 2.2). It is dedicated to have antenna measurements in presence of phantom in different directions and distances from this antenna. The platform was made of dielectric with relative permittivity $\epsilon_r \approx 1$ such that the impact to the platform could be kept at a minimum. A distance scale on the bottom side of the platform was used to measure the position of the phantom in the groove. As can be seen in Figure 2.2, the holes in the platform were labeled for easy reference.

2.2 System for Antenna and Phantom Positioning System

A main cylinder stand is fixed with the StarGate positioner. A bottom washer and a top flange permits to fix the platform on the stand. A removable tube is inserted in the main cylindrical stand in order to fix the antenna.

- Main cylinder stand
  Material: Bottom part in Teflon, main cylinder in PA6 Nylon.
  Function: To fix the platform with the StarGate positioner at a suitable height (middle of the StarGate) seen in Figure 2.3.
- Bottom washer
  Function: To fix the platform with the StarGate positioner at a suitable height (middle of the StarGate)
  Function: To stabilize the platform.
- Platform
  Material: In Rohacell.
  Function: To place the phantom at different positions around the antenna (see Figure 2.4).
- Top flange
  Material: In white PVC.
  Function: To fix the platform (see Figure 2.5).
- Removable tube
  Material: In PVC.
  Function: To fix the antenna in the main cylinder (Figure 2.5).

Figure 2.1: The measurement platform placed in the anechoic chamber on Satimo positioner. The cross-shaped probes are also visible in the SG32 measurement arch.

Platform Fixing System

The platform is fixed on the main cylinder stand using the flange and a screw. The removable tube which is inserted into the main cylinder permits to fix the antenna connector using a small plastic screw. See Figure 2.6

Phantom Positioning Groove and Holes

The platform has two different phantom positioning capabilities:

- The groove allows a continous positioning from 10mm to 160mm, which is the distance measured from the bottom washer (see Figure 2.7).
- 21 positioning holes named with letters indicating the angle (A=45°, B=90°, C=135°, D=180°, E =225°, F=270°, and G=315°,) with re-

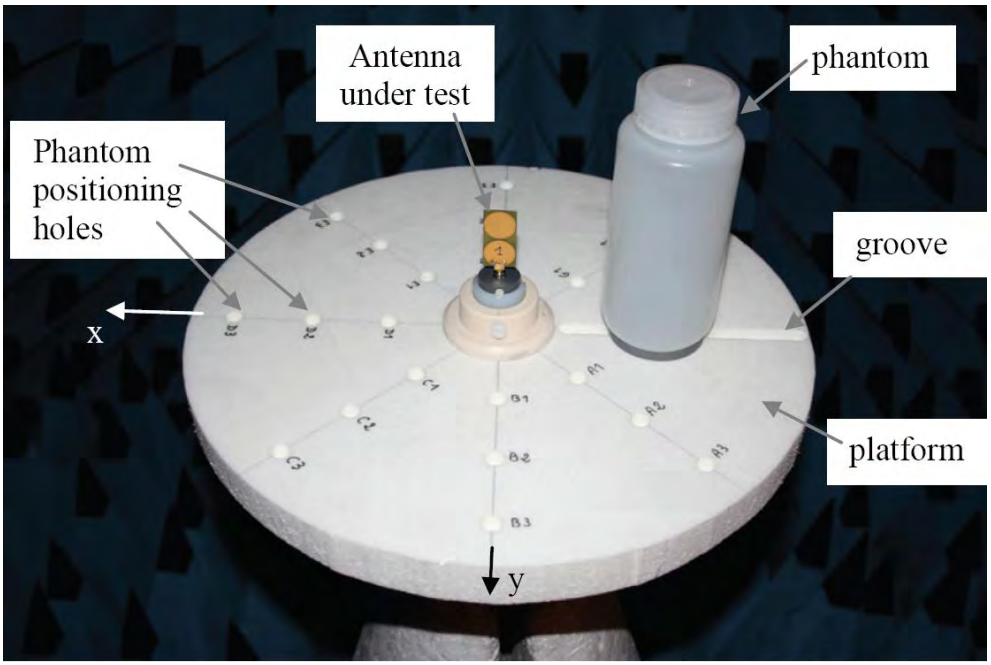

Figure 2.2: Measurement platform with coordinate system.

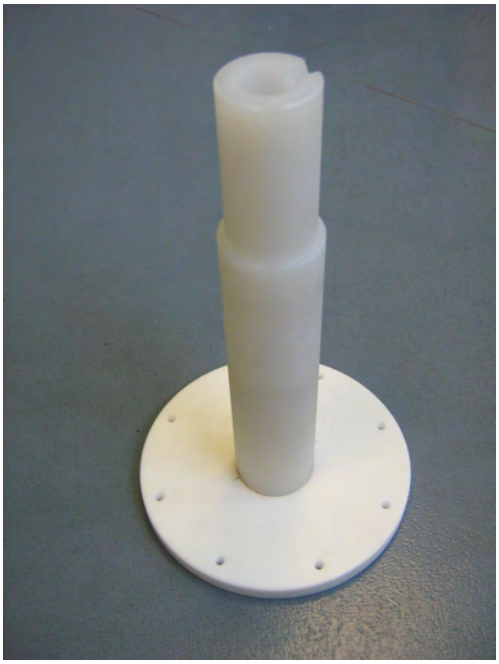

Figure 2.3: Main cylinder stand.

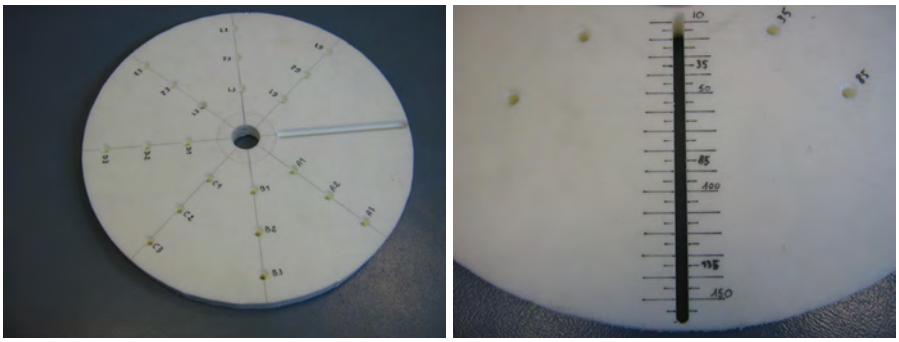

Figure 2.4: Photos of platform on two sides.

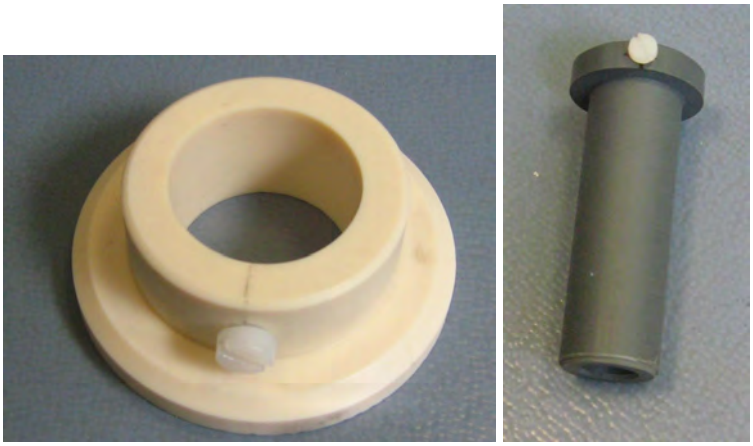

Figure 2.5: Photos of top flange (left) and removable tube (right).

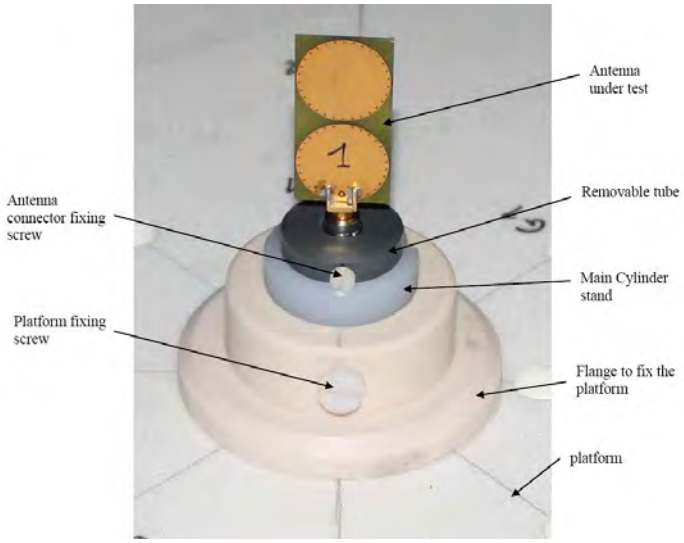

Figure 2.6: Detailed view of the platform and antenna fixing system.

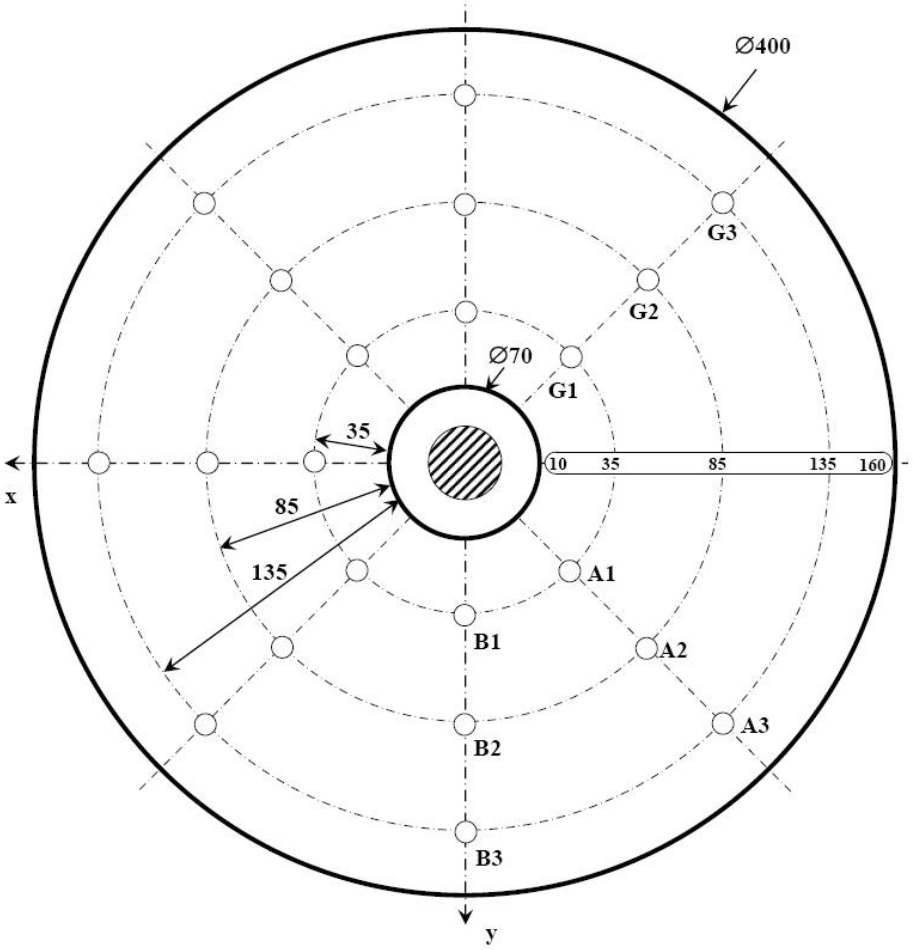

Figure 2.7: Detailed description of holes and groove positions.

spect to the groove and with numbers indicating the distance from the bottom washer (see Figure 2.7).

2.3 Phantom

The custom-built phantom (depicted in Figure 2.8) was a nearly cylindrical plastic bottle filled with MSL1800 phantom liquid. The size of the phantom was chosen to represent that of a human arm, while still being light enough for the platform to support it. The bottle was fitted with a screw in the bottom to allow for mounting on the platform groove or holes.

2.4 Antennas

To allow for statistical description of the radiation pattern, we measured radiation patters of in total 17 UWB antennas. The antennas are listed in Table 2.1

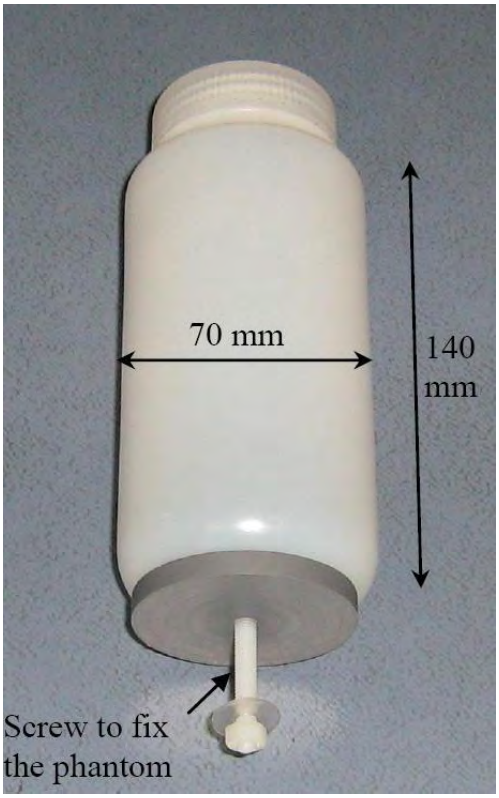

Figure 2.8: Phantom used in the measurement.

and depicted in Figure 2.9. The antennas were photographed one by one next to a ruler for possible later use in publication. Also the S_{11} pattern were measured using a network analyzer. The antennas are chosen to have roughly similar characteristics, but to represent different kinds (see Table 2.1). Some antennas (Th1–Th4 and F1&F2) were of identical type.

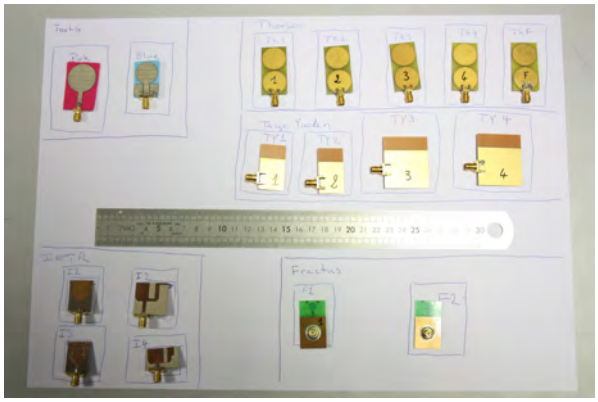

Figure 2.9: The 17 UWB antennas used in the measurement. To keep track of the antennas during measurement they were stored (when not in use) on a marked sheet of paper with the names, photo filename and drawings.

Label	Manufacturer	Photo	S_{11}-file	Comment
Th1	Thomson	IMG_2856.JPG	th1.s1p	[2]
Th2	Thomson	IMG_2857.JPG	th2.s1p	[2]
Th3	Thomson	IMG_2858.JPG	th3.s1p	[2]
Th4	Thomson	IMG_2859.JPG	th4.s1p	[2]
ThF	Thomson	IMG_2860.JPG	thF.s1p	[2] Notch filtering antenna
TY1	Tayo Yuden	IMG_2861.JPG	TY1.s1p	[3]
TY2	Tayo Yuden	IMG_2862.JPG	TY2.s1p	[3]
TY3	Tayo Yuden	IMG_2863.JPG	TY3.s1p	[3]
TY4	Tayo Yuden	IMG_2864.JPG	TY4.s1p	[3]
F1	Fractus	IMG_2866.JPG	F1.s1p	[4]
F2	Fractus	IMG_2868.JPG	F2.s1p	[4]
TexPink	IETR	IMG_2869.JPG	TexPink.s1p	Textile antenna, Nacer, Unpublished
TexBlue	IETR	IMG_2870.JPG	TexBlue.s1p	Textile antenna, Nacer, Unpublished
I1	IETR	IMG_2871.JPG	I1.s1p	Monopole
I2	IETR	IMG_2872.JPG	I2.s1p	[5]
I3	IETR	IMG_2873.JPG	I3.s1p	As I1, but with a frequency notch
I4	IETR	IMG_2874.JPG	I4.s1p	Derived from I2, Unpublished

Table 2.1: Antennas used in the experiments.

3 Measurement Series

The complete measurement campaign consists of four measurement series. Each series consists of a number of runs. A measurement run is defined as one antenna measurement resulting in one data file.

A photo was taken of the platform and antenna prior to each measurement run. The photos where taken using a handheld camera, but we strived at obtaining the same view every time to allow us to use the photos as a kind of "stop-motion" movie of the phantom settings for S2 and S3.

Naming convention: Series X of Run Y is named SXRY, e.g. S1R5 is Series 1 Run 5.

3.1 Measurement Series S1

The primary focus of S1 is to collect measurement data of the antennas listed in Table 2.1. The antennas were one by one placed in the measurement platform without the phantom.

S1R1–S1R17: Measurements of antennas are listed in Table 2.1.

3.2 Measurement Series S2

The purpose of this measurement series is to measure how the antenna response varies in the presence of the phantom at various antenna-phantom distances. Antenna Th1 was used for all runs of series S2. The phantom was placed in the groove.

S2R1 Re-calibration without phantom (same setting and antenna as in S1R1).

S2R2–S2R21 Measurement with phantom at different radial distances using the groove. We start by minimum distance and increase the distance in steps of 5 mm.

3.3 Measurement Series S3

The purpose of S3 is to measure how the antenna response varies with phantom-antenna angle and distance. Antenna Th1 was used for all runs of series S3. The phantom-antenna angle and distance varies using the holes, and the corresponding three positions in the grove.

S3R1 Re-calibration without phantom (same setting and antenna as in S1R1).

S3R2–S3R4 Phantom placed in the grove at distances matching the distances of the holes.

S3R5–S3R25 The phantom is placed in the holes.

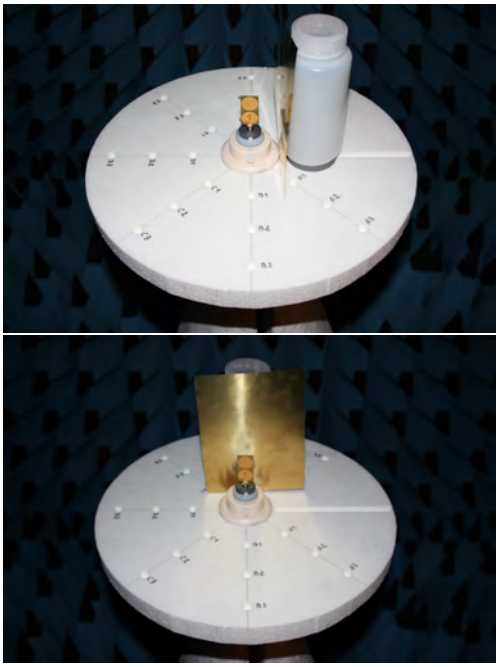

Figure 3.1: Setup for S4R1 (left) and S4R2 (right).

3.4 Measurement Series S4

The measurement series S4 is an auxiliary measurement series containing some measurements with the common purpose to ensure the integrity of the data after postprocessing and to evaluate the repetition error of the measurement technique.

S4R1–S4R2 Metal screen fixed on phantom. This gives a strongly directive pattern with main lobe opposite to the screen, which may be used to ensure that we can interpret the angles recorded by Satimo unambiguously and transform these into the defined coordinate system on the platform. S4R1 with the phantom placed in the groove at distance 35 mm, and S4R2 with the phantom in position F1 (see Figure 3.1).

S4R3–S4R6 Changing the antenna orientation with respect to the platform. Notice that S4R3 is with the same orientation as used in all measurement runs, except S4R4, S4R5, and S4R6. Thus S4R3 may also be used to compare repeatability of the calibration measurement for antenna Th1.

S4R7–S4R8 The antenna was unmounted, then mounted in the platform again in the standard orientation and then measured without the phantom. These two runs will, together with the S1R1, S2R1, S3R1 and S4R3 allow for evaluation of the repeatability of the measurement procedure.

S4R9 The measurement was performed with the filled and empty phantom, i.e., with the plastic container alone without phantom liquid. This allows to evaluate the impact of the plastic container itself.

4 Measurement Log

During the measurement campaign, the setup and filenames of photos and measurement data were recorded in an Excel file which served as a measurement log. In addition, during the measurements, handwritten notes documented the procedure.

4.1 Comment Measurement Day 1: April 12

The S_{11} parameters were measured for the 17 antennas using a vector network analyzer prior to the measurements in the near field chamber. The measurement equipment was set up and performed several test runs. Some startup problems were sorted out with the help of Jerome Sol.

Measurements S1 started after setup and instruction at 16:00h and ended at approximately 18:00. The duration of each measurement run was 6 to 7 min. The start time of each run was entered in the measurement log. Photos of the setup in the platform were taken before each measurement run and the filename of the photo was entered in the log. Measurement data was exported in ASCII txt format in a .trx file for easy access. The filenames of photos and antenna data files are all entered in the measurement log.

Measurement apparatus is left ON overnight to avoid startup difficulties on Day 2.

4.2 Measurement Day 2: April 13

Overnight, Bernard checked some of the data during the evening to see if there should be any problems with the data. He detected a problem with the definition of the coordinate system used by the Satimo equipment. Apparently the Satimo chamber uses a left-handed coordinate system with strange ranges for the co-elevation and azimuth angles. To eliminate any ambiguity in the use of the data it was decided to perform the runs S4R1 and S4R2, where a metal screen ensured an antenna radiation pattern with a strong main-lobe in a controlled direction. The measurements continued using the same format as we started to keep data consistent. The data was transformed into a natural right-handed coordinate system.

The measurement data was transferred from the measurement computer. Also, the probe-corrected near field data was exported and stored in ASCII format. This data may be later transformed using a custom algorithm to perform the near field to far field transformation.

4.3 Printout of Logfile

Series	Run	Antenna	Phantom	Phant. pos.	Phant. dist.	Photo file	Data file	Date	Start time	Notes
1	1	Th1	No			IMG_2839	S1R1	04/12/12	15:55	Mohamed at the log
1	2	Th2	No			IMG_2840	S1R2	04/12/12	16:03	
1	3	Th3	No			IMG_2841	S1R3	04/12/12	16:09	
1	4	Th4	No			IMG_2842	S1R4	04/12/12	16:18	
1	5	ThF	No			IMG_2843	S1R5	04/12/12	16:24	
1	6	TY1	No			IMG_2844	S1R6	04/12/12	16:30	
1	7	TY2	No			IMG_2845	S1R7	04/12/12	16:35	post processing re-done due to export error
1	8	TY3	No			IMG_2846	S1R8	04/12/12	16:41	
1	9	TY4	No			IMG_2847	S1R9	04/12/12	16:52	
1	10	F1	No			IMG_2848	S1R10	04/12/12	16:57	
1	11	F2	No			IMG_2849	S1R11	04/12/12	17:04	
1	12	TexPink	No			IMG_2850	S1R12	04/12/12	17:11	
1	13	TexBlue	No			IMG_2851	S1R13	04/12/12	17:17	
1	14	I1	No			IMG_2852	S1R14	04/12/12	17:24	
1	15	I2	No			IMG_2853	S1R15	04/12/12	17:30	
1	16	I3	No			IMG_2854	S1R16	04/12/12	17:36	
1	17	I4	No			IMG_2855	S1R17	04/12/12	17:42	
4	1	Th1	See note	groove	40	IMG_2875	S4R1	04/13/12	09:27	metallic screen attached to empty phantom
4	2	Th1	See note	F1		IMG_2876	S4R2	04/13/12	09:37	metallic screen attached to empty phantom
2	1	Th1	No			IMG_2877	S2R1	04/13/12	09:49	reference measurement run
2	2	Th1	Yes	groove	30	IMG_2878	S2R2	04/13/12	09:59	
2	3	Th1	Yes	groove	35	IMG_2879	S2R3	04/13/12	10:08	
2	4	Th1	Yes	groove	40	IMG_2880	S2R4	04/13/12	10:14	break after this run
2	5	Th1	Yes	groove	45	IMG_2881	S2R5	04/13/12	10:48	
2	6	Th1	Yes	groove	50	IMG_2882	S2R6	04/13/12	10:55	
2	7	Th1	Yes	groove	55	IMG_2883	S2R7	04/13/12	11:03	
2	8	Th1	Yes	groove	60	IMG_2884	S2R8	04/13/12	11:08	
2	9	Th1	Yes	groove	65	IMG_2885	S2R9	04/13/12	11:16	
2	10	Th1	Yes	groove	70	IMG_2886	S2R10	04/13/12	11:22	
2	11	Th1	Yes	groove	75	IMG_2887	S2R11	04/13/12	11:28	
2	12	Th1	Yes	groove	80	IMG_2888	S2R12	04/13/12	11:34	
2	13	Th1	Yes	groove	85	IMG_2889	S2R13	04/13/12	11:40	
2	14	Th1	Yes	groove	90	IMG_2890	S2R14	04/13/12	11:46	
2	15	Th1	Yes	groove	95	IMG_2891	S2R15	04/13/12	12:59	Reboot of Satimo needed only Bernard, Troels and Stephane present, Troels at the log
2	16	Th1	Yes	groove	100	IMG_2892	S2R16	04/13/12	13:05	Only Bernard, Troels and Stephane present
2	17	Th1	Yes	groove	105	IMG_2893	S2R17	04/13/12	13:12	Only Bernard, Troels and Stephane present
2	18	Th1	Yes	groove	110	IMG_2894	S2R18	04/13/12	13:19	Only Bernard, Troels and Stephane present
2	19	Th1	Yes	groove	115	IMG_2895	S2R19	04/13/12	13:25	Only Bernard, Troels and Stephane present
2	20	Th1	Yes	groove	120	IMG_2896	S2R20	04/13/12	13:31	Meriem joined again
2	21	Th1	Yes	groove	125	IMG_2897	S2R21	04/13/12	13:27	Mohamed joined again
2	22	Th1	Yes	groove	130	IMG_2898	S2R22	04/13/12	13:44	
2	23	Th1	Yes	groove	135	IMG_2899	S2R23	04/13/12	13:51	

Series	Run	Antenna	Phantom	Phant. pos.	Phant. dist.	Photo file	Data file	Date	Start time	Notes
3	1	Th1	No			IMG_2900	S3R1	04/13/12	14:23	Mohamed at the log
3	2	Th1	Yes	groove	35	IMG_2901	S3R2	04/13/12	14:29	
3	3	Th1	Yes	groove	85	IMG_2902	S3R3	04/13/12	14:36	
3	4	Th1	Yes	groove	135	IMG_2903	S3R4	04/13/12	14:42	
3	5	Th1	Yes	A1		IMG_2904	S3R5	04/13/12	14:48	
3	6	Th1	Yes	A2		IMG_2905	S3R6	04/13/12	14:54	
3	7	Th1	Yes	A3		IMG_2906	S3R7	04/13/12	15:00	
3	8	Th1	Yes	B1		IMG_2907	S3R8	04/13/12	15:07	
3	9	Th1	Yes	B2		IMG_2908	S3R9	04/13/12	15:13	
3	10	Th1	Yes	B3		IMG_2909	S3R10	04/13/12	15:19	
3	11	Th1	Yes	C1		IMG_2910	S3R11	04/13/12	15:26	
3	12	Th1	Yes	C2		IMG_2911	S3R12	04/13/12	15:32	
3	13	Th1	Yes	C3		IMG_2912	S3R13	04/13/12	15:38	
3	14	Th1	Yes	D1		IMG_2913	S3R14	04/13/12	15:44	
3	15	Th1	Yes	D2		IMG_2914	S3R15	04/13/12	15:50	
3	16	Th1	Yes	D3		IMG_2915	S3R16	04/13/12	15:56	
3	17	Th1	Yes	E1		IMG_2916	S3R17	04/13/12	16:03	
3	18	Th1	Yes	E2		IMG_2917	S3R18	04/13/12	16:10	
3	19	Th1	Yes	E3		IMG_2918	S3R19	04/13/12	16:16	
3	20	Th1	Yes	F1		IMG_2919	S3R20	04/13/12	16:23	
3	21	Th1	Yes	F2		IMG_2920	S3R21	04/13/12	16:29	
3	22	Th1	Yes	F3		IMG_2921	S3R22	04/13/12	16:36	
3	23	Th1	Yes	G1		IMG_2922	S3R23	04/13/12	17:01	
3	24	Th1	Yes	G2		IMG_2923	S3R24	04/13/12	17:07	
3	25	Th1	Yes	G3		IMG_2925	S3R25	04/13/12	17:14	unfocused photo (IMG_2924)
4	3	Th1	No			IMG_2926	S4R3	04/13/12	17:27	Ant. Orient. B
4	4	Th1	No			IMG_2927	S4R4	04/13/12	17:33	Ant. Orient. D, antenna disconnected then connected
4	5	Th1	No			IMG_2928	S4R5	04/13/12	17:40	Ant. Orient. F, antenna disconnected then connected
4	6	Th1	No			IMG_2929	S4R6	04/13/12	17:47	Ant. Orient. Groove, antenna disconnected then connected
4	7	Th1	No			IMG_2930	S4R7	04/13/12	17:54	Another reference meas. Ant. Orient. B, antenna disconnected then connected
4	8	Th1	Yes	groove	35	IMG_2931	S4R8	04/13/12	18:00	Empty Phantom
										Finished at 18:10

5 Postprocessing and Organization of Measurement Data Files

As the collected data is post-processed to transform the coordinate system into a standard right-handed coordinate system with co-elevation $0 \geq \theta \geq \pi$ and azimuth $0 \geq \phi > 2\pi$. The data which comes out the near field to far field transformation are expressed in a coordinate system which is strongly related to the near field chamber. The data stored in the Matlab files have been processed to be expressed in a natural spherical coordinate system.

The transformation from chamber coordinate system (1) to the natural spherical coordinate system (2) (materialized in the near field in Figure 5.1) can be expressed as follows:

$$\begin{aligned} \theta_2 &= |\theta_1| \\ \phi_2 &= \phi_1 + (1 - \text{sign}(\theta_1))\frac{\pi}{2} \end{aligned}$$

The effect of this peculiar angular transformation for a given frequency index is illustrated in Figure 5.2.

5.1 Organization of the Data

The data are gathered in the following directories:

- **NFTRX**: In this directory we have the near field measurement files in the `trx` format. The format provide a preamble defining the the data columns in the second part of the file. The data columns are in this case, the frequency band and the sampling frequency, theta and phi ranges and the field component. The data is the measured output of each probe of the SG32 after calibration done by the measurement computer. This information is then post-processed using the near field to far field transform in order to get an ascii `trx` file containing the whole radiation information in the far field of the antenna. The `trx` files can be used for validation of customized near field to far field transform if later desired.
- **FFTRX**: This directory includes the `trx` files of the far field data as exported from the control computer.
- **Matfile**: This directory contains Matlab files of the different measurements series and runs. Each Matlab file is created from a corresponding python dictionary structure giving all the information about measurement series and runs :
  - Circumstance: Series and Run numbers, date and Start time of the run
  - Antenna field data : AntennaName, phi, theta, Ftheta, Fphi and frequency range

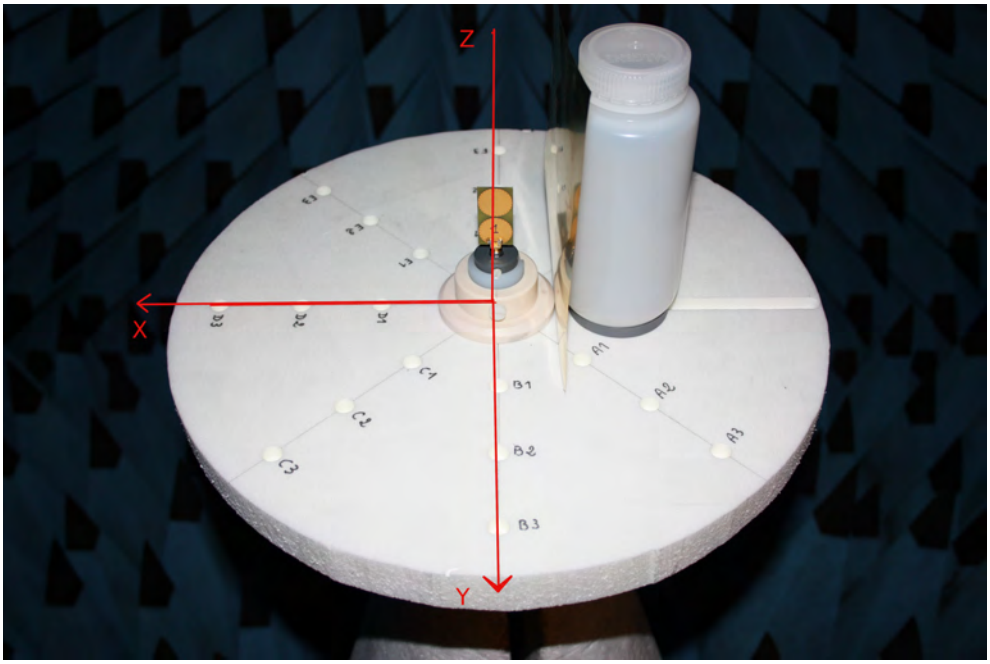

Figure 5.1: Natural coordinate system (2) represented in the Near Field Chamber - Photo Serie 4 Run 1

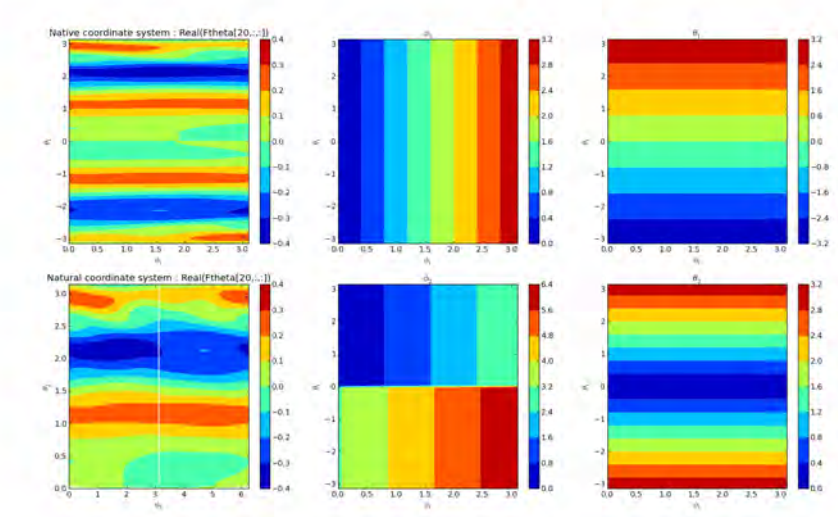

Figure 5.2: Effect of the coordinate system transformation, file S1R1.trx - frequency index 20

  - Related files: Photofile and Datafile
  - Observation: some Notes are included and the presence or absence of the Phantom is mentioned

- **S11**: This directory includes the S11 parameters of the 17 antennas used during the measurement campaign.
- **Documentation**: This report and various documents related to the near field chamber.
- **PhotosVideos**: The set of photos and videos related to this measurement campaign.

5.2 Python Code to Transform Far Field .trx to Matlab File : `parsedata.py`

```
import scipy as sp
import scipy.io as  io
import numpy as np
import re

#
#  Measurement camapaign 11 12 April 2012
#
#  This program transforms the data from the native SATIMO
#  .trx format to a .mat file including meta data extracted
#  from the measurement logfile
#
#  Run this program in the directory FFTRX
#  The directory must contain the MeasurementLog.csv file
#

fd    = open('MeasurementLog.csv','r')
lines = fd.readlines()
vt = []
for li in lines:
    u = li.replace("\"",'')
    t = u.split(',')
    vt.append(t)
#
# Entry keys
#
keys = ['Serie','Run','AntennaName','Phantom','PhantomPosition',
        'PhantomDistance','PhotoFile','DataFile','Date','StartTime',
        'Notes','freq','theta','phi','Ftheta','Fphi']
#
# creating a list of dictionnaries
```

```
#
for t in vt[2:-1]:
    entry  = t[7]
    d      = {}
    d[entry] = {}
    d[entry][keys[0]] = eval(t[0])
    d[entry][keys[1]] = eval(t[1])
    d[entry][keys[2]] = t[2]
    d[entry][keys[3]] = t[3]
    if t[4]!='':
      d[entry][keys[4]] = t[4]
    if t[5]!='':
        d[entry][keys[5]] = eval(t[5])
    d[entry][keys[6]] = t[6]
    d[entry][keys[7]] = t[7]
    d[entry][keys[8]] = t[8]
    d[entry][keys[9]] = t[9]
    d[entry][keys[10]] = t[10]
#-------------------------------------------------
#
#  Start parsing the trx file
#
#-------------------------------------------------
    filetrx  = t[7]+'.trx'
    pattern  = """^.*\t.*\t.*\t.*\t.*\t.*\t.*$"""
#
#  1) Open Read Close trx file
#
    fd       = open(filetrx,'r')
    data     = fd.read().split('\r\n')
    fd.close()
#
#  2 ) Detect data start ( end of header)
#
    k        = 0
    while re.search(pattern,data[k]) is None :
        k = k+1
#
#  3) Cleaning Splitting and str -> float
#
    data = data[k:]
    N = len(data)
    del data[N-1]
    r        = '\t'.join(data)
    r.replace('␣','')
    data     = np.array(r.split()).astype('float')
```

```
#
#
#  4) Reading reshaping and reorganizing the data
#
    ntheta = 181
    nphi = 90
    nf  = 104
    N   = nf*nphi*ntheta
    data   = data.reshape(N,7)

    F      = data[:,0]
    PHI    = data[:,1]
    THETA  = data[:,2]
    Fphi   = data[:,3]+data[:,4]*1j
    Ftheta = data[:,5]+data[:,6]*1j

    Fphi    = Fphi.reshape((nf,nphi,ntheta))
    Ftheta  = Ftheta.reshape((nf,nphi,ntheta))
    Tf      = F.reshape((nf,nphi,ntheta))

    Fphi    = Fphi.swapaxes(1,2)
    Ftheta  = Ftheta.swapaxes(1,2)
    Tf      = Tf.swapaxes(1,2)

    freq    = Tf[:,0,0]
#
#  5) Transformation from the measurement base coordinate system
#      to a natural coordinate system
#
#      x axis : When looking to the measurement arch from the front,
#               a vector going from the arch origin to the left
#      y axis : When looking to the measurement arch from the front,
#               a vector going from the arch origin to the observer
#      z axis : When looking to the measurement arch from the front,
#               a vector going from the arch origin to the top
#
#   The following lines implement the transformation between
#   the two cpoordinates system
#
    A1 = Fphi[:,91:181,:]
    A2 = Fphi[:,0:90,:]
    A3 = np.zeros((104,1,180))*1j
    A3[:,0,0:90]    = -Fphi[:,90,:]
    A3[:,0,90:180]  =  Fphi[:,90,:]
    A4   = np.concatenate((A1,A2[:,::-1,:]),axis=2)
    Fphi = np.concatenate((A3,A4),axis=1)
```

```
    B1   = Ftheta[:,91:181,:]
    B2   = Ftheta[:,0:90,:]
    B3   = np.zeros((104,1,180))*1j
    B3[:,0,0:90]    = -Ftheta[:,90,:]
    B3[:,0,90:180]  =  Ftheta[:,90,:]
    B4  = np.concatenate((B1,B2[:,::-1,:]),axis=2)
    Ftheta = np.concatenate((B3,B4),axis=1)
#
#  angular bases
#
    theta = np.linspace(0,np.pi,91)
    phi   = np.linspace(0,2*np.pi,180,endpoint=False)

#
# Appending data to the Matlab structure
#
    d[entry][keys[11]] = freq
    d[entry][keys[12]] = theta
    d[entry][keys[13]] = phi
    d[entry][keys[14]] = Ftheta
    d[entry][keys[15]] = Fphi

    filemat  = t[7]+'.mat'
    print 'Creating ',filemat
    io.savemat(filemat,d)
```

6 Known Error Sources

- We estimate the displacement of the phantom in the groove is accurate to $\pm$ 2 mm.
- We estimate that the phantom positions in the holes, is accurate to $\pm$ 1 mm
- The SMA connectors of the antennas were tightened manually without control of the torque. However, the connector repeatability can be checked by runs S1R1, S2R1, S3R1, S4R3, S4R7, and S4R8.
- The reference plane of the far field plane is delayed. A proper application of an electrical delay can be applied to compensate this effect which can be observed in and estimated from the data set.

7 Acknowledgements

We are grateful to Jerome Sol who helped sorting out some technical difficulties during the measurement campaign. We are also grateful to Laurent Crosnier and Christophe Guitton who built the measurement platform in a very short period of time. Thank you for that.

This work was performed in the framework of the *WHERE2* (ICT-248894) project, which is funded by the European Commission and in the framework of the french ANR Project CORMORAN.

Bibliography

[1] Satimo, “Product Sheet SG32,” Satimo, Tech. Rep., 2010. [Online]. Available: http://www.satimo.com/content/products/sg-32

[2] E. Gueguen, F. Thudor, and P. Chambelin, “A low cost UWB printed dipole antenna with high performance,” in *IEEE Int. Conf. Ultra-Wideband, 2005.*, Sept. 2005, pp. 89–92.

[3] T. Yuden, “3.1 – 8GHz Multilayer Monopole Antenna (for UWB , WiMAX), AH 086M555003,” Tayo Yuden, Tech. Rep., Sept. 2011.

[4] Fractus, “Fractus Media+ UWB Chip Antenna, P/N: FR05-S1-P-0-107,” Fractus, Tech. Rep., 2011. [Online]. Available: http://www.fractus.com/sales_documents/FR05-S1-P-0-107/DS_FR05-S1-P-0-107.pdf

[5] Z. N. Chen, T. S. P. See, and X. Qing, “Small Printed Ultrawideband Antenna With Reduced Ground Plane Effect,” *IEEE Trans. Antennas Propagat.*, vol. 55, no. 2, pp. 383–388, Feb. 2007.

A.10 UWB Measurement and Simulation Report for the Verification of the Band-divided UWB Ray Tracing Method

M.Raspopoulos, M. Tziakouris and S.Stavrou Band-Divided UWB Ray Tracing Method Verification. *Internal Report*, June , 2012, Sigint Solutions Ltd., Cyprus.

Band-Divided UWB Ray Tracing Method Verification, June, 2012

Marios Raspopoulos, Marios Tziakouris, Stavros Stavrou

June 22, 2012

Contents

1 Introduction

This report describes the simulation setup and the UWB measurement campaign performed at Sigint Solutions premises in order to verify the Band-Divided Ray Tracing method implemented to convert Sigint Solutions Ray Tracing Simulator (*3DTruEM*) to Utra-WideBand (UWB).

The algorithm which is shown in Figure 1.1 goes like this:

1. Firstly the UWB spectrum is split into narrow sub-bands which would allow conventional narrowband Ray-Tracing techniques to be used in order to calculate the power delay profile of the impulse responses.

2. Then, for each of these impulse responses a Fourier Transform is performed to calculate the narrowband channel frequency response of the channel. A filter is used to filter out the sub-band of interest

3. The filtered individual sub-band frequency responses are combined in order to obtain the UWB channel frequency response

4. Inverse Fourier Transform is performed on the UWB channel frequency response to obtain the UWB impulse response.

The method which has been implemented in *MATLAB* reads the Impulse Responses (IR) of each narrowband simulation obtained using *3DTruEM*, combines them using the algorithm described above and generates an UWB Impulse Response. Depending on the required bandwidth of the UWB simulation the band is split into a number of sub-bands of narrower bandwidth in each of which the characteristics of the antennas and electrical parameters are assumed constant.

The measurement campaign was planned and carried out in the the basement of Sigint Solutions Premises by a team consisting of

- Dr Marios Raspopoulos. (Sigint Solutions , Cyprus)
- Dr. Stavros Stavrou. (Sigint Solutions , Cyprus)
- Mr. Marios Tziakouris. (Sigint Solutions , Cyprus)

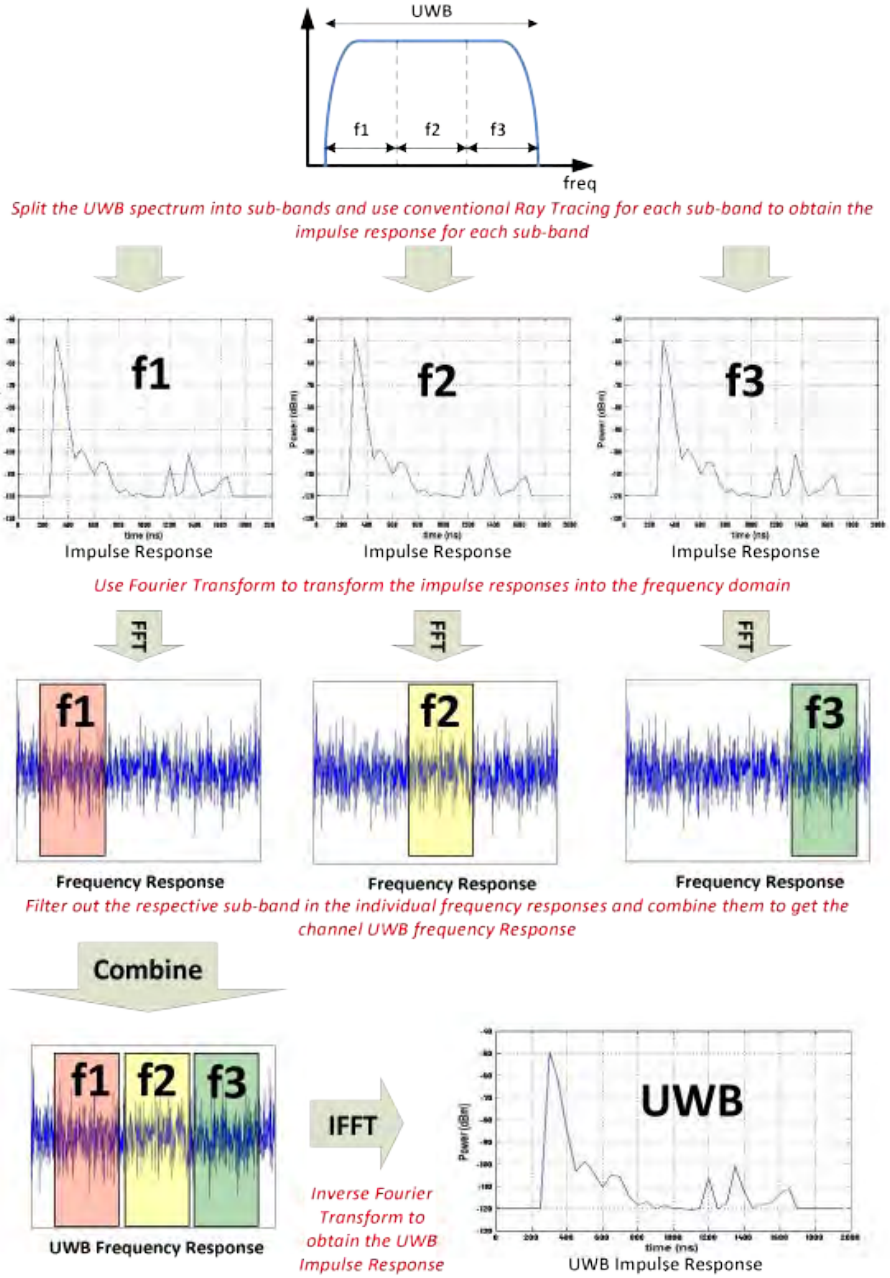

Figure 1.1: UWB Ray Tracing Algorithm

2 Simulations

As mentioned in the Introduction the developed UWB method acts as an add-on module to the existing Ray Tracing Simulator developed by Sigint Solutions (*3DTruEM*).

2.1 3DTruEM Simulator

3DTruEM is a 3D Ray Tracing Simulator developed by Sigint Solutions Ltd. 3DTruEM calculation engine uses a Ray Tracing algorithm offering improved accuracy and efficiency. It utilises the 3D electromagnetic (EM) formulation of reflection, refraction and diffraction based on the Universal Theory of Diffraction (UTD), to provide accurate site-specific radio propagation predictions for a wide range of wireless communication systems. The 3D environment description can be defined by means of a built-in 3D-CAD application or by importing standard DXF files (see Figure 2.1) . It offers the ability to define the receiver and transmitter antenna characteristics from a wide range of standard antennas but also the flexibility to import a custom-made antenna by importing its 3D radiation pattern/characteristics including also its polarisation characteristics (see Figure 2.2). In addition to its sophisticated algorithm that significantly improves speed, 3DTruEM also offers the ability of running a distributed-parallel multi-threaded simulation on a cluster of computers.

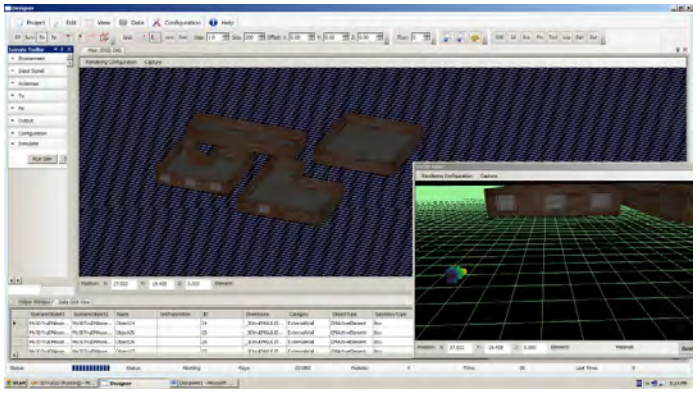

Figure 2.1: 3DTruEM environment designer.

One of the great features supported by 3DTruEM is its ability to calculate the electric field in every individual grid location in the entire specified 3D domain instead of a single plane or route as shown in Figure 2.3. The great thing is that this computation is done at no extra simulation time overhead. 3DTruEM offers the ability to export all the results and manipulate them in MATLAB. This includes signal strength, Power Delay Profile (PDP) or impulse response, Angle of Arrival (AoA) and Angle of Departure (AoD) of the individual ray components received by each receiver.

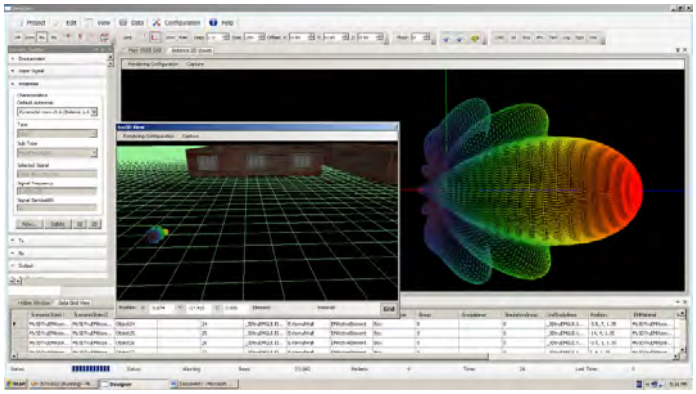

Figure 2.2: 3DTruEM antenna designer/viewer (Pyramidal Horn Example).

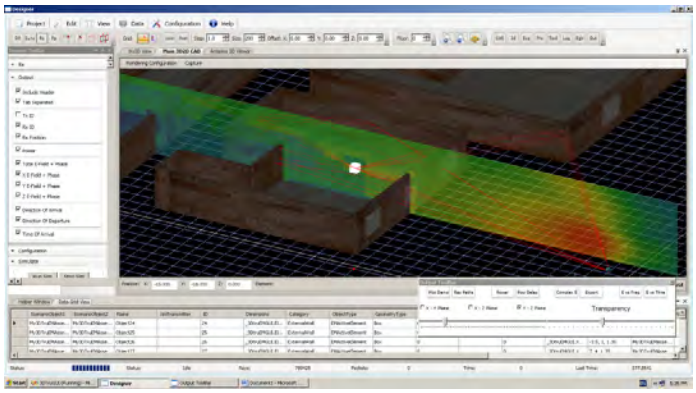

Figure 2.3: 3DTruEM antenna 3D results.

2.2 Simulation Setup

To test the method the basement of Sigint Solution Premises (illustrated in 2.4) has been modeled and simulated using *3DTruEM*. This environment was selected because of its simplicity, it does not have any low stationary clutter such as furniture and most of the walls are made of concrete, brick, metal and wood which means that only few electrical parameters need to be defined into the simulation. Figure 2.5 shows the 3D geometrical description of this environment as it has been imported into *3DTruEM*. The figure also depicts the locations of the 6 Transmitters and 7 Receivers that have been defined into the simulation. These TX and RX locations have been selected in such a way as to provide both Line of Sight (LoS) and Non Line of Sight (NLoS) situations.

The UWB bandwidth of $1.5GHz$ (3.1-4.6GHz) has been split into 15 sub-bands of $100MHz$. It has been assumed that throughout the whole bandwidth of investigation the complex electrical permittivity of the facets defined in the 3D model of environment has a constant value. In practice, this is not the case since different materials have different parameters and different frequency selectivity at different frequency bands. The parameters used are tabulated in

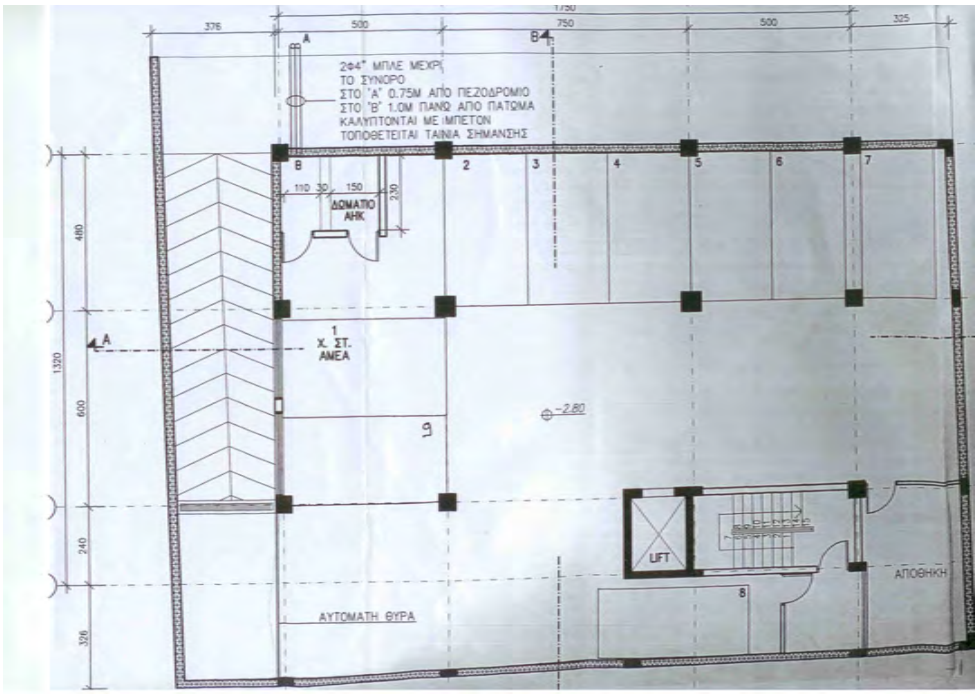

Figure 2.4: Measurement Environment Blueprints

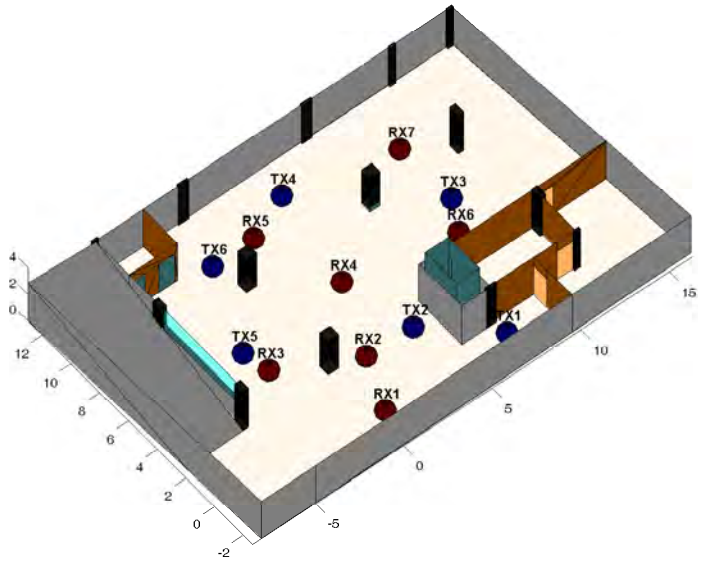

Figure 2.5: 3D Geometrical Model of the Environment - Input in *3DTruEM*

Table 2.1: Complex Permittivity ($\epsilon = \epsilon' + j\epsilon''$) for the facets of the environment under investigation

	ϵ'	ϵ''	Thickness (meters)
Concrete	8	-2	0.5
Brick	3	-0.8	0.1
Wood	2.5	-0.03	0.08
Metal	1	-100000	0.1
Glass	19	-0.1	0.05

Table 2.1. For the transmitters and receivers shown in Figure 2.5 which have been set at a height of $1.3m$ we have used *Fractus* UWB antennas. The antenna patterns at various frequencies as modeled into *3DTruEM*, are shown in Figure 2.6. They have been These 3D antenna pattern has been calculated from their vertical and horizontal cuts using classical antenna interpolation techniques.

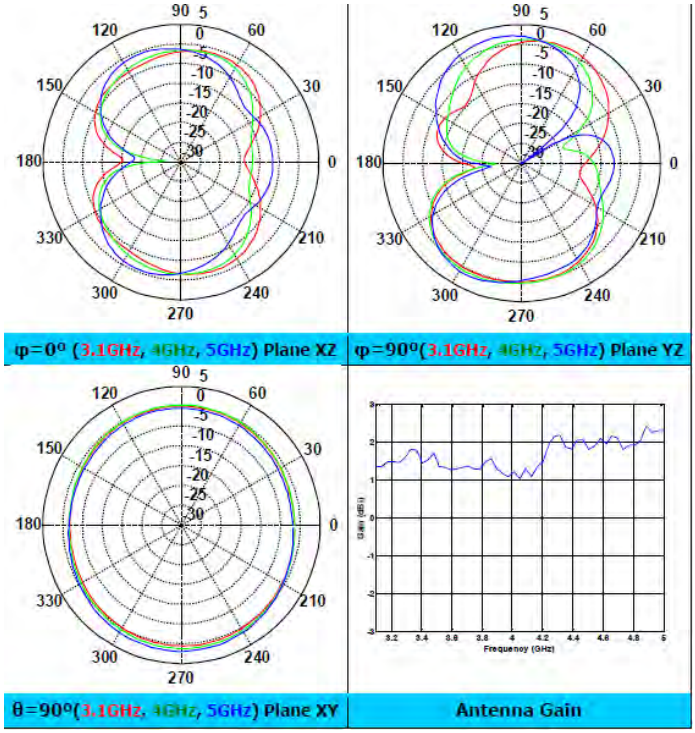

Figure 2.6: Antenna patterns of the *Fractus* antennas defined into *3DTruEM*

2.3 Simulation Results

Figures 2.7 and 2.8 show Impulse Response simulation results for various Line of Sight and Non-Line of Sight cases. In these figures the solid pink line represents the UWB IR calculated using the developed method and is printed on

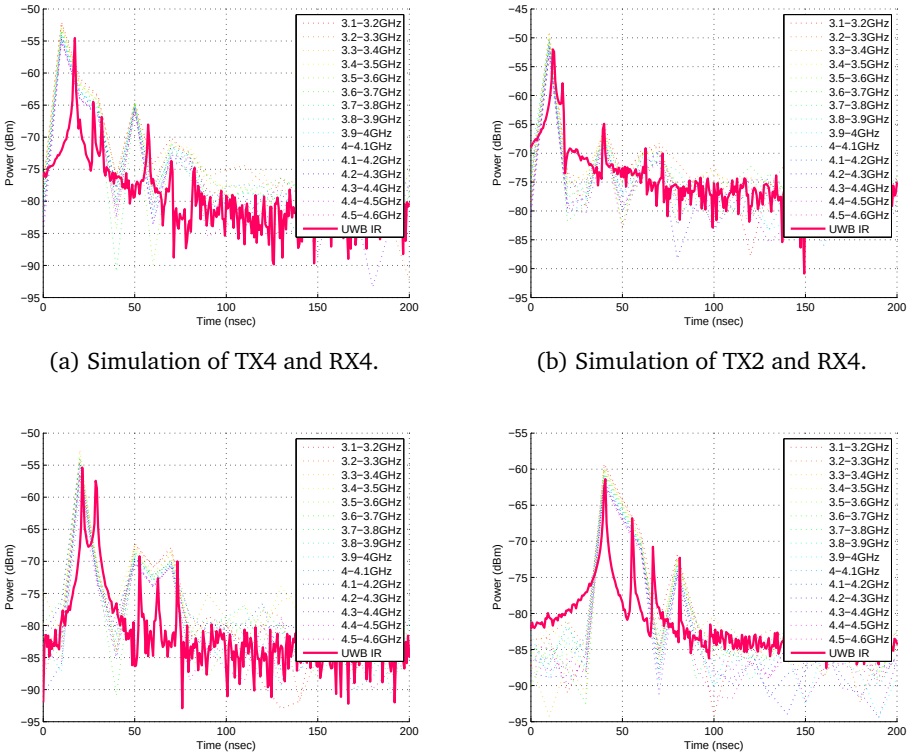

(a) Simulation of TX4 and RX4.

(b) Simulation of TX2 and RX4.

(c) Simulation of TX3 and RX4.

(d) Simulation of TX3 and RX3.

Figure 2.7: Simulation Results for various LoS TX Combinations.

top of the respective (15) narrowband responses which have been used for the estimation of the combined UWB IR.

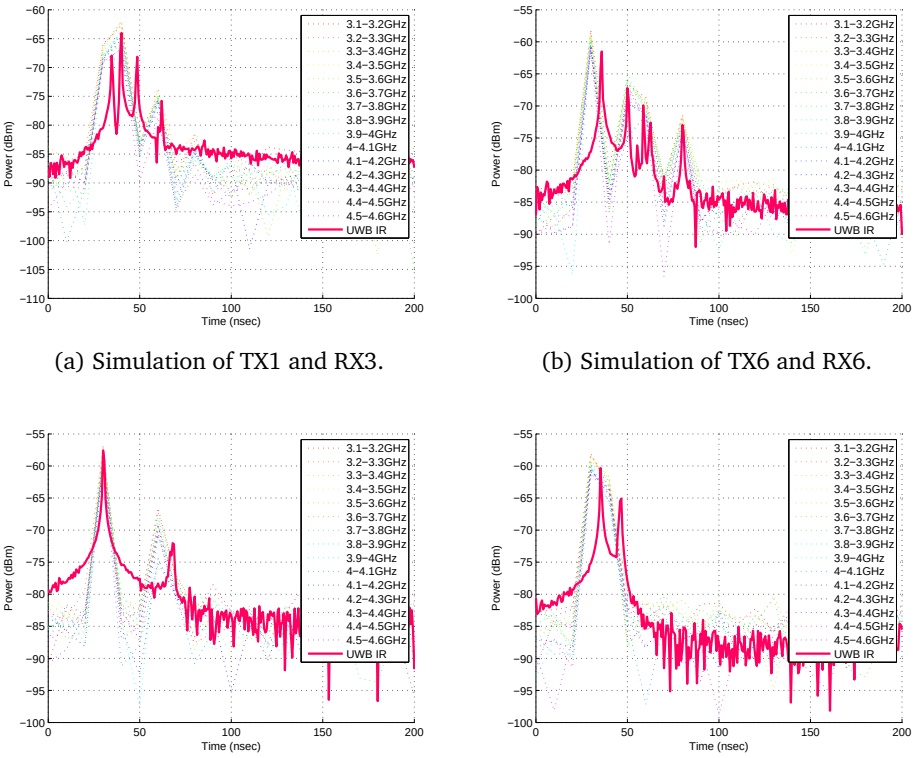

(a) Simulation of TX1 and RX3.

(b) Simulation of TX6 and RX6.

(c) Simulation of TX3 and RX2.

(d) Simulation of TX6 and RX1.

Figure 2.8: Simulation Results for various NLoS TX Combinations.

3

Measurements

In order to verify the developed UWB model measurements were carried out in the same environment in the Frequency Domain. A *Rohde&Schwarz FSH-8* Vector Network Analyser (see Figure 3.1a) was used together with *Fractus* UWB patch antennas (see Figure 3.1b). Figure 3.2 shows two pictures of the measurement process. The antennas have been placed set at the same location and height for which they have been simulated. Inverse Fast Fourier Transform (iFFT) has been applied to the obtained frequency response for every TX-RX combination and the respective IR has been obtained. These IRs have been compared against to the respective IRs obtained using the UWB RT method. Some of the comparison results are shown in Figures 3.4 and 3.4 for Line of Sight and Non-Line of Sight Cases. They indicate a mean error of $5 \pm 2dB$ but most importantly the dominant propagation paths with respect to their arrival time are determined. This would be very useful for UWB positioning which utilises timing information.

(a) *R& S FSH8* VNA.

(b) *Fractus* UWB antennas.

Figure 3.1: UWB Measurement Hardware

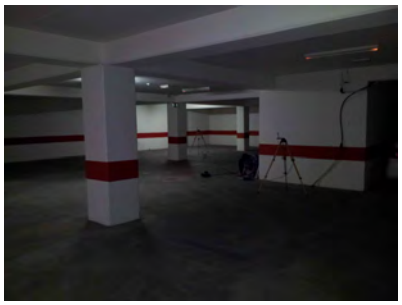

(a) Measurement Setup 1

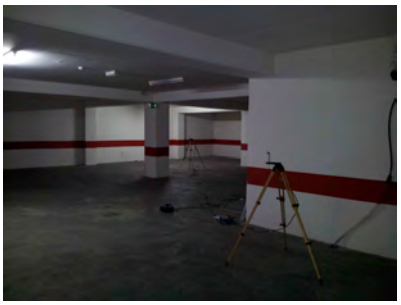

(b) Measurement Setup 1

Figure 3.2: Measurement Setup

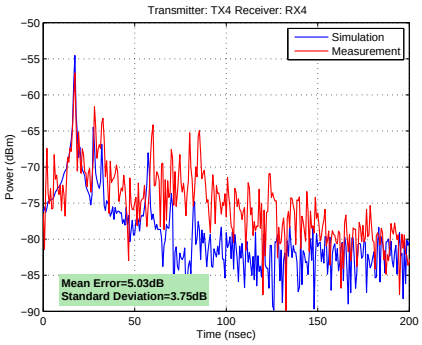

(a) Simulation Vs Measurement for TX4-RX4.

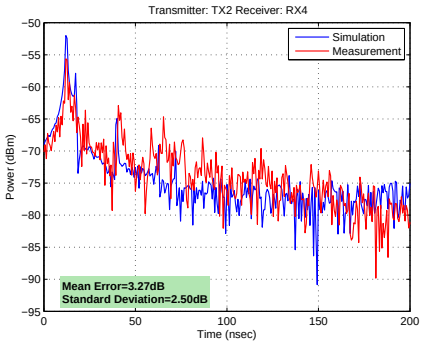

(b) Simulation Vs Measurement for TX2-RX4.

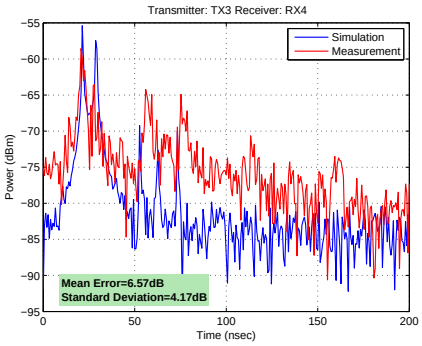

(c) Simulation Vs Measurement for TX3-RX4.

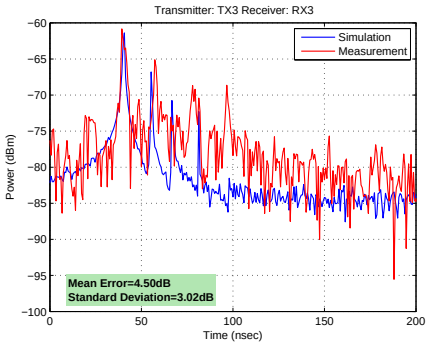

(d) Simulation Vs Measurement for TX3-RX3.

Figure 3.3: Comparison Results for various LoS TX Combinations.

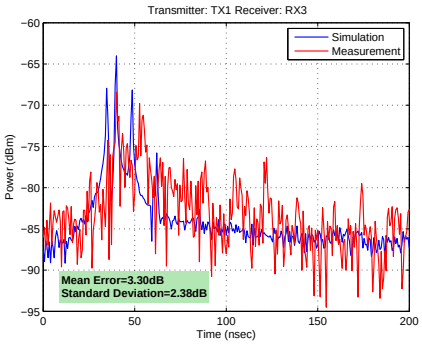

(a) Simulation Vs Measurement for TX1-RX3.

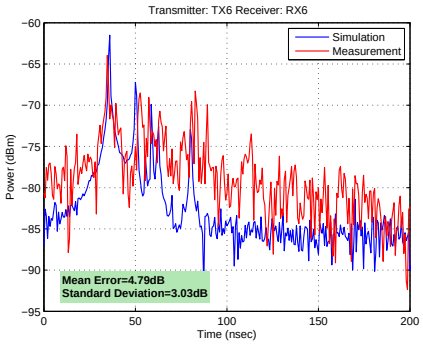

(b) Simulation Vs Measurement for TX6-RX6.

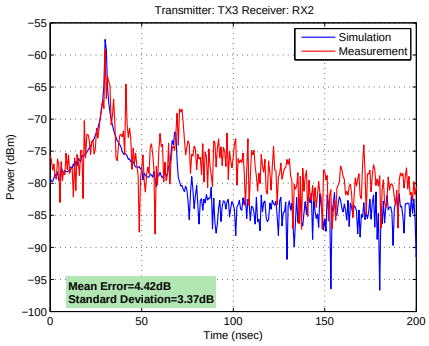

(c) Simulation Vs Measurement for TX3-RX2.

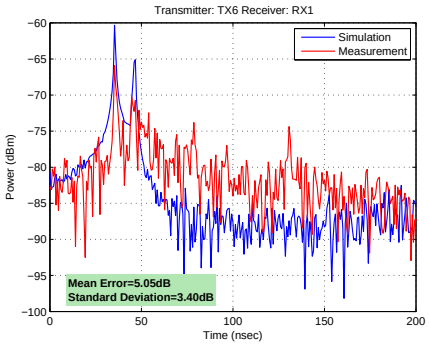

(d) Simulation Vs Measurement for TX6-RX1.

Figure 3.4: Comparison Results for various NLoS TX Combinations.

REFERENCES

[1] WHERE2 Partners. Deliverable D1.1: Scenarios and parameters. Deliverable FP7–ICT–248894, WHERE2, 2011.

[2] WHERE2 Partners. Deliverable D1.3: Short report on the first draft multi-link channel model. Deliverable FP7–ICT–248894, WHERE2, 2011.

[3] WHERE2 Partners. Deliverable D1.4: Short report on models that incorporate non-stationary time variant effects. Deliverable FP7–ICT–248894, WHERE2, 2011.

[4] WHERE2 Partners. Deliverable D1.5: Ray–tracing tools for dynamic positioning. Deliverable FP7–ICT–248894, WHERE2, 2011.

[5] WHERE2 Partners. D1.6: Ray-tracing tool for heterogeneous distributed positioning. Deliverable, WHERE2, 2011.

[6] WHERE2 Partners. Deliverable D2.2: Intermediate report on location information extraction. Deliverable FP7–ICT–248894, WHERE2, 2011.

[7] C.L. Holloway, M.G. Cotton, and P. McKenna. A model for predicting the power delay profile characteristics inside a room. *IEEE Trans. Veh. Technol.*, 48(4):1110–1120, 1999.

[8] J.B. Andersen, J.O. Nielsen, G.F. Pedersen, G. Bauch, and J.M. Herdin. Room electromagnetics. *IEEE Antennas Propag. Mag.*, 49(2):27–33, 2007.

[9] Heinrich Kuttruff. *Room Acoustics*. Taylor & Francis, London, fourth edition, 2000.

[10] David A. Hill. *Electromagnetic Fields in Cavities: Deterministic and Statistical Theories*. IEEE Press Series on Electromagnetic Wave Theory. Wiley/IEEE Press, Piscataway, NJ, 2009.

[11] G. Steinböck, T. Pedersen, B.H. Fleury, W. Wang, and R. Raulefs. Model for the Path Loss of In-room Reverberant Channels. In *Vehicular Technology Conference (VTC 2011-Spring), 2011 IEEE 73rd*, pages 1–5, May 2011.

[12] G. Steinböck, T. Pedersen, B.H. Fleury, W. Wang, and R. Raulefs. Distance Dependent Model for the Delay Power Spectrum of In-room Reverberant Channels. *submitted to IEEE Trans. Antennas Propagat.*, 2012.

[13] G. Turin, F. Clapp, T. Johnston, S. Fine, and D. Lavry. A statistical model of urban multipath propagation channel. *IEEE Trans. Veh. Technol.*, 21:1–9, February 1972.

[14] Adel A. M. Saleh and Reinaldo A. Valenzuela. A statistical model for indoor multipath propagation channel. *IEEE J. Select. Areas Commun.*, SAC-5(2):128–137, February 1987.

[15] N. Jalden, P. Zetterberg, B. Ottersten, Aihua Hong, and R. Thomä. Correlation Properties of Large Scale Fading Based on Indoor Measurements. In *Wireless Communications and Networking Conference (WCNC)*, March 2007.

[16] H Sugahara, Y Watanabe, T Ono, K Okanoue, and S Yarnazaki. Development and experimental evaluations of "rs-2000" - a propagation simulator for uwb systems. In *International Workshop on Ultra Wideband Systems*, 2004.

[17] WHERE2 Partners. D2.2: Intermediate: Location information extraction. Deliverable, WHERE2, 2012.

[18] Y. Corre and Y. Lostanlen. 3D urban EM wave propagation model for radio network planning and optimization over large areas. *IEEE Transactions on Vehicular Technologies*, Sept 2009.

[19] B.H. Fleury, M. Tschudin, R. Heddergott, D. Dahlhaus, and K. Pedersen. Channel Parameter Estimation in Mobile Radio Environments Using the SAGE Algorithm. *IEEE J. Select. Areas Commun.*, 17(3):434–450, March 1999.

[20] WHERE2 Partners. Deliverable D2.3: Intermediate report on self-learning positioning using inferred context information. Deliverable FP7–ICT–248894, WHERE2, 2011.

[21] Julien Stephan, Yves Lostanlen, Julien Keignart, Wei Wang, Dirk Slock, and Florian Kaltenberger. Deliverable 4.1: Measurements of location-dependent channel features. Deliverable, WHERE1, 2008.

[22] B. Uguen, M. Laaraiedh, B. Denis, J. Keignart, J. Stephan, and Y. Lostanlen. Extraction and characterization of location-dependent uwb radio features with practical implications for indoor positioning. In *Proc. of 18th European Wireless Conference (EW2012)*, Poznan, Poland, April 2012.

[23] J.W. McKown and Jr. Hamilton, R.L. Ray tracing as a design tool for radio networks. *Network, IEEE*, 5(6):27 –30, nov. 1991.

[24] S.Y. Seidel and T.S. Rappaport. Site-specific propagation prediction for wireless in-building personal communication system design. *Vehicular Technology, IEEE Transactions on*, 43(4):879 –891, nov 1994.

[25] M.F. Catedra, J. Perez, F. Saez de Adana, and O. Gutierrez. Efficient ray-tracing techniques for three-dimensional analyses of propagation in mobile communications: application to picocell and microcell scenarios. *Antennas and Propagation Magazine, IEEE*, 40(2):15 –28, apr 1998.

[26] E. Plouhinec and B. Uguen. Ray-tracing and multiple reflections inside materials applied to UWB localization. In *Electromagnetics in Advanced Applications, 2009. ICEAA '09. International Conference on*, pages 674 –677, sept. 2009.

[27] Josefa Gomez, Abdelhamid Tayebi, Francisco Saez de Adana, and Oscar Gutierrez. 3D Localization method based on ray-tracing considering the presence of moving people. In *Antennas and Propagation (EuCAP), 2010 Proceedings of the Fourth European Conference on*, pages 1–4, april 2010.

[28] P. Meissner, D. Arnitz, T. Gigl, and K. Witrisal. Analysis of an indoor UWB channel for multipath-aided localization. In *Ultra-Wideband (ICUWB), 2011 IEEE International Conference on*, pages 565 –569, sept. 2011.

[29] M. Raspopoulos, C. Laoudias, L. Kanaris, A. Kokkinis, C. G. Panayiotou, and S. Stavrou. 3D Ray Tracing for Device-Independent Fingerprint-based Positioning in WLANs. In *2012 Workshop on Positioning, Navigation, and Communication (WPNC)*, March 2012.

[30] Bernard Uguen, Nicolas Amiot, and Mohamed Laaraiedh. Exploiting the Graph Description of Indoor Layout for Ray Persistency Modeling in Moving Channel. In *Proceedings of the 6th European Conference on Antennas and Propagation (EuCAP 2012)*, Prague, Czech Republic, March 2012.

[31] W. Wang, T. Jost, and A. Dammann. Estimation and Modelling of NLoS Time-Variant Multipath for Localization Channel Model in Mobile Radios. In *IEEE Global Communications Conference (GLOBECOM)*, Miami, USA, Dec. 2010.

[32] T. Zwick, C. Fischer, and W. Wiesbeck. A Stochastic Multipath Channel Model Including Path Directions for Indoor Environments. *IEEE J. Select. Areas Commun.*, 20:1178–1192, 2002.

[33] N.L. Pedersen, D. Shutin, C. Navarro Manchón, and B.H. Fleury. Sparse estimation using Bayesian hierarchical prior modeling for real and complex models. *submitted to IEEE Trans. Signal Processing, arXiv:1108.4324 [stat.ML]*, April 2012.

[34] D.P. Wipf and B.D. Rao. Sparse Bayesian learning for basis selection. *IEEE Trans. Signal Processing*, 52(8), August 2004.